

A SEGMENT-BASED APPROACH TO CLASSIFY AGRICULTURAL LANDS
USING MULTI-TEMPORAL KOMPSAT-2 AND ENVISAT ASAR DATA

A THESIS SUBMITTED TO
THE GRADUATE SCHOOL OF NATURAL AND APPLIED SCIENCES
OF
MIDDLE EAST TECHNICAL UNIVERSITY

BY

ASLI ÖZDARICI OK

IN PARTIAL FULFILLMENT OF THE REQUIREMENTS
FOR
THE DEGREE OF DOCTOR OF PHILOSOPHY
IN
GEODETIC AND GEOGRAPHIC INFORMATION TECHNOLOGIES

FEBRUARY 2012

Approval of the thesis:

**A SEGMENT-BASED APPROACH TO CLASSIFY AGRICULTURAL LANDS
USING MULTI-TEMPORAL KOMPSAT-2 AND ENVISAT ASAR DATA**

submitted by **ASLI ÖZDARICI OK** in partial fulfillment of the requirements for the degree of **Doctor of Philosophy in Geodetic and Geographic Information Technologies Department, Middle East Technical University** by,

Prof. Dr. Canan Özgen
Dean, Graduate School of **Natural and Applied Sciences** _____

Assoc. Prof. Dr. Ayşegül Aksoy
Head of Department, **Geodetic and Geographic Information Techn.** _____

Assoc. Prof. Dr. Zuhal Akyürek
Supervisor, **Geodetic and Geographic Information Techn. Dept., METU** _____

Examining Committee Members:

Assoc. Prof. Dr. Lütfi Süzen
Dept. of Geological Engineering, METU _____

Assoc. Prof. Dr. Zuhal Akyürek
Dept. of Civil Engineering, METU _____

Prof. Dr. Yusuf Kurucu
Dept. of Soil Science, Ege University _____

Prof. Dr. Yalçın Memlük
Dept. of Landscape Architecture, Ankara University _____

Assist. Prof. Dr. İlkay Ulusoy
Dept. of Electrical and Electronics Engineering, METU _____

Date: 10. 02. 2012

I hereby declare that all information in this document has been obtained and presented in accordance with academic rules and ethical conduct. I also declare that, as required by these rules and conduct, I have fully cited and referenced all material and results that are not original to this work.

Name, Last name: Aslı, Özdarıcı Ok

Signature :

ABSTRACT

A SEGMENT-BASED APPROACH TO CLASSIFY AGRICULTURAL LANDS USING MULTI-TEMPORAL KOMPSAT-2 AND ENVISAT ASAR DATA

ÖZDARICI OK, Aşlı

PhD. Department of Geodetic and Geographic Information Technologies

Supervisor: Assoc. Prof. Dr. Zuhal AKYÜREK

February 2012, 258 pages

Agriculture has an important role in Turkey; hence automated approaches are crucial to maintain sustainability of agricultural activities. The objective of this research is to classify eight crop types cultivated in Karacabey Plain located in the north-west of Turkey using multi-temporal Kompsat-2 and Envisat ASAR satellite data. To fulfill this objective, first, the fused Kompsat-2 images were segmented separately to define homogenous agricultural patches. The segmentation results were evaluated using multiple goodness measures to find the optimum segments. Next, multispectral single-date Kompsat-2 images with the Envisat ASAR data were classified by MLC and SVMs algorithms. To combine the thematic information of the multi-temporal data set, probability maps were generated for each classification result and the accuracies of the thematic maps were then evaluated using segment-based manner. The results indicated that the segment-based approach based on the SVMs method using the multispectral Kompsat-2 and Envisat ASAR data provided the best classification accuracies. The combined thematic maps of June-August and June-July-August provided the highest overall accuracy and kappa value around 92% and 0.90, respectively, which was 4% better than the highest result computed with the MLC method. The produced thematic maps were also evaluated based on field-based manner and the analysis revealed that the classification performances are directly proportional to the size of the agricultural fields.

Keywords: Multi-Temporal Image Classification, Agriculture, SVMs, Kompsat-2, Envisat ASAR

ÖZ

TARIM ALANLARININ ÇOK TARİHLİ KOMPSAT-2 VE ENVİSAT ASAR GÖRÜNTÜLERİ KULLANILARAK SINIFLANDIRILMASINDA BÖLÜT TABANLI BİR YAKLAŞIM

ÖZDARICI OK, Aslı

Doktora, Jeodezi ve Coğrafi Bilgi Teknolojileri Bölümü

Tez Yöneticisi: Doç. Dr. Zuhal AKYÜREK

Şubat 2012, 258 sayfa

Tarım Türkiye’de önemli bir role sahiptir, bu nedenle sürdürülebilirliğinin sağlanabilmesi açısından tarımsal faaliyetlerin otomatik yaklaşımlar ile yürütülmesinin önemi büyüktür. Bu çalışmanın amacı, Türkiye’nin kuzey batısında yer alan Karacabey ovasında yetiştirilen sekiz ürün türünün çok tarihli Kompsat-2 ve Envisat ASAR uydu görüntüleri kullanılarak sınıflandırılmasıdır. Bu amaç doğrultusunda, ilk olarak, homojen tarım alanlarını bulabilmek için keskinleştirilmiş (fused) Kompsat-2 görüntülerine bölütleme işlemi uygulanmıştır. En uygun bölütlerin belirlenebilmesi için üretilen bölütler çoklu istatistiksel indeksler yardımıyla değerlendirilmiştir. Ardından çok bantlı ve tek tarihli Kompsat-2 görüntüleri, Envisat ASAR verileri ile En Büyük Olasılık ve Destek Vektör Makineleri sınıflandırma yöntemleri yardımıyla sınıflandırılmıştır. Çok tarihli görüntülerin sınıflandırılması yoluyla elde edilen tematik haritala ait bilgilerin birleştirilebilmesi amacıyla her bir tematik harita için olasılık haritaları üretilmiş ve tematik haritalara ait doğruluk oranları bölüt bazında değerlendirilmiştir. Sonuçlar, en yüksek sınıflandırma doğruluklarının Kompsat-2 ve Envisat ASAR görüntülerinin bölüt tabanlı Destek Vektör Makineleri yöntemiyle sınıflandırılması sonucunda elde edildiğini göstermiştir. Tematik haritaların birleştirilmesi yoluyla elde edilen Haziran-Ağustos ve Haziran-Temmuz-Ağustos aylarına ait görüntülerin en yüksek genel ortalama hataları

(%92 genel hata oranı ve 0.90 kappa) sağladığı gözlenmiştir. Elde edilen doğrulukların bölüt tabanlı olarak gerçekleştirilen En Büyük Olasılık sınıflandırma yöntemiyle elde edilen en iyi sonuçtan %4 oranında daha yüksek olduğu saptanmıştır. Bu çalışmada ayrıca, üretilen tematik haritalar gerçek tarım parselleri ile karşılaştırılarak parsel tabanlı analiz sonuçları da incelenmiştir. Analizler, sınıflandırma doğruluklarının parsel büyüklükleri ile doğru orantılı olduğunu göstermiştir.

Anahtar Kelimeler: Çok Tarihli Görüntü Sınıflandırması, Tarım, Destek Vektör Makineleri, Kompsat-2, Envisat ASAR

To
My Parents
and
My Husband

ACKNOWLEDGMENTS

I would like to express my deepest gratitude to my supervisor, Assoc. Prof. Dr. Zuhâl Akyürek, for her guidance, encouragement, and support during the preparation of this thesis. I will never forget her assistance and positive approach during my PhD period.

I owe my deepest gratitude to Assoc. Prof. Dr. Lütflî Süzen and Assist. Prof. Dr. İlkey Ulusoy for their contributions and comments during the thesis. I would like to extend my gratitude to Prof. Dr. Yusuf Kurucu and Prof. Dr. Yalçın Memlük, for their valuable comments, suggestions, and evaluations.

I would like to thank Prof. Dr. Peng Gong for his valuable comments, assistance, and understanding during my visit to University of California, Berkeley, USA for six months. It was honor for me to study under his supervision.

I would like to thank my dear friends Xiaohong Gao and Shaoqing Shen for their friendship during the time I spent in Berkeley.

I would like to show my gratitude to amazing boy, Aydın and his parents Maria, and Selim Zeyrek for their friendship, helps, and support during my visit to Berkeley. Words cannot express what I owe them. They are my second family in USA. Thank you for everything!

I would like to thank my close friends Sibel Korkmazgil, Ferhunde Ayşin, Sündüs Yerdelen, Aslıhan Osmanođlu, Duygu Fındık and Mine Müftüler for their motivation, patience, and friendship, which gave me strength to overcome the difficulties during this thesis. Thank you girls!

I would like to thank my friends in Geodetic and Geographic Information Technologies (GGIT) department for their friendship and encouragement.

I also would like to thank farmers and staff working in irrigation department of Karacabey Plain for their helps during the field observations of this research.

I would like to express my heartfelt gratitude to my mother Fatma, my father Akil, my sisters Öznur and Gül, whose patient love and motivation enabled me to complete this thesis. Thank you for everything!

I cordially would like to thank my mother-in-law Semra Ok and father-in-law Nuri Ok for their motivation, encouragement, and patient during the preparation of this thesis. I also would like to send my special thanks my mother-in-law Semra Ok for helps especially for the celebration party.

I would like to send my special thanks to my husband Ali Özgün Ok. Words alone cannot express what I owe him for his encouragement, guidance, insight, and patience throughout this thesis. I am very happy to have a husband like you. Thank you for everything!

This research was supported by ÖYP research foundation for six years and Scientific and Technological Research Council of Turkey for six months. The Kompsat-2 data was provided by a project called DAP-2008-07-02-07 funded by Geodetic and Geographic Information Technologies (GGIT) Department in Middle East Technical University (METU) in Turkey.

TABLE OF CONTENTS

ABSTRACT.....	iv
ÖZ	vi
ACKNOWLEDGEMENTS.....	ix
TABLE OF CONTENTS.....	xi
LIST OF TABLES.....	xiv
LIST OF FIGURES	xix

CHAPTERS

1. INTRODUCTION	1
1.1 Purpose and Scope.....	1
1.2 Objectives of the Study	4
1.3 The Software Used in the Study.....	4
1.4 Organization of the Thesis.....	5
2. LITERATURE REVIEW	6
3. STUDY AREA, DATA SET, AND DATA PREPARATION	24
3.1 Study Area and Data Set.....	24
3.1.1 Study Area.....	24
3.1.2 Data Set	28
3.1.2.1 Optical Data	28
3.1.2.2 Microwave Data.....	29
3.1.2.3 Vector Data.....	30
3.2 Data Preparation	31
3.2.1 Image Fusion	32
3.2.2 Atmospheric Correction of Kompsat-2 Data.....	34
3.2.3 Generation of Digital Terrain Model (DEM).....	34
3.2.4 Orthorectification	35
3.2.5 Map Updating.....	37
3.2.6 Speckle Reduction of Microwave Data.....	37

3.2.7	Generation of Backscattering Maps	39
4.	METHODOLOGY	43
4.1	Image Fusion	44
4.2	Image Segmentation	44
4.2.1	Mean-Shift Method	45
4.2.2	Quality Assessment of the Segments	46
4.3	Image Classification	51
4.3.1	Training Site Selection	52
4.3.2	Pixel-Based Analysis.....	60
4.3.2.1	Maximum Likelihood Classification (MLC).....	61
4.3.2.2	Support Vector Machine Classification.....	65
4.3.3	Probability Estimation.....	72
4.3.4	Segment-Based Analysis.....	76
4.3.5	Field-Based Analysis.....	80
5.	RESULTS AND DISCUSSION.....	82
5.1	Reference Data	82
5.2	Evaluation Method	84
5.3	Results of the Pixel-Based Analysis.....	89
5.3.1	Results of the MLC Method.....	89
5.3.2	Results of the SVMs Method	92
5.4	Results of the Segment-Based Analysis.....	94
5.4.1	Results of the MLC Method.....	94
5.4.2	Results of the SVMs Method	97
5.4.3	Results of the Field-Based Analysis.....	99
6.	CONCLUSIONS AND RECOMMENDATIONS	102
6.1	Conclusions	102
6.2	Recommendations	106
	REFERENCES	108
	APPENDICES	
A.	Photographs of the Crop Types Cultivated in the Study Area.....	121
B.	Görüntü Zenginleştirme Yöntemlerinin Tarımsal Ürün Sınıflandırması Üzerindeki Etkilerinin Değerlendirilmesi.....	129
C.	Evaluation of Image Fusion Methods on Agricultural Lands.....	157

D. A Comparison of SAR Filtering Techniques on Agricultural Area Identification.....	171
E. Ortalama Kaydırma ve Berkeley Görüntü Segmentasyon (BIS) Yöntemlerinin Çok Zamanlı Kompsat-2 Görüntüleri Kullanılarak Değerlendirilmesi.	187
F. Signature Separability Values.....	203
G. The Collected Training Samples.....	212
H. The Produced Thematic Maps.	214
I. Confusion Matrices of the Produced Thematic Maps.....	234
CURRICULUM VITAE.....	256

LIST OF TABLES

TABLES

Table 2.1	Summary of the previous works about the image classification methodologies.	21
Table 3.1	Acquisition details of the Kompsat-2 data used in this study.	28
Table 3.2	Technical details of the Kompsat-2 data used in this study.	29
Table 3.3	Acquisition details of the Envisat ASAR data used in this study.	29
Table 3.4	Technical details of Envisat ASAR data used in this study.	30
Table 3.5	Statistical evaluation indicators of the image fusion methods.	33
Table 3.6	The number of GCPs utilized, resampling method and the RMSE values computed for each image.	36
Table 4.1	Goodness measures used in the study	47
Table 4.2	The matrices of Bhattacharya distance for the four-band Kompsat-2 MS images taken in June, July, and August (a, c, e), with the Envisat ASAR data (b, d, f).....	55
Table 4.3	The matrices of Transformed Divergence Index for four-band Kompsat-2 MS images taken in June, July, and August (a, c, e), with the Envisat ASAR data (b, d, f).	58
Table 4.4	Gamma functions (γ) and penalty parameters(C) utilized for SVMs classification of the images	70
Table 5.1	Summary table of the analyzed data	85
Table 5.2	MLC results of the thematic maps computed for different image combinations based on pixel-based and segment-based manners.....	87
Table 5.3	SVMs results of the thematic maps computed for different image combinations based on pixel-based and segment-based manners.....	88
Table 5.4	The overall accuracies of the pixel-based classifications for the thematic maps generated.....	89
Table 5.5	Confusion matrix of the combined map of June-July-August	90
Table 5.6	Confusion matrix of the map of June including the class pea.....	91
Table 5.7	Confusion matrix for the map of July including the late corn.....	92

Table 5.8	The overall accuracies of the pixel-based classifications for the thematic maps	93
Table 5.9	Confusion matrix of the combined map of June-July-August	94
Table 5.10	The overall accuracies of the segment-based MLC classifications for the thematic maps generated	95
Table 5.11	Confusion matrix of the combined map of June-July-August	95
Table 5.12	The confusion matrix of the reclassified map including pea.....	96
Table 5.13	The confusion matrix of the reclassified map including late corn	97
Table 5.14	The overall accuracies of the segment-based SVMs classifications for the thematic maps	98
Table 5.15	Confusion matrix of the combined map of June-July	98
Table 5.16	Confusion matrix of the field-based analysis.....	100
Table 5.17	Confusion matrix of the small fields (0.1 ha and 4.9 ha).....	100
Table 5.18	Confusion matrix of the medium fields (5 ha and 9.9 ha).....	101
Table 5.19	Confusion matrix of the large fields (10 ha and 38 ha).....	101
Table F.1	The matrices of Bhattacharya distance for three-band, blue, green, red, of the Kompsat-2 MS images taken in June, July, and August (a, c, e), with the Envisat ASAR data (b, d, f).....	203
Table F.2	The matrices of Bhattacharya distance for three-band, green, red, NIR, of the Kompsat-2 MS images taken in June, July, and August (a, c, e), with the Envisat ASAR data (b, d, f).....	205
Table F.3	The matrices of Bhattacharya distance for three-band, blue, red, NIR, of the Kompsat-2 MS images taken in June, July, and August (a, c, e), with the Envisat ASAR data (b, d, f).....	208
Table F.4	The matrices of Bhattacharya distance for three-band, blue, green, NIR, of the Kompsat-2 MS images taken in June, July, and August (a, c, e), with the Envisat ASAR data (b, d, f).....	210
Table I.1	Confusion matrix of the (a) pixel-based and (b) segment-based MLC, respectively, for the map of June classified with Kompsat-2 data.	234
Table I.2	Confusion matrix of the (a) pixel-based and (b) segment-based MLC, respectively, for the map of July classified with Kompsat-2 data.....	235
Table I.3	Confusion matrix of the (a) pixel-based and (b) segment-based MLC, respectively, for the map of August classified with Kompsat-2 data	235

Table I.4	Confusion matrix of the (a) pixel-based and (b) segment-based MLC, respectively, for the map of June-July classified with Kompsat-2 data	236
Table I.5	Confusion matrix of the (a) pixel-based and (b) segment-based MLC, respectively, for the map of June-August classified with Kompsat-2 data	237
Table I.6	Confusion matrices of the (a) pixel-based and (b) segment-based MLC, respectively, for the map of July-August classified with Kompsat-2 data	237
Table I.7	Confusion matrices of the (a) pixel-based and (b) segment-based MLC, respectively, for the combined map (June-July-August) classified with Kompsat-2 data	238
Table I.8	Confusion matrix of the (a) pixel-based and (b) segment-based MLC, respectively, for the map of June classified with Kompsat-2 data and Envisat ASAR data	239
Table I.9	Confusion matrix of the (a) pixel-based and (b) segment-based MLC, respectively, for the map of July classified with Kompsat-2 data and Envisat ASAR data	239
Table I.10	Confusion matrix of the (a) pixel-based and (b) segment-based MLC, respectively, for the map of August classified with Kompsat-2 data and Envisat ASAR data	240
Table I.11	Confusion matrices of the (a) pixel-based and (b) segment-based MLC, respectively, for the map of June-July classified with the MS Kompsat-2 and Envisat ASAR data.....	241
Table I.12	Confusion matrices of the (a) pixel-based and (b) segment-based MLC, respectively, for the map of June-August classified with the MS Kompsat-2 and Envisat ASAR data.....	241
Table I.13	Confusion matrices of the (a) pixel-based and (b) segment-based MLC, respectively, for the map of July-August classified with the MS Kompsat-2 and Envisat ASAR data.....	242
Table I.14	Confusion matrices of the (a) pixel-based and (b) segment-based MLC, respectively, for the combined map (June-July-August) classified with the MS Kompsat-2 and Envisat ASAR data	243
Table I.15	Confusion matrix of the (a) pixel-based and (b) segment-based SVM, respectively, for the map of June classified with Kompsat-2 data.....	243

Table I.16	Confusion matrix of the (a) pixel-based and (b) segment-based SVM, respectively, for the map of July classified with Kompsat-2 data.....	244
Table I.17	Confusion matrix of the (a) pixel-based and (b) segment-based SVM, respectively, for the map of August classified with Kompsat-2 data	245
Table I.18	Confusion matrix of the (a) pixel-based and (b) segment-based SVM, respectively, for the map of June-July classified with Kompsat-2 data.....	245
Table I.19	Confusion matrix of the (a) pixel-based and (b) segment-based SVM, respectively, for the map of June-August classified with Kompsat-2 data	246
Table I.20	Confusion matrix of the (a) pixel-based and (b) segment-based SVM, respectively, for the map of July-August classified with Kompsat-2 data	247
Table I.21	Confusion matrix of the (a) pixel-based and (b) segment-based SVM, respectively, for the map of the combined map (June-July-August) classified with Kompsat-2 data	247
Table I.22	Confusion matrix of the (a) pixel-based and (b) segment-based SVM, respectively, for the map of June classified with Kompsat-2 data and Envisat ASAR data	248
Table I.23	Confusion matrix of the (a) pixel-based and (b) segment-based SVM, respectively, for the map of July classified with Kompsat-2 data and Envisat ASAR data	249
Table I.24	Confusion matrix of the (a) pixel-based and (b) segment-based SVM, respectively, for the map of August classified with Kompsat-2 data and Envisat ASAR data	249
Table I.25	Confusion matrix of the (a) pixel-based and (b) segment-based SVM, respectively, for the map of June-July classified with Kompsat-2 data and Envisat ASAR data	250
Table I.26	Confusion matrix of the (a) pixel-based and (b) segment-based SVM, respectively, for the map of June-July classified with Kompsat-2 data and Envisat ASAR data	251
Table I.27	Confusion matrix of the (a) pixel-based and (b) segment-based SVM, respectively, for the map of July-August classified with Kompsat-2 data and Envisat ASAR data.....	251

Table I.28	Confusion matrix of the (a) pixel-based and (b) segment-based SVM, respectively, for the combined map (June-July-August) classified with Kompsat-2 data and Envisat ASAR data	252
Table I.29	Segment-based results of the MLC method of the (a) class pea and (b) late corn computed for the Kompsat-2 and Envisat ASAR data.....	253
Table I.30	Confusion matrix of the MLC field-based results for all the reference fields computed for the Kompsat-2 and Envisat ASAR data.....	253
Table I.31	Confusion matrix of the field-based results for the MLC method computed for small fields (0.1-4.9 ha) with the Kompsat-2 and Envisat ASAR data	254
Table I.32	Confusion matrix of the field-based results for the MLC method computed for medium fields (5 - 9.9 ha) with the Kompsat-2 and Envisat ASAR data	254
Table I.33	Confusion matrix of the field-based results for the MLC method computed for large fields (10 - 38 ha) with the Kompsat-2 and Envisat ASAR data	254
Table I.34	Confusion matrix of the field-based results for the SVMs method computed for all the fields with the Kompsat-2 and Envisat ASAR data.....	255

LIST OF FIGURES

FIGURES

Figure 1.1	Variation of rural and urban population between the years 1995 and 2010 in Turkey.....	2
Figure 1.2	Variation of land use types between the years 1994 and 2009 in Turkey.	3
Figure 3.1	(a) Study area, (b) Kompsat-2 MS data taken in July, 11, 2008.....	25
Figure 3.2	(a) Soil types exist in the region, and (b) soil characteristics categorized based on the agricultural ability.....	26
Figure 3.3	Phenological characteristics of different crop types.....	27
Figure 3.4	Agricultural field boundaries of the study area.....	31
Figure 3.5	Flowchart of the pre-processing steps applied on Kompsat-2 and Envisat ASAR data.....	32
Figure 3.6	(a) Kompsat-2 PAN and, (b) MS image, (c) the fused result of the false color composite image.....	34
Figure 3.7	The generated DEM and the related statistics.....	35
Figure 3.8	a) Exiting vector data, (b) Digitized agricultural field boundaries.	37
Figure 3.9	A small part of (a) original Envisat ASAR data and (b) the Lee filtered image with a filter size of 5x5.....	38
Figure 3.10	Mean backscatter changes of the crops having common planting period; (a) corn,(b)tomato, (c) rice, (d) sugar beet, (e) wheat, and (f) grassland.	40
Figure 3.11	Mean backscatter values of the crops computed for each date.....	41
Figure 4.1	The overall flowchart of the proposed method.....	43
Figure 4.2	The flowchart of the image segmentation section of the study.....	44
Figure 4.3	The selected reference polygons of the vector data.....	49
Figure 4.4	The optimum segmentation result and the results of goodness measures produced for the fused Kompsat-2 image taken in July (hs:5, hr:10).....	50
Figure 4.5	(a) The original segmentation result of the fused Kompsat-2 image (July) and (b) the final segmentation result of a small part of area.....	51
Figure 4.6	The selected training sites of the MS Kompsat-2 image taken in July. ...	53
Figure 4.7	The flowchart of the pixel-based image classification process.....	62

Figure 4.8	(a, c, e) The pixel-based results of the MLC for the four-band MS Kompsat-2 images acquired in June, July, and August, respectively. (b, d, f). The classification results of the same optical images with Envisat-ASAR data	64
Figure 4.9	Examples of hyper planes and the optimum hyper plane (b) in the linear situation.....	66
Figure 4.10	Linear hyper planes for two classes that do not totally separated.....	68
Figure 4.11	(a, c, e) The pixel-based results for the SVMs classification for the four-band MS Kompsat-2 images acquired in June, July, and August, respectively. (b, d, f). The classification results of the same optical images with Envisat-ASAR data	71
Figure 4.12	The combined thematic map (June-July-August) of the four-band Kompsat-2 and Envisat ASAR data by the MLC method with the probability map.....	73
Figure 4.13	(a) The combined thematic map of SVMs method and (b) its probability map	75
Figure 4.14	(a) Correctly classified pixels and (b) the new thematic map of June including pea.....	76
Figure 4.15	A small part of (a) false color composite MS Kompsat-2 image (taken in July), (b) the result of MLC classification (blue, green, red, NIR), and (c) the classification result of the segment-based approach overlaid with the produced segments.....	77
Figure 4.16	The flowchart of the segment-based image classification methodology	78
Figure 4.17	(a) The combined (June-July-August) thematic maps produced by the segment-based approach using MLC method of four-band Kompsat-2 MS images (b) with Envisat ASAR data.	79
Figure 4.18	(a) The combined (June-July-August) thematic maps produced by the segment-based approach using SVMs method of four-band MS Kompsat-2 images (b) with Envisat ASAR data	79
Figure 4.19	Agricultural fields classified based on the field-sizes.....	80
Figure 4.20	(a) The field-based results of the combined (June-July-August) thematic map of the	81

Figure 4.21	(a) The field-based result of the combined (June-July-August) thematic map of the SVMs method for four-band Kompsat-2 MS images with (b) the Envisat-ASAR data.....	81
Figure 5.1	Reference map for six crop types (corn, tomato, rice, sugar beet, wheat, and grass land)	83
Figure A.1	A wheat field in the test site (April 2008).....	121
Figure A.2	A wheat field in the test site (April 2008).....	121
Figure A.3	A wheat field in the test site (April 2008).....	122
Figure A.4	A wheat field in the test site (June 2008).....	122
Figure A.5	A wheat field in the test site (June 2008).....	123
Figure A.6	A sugar beet field in the test site (June 2008).....	123
Figure A.7	A tomato field in the test site (June2008).....	124
Figure A.8	A tomato field in the test site (June 2008).....	124
Figure A.9	A tomato field in the test site (June 2008).....	125
Figure A.10	An irrigated rice field in the test site (June 2008).....	125
Figure A.11	An irrigated rice field in the test site (June 2008).....	126
Figure A.12	A rice field in the test site (June 2008)	126
Figure A.13	A corn field in the test site (June 2008)	127
Figure A.14	A corn field in the test site (June 2008).....	127
Figure A.15	A corn field in the test site (June 2008).....	128
Figure G.1	The collected training sites of the MS Kompsat-2 image (green band) taken in June	212
Figure G.2	The collected training sites of the MS Kompsat-2 image (green band) taken in August.....	213
Figure H.1	Results of the pixel-based MLC of the four-band Kompsat-2 data (a, c, e, g, i, k, m) with the probability maps (b, d, f, h, j, l, n).....	214
Figure H.2	Results of the pixel-based MLC of the four-band Kompsat-2 and Envisat ASAR data (a, c, e, g, i, k, m) with the probability maps (b,d,f,h,j,l,n).216	216
Figure H.3	Results of the pixel-based SVMs of the four-band Kompsat-2 data (a, c, e, g, i, k, m) with the probability maps (b, d, f, h, j, l, n)	219
Figure H.4	Results of the pixel-based SVMs of the four-band Kompsat-2 and Envisat ASAR data (a, c, e, g, i, k, m) with the probability maps (b, d, f, h, j, l, n).....	221

Figure H.5	(a, c, e, g, i, k, m) The segment-based results of the MLC for the four-band MS Kompsat-2 images. (b, d, f, h, j, l, n) The classification results of the same optical images with the Envisat-ASAR data.	224
Figure H.6	(a, c, e, g, i, k, m) The segment-based results of the SVMs classification for the four-band MS Kompsat-2 images. (b, d, f, h, j, l, n). The classification results of the same optical images with Envisat ASAR data	226
Figure H.7	(a, c, e, g, I, k, m) The field-based results of the MLC method for the MS Kompsat-2 images, (b, d, f, h, i, l, n) The classification results of the same optical images with Envisat ASAR data.....	229
Figure H.8	(a, c, e, g, i, k, m) The field-based results of the SVMs method for the MS Kompsat-2 images acquired in June, July, and August, respectively. (b, d, f, h, j, l, n). The classification results of the same optical images with Envisat-ASAR data.....	231

CHAPTER 1

INTRODUCTION

1.1 Purpose and Scope

Due to the rapid increase of urban population, a dramatic decrease of agricultural lands of Turkey is evident as in the case of most of the developing countries (Fig.1.1). A rapid growth of urban population is clear within the fifteen years period between 1995 and 2010 (Figure 1.1) while a reasonable drop of the rural population between those years are also obvious. Besides, for the same time periods, the variation of land use types is depicted in Figure 1.2, in which a drop in the rural population is observed for arable lands while the sizes of the other land types are slightly increased. According to the figures, it can be stated that demand of agricultural products has gained more importance to provide agricultural needs in Turkey. In order to supply an extensive knowledge about the agricultural products, one important way is accurate yield estimation. In traditional agricultural applications, up-to-date information of crops is generally acquired by farmer declarations and/or ground visits of the fields. As already stated by Penã-Barragán et al. (2011), this procedure is not only subject to some errors and discrepancies in farmer declarations but also quite expensive and requires substantial time. Therefore, in order to perform fast and accurate yield estimation, automated methods based on the development stage are necessary to identify crop types of agricultural lands. At this point, analysis of satellite images and/or aerial photographs could be more reliable and cost-effective way to monitor agricultural areas. With the current developments involved in satellite sensor technology, the availability of high spatial resolution images increases (e.g. Geoeye, Worlview-2, QuickBird, Kompsat-2, and IKONOS). While that technological improvement provides several advantages to detect distinct small objects with a better precision in agricultural studies, it may increase the within field spectral variability of agricultural lands and affect the final accuracies of the thematic maps (e.g. Gong and

Howarth, 1990; De Wit and Clevers, 2004; Smith and Fuller, 2001). In order to handle this problem, discovering individual pixels as groups of connected pixels based on their textural and contextual properties are necessary to delineate more meaningful objects, which is the major interest of Object Based Image Analysis (OBIA) community (e.g. Gong et al. 1992; Gong and Howarth, 1992; Yu et al. 2006). In the literature, most of the researchers have developed effective segmentation algorithms and utilized the resulting segments in parallel to the OBIA (e.g. Schoenmakers et al. 1994; Cheng, 1995; Rydberg and Borgefors, 2001; Mueller et al. 2003; Zhan et al. 2005; Lee and Warner 2006; Chen et al. 2006; Li and Xiao., 2007; Lu et al. 2007; Wang et al. 2010; Xiao et al. 2010; Corcoran et al. 2010). Although a wide variety of results can be obtained through different parameter combinations and different softwares, additional steps are required to find more appropriate segmentation results.

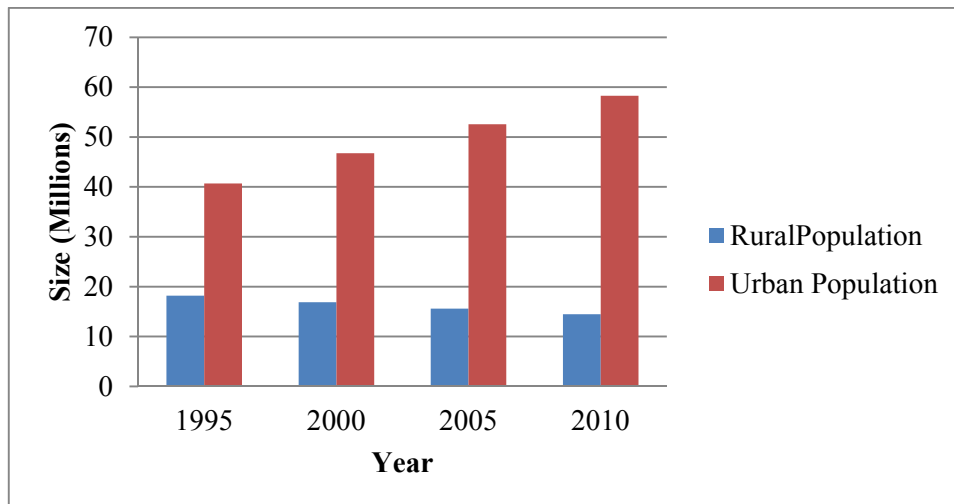


Figure 1.1 Variation of rural and urban population between the years 1995 and 2010 in Turkey (FAOSTAT, 2011)

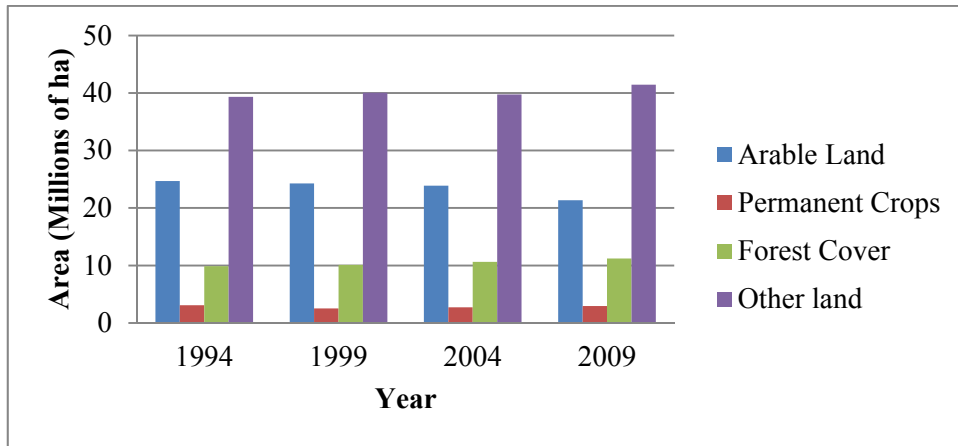


Figure 1.2 Variation of land use types between the years 1994 and 2009 in Turkey (FAOSTAT, 2011)

In crop classification, multi-temporal approaches provide advantages by including the phenological characteristics of the crops in the analyses. According to the studies related with multi-temporal approaches, reliable thematic maps are produced with high accuracies (e.g. Parmuchi et al. 2002; Ban, 2003; Blaes et al. 2005; Turker and Arikan, 2005; Stankiewicz, 2006; Liu et al. 2006; Wang et al. 2010; Penã-Barragán et al. 2011; Skriver et al., 2011). However, most of the multi-temporal studies are based on a rule-based approach, which requires a good knowledge about the data itself. Hence, in this study, a new multi-temporal classification strategy that combines different individual classification results in a joint probabilistic approach is proposed. To do that, three-dates (June, July, and August, 2008) multi-temporal Kompsat-2 MS (4m) and Envisat ASAR (15 m) data are utilized to classify eight crop types cultivated in a specific agricultural region of Turkey. Radar satellites sense objects in microwave portion of the electromagnetic spectrum, which provide information about surface roughness, dielectric properties, and moisture content. Thus, the contributions of microwave imagery on the multi-temporal classification performance are also investigated.

The crop types are classified by MLC and SVMs classification methods with pixel-based, segment-based, and field-based manners. Multi-temporal images are combined based on the maximum membership values of the pixels computed during the classifications. Effects of the field sizes on classification accuracies for the original agricultural fields are

also examined in this study. The produced thematic maps are then evaluated based on confusion matrices and the results are presented.

1.2 Objectives of the Study

The major objectives of this study are stated below:

- to develop an automated multi-temporal classification methodology to provide a reliable classification results for major crop types cultivated in the region,
- to examine the effect of segment-based approach on the classification performance,
- to investigate the performance of the microwave data on the classification framework,
- to compare the performances of the MLC and SVMs methods for the proposed multi-temporal classification,

Minor contributions of this study are:

- to define an effective image fusion method on the optical data used for the study,
- to produce optimum segmentation results for the agricultural fields by multiple goodness measures,
- to provide an automated strategy to collect training samples from segments,
- to define an optimum speckle reduction method for the microwave data,
- to find out the field size effect on the classification performance.

1.3 The Software Used in the Study

Several software packages were utilized in this thesis. The Kompsat-2 images were fused with the “Panshar” module of PCI Geomatica. For the other image fusion methods applied, ERDAS Imagine and ENVI softwares were utilized. Evaluation of the fused products was performed in MatLab environment. To atmospherically correct Kompsat-2 data the “Atcor2” module of PCI Geomatica was used. Speckle effect of Envisat ASAR data was minimized by the “Radar” module of ERDAS software. “OrthoEngine” module

of PCI Geomatica was utilized for DTM generation and orthorectification. Map updating and generation of backscattering maps were performed by “Focus” and “Sarsigm” modules of PCI Geomatica, respectively. Open source Edge Detection and Image SegmentatiON (EDISON) software was utilized for the segmentation process. Performance evaluation of the segments was carried out by different open source software called Alpha. The classification of the images was performed via ERDAS and ENVI softwares. The proposed multi-temporal classification was performed by a script written in MatLab environment. Finally, the evaluation of the thematic maps was performed by PCI Geomatica.

1.4 Organization of the Thesis

This thesis is organized as six chapters, in which the improvement of the study is examined in sequence.

Chapter 2 provides an extensive survey about image classification approaches on different plant species followed by an introduction section presented in Chapter 1.

In Chapter 3, characteristics of the study area, technical details of the Kompsat-2, Envisat ASAR, and the other data utilized in the study and data preparation steps are presented. In this part, the data preparation steps are examined as seven titles: (i) image fusion, (ii) atmospheric correction, (iii) DTM generation, (iv) orthorectification, (v) map updating, (vi) speckle reduction, and (vii) generating backscattering maps.

Methodological details are presented in Chapter 4, where the image segmentation methods applied on the fused images and the evaluation of the segments are included. The classification algorithms of MLC and SVMs methods are described with the probabilistic approach in this section.

In Chapter 5, the results computed for the thematic maps are presented and discussed. Confusion matrices of the thematic maps provided the highest classification performance is presented in this chapter.

Finally, chapter 6 involves the conclusions and recommendations for future studies.

CHAPTER 2

LITERATURE REVIEW

Automated image classification has an important role in remote sensing, which “lies at the heart of the transformation from satellite image to usable geographic products” (Wilkinson, 2005). It is a most commonly used technique to extract thematic information from remotely sensed data. However, classifying remotely sensed data into a thematic map still remains a big challenge. The study conducted by Lu and Weng (2007) presented a survey of image classification methods. Different factors such as; complexity of the landscape, the remotely sensed data selected, the inclusion of different image processing steps and classification approaches are examined in this study. They concluded that the classification performance is affected by many factors therefore further researches are necessary to compare the available methods and develop new classification algorithms (Lu and Weng, 2007). Wilkinson (2005) evaluated the degree of progress in thematic mapping through the development of classification algorithms and approaches. He evaluated the results over 500 reported classification experiments published in the journal of Photogrammetric Engineering and Remote Sensing by examining various experimental parameters including the number of classes, size of feature vector, resolution of satellite data, test area etc. In the paper, the mean value of the kappa coefficient of all the studies was computed as 0.65 with a standard deviation of 0.19. He found out that while the individual studies performed between 15 years period have some advantages; this is not effective to explain the overall picture. This can be due to the quality of the collected ground truth data, classification methods of class labeling, spatial boundaries used for the class definition, scale, and fractal effects. The requirement of new methods to classify the complexity of new satellite products is another factor that limits the classification accuracy. Therefore, it is concluded that although important advances are achieved, further researches that develop advanced classification techniques and methodologies are necessary to improve the classification accuracies.

The experiments examined in the papers described above (Lu and Weng (2007) and Wilkinson (2007)) indicated that up to now a significant effort is dedicated to obtain reliable information from the earth surface by remote sensing technology. According to the studies, one significant way to obtain up-to-date information is to retrieve data from space-borne optical systems, in which the visible and infrared portions of the Electro Magnetic Spectrum (EMS) are very widely used. Acquisitions of that kind of systems are performed in day-time; therefore it is called *passive systems*. In recent decades, earth observation researchers have produced different satellite systems called *active systems* to produce information at varying atmospheric conditions even at night. The active systems are capable of collecting microwave data, which illuminates ground targets with its own radar beam. Therefore, the role of optical and microwave sensors in land-use monitoring can be viewed as complementary (Liu et al. 2006). This can be achieved by a number of image fusion methods, decision rules and/or multi-temporal approaches. The multi-temporal approaches are necessary especially for the agricultural studies, in which the phenological characteristics of the crops can be a good indicator to improve the classification performance.

Mapping of crop rotation using multi-temporal Indian Remote Sensing Satellite data was investigated by Panigrahy and Sharma (1997). They classified six major crop types by Maximum Likelihood Classification (MLC) method on seven images acquired from IRS LISS satellite. Results indicated that the images taken between October and March were found to be optimum to classify the major crop types cultivated in the area with an overall accuracy over 90%.

Tso and Mather (1999) investigated the performance of multi-temporal SAR imagery on crop discrimination based on pixel-based and field-based approach. In pixel-based classifications, they utilized raw intensity images, temporal subtraction images, filtered images, and textural features. The field-based analyses were performed by computing the mean backscatter coefficients of the fields. The images were classified by Maximum Likelihood classifier and Self Organizing Map (SOM) algorithm. For the pixel-based classifications, the best results were obtained around 60% for the filtered images. They found out that the texture features did not contribute the classification results. The images

classified with SOM algorithm improved the pixel-based results and the accuracy was computed greater than 75%.

Haack et al. (2000) evaluated the advantages of combining the optical and radar data. They used one of the traditional classification techniques, parallel-piped, on three study sites. The classification components included settlements, natural vegetation, and agriculture. They acquired that the fusion of optical and radar data improved the classification accuracy although different manipulations such as texture, spatial filtering, and de-speckling of the radar data are necessary in order to obtain more reliable results. It was observed that the image fusion improved the classification accuracies especially for the settlements.

Lee et al. (2001) examined fully polarimetric synthetic aperture radar (SAR) versus dual-polarization and single-polarization SAR data for P-, L-, and C-band frequencies in order to understand the land-use classification capabilities. Several crop types and trees were classified using complex Wishart distribution and Maximum Likelihood classification algorithm. For the fully polarimetric crop classification, the L-band provided the best classification accuracy of 81.65%. The classification result was dramatically increased to 91.21%, when each band was included in the classification. For dual polarization of the crops, the highest accuracy of 80.91% was computed for the L-band classification of complex HH and HV polarizations. Result of the single polarization data was revealed that the complex VV and HV polarizations were provided the best overall accuracy (59.72%). When the tree-based classifications were examined, it was observed that the P-band HH and HV polarizations were the best choice. On the other hand, in all cases, it was found out that the multi-frequency fully polarimetric SAR data was highly preferable.

Three-based approaches were examined by Dabrowska-Zielinska (2001) using optical and microwave remotely sensed data to estimate soil moisture. In the first method, NOAA/AVHRR images and meteorological data were utilized to estimate the moisture content of the soil by applying H₂O index (ratio of sensible to latent heat). Although there was a good relationship between soil moisture and the defined index, the application had some limitations due to the existing cloud cover. For the second method, the relationship between backscattering coefficient and soil moisture were analyzed using

ERS-2 SAR and NOAA data. It was concluded that soil moisture and geometrical properties of vegetation were primarily based on the backscattering coefficient. The third method was applied on the ERS-2 SAR and JERS SAR data set based on the Leaf Water Area Index. Highest correlation was observed between measured and estimated soil moisture. In conclusion, it was suggested that the incidence angles smaller than 30° was found to be more useful to estimate soil moisture and more reliable results can be obtained using radar satellites with various bands.

The effect of multi-temporal ERS-1 ASAR and Landsat TM data on classification performance of eight agricultural crop types cultivated in Canada were examined by Ban Y. (2003). Multiple image combinations were classified by a per-field Artificial Neural Network approach. The images were also classified by Maximum Likelihood Classifier for comparison purposes. Based on the results, it was observed that thematic maps produced with both SAR and Landsat TM image provided higher accuracies than the results of single-date images.

Classification accuracies of space-borne radar images were analyzed by Herold et al. (2005) for two test sites in East Africa and one in Nepal. Original radar data were investigated by applying post-classification smoothing and texture feature extraction techniques. A traditional classification technique was used to classify four land cover types. Analyses indicated that the original radar data did not separate the classes accurately. On the other hand, radar derived measures based on spatial attributes of the original data increased the overall accuracies of about 30% for each test site. The best results were obtained when two radar or textural/contextual information of radar derived bands were utilized in the study.

Panigrahy et al. (2005) examined various indices on the eastern coast of India to assess efficiency and sustainability of the cropping system generally computed by traditional survey methods. IRS and Radarsat SAR data taken multiple dates were utilized in the study. Three main indices called Multiple Cropping Index, Area Diversity Index, and Cultivated Land Utilization Index were evaluated. Results showed that spatial resolution of IRS data (188 m) was found to be effective to evaluate the rice cropping system. It was also pointed out the potential of RS and GIS in generating system database and management issues.

An investigation on potential SAR signatures to monitor rice crops using multi-temporal RADARSAT data was performed by Indrani and Chakraborty (2006). Two different separability tests and knowledge-based classification were utilized to detect rice. According to the separability tests it was observed that, except for the early rice, other rice classes were detachable. On the whole, knowledge-based classification of the rice and non-rice areas produced an overall accuracy over 98%.

An object-based classification using high spatial resolution airborne images Digital Airborne Imaging Spectrometer (DAIS) was carried out by Yu et al. (2006). In total, forty three vegetation and five non-vegetation classes were segmented by eCognition software. The classifications of the images were performed by K-NN algorithm in Classification and Regression Trees (CART) followed by the definition of feature objects derived from eleven spectral and ancillary channels, three intensity-hue-saturation (IHS) transform indices, and four topographic parameters. Accuracies obtained for the classification algorithm were then compared with the traditional MLC method. Results indicated that the object-based 1-NN classification method provided better performance than the pixel-based MLC classification method. They stated that although it was observed an average accuracy around 50%, using high spatial resolution images in mapping detailed vegetation was important. They also stated that sample size and quality, classification method, distribution and characteristics of the vegetation directly affect the classification performance.

Baghdadi et al. (2006) evaluated several ASAR acquisition configurations to acquire the surface soil moisture over bare soil from backscattering measurements. To do that, the ASAR images were acquired at various incidence angles and in HH and HV polarization combinations. The study consisted of two main steps: (i) a calibration phase and (ii) a validation phase. First, the data were divided into equal sets. Then, an empirical relationship was constructed between the backscattering coefficients and the ground truth volumetric soil moisture. Next, an inversion process was performed on the validation set in order to calculate the soil moisture. Results indicated that the higher accuracies could be obtained when both the high and low incidence angles were utilized. Poor results were acquired for only high incidence angles (40° - 43°). This is due to the strong variations formed between the low sensitivity to soil moisture and the high sensitivity of the

backscattering coefficients. One other result is that multi-polarized data did not provide significant improvement for estimating the soil moisture content.

Liu et al. (2006) investigated the winter wheat condition, grain yield and protein content with the help of Landsat TM and Envisat-ASAR data. Aims were (i) to find out the backscatter behavior of winter wheat of different growth stages, (ii) to examine and compare the ability of Envisat-ASAR and Landsat TM data for crop mapping, and (iii) to explore the information content and temporal limitations of Envisat-ASAR and Landsat TM for predicting yield and grain protein content of winter wheat. Three growth stages of the images and five indices were utilized to fulfill those objectives. Results indicated that reliable crop maps were produced when the Envisat-ASAR and Landsat TM data were used, together. It was stated that the acquisition dates of the images were quite important for the analyses. On the other hand, the spectral response of the SAR imagery on crop or soil changes was found to be difficult to explain. Therefore, it was stated that further analyses should be performed on SAR response related with soil and crop conditions under different incidence angles.

Crop characteristics were examined using multi-temporal series of Advanced Synthetic Aperture Radar (ASAR) data by Stankiewicz (2006). Different polarizations during two consecutive growing seasons were utilized in the study. Crop signatures were computed as an arithmetic mean using the agricultural plots. After the segmentation, a Neural Network (NN) classifier was utilized to classify crop types. Results indicated that the usage of various polarizations enhanced the classification accuracy. On the other hand, it was stated that high accuracies over 90% cannot be acquired using only the Envisat ASAR data.

Blaes et al. (2007) examined discrimination of six crop types based on simulated fifteen multi-temporal Envisat ASAR data. In the study, they not only evaluated the impact of spatial resolution on the field size but also the effect of multi-temporal data set in discriminating crop types. As a result, they found out that the multi-temporal data set was suitable to extract the crop types for the study. They obtained an overall accuracy of 83% using a field-based unsupervised classification strategy for large parcels.

Chen et al. (2007) tested different classification methods using single-band full polarization SAR data for agricultural crop identification. The classification methods used were Wishart-Maximum Likelihood Classifier (WML), Normal Distribution Probability Density Functions (PDF) Based Maximum Likelihood (NML) classifier, and Spatial-Spectral classifiers. Same training sites were utilized in order to perform a reliable comparison between the methods. Results indicated that only the Maximum Likelihood classifiers such as WML and NML provided better results. It was indicated that the results of WML were superior to the results of the NML if the intensity and phase images were directly used for training the classifier. They found out that when the images are supplied to a Spatial-Spectral-Based classifier, the accuracy could be increased.

Support Vector Machine (SVM) based classifier was examined in order to improve the classification accuracy by means of fusing additional data sources by Watanachaturaporn et al. (2008). Indian Remote Sensing Satellite IRS-1C Linear Imaging Self Scanning Sensor (LISS) III having spatial resolution of 23.5 m was acquired over a mountainous region including nine land cover types. Normalized Difference Vegetation Index (NDVI) and Digital Elevation Model (DEM) data were used as ancillary data to improve the quality of the classification. The SVM was implemented using different types of kernel. The results were compared with four other well-known classifiers called as MLC, a Decision Tree Classification (DTC), a Back-Propagation Nearest Neighbor (BPNN), and a Radial Basis Function Network (RBFNET) classifier using the same data set. A significant increase in the accuracy of the SVM-based classifier was observed by different kernels and the integration of the ancillary data.

Slazar et al. (2008) investigated the possibility of predicting corn yield using the Advanced Very High Resolution Radiometer (AVHRR) sensor with Partial Least Squares (PLS) method. In order to construct a model and validation, 23 years (1982-2004) of AVHRR data with the official corn yield statistics of Haskell County, USA, were utilized. The images were used to compare the Vegetation Health (VH) Indices, Vegetation Condition Index (VCI) and Temperature Condition Index (TCI). The PLS method was utilized to construct a model relating corn yield anomaly with VH indices. Results showed that the error of corn yield prediction in the study were around 6%, which was an acceptable error in that kind of applications.

A Support Vector Machines (SVMs) method was applied to classify paddy rice with multi-temporal ALOS/PALSAR imagery in southeast China by Zhang et al. (2009). Three growing seasons were selected to apply the SVMs classification on the images followed by computing backscattering coefficients of the data. A conditional kappa value of 0.87 was obtained by the SVMs method. Results revealed that besides the advantage of SVMs algorithm, multi-temporal analysis of the backscatter information improved the classification performance.

McNairn et al. (2009) investigated integration of optical and Synthetic Aperture Radar (SAR) imagery to classify Canada's large agricultural lands. In this way, they tried to answer some critical questions about level of accuracy, satellite data to be utilized, acquisition times of the satellite images, and classification model. In three-year project, RADARSAT-1 (HH), Envisat ASAR (alternating polarization: VV, VH), SPOT-4/5, and Landsat-5 images acquired during the growing period were classified based on Decision Tree, Neural Network and Maximum Likelihood classifiers. Multi-temporal optical and SAR data provided consistent results around 85% for each classification method. It was observed that the best results were computed when dual-polarization mode of VV-VH combination was used.

Wang et al. (2010) proposed a method using six scenes of multi-temporal, multi-polarization Envisat ASAR data to produce an agricultural map of Pearl River Delta in China. They established a decision tree followed by interpreting signature profiles of land cover types. Results indicated that basic land cover types could be classified effectively with overall accuracy of 80% when the multi-temporal, multi-polarization data were utilized. They also proved that the decision tree approach was appropriate to get satisfactory classification results if appropriate images were used based on the growing periods of the agricultural classes.

Both object-based and knowledge-based strategies were applied on the fused QuickBird MS and RADARSAT SAR data to classify sixteen urban land cover types by Ban et al. (2010). It was observed from the general results that the highest accuracy around 90% was obtained when optical and SAR data were classified along with object-based and rule-based approaches.

Among the studies published so far, object-based image analyses received considerable attention over pixel-based analyses in land cover classifications due to the reason that better results can be achieved. At this point two approaches became popular especially for agricultural applications: (i) field-based, and (ii) segment-based. In field-based classification, the field geometry defines the spatial relationship between the pixels falling within the field by the rule-based re-labeling of image classification results. Jansen et al. (1990) treated the map polygons as objects by expecting only one cover type was available in each polygon. An improvement of 12% and 20% over a per-pixel MLC were reported for two agricultural test sites.

Pedley and Curran (1991) compared per-pixel and per-field classification approaches using SPOT High Resolution Visible (HRV) imagery. The study area covers 10 km by 10 km with well drained and virtually flat area. They applied two classification approaches on the SPOT image based on MLC method; however they could not acquire high classification accuracy from those classifications. Therefore, they refined the results by using prior probabilities, low-pass filters, and image texture. At the end of the analyses, they had nine classification results, a basic and four refined versions of the per-pixel classification and three refined versions of the per-field classification for twelve classes. Among all the results, the highest accuracy was obtained for the per-field classification as 62.1% using the prior probabilities and image texture.

Congalton et al. (1998) proposed a methodology to develop a water model from remotely sensed data using an agricultural crop map and other vegetation on Lower Colorado River Basin. For that purpose, Landsat Thematic Mapper image taken four times per-year integrated with GIS were used to produce an accurate map and to monitor land cover types. Final thematic accuracy was computed around 90% via the proposed automated extraction process and data exploration techniques.

Aplin et al. (2001) developed a set of classification methods to detect land cover types on a per-field basis from high resolution satellite imagery. A Compact Airborne Spectrographic Imager (CASI) with 4m resolution was used to classify urban and rural areas in the United Kingdom. Aim of the study was to develop four tools related with the per-field classification to improve the results. Results indicated that of the methods the per-field texture filtered classification provided the best performance.

A field-based land cover map was generated for Jersey by Smith and Fuller (2001), in which a vector land parcel boundaries were utilized to subdivide the images. The accuracy of the per-field approach was increased by the knowledge-based corrections; a GIS database was produced at the end of the analyses with accuracy between 85% and 95%.

De Wit and Clevers (2004) developed a methodology by integrating multi-temporal and multi-sensor satellite imagery for producing a crop map of the Netherlands. They achieved 90% overall accuracy and concluded that per-field classification was a more effective way to produce crop maps than per-pixel approach. They also stated that dynamic crop boundaries can be determined easily by applying automatic segmentation techniques.

Lloyd et al. (2004) classified the land cover of a Mediterranean region using an artificial neural network (ANN) on per-field basis. In addition to spectral information, geo-statistical and textural measures extracted from the co-occurrence matrix were utilized.

Aplin and Atkinson (2004) developed a method to predict the missing field boundaries in order to increase the accuracy of per-field classification. The technique was based on a comparison of the within-field modal land cover proportion and local variance, which provided an indication of the missing field boundaries.

A tree-based vegetation classification was performed with fuzzy approach using multi-temporal NDVI data of India by Krishnaswamy et al. (2004). Two IRS LISS data acquired on November 1998 and April 1999 were used to classify eight vegetation types in the study. A knowledge-based classification strategy was applied with membership information and overall kappa value of vegetation classes were computed around 60%. They concluded that the proposed approach was relatively simple and cost effective to apply on other applications about vegetation classification. Results achieved for the proposed method were then utilized to complete the existing reference map of study area.

Blaes et al. (2005) aimed to develop a robust approach in order to discriminate agricultural crop types. Their strategy was based on a parcel-based classification of multi-

spectral and multi-temporal images. For that purpose, they used three optical imagery (SPOT XS and Landsat ETM), fifteen ERS and Radarsat data. Various combinations of images were utilized to classify a set of 6571 parcels into 39 crop types. A hierarchical classification strategy was adapted to the classification. Results showed that ERS and Radarsat data produced similar accuracies. When optical images were included in the classification, the accuracy was improved by at least 5%. They concluded that the performance of the classification depends on the sensor types and acquisition dates of the images.

A recent study was performed by Turker and Ozdarici (2011). They compared the effect of pre- and post-polygon classification performance on five agricultural crop types cultivated in north-west of Turkey using SPOT4, SPOT5, IKONOS, and QuickBird images. They obtained promising results for the post-polygon classification of IKONOS and QuickBird data, yielding overall accuracies above 83%.

Although satisfactory results are achieved for the field-based analyses, requirement of precise agricultural field boundaries is a big limitation to apply the method. This is because digitizing agricultural fields for especially large areas is an expensive and also time consuming process. Hence, in recent years, the field-based approach is replaced with more automated methods like *image segmentation*. The idea behind the image segmentation is to partition an image into multiple meaningful objects by searching homogeneity criteria/s in groups of connected pixels (Cheng et al., 2001). As a result of continuous development in satellite sensor technology, the availability of high spatial resolution space images has greatly increased. That development provided a significant improvement to perceive targets of images, while it increased the spectral within-field variability. In order to overcome the problems caused by the heterogeneous pixels within the field, the segment-based approaches have been increasingly utilized in parallel to Object Based Image Analysis (OBIA) (Blaschke, 2010). On the other hand, delineating meaningful features from satellite images is a critical step because the resulting output directly affects the accuracy of subsequent analyses. Hence, significant effort is spent to develop effective segmentation algorithms.

An early study that implemented a new segmentation method was performed on crop mapping in the Netherland for the combined high resolution optical and radar data by

Schoenmakers et al. (1994). Different segmentation products derived from SPOT XS (20m), CAESAR (5m), L band HH JPL-AIRSAR intensity data, a multi-channel combination of SPOT XS, and CAESAR data were compared in this study. The proposed segmentation method was based on region growing followed after edge detection. The edge detection method was utilized in order to compute per-pixel magnitude and edge direction. After applying an appropriate threshold on the edges, final edge composition was acquired. Then, a region growing method was applied within the closed polygons. They concluded that the segmented radar image provided better results after filtering the microwave data. It was observed that the filtered radar data exhibited good results as the optical data. On the other hand, the radar signal of L-band and HH polarization provided an ineffective performance to the increase of biomass. The best results were obtained when both optic and radar data was segmented together.

For the automated extraction of agricultural field boundaries, the multispectral segmentation method of ISODATA algorithm was examined by Rydberg and Borgefors in 2001. In the study, the segmentation algorithm was integrated with the edge information generated from the gradient edge detector. After computing the initial point distance from the edges, the segmentation of ISODATA classifier was applied on the SPOT image. Next, each segment was labeled with a separate id number. The number of regions produced by the segmentation procedure exceeded the actual number of the fields in the image. In order to merge the fields, a likelihood-ratio test was applied on the image. Results were compared with the manually extracted boundaries and 83% of the ground truth edges were detected by the proposed algorithm at correct pixels. However, some of the extra edges representing the within field variation were assumed to be correct.

Du et al. (2002) proposed an approach about segmentation of Synthetic Aperture Radar (SAR) images based on statistics of the amplitude and textural characteristics of the data. Both co-polarized and cross-polarized amplitude images were utilized in the study. In the first case, a filter that preserves the details and edges of the images was applied. Next, clusters were determined by using a scanning window. After the merging procedure applied on the segments, the images were classified using a Bayes Maximum Likelihood classifier. In the second case, the second-order Gaussian Markov random field models were applied on the unfiltered images to extract textural characteristics of the data. The results of the two methods were also compared in the study. It was found out that the

segmentation procedure on the filtered image reduced the speckle and preserved the edges. On the other hand, the segmentation of the texture measure blurred the borders and produced smaller unnecessary segments. As a result, the two methods could not eliminate the user's judgments and decision on splitting into sub-classes of the segments.

Wang et al. (2004) compared the classification performance of IKONOS and QuickBird image acquired under similar conditions to classify mangrove species. They used textural information together with object-based classification. The results showed that the classification accuracy did not increase when using only the panchromatic channels for each image. The results also revealed that object-based classification provided more accurate results for IKONOS imagery.

A segment-based approach was applied on a combination of optical and microwave data in Kaifeng Township in China by Xu et al. (2004) in order to extract agricultural crop structure using two dates of last season RADARSAT C band (HH) having 6.25 pixel size and two dates of mid-season Landsat ETM+ data (15m). Six classes were included in the analyses. After applying the pre-processing operations such as atmospheric and geometric corrections, reducing speckle effects, the optical and radar data were combined. The combined images were then segmented using an object oriented software, e-Cognition. Similar, adjacent pixels were aggregated by e-Cognition software. After the segmentation, a supervised image classification was applied on the images. It was stated that reliable results especially in residential areas were obtained for agricultural crops. The resulting accuracy (overall) was computed as 90% for the proposed approach.

Lee and Warner (2006) compared five aspatial and spatial methods in the study called "Segment based image classification". These are: (i) standard per-pixel MLC; (ii) Kettig and Landgrebe's ECHO classification; (iii) maximum likelihood classification using the segment mean; (iv) maximum likelihood classification using the segment divergence index; and (v) maximum likelihood classification using the segment probability density function (PDF). In order to compare these methods a digital aerial imagery with a 1m pixel size and four multispectral bands acquired over Morgantown, West Virginia, USA were utilized. At the end of the analyses, it was observed that the MLC using the segment PDF provided the highest accuracy of 0.78 (kappa) while the lowest accuracy was computed for the segment divergence index.

Xiao et al. (2010) applied a watershed segmentation algorithm on a multispectral high resolution satellite imagery using log Gabor filter. First, IKONOS panchromatic and multispectral images were converted from spatial domain to frequency domain. Next, log Gabor filtering was applied on the panchromatic band of the IKONOS image to compute texture features. Next, edges were extracted by the pan-sharpened multispectral IKONOS imagery. Both texture and edge features were represented with gradient in the study. In order to combine edge and texture information of the objects, a watershed transform was then applied based on the edges and integrated with the texture features. The proposed method provided effective performance and it also reduced the over-segmentation problem of the watershed algorithm. It was stated that further research/s should be performed to reduce computational load of the method.

An optimal region growing segmentation and the effect of the segments on classification accuracy was examined by Gao et al. (2011). A region growing algorithm was performed on Landsat multispectral imagery by setting nine different parameter combinations. The quality of the segments was evaluated by a statistical test, McNemar test, and segment-based classifications were performed on the image. Based on the results it was concluded that the classification accuracy is directly related with the quality of the segments.

A new methodology called Object-based Crop Identification and Mapping (OCIM) was developed Peña-Barragán et al. (2011) for thirteen major crop types cultivated in California by combining Object-based Image Analysis (OBIA) and decision tree (DT) algorithms. Several vegetation indices and textural features were obtained from the images taken three planting period and included in the OCIM methodology. Promising results were obtained when the extracted features were utilized in the classifications. It was observed that SWIR band had significant effect on the results to improve the classification performance.

Major wetland cover types and their classification uncertainty of Poyang Lake in China were investigated based on an object-based analysis and change detection method by Dronova et al. (201X). In the analyses, they utilized four multi-temporal images of Beijing-1 microsatellite (32m) acquired on November 2007 and March 2008. By spectral indices estimated from the satellite images, they proposed a new semi-automated training

site selection method. A hard classification was performed to the objects. The classification uncertainty was then evaluated by fuzzy thresholds. It was found out that the ‘Vegetation’ was the major class in all the scenes. The highest change was observed for ‘Mudflat’ among the other classes in the study.

Up to know, a significant number of research papers have been published in the field of land cover mapping (Table 2.1). However, most of the proposed methods or approaches are site-specific and requires extensive knowledge to adapt the rules on the data. Therefore, additional effort should be spent to develop fast and accurate classification approaches/algorithms based on the phenological characteristics of agricultural crop types (Wilkinson, 2005; Xiao et al., 2010).

Table 2.1 Summary of the previous works about the image classification methodologies

* Spatial resolutions of the satellites are categorized in the table as follows: High Spatial Resolution refers Pixel Size ≤ 5 , Medium Spatial Resolution means $5 > \text{Pixel Size} > 15$, Low Spatial Resolution is Pixel Size ≥ 15 .

Previous Study	Data Source	Spatial Resolution*		Method
		<i>Optic</i>	<i>Radar</i>	
Jansen et al. (1990)	Multispectral	Low	-	Maximum Likelihood
Pedley and Curran, (1991)	Multispectral	Low	-	Maximum Likelihood
Panigrahy and Sharma, (1997)	Multispectral	Low	-	Maximum Likelihood
Congalton et al. (1998)	Multispectral	Low	-	Maximum Likelihood
Aplin et al. (2001)	Multispectral	High	-	Maximum Likelihood
Rydberg and Borgefors (2001)	Multispectral	Low	-	ISODATA
Smith and Fuller (2001)	Multispectral	Low	-	Maximum Likelihood
Lloyd et al. (2004)	Multispectral	Low	-	Artificial Neural Network
Aplin and Atkinson (2004)	Multispectral	High, Low	-	Maximum Likelihood
Yu et al. (2006)	Multispectral	High	-	eCognition, K-NN algorithm
Lee and Warner (2006)	Multispectral	High	-	ECHO Classifier, Maximum Likelihood
Watanachaturaporn et al. (2008)	Multispectral	Low	-	Support Vector Machines
Slazar et al. (2008)	Multispectral	Low	-	Partial Least Squares
Xiao et al. (2010)	Multispectral	High	-	Watershed Segmentation
Gao et al. (2011)	Multispectral	Low	-	Maximum Likelihood
Peña-Barragán et al. (2011)	Multispectral	Low	-	Decision Tree Classifier

Table 2.1 (cont'd)

Previous Study	Data Source	Spatial Resolution*		Method
		<i>Optic</i>	<i>Radar</i>	
Dronova et al. (2011)	Multispectral	Low	-	eCognition Fuzzy Classification
Turker and Ozdarici (2011)	Multispectral	High, Medium, Low	-	Maximum Likelihood
Tso and Mather (1999)	Radar	-	Low	Maximum Likelihood, SOM
Lee et al. (2001)	Radar	-	Medium & Low	Maximum Likelihood
Du et al. (2002)	Radar	-	-	Segmentation, Maximum Likelihood, Gaussian Markov Random Field
Herold et al. (2005)	Radar	-	Low	Maximum Likelihood
Baghdadi et al. (2006)	Radar	-	Low	Index-Based Analyses
Stankiewicz (2006)	Radar	-	Low	Segmentation, Neural Network
Indrani and Chakraborty (2006)	Radar	-	Low	Rule-Based Classifier
Blaes et al. (2007)	Radar	-	Low	Spectral Indices, Backscattering Analyses
Chen et al. (2007)	Radar	-	Medium	Maximum Likelihood, ECHO
Zhang et al. (2009)	Radar	-	Medium	SVMs
Wang et al. (2010)	Radar	-	Low	Decision Tree Classifier
Schoenmakers et al. (1994)	Multispectral & Radar	Low	High	Segmentation
Haack et al. (2000)	Multispectral & Radar	Low	Medium	Parallel-Piped
Dabrowska-Zielinska (2001)	Multispectral & Radar	Low	Low	Spectral Indices, Backscattering Analyses

Table 2.1 (cont'd)

Previous Study	Data Source	Spatial Resolution*		Method
		<i>Optic</i>	<i>Radar</i>	
Ban, Y. (2003)	Multispectral & Radar	Low	Low	Maximum Likelihood Artificial Neural Network
De Wit and Clevers (2004)	Multispectral & Radar	Low	Low	Maximum Likelihood
Xu et al. (2004)	Multispectral & Radar	Low	Medium	E-Cognition
Krishnaswamy et al., (2004)	Multispectral	Low	-	Rule-Based Fuzzy Classifier
Blaes et al. (2005)	Multispectral & Radar	Low	Low	Parcel-based Classification
Panigrahy et al. (2005)	Multispectral & Radar	Low	Low	Index-Based Analyses
Liu et al. (2006)	Multispectral & Radar	Low	Low	Index-Based Analyses, Backscattering Analyses
McNairn et al. (2009)	Multispectral & Radar	Low	Medium & Low	Decision Tree, Neural Network, Maximum Likelihood
Ban et al. (2010)	Multispectral & Radar	High	Medium	eCognition

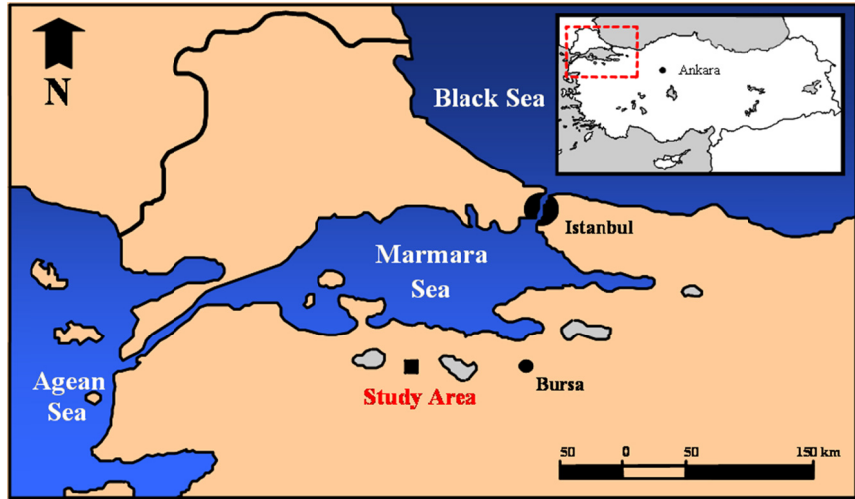
CHAPTER 3

STUDY AREA, DATA SETS, AND DATA PREPARATION

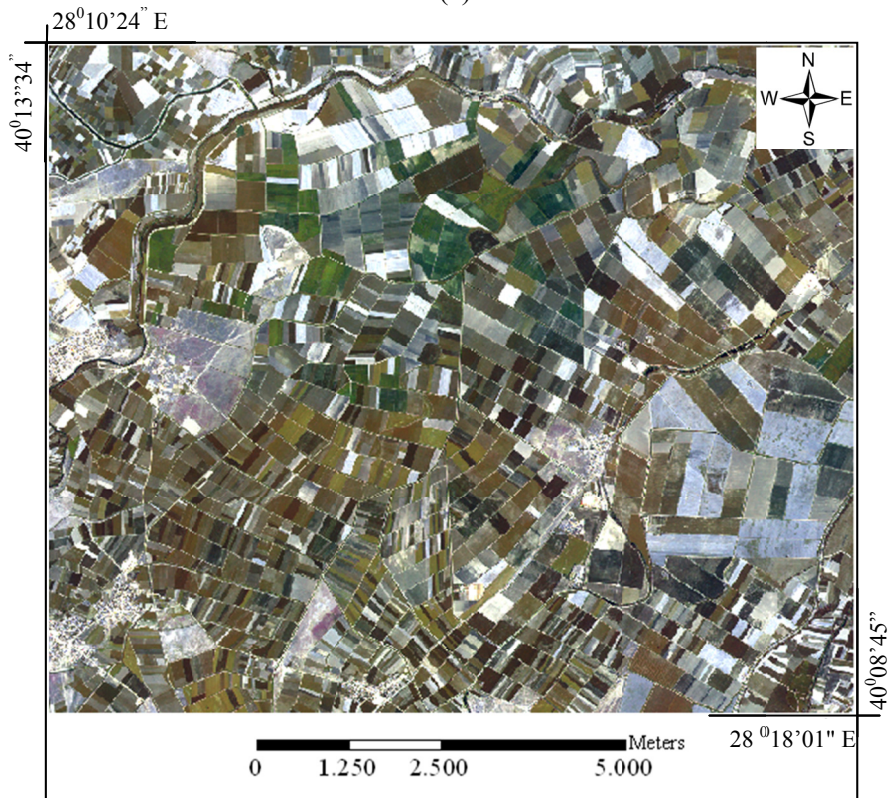
3.1 Study Area and Data Set

3.1.1 Study Area

The study area is situated in Karacabey, an agricultural area in Bursa, northwest of Turkey (Fig. 3.1a). It covers an approximately 100 km² and has central geographic coordinates at 28⁰14'12'' E and 40⁰11'09'' N (Fig. 3.1b). The area is one of the most productive and valuable agricultural regions of Turkey with its rich soils and good weather conditions. It is surrounded by nine villages (Hotanlı, Sultaniye, Küçükarağaç, Yolağazı, Akhisar, Yenisaribey, Ortasaribey, Eskisaribey, and İsmet Paşa) and Lake Manyas, an important lake for Turkey, which provides water supply for the crop types. The region has a temperate and semi-humid climate with a mean annual temperature of 14.4 °C and a mean annual precipitation of 706 mm. The area has a flat terrain and the mean elevation above sea level is 10 m. The soil map of the test site is provided in Figure 3.2(a) and Figure 3.2(b), where four soil types (alluvial soil, vertisols, colluvial soils, and rendzina) and four soil characteristics (I, II, III, and VIII) are available in the region. Most of the fields have regular shape in the area based on the land consolidation project performed between 1988 and 1992 (Turker and Ozdarici, 2011).



(a)



(b)

Figure 3.1(a) Study area, and (b) Kompsat-2 MS data taken in July, 11, 2008

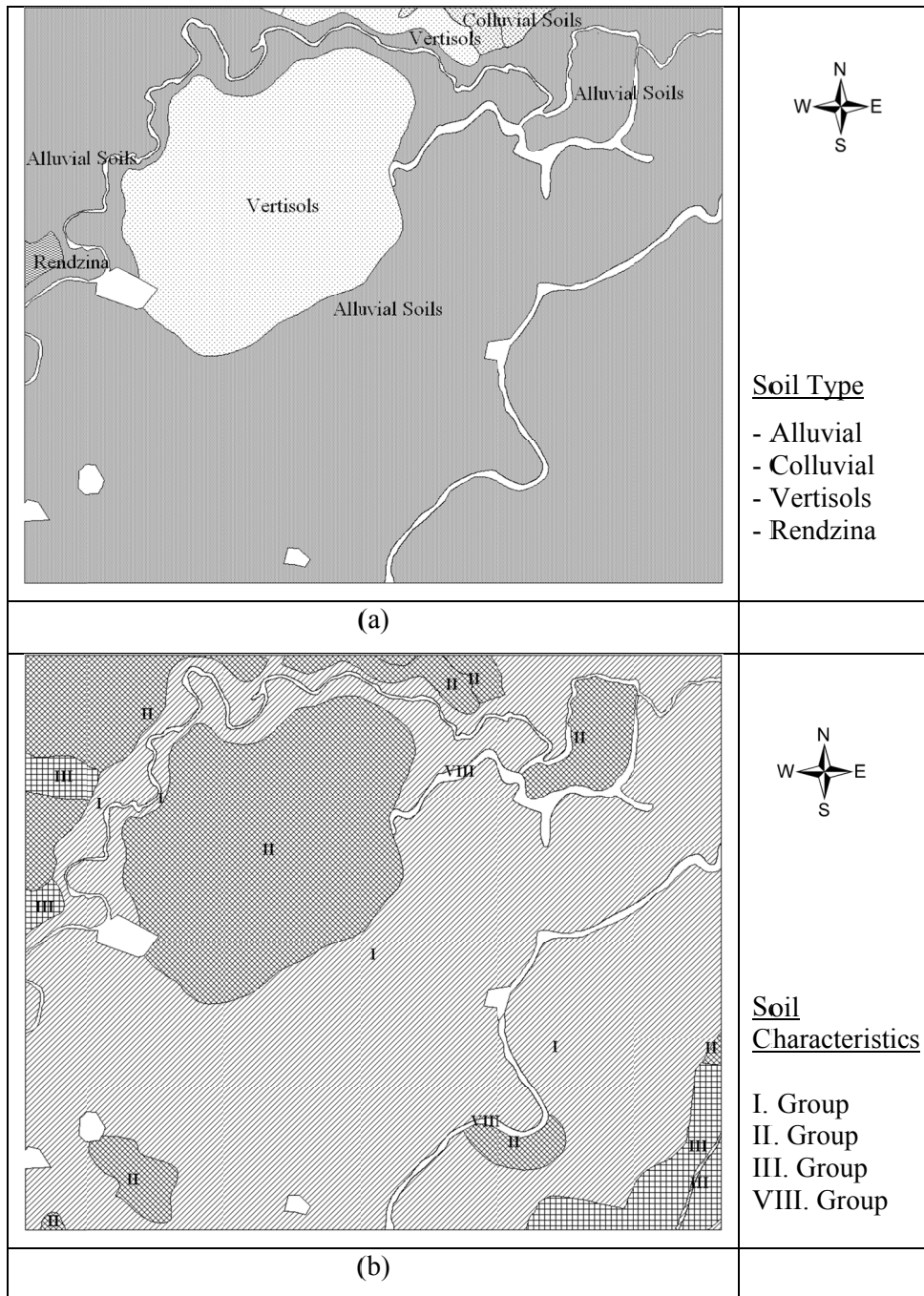


Figure 3.2 (a) Soil types exist in the region, and (b) soil characteristics categorized based on the agricultural ability (e.g. the soil category I is productive while the category VIII is not suitable for agriculture)

The major crop types cultivated in the area are corn, tomato, rice, wheat, sugar beet, and pea. The area also contains several grass land fields to provide feed to animals.

Photograph for some of the crops are presented in Appendix A. Figure 3.3 represents the phenological characteristics of the crops. In the figure, the black color represents dense canopy closure, the gray color indicates open canopy closure, and the white color means the areas having no vegetation, bare soil. As can be seen in the Figure 3.3, the planting period of corn starts at the end of April and the fields are covered with small corn leaves in May. In November, harvesting period of the corn fields starts and it continuous until the end of the November. There are also late corn cultivated in the area between July and December. These fields are planted generally after harvesting some fields of pea, tomato, and sugar beet. Wheat is the other major crop type in the region. Its planting date lies between November and the next July. Except for the wheat, all the crop types are irrigated in the area. It is also observed from the figure that tomato and rice fields have similar planting dates between May and October. The rice has completely different characteristics within the region, because the water necessity of this crop type is more than the other crops. The rice fields are filled with water at the beginning of the development stages, April, May, June and July. A root drying process is applied on the rice fields after fifteen or thirty days and then the rice plots are filled with water again until mid-July. The planting period of the sugar beet starts in March and ends in November. The class sugar beet has the third longest planting period after the grass land and wheat in the area. The grass land is also other interesting crop type of the region. It is generally seen as green color all the year provided that there is no snow on it. The class pea has a short planting cycle when compared with the other crop types. Its planting date lies between April and July (Turker and Ozdarici, 2011).

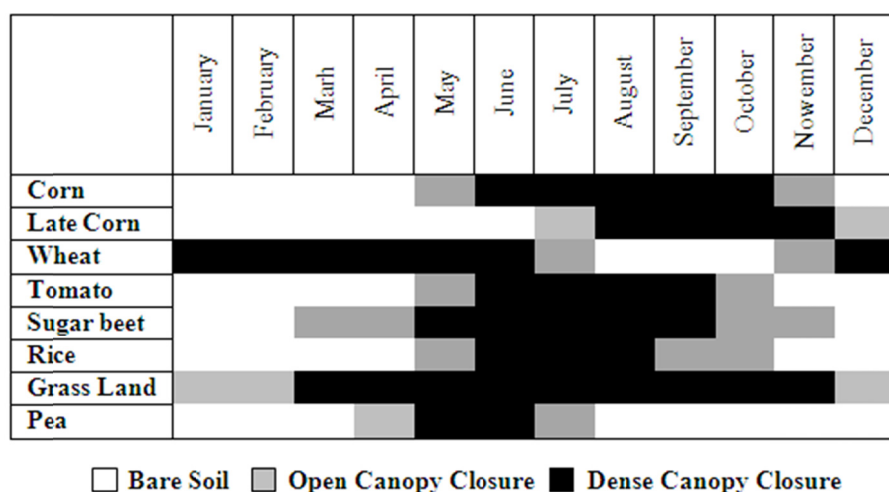


Figure 3.3 Phenological characteristics of different crop types

3.1.2 Data Set

Three different data sets were utilized in this study: (i) optical data, (ii) microwave data, (iii) vector data of the study area.

3.1.2.1 Optical Data

Three Kompsat-2 panchromatic (PAN) and multispectral (MS) optical data acquired with a cloud free condition in June, 13 (early season); July, 11 (mid season); August, 18 (late season) were used in the study (Table 3.1). Technical characteristics of the Kompsat-2 data are given in Table 3.2. The spectral range of PAN image (1m) is between 0.5-0.9 μm . Kompsat-2 MS (4m) data has four spectral bands: blue, green, red, and near infrared (NIR). The spectral ranges of these bands lie between 0.45-0.52, 0.52-0.60, 0.63-0.69 and 0.76-0.90 μm , respectively (Spot Image, 2008). The pre-processing level of the Kompsat-2 images is level 2A; in which radiometric correction is applied on the images to minimize the sensor-based radiometric errors. Besides the radiometric correction, the geometric corrections have also been applied on the images; where the images have been projected to a standard cartographic projection (UTM WGS 84) without any ground control points.

Table 3.1 Acquisition details of the Kompsat-2 data used in the study.

GTM: Greenwich Meridian Time

Kompsat-2 PAN&MS			
Acquisition Date	13 June 2008	11 July 2008	18 August 2008
Time (GMT)	08:18	08:16	08:06

Table 3.2 Technical details of the Kompsat-2 data used in this study

Kompsat-2		
Products	PAN	MS
Spectral Bands (μm)	0.50-0.90	blue: 0.45-0.52 green: 0.52-0.60 red: 0.63-0.69 nir: 0.76-0.90
Spatial Resolution	1m	4m
Footprint	15 kmx15 km	
Viewing angle	Revisit rate of 3 days with roll angle of 30°	
Pre-processing level	Level 2A	
Datum	WGS 84	
Map Projection	UTM	
Zone Number	35	

3.1.2.2 Microwave Data

The Envisat ASAR images (15m) used in this study was acquired in June, 28; July, 18; August 03, 2008 in Precision Image mode (Table 3.3). This mode provides both HH and VV polarization images with a spatial resolution between 15 m and 150 m and ground coverage of 56x105 km². Due to the technical problems occurred during image acquisition, only the VV polarization images were available in this study. Envisat ASAR operates in C-band and the images can be acquired with various incidence angles ranging between 15⁰ and 45.2⁰. A total of seven acquisition configurations (IS1-...-IS7) are available for the Envisat ASAR data, however, due to the limitations occurred on data acquisition, only the configurations of IS2, IS6 and IS7 could be utilized (Euroimage, 2009) (Table 3.4).

Table 3.3 Acquisition details of the Envisat ASAR data used in this study

Envisat ASAR			
Acquisition Date	28 June 2008	18 July 2008	03 August 2008
Time (GMT)	19:52	08:07	08:04
Beam	IS2	IS6	IS7
Pass	Ascending	Descending	Descending
Polarization	VV	VV	VV

Table 3.4 Technical details of Envisat ASAR data used in this study

Envisat ASAR	
Wavelength	C-band
Frequency Range	5.331 GHz
Spatial Resolution	15 m
Footprint	56 kmx105 km
Acquisition Configuration	IS2, IS6, IS7
Swath Width	IS2: 105km, IS6: 70km, IS7: 56 km
Incidence Angle Range	IS2: 19.2 ⁰ - 26.7 ⁰
	IS6: 39.1 ⁰ - 42.8 ⁰
	IS7: 42.5 ⁰ - 45.2 ⁰
Pre-processing level	Level 1B
Polarization	VV
Datum	WGS 84
Map Projection	UTM
Zone Number	35

3.1.2.3 Vector Data

Two types of vector data were used in the study: (i) field boundaries, (ii) contour maps.

(i) Field Boundaries

The vector data used in this study consists of cadastral maps including agricultural field boundaries, which was produced by a land consolidation project conducted between the years 1988 and 1992. The field boundaries were manually digitized and updated by 1:5 000 cadastral maps in a previous work performed by Turker and Arikan (2005) and it was further modified for this study (Ozdarici and Akyurek, 2009) by manually digitizing the within field boundaries based on the fused Kompsat-2 data (1 m). After the final modification, a total of 4689 agricultural fields were provided in Gauss-Kruger (Zone 5) projection and European datum 1950 (ED 50) (Figure 3.4). The vector data includes crop information cultivated in the area, which was collected by field works performed concurrently with the image acquisitions (June, July and August).

(ii) Contour Maps

In this study, 1:25 000- scale digital contour maps covering the test site were obtained from General Command of Mapping, which is a national mapping agency of Turkey.

These maps are compiled with NATO level standards and referenced to the Universal Transverse Mercator (UTM) projection and European Datum 1950 (ED 50). The average planimetric and vertical accuracies of these maps are stated to be $\pm 5\text{m}$ and 2.5 m , respectively (HGK, 2007).

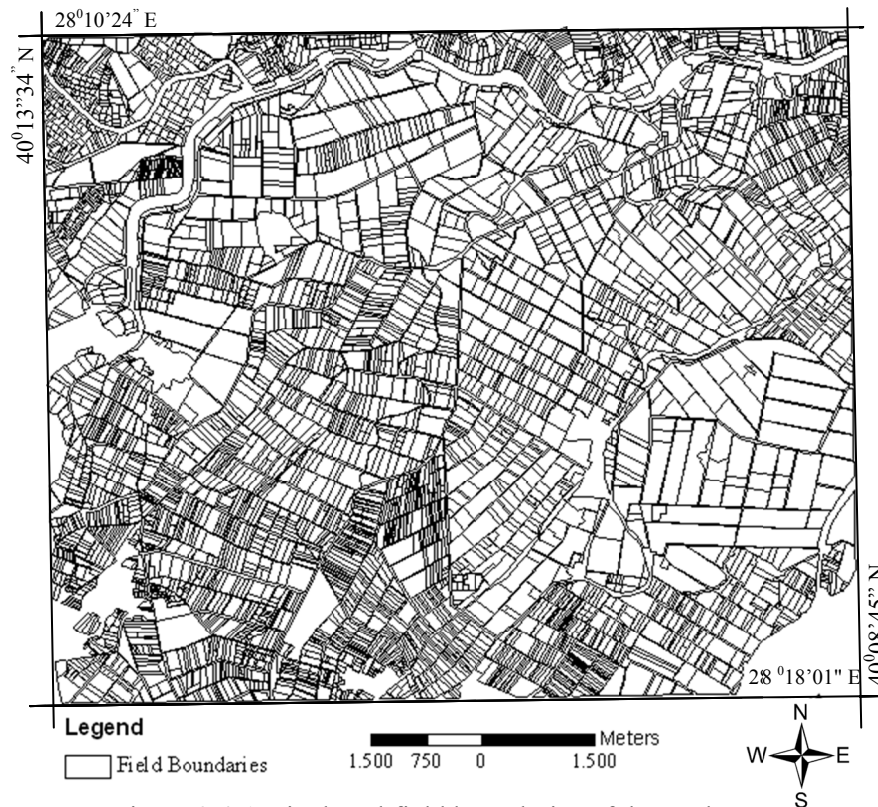


Figure 3.4 Agricultural field boundaries of the study area

3.2 Data Preparation

Data preparation part of this study includes image fusion and atmospheric correction of the Kompsat-2 PAN and MS images, map updating, speckle reduction of Envisat ASAR data, DEM generation and orthorectification of the optical and microwave data, and generation of backscattering maps. The flowchart of the pre-processing steps is presented below (Figure 3.5):

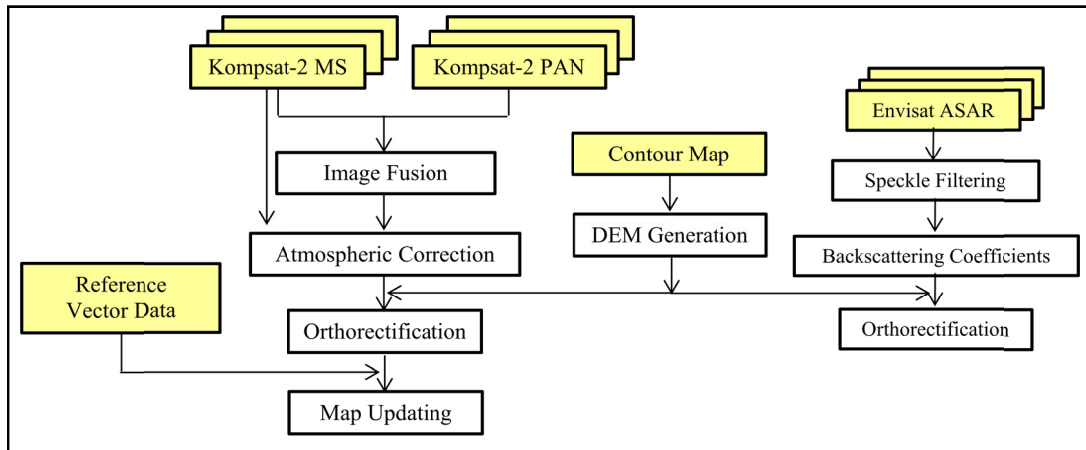


Figure 3.5 Flowchart of the pre-processing steps applied on Kompsat-2 and Envisat ASAR data

3.2.1 Image Fusion

Remote Sensing technology provides researchers numerous products with different spatial, spectral and temporal information covering large proportions of electromagnetic spectrum. Basic aim is to provide more information from satellite products to solve the specific problems. On the other hand, the large amount of data acquired by the sensors brings some problems. The main problem is combining large amount of data with an abstraction of higher quality and less redundancy. One of the most important methods to solve the problem is *image fusion*. Image fusion is a process to generate a new image by integrating different spatial, spectral and/or temporal characteristics of the data (Pohl and Van Genderen 1998).

In order to produce color composite images with higher spatial resolution, Kompsat-2 PAN (1m) and MS (4m) data were fused in this study. In order to select a proper method, nine different image fusion methods frequently used in the literature were tested. Those methods include; Hue-Saturation-Value (HSV), Brovey, Modified Intensity-Hue-Saturation (IHS) Resolution Merge, Principle Component (PC) Spectral Sharpening, Least Square Fusion (LSF), Gram-Schmidt, High Pass Filter (HPF), Wavelet-integrated IHS and Wavelet-integrated PCA. The detailed explanation of those methods can be found in Ozdarici and Akyurek (2009) and Ozdarici and Akyurek (2011) in Appendix B

and Appendix C, respectively. The fused results were evaluated visually, statistically and in terms of the classification performance. The analyses were conducted for two different image patches ($\sim 5\text{km}^2$) selected from the entire test site, and multiple evaluation indicators were used in statistical evaluations: relative mean difference, relative variation difference, correlation, peak signal to noise ratio, universal image quality index, and ERGAS (erreur relative globale adimensionnelle desynthèse) (Table 3.5). Each image patch fused was then classified with MLC method and the results were evaluated by confusion matrices. Based on the analyses, it was found that the LSF method was provided the best performance, therefore the LSF method utilized for the fusion task of the PAN and MS Kompsat-2 images for this study (Figure 3.6).

Table 3.5 Statistical evaluation indicators of the image fusion methods

<i>Relative Mean Difference</i>	$\frac{(\overline{F} - \overline{LR})}{\overline{LR}}$
<i>Relative Variation Difference</i>	$\frac{(\hat{\sigma}_F^2 - \hat{\sigma}_{LR}^2)}{\hat{\sigma}_{LR}^2}$
<i>Correlation</i>	$\delta_{Fi.LRi} = \frac{\text{COV}_{Fi.LRi}}{\hat{\sigma}_{Fi} \times \hat{\sigma}_{LRi}}$
<i>Peak Signal to Noise Ratio</i>	$MSE = \frac{1}{N} \sum_{i=1}^N (F_i - LR_i)^2$, $PSNR = 20 \log_{10} \frac{Peak}{\sqrt{MSE}}$
<i>Universal Image Quality Index</i>	$Q = \frac{\partial_{F.LR}}{\partial_F \partial_{LR}} \frac{2\overline{F.LR}}{(\overline{F})^2 + (\overline{LR})^2} \frac{2\partial_F \partial_{LR}}{\hat{\sigma}_F^2 + \hat{\sigma}_{LR}^2}$
<i>ERGAS</i>	$ERGAS = 100 \frac{h}{l} \sqrt{\frac{1}{N} \sum_{k=1}^N \frac{RMSE(B_k)^2}{(M_k)^2}}$

Where;

i mean the image pixel value,

\overline{F} refers to the mean value of the fused image,

\overline{LR} is the mean value of the original low resolution image,

$\hat{\sigma}_F^2$ is the variance of the fused product and,

$\hat{\sigma}_{LR}^2$ is the variance of the original multispectral image,

h, l refers to the high and low spatial resolution,

N is the number of bands,

$Peak$ is the maximum possible pixel value which is equal to 255 for 8 bit images,

$RMSE (B_k)$ means the root mean square error between the degraded fused image and the original MS image,

M_k is the mean value of the original multispectral image for the k^{th} band.

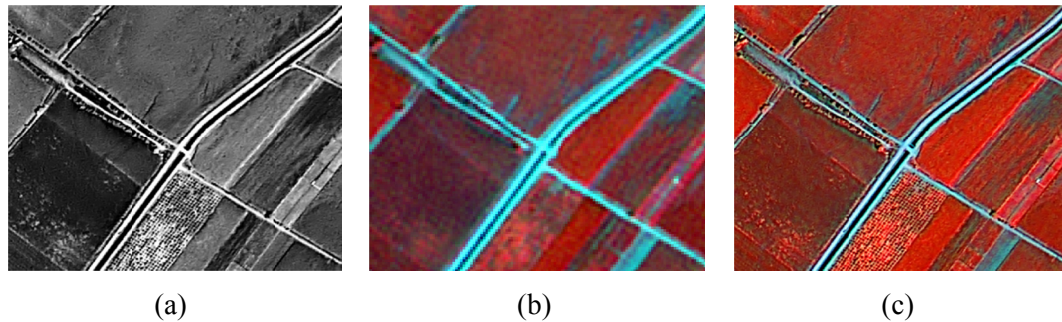


Figure 3.6 (a) Kompsat-2 PAN and, (b) MS image, (c) the fused result of the false color composite image

3.2.2 Atmospheric Correction of Kompsat-2 Data

Electromagnetic energy sensed by optical satellites has a mixture of energy due to the atmospheric absorption and reflectance characteristics of the targets. Hence, digital values of the images in optical region of the electromagnetic spectrum do not accurately represent the spatial distribution of the ground surface reflectance. In order to make reliable measurements, atmospheric correction is necessary especially when a comparison is performed on the images that contain the same objects (Jensen, 2005; Tso and Mather, 2009). Therefore, prior to the analyses, three dates of the Kompsat-2 images (PAN and MS) were atmospherically corrected using ATCOR-2 module of PCI Geomatica software (Richter, 1990).

3.2.3 Generation of Digital Elevation Model (DEM)

In order to remove the relief distortion from the image and provide data with better geometric quality to the analysis, a **Digital Elevation Model (DEM)** of the area was generated to utilize in orthorectification process. As mentioned in section 3.1.2.3 (i), the 1:25 000-scale digital contour maps were used for the generation of DEM. Detailed

information about the source data (contour maps) can be found in section 3.1.2.3. “Finite Difference” interpolation method was used to produce DEM from the contours. The method includes three steps. At an initial step, a raster DEM is produced by assigning the elevation values of the contours to the relevant pixels. Second, the remaining pixels are interpolated by a Distance Transform algorithm. In the final step, a smoothing process is performed by the “Finite Difference” method. During the smoothing process, the original pixel values encoded in the first step are not changed while other pixel values are updated (PCI Geomatica, 2009). The produced DEM and its statistics for the study area are given in Figure 3.7.

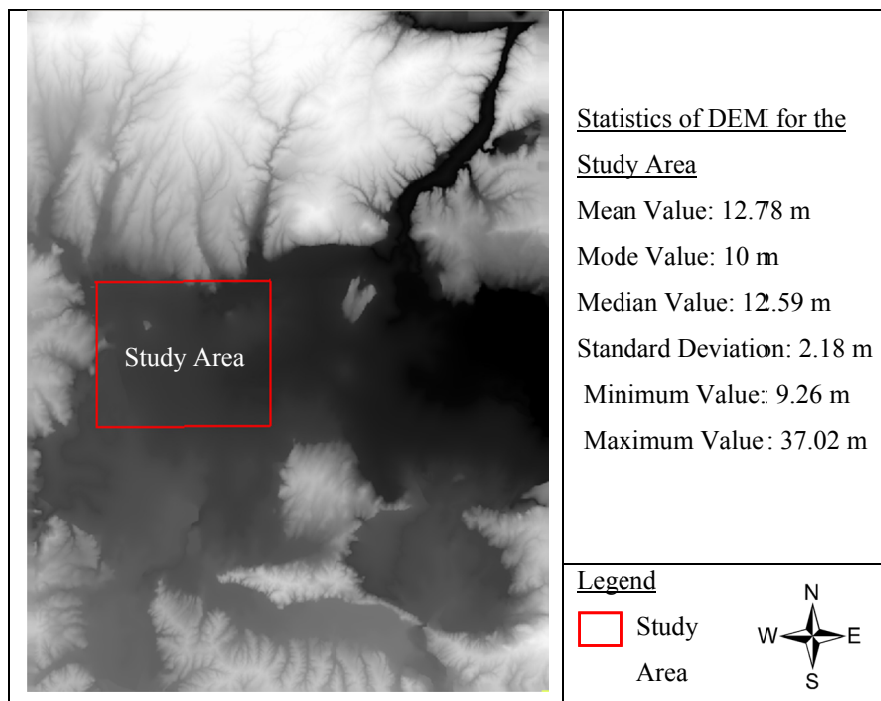


Figure 3.7 The generated DEM and the related statistics for the study area

3.2.4 Orthorectification

Images acquired by satellite platforms inherently involve a number of systematic and non-systematic geometric distortions. In order to provide images with proper geometric conditions, those errors must be corrected prior to the analyses. The correction process may incorporate the topographic maps with other related information sources (Jensen, 2005). The systematic errors can be corrected if the orbital characteristic of the satellite platform is known a priori. On the other hand the non-systematic errors can only be removed or minimized after performing a geometric rectification to the imagery. In this

respect, two common correction methods are used to correct raw (distorted) images: (i) rectification, (ii) orthorectification. The difference of the two methods can be explained by the accuracy level of the final product. The rectification process corrects any kind of distortions except for relief distortion, which is caused by elevation differences occur due to the rugged topography. The relief distortion can be corrected or minimized with the help of external elevation information when the orthorectification process is utilized (Manual of Photogrammetry, 2004).

In this study, the generated DEM of the study area and well distributed Ground Control Points (GCP) that were collected from fieldworks by sub-pixel Differential Global Positioning System (DGPS) measurements (Mini MAX, 2004) were used during the orthorectification process. In terms of the integrity, those GCPs were collected from distinct features, such as intersection of the roads, within the study area. As a geometric model, the rigorous ‘‘Satellite Orbital Modeling’’ (PCI Geomatica, 2009) was used for the entire Kompsat-2 and Envisat ASAR data. For the orthorectification process, at least 6 and 14 evenly distributed GCPs were selected for the Envisat and Kompsat-2 datasets respectively, and all Root Mean Square Error (RMSE) values of the geometric model were computed to be less than one pixel size. The number of GCPs used, RMSE values, and the method used for the resampling are given in Table 3.6.

Table 3.6 The number of GCPs used, resampling method and the RMSE values computed for each image

Data	Acquisition Date	# of GCPs	Resampling	RMSE (pixels)
Envisat ASAR	28 June 08	6	NN	0.55
	18 July 08	8	NN	0.45
	03 August 08	10	NN	0.50
Kompsat-2	13 June 08	16	NN	0.34
	11 July 08	19	NN	0.47
MS data	18 August 08	18	NN	0.41
	13 June 08	14	NN	0.80
Kompsat-2 (fused) data	11 July 08	15	NN	0.85
	18 August 08	20	NN	0.75

NN: Nearest Neighbor

3.2.5 Map Updating

After performing the orthorectification process, the vector data was overlapped with the fused optical images and the within field agricultural boundaries were manually digitized (Figure 3.8). During the digitization process, the vector database was also updated based on the field works performed in June, July, and August, 2008 and crop declarations gathered from the farmers. In this way, the vector data was prepared as a reference source to be used in accuracy assessment routines.

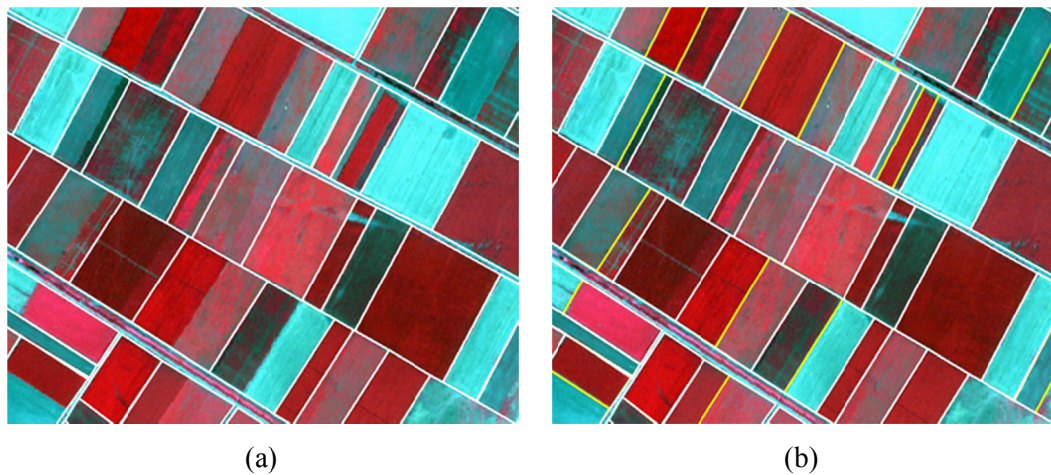


Figure 3.8 (a) Existing vector data, (b) digitized agricultural field boundaries

3.2.6 Speckle Reduction of Microwave Data

In consequence of random variation in the signal detected from a target, microwave images can have a random pattern of brighter and darker pixels called *speckle* (Tso and Mather, 2009). The presence of speckle in microwave imaging systems seriously affects the interpretability of the imagery even it carries out valuable information about the imaging system itself (Henderson and Lewis, 1998). Hence, to provide a better interpretation, the speckle should be reduced prior to the analyses. One traditional way of reducing the speckle is image filtering (Tso and Mather, 2009). Image filtering is a local operation that modifies the original pixels of the image with its neighbors (Lillesand et al., 2004). So far, multiple image filtering methods were tested and presented in a number of studies (e.g. Lee, 1980; Frost et al., 1982; Kuan et al., 1985; Serkan et al., 2008). Besides the filtering methods, filter size is an important factor affecting the image quality.

In order to select the method and filter size that are the most suitable choices for the study, seven non-adaptive and adaptive image filtering methods were tested; Mean, Median, Lee, Lee-sigma, Local Region, Frost and Gamma-MAP were evaluated with 3x3, 5x5, 7x7, and 9x9 filter sizes based on several statistical techniques: mean, standard deviation, correlation, and quality factor on the Envisat ASAR data. The details of those methods can be found in Ozdarici and Akyurek (2010a) in Appendix D. Results indicated that the Lee filter with 5x5 windows was found to be the most suitable method to decrease the speckle of the Envisat ASAR data (Figure 3.9).

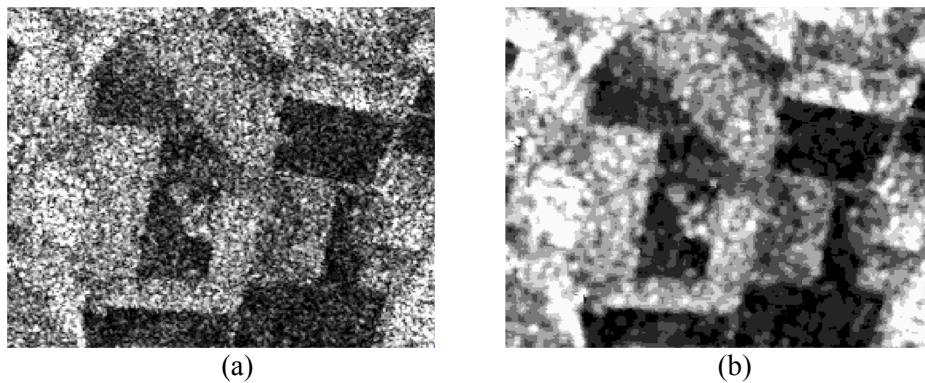


Figure 3.9 A small part of (a) original Envisat ASAR data and (b) the Lee filtered image with a filter size of 5x5.

The Lee filter is an adaptive speckle filter, which is based on a noise model that involves three assumptions:

- (i) SAR speckle is modeled as multiplicative noise that means the brighter the area the noisier it is,
- (ii) The noise and the signal are statistically independent to each other,
- (iii) The sample mean and the variance of a pixel are equal to the local mean and the local variance within a fixed window (Lee 1980; Tso and Mather, 2001).

In order to apply the Lee filter, the minimum mean-square error is estimated to construct the filtering algorithm followed by computing priori mean and variance of each pixel by its local mean and variance. Based on the computations, the best possible linear approximation is performed as follows (Lee 1980) (Eq.1):

$$\hat{X} = \left(\frac{z}{\mu_v} \right) \left(\frac{C_z^2 - C_v^2}{C_z^2 + C_v^2} \right) + \left(\frac{\mu_z}{\mu_v} \right) \left(\frac{C_z^2 + C_v^2}{C_z^2 + C_v^2} \right) \quad \text{Eq.1)$$

Where

z is the noise affected image pixel,

μ_v is mean of the noise,

μ_z is mean of the noise effected pixel,

C_z and C_v refer to the coefficient of variations of the noise effected pixel and the noise, respectively.

3.2.7 Generation of Backscattering Maps

The signals transmitted by a radar system are scattered in all directions, hence, the radar records only the backscattered energy taken by the sensor. The proportion of the density of energy scattered to the density of energy transmitted from the objects forms the intensity of each pixel and it provides backscatter information in a radar image (Waring et al. 1995). The backscattering coefficient (σ^0) is defined by the characteristics of the scattering behavior of all targets within a pixel and it is expressed a logarithm with decibel units (Waring et al. 1995). In order to facilitate making absolute comparisons of the temporal changes of the backscatter behavior, the radar backscattering coefficients were generated for each Envisat ASAR data to be used in image classification operations. σ^0 is computed by the local incidence angle of each pixel across the range direction. This information is stored in header files of the acquired images. The digital number (DN) of the ASAR image can be converted to backscatter coefficients using the following equation (Eq. 2) (Liu, et.al, 2006):

$$\sigma_{ij}[dB] = 10 \log_{10} \left(\frac{DN_{ij}^2}{K} \sin(\alpha_{i,j}) \right) \quad \text{(Eq.2)}$$

Where;

DN_{ij} is the digital number of the (i, j) pixel, $\alpha_{i,j}$ is the angle of the (i, j) pixel and K is the calibration constant.

In order to provide priori knowledge to the classification, the backscatter maps were integrated with the original agricultural fields and the variation of the backscattering coefficients were computed for six crop types cultivated in a common planting period (June, July, and August) are provided in Figure 3.10.

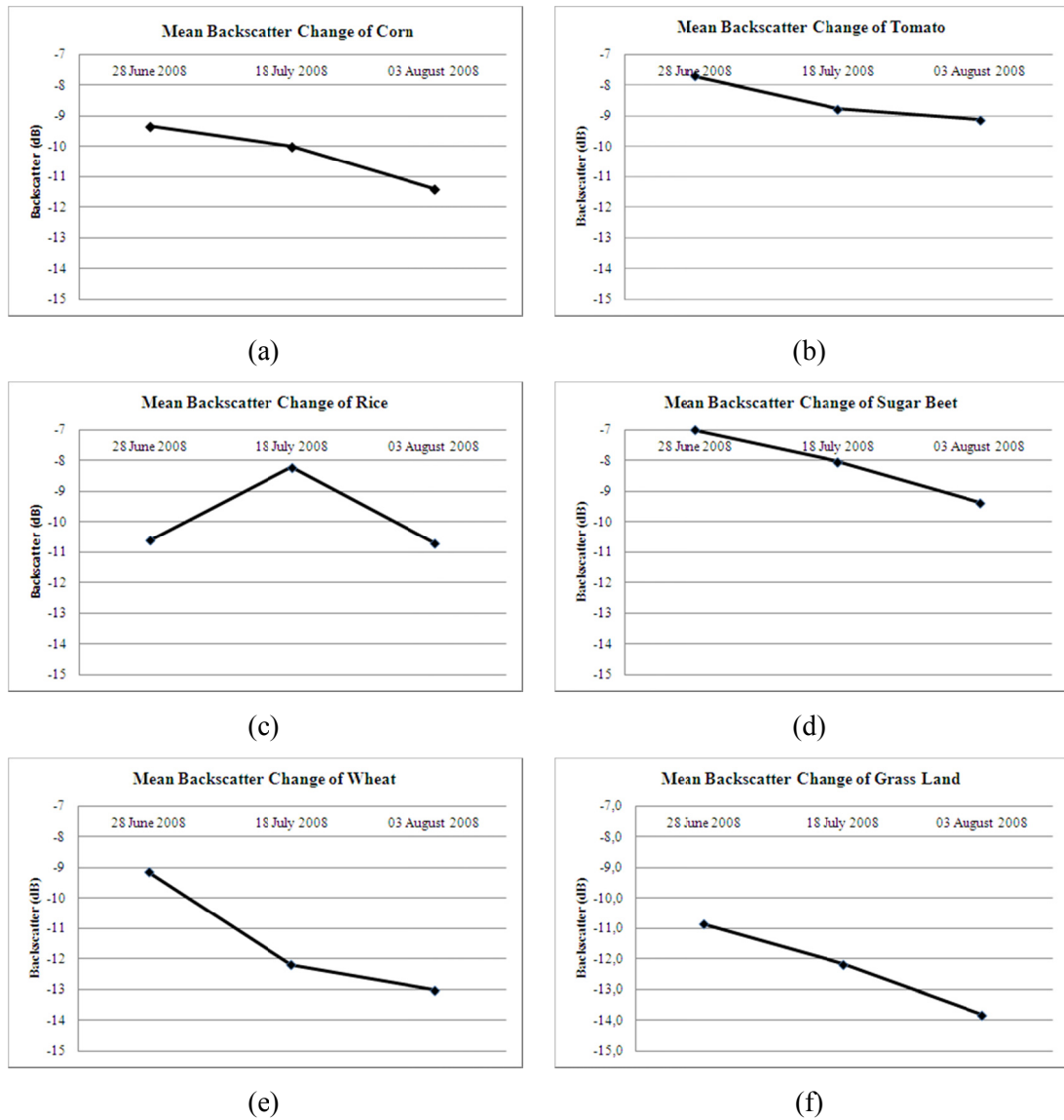


Figure 3.10 Mean backscatter changes of the crops having common planting period; (a) corn, (b) tomato, (c) rice, (d) sugar beet, (e) wheat, and (f) grass land

The mean backscatter value of the corn fields was computed to be -9.33 dB, -10.01 dB and, -11.41 dB in June, July, and August, respectively. The class tomato exhibits the highest backscattering coefficient in June, -7.71 dB, because most of the tomato fields

provide a dense canopy structure in this month. After June, in parallel to the development stage of tomato, a slight decrease is observed from -8.78 dB to -9.13 dB in July and August, respectively. Due to the unique tillage characteristics, the rice fields exhibits a different temporal behavior when compared with the other crop types. The highest backscattering value (-8.12 dB) is computed in July because the fields have a dense vegetation structure in this month. The lowest mean backscattering value (-10.62 dB) can be explained by the effect of bare soil during the first and last planting period of rice. In August (-10.71 dB) the harvesting period of the rice starts, hence a dramatic decrease is observed. A slight decrease is obtained for the mean backscatter values of the sugar beet. The mean backscattering values of this crop type was computed to be -7 dB, -8.04 dB, and -9.37 dB for June, July, and August, respectively. The temporal fluctuation ranging between -9.14 dB and -13.01 dB of the class wheat reveals the dramatic decrease in this time period. Based on the early sowing phase of wheat, the dense canopy closure exists in June. Together with the harvesting period in July, the bare soil and different tillage practices may affect the backscatter variation, which may cause a dramatic drop for the wheat fields. The seasonal variation of mean backscatter coefficients of grass land is computed to be -10.87 dB, -12.18 dB and -13.82 dB in June, July, and August, respectively.

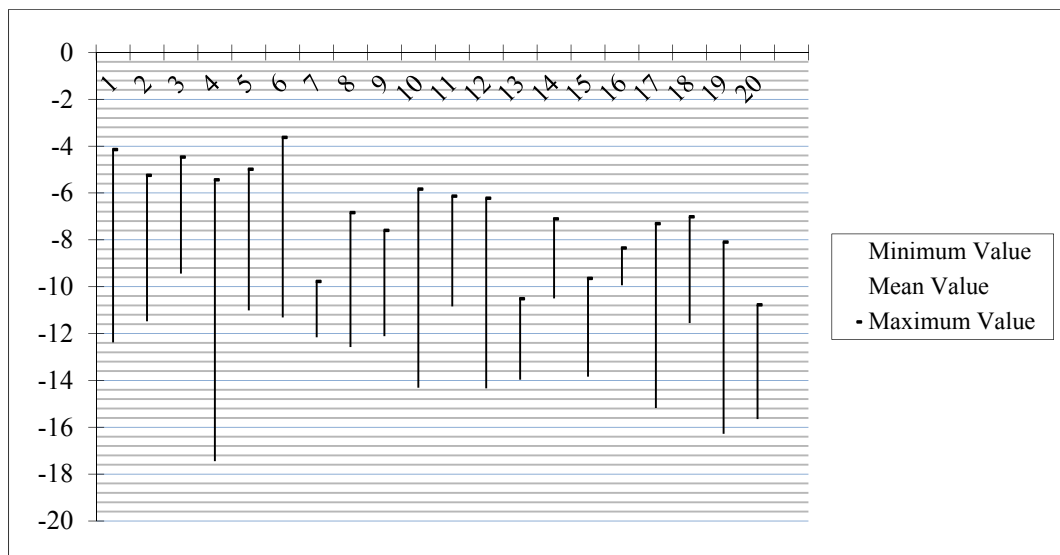


Figure 3.11 Mean backscatter values of the crops computed for each date (1: Pea, 2: Corn, 3: Tomato, 4: Rice, 5: Sugar beet, 6: Wheat, 7: Grass Land cultivated in **June**; 8: Corn, 9: Tomato, 10: Rice, 11: Sugar beet, 12: Wheat, 13: Grass Land, 14: Late Corn cultivated in **July**; and 15: Corn, 16: Tomato, 17: Rice, 18: Sugar beet, 19: Wheat, 20: Grass land cultivated in **August**).

The max, min, and mean backscatter characteristics of all the crop types included in the analysis are presented in Figure 3.11, where a slight decrease is observed for the crops cultivated in August. This can be explained by the acquisition characteristics of the microwave data, because the Envisat ASAR data acquired in August has higher viewing angles (42.5° - 45.2°) than the other microwave images due to the characteristics of different acquisition configuration (IS7).

CHAPTER 4

METHODOLOGY

The overall methodology of the proposed approach is presented in Figure 4.1. The methodology is composed of four main sections; (i) image fusion, (ii) image segmentation, (iii) image classification, and (iv) accuracy assessment. Each section is described in detail below:

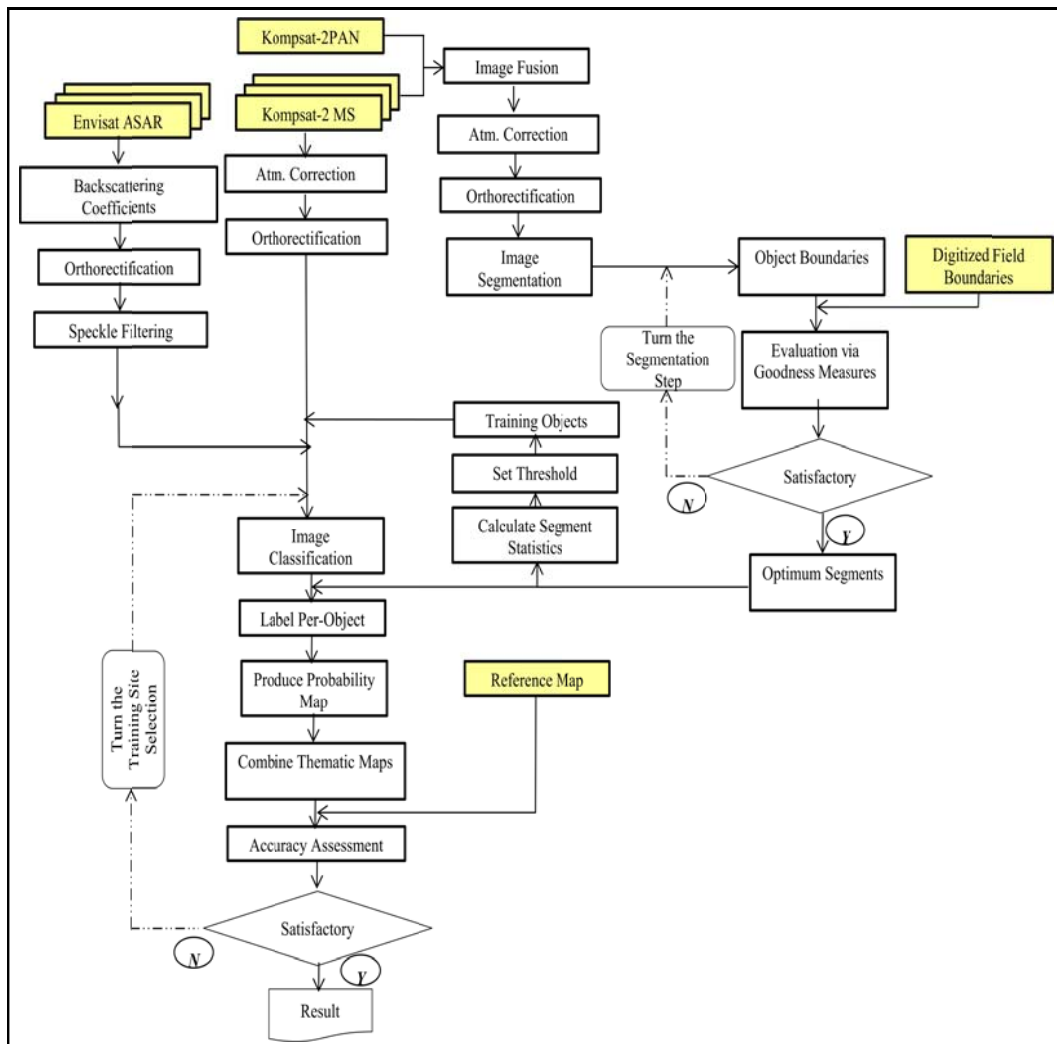


Figure 4.1 The overall flowchart of the proposed method

4.1 Image Fusion

Definition of image fusion and the method applied on the PAN and MS Kompsat-2 images are provided in previous chapter in section 3.2.1.

4.2 Image Segmentation

In this study, two different image segmentation approaches, Mean-Shift and Berkeley Image Segmentation, were tested on the study area and segmentation results were evaluated based on both area- and location-based similarities by the pre-defined agricultural fields using multiple goodness measures in Ozdarici and Akyurek (2010b) provided in Appendix E. Based on the results, the Mean-Shift method provided better segmentation results compared to the results of the Berkeley Image Segmentation method; hence the Mean-Shift method was utilized in this study and explained in this section. The flowchart of the image segmentation process is provided in Figure 4.2.

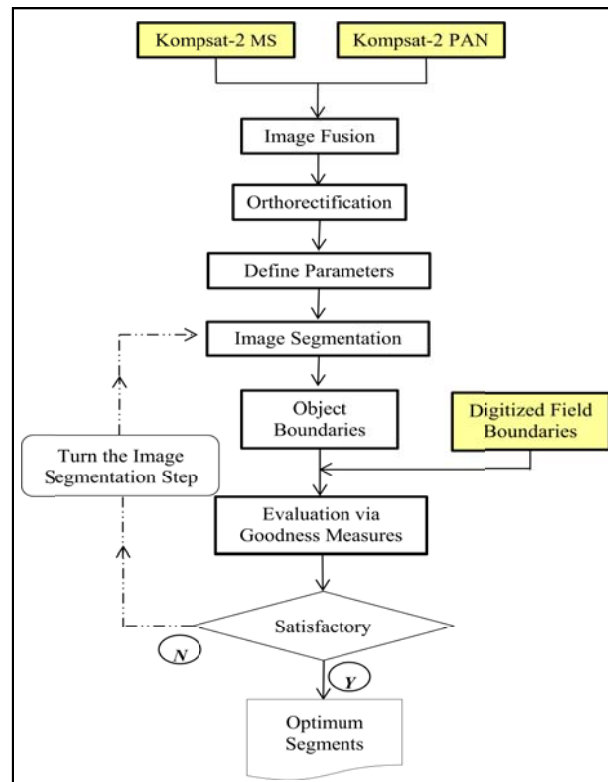


Figure 4.2 The flowchart of the image segmentation part of the study

4.2.1 Mean-Shift Method

A popular pattern recognition procedure (Fukunaga and Hostetler, 1975), *Mean-Shift*, was utilized in this study to segment homogenous agricultural patches. Mean-Shift examines each data point in its neighborhood by computing the center of mass of the pre-defined kernel and shifts the center of the kernel to a new center. The direction between the recent and the shifted center of the kernel forms the Mean-Shift vector. This kernel shifting process is repeated until there is no (or a slight) change on the position of the kernel (Comaniciu and Meer, 1997, 2002; Friedman et al., 2003) (Eq. 4.1).

$$m_K(x) \equiv \frac{\sum_{i=1}^n x_i K\left(\frac{x-x_i}{h}\right)}{\sum_{i=1}^n K\left(\frac{x-x_i}{h}\right)} - x \quad (\text{Eq.4.1})$$

Where

$K(x)$ is the kernel defined for the Mean-Shift process

x denotes the center of the kernel used,

h is the size of the kernel,

n is number of the data values (Comaniciu and Meer, 2002)

The formula of the Mean-Shift method adapted to an image space requires three parameters to be defined; (i) kernel type, (ii) bandwidth, and (iii) minimum region. Several kernel types such as; Flat, Gaussian, Epanechnikov are utilized in different studies during the Mean-Shift (Cheng, 1995). Besides the kernel type, two bandwidth parameters namely; (i) spatial (h_s) and (ii) range (h_r) determine the final quality of the segments. The spatial (h_s) domain is explained by the positional information of a pixel while the range (h_r) domain describes the gray level of the pixel in a two-dimensional lattice (e.g. satellite image) (Eq. 4.2). In order to eliminate the segments smaller than a pre-defined minimum object size, a minimum region (MR) threshold must also be defined prior to the segmentation operation. The formula of the Mean-Shift method adapted to an image space is given in Equation 4.2. Further details about the Mean-Shift segmentation method can be found in Comaniciu and Meer (1997) and Comaniciu and Meer (2002).

$$K_{h_s, h_r}(x) = \frac{C}{h_s^2 h_r^p} k\left(\left\|\frac{x^s}{h_s}\right\|^2\right) k\left(\left\|\frac{x^r}{h_r}\right\|^2\right). \quad (\text{Eq.4.2})$$

Where;

x^s is the spatial part,

x^r defines the range part of a vector,

$k(x)$ means the common profile used in both domains,

h_s and h_r are the employed kernel bandwidths that are used to determine the resolution of the mode detection by controlling the size of the kernel, and C is the corresponding normalization constant (Comaniciu and Meer, 2002).

The Mean-Shift method was applied on the fused Kompsat-2 images taken in June, July, and August by open source segmentation software called **Edge Detection and Image SegmentatiON** (EDISON) (EDISON software). The software is capable of segmenting both gray scale and color images, however it can process color images with three bands at a time since the color image is converted to Luv color space prior to the segmentation. Therefore, different band combinations of the image were tested and it was found that the band combinations, green, red, and near-infrared, provided the most effective solutions and therefore used for the segmentation. Principle Component Analysis (PCA) was also applied on the images and the first three PC bands were segmented separately for each image. However, the produced segments did not provide satisfactory results therefore the PCA were not included in the analysis. Epanechnikov kernel that provided high performance in most of the studies (e.g. Commaniciu and Meer, 1999; Friedman et al., 2003) was utilized in this study. The MR parameter was determined as 1000 pixel which was based on the total number of pixels that belongs to the smallest agricultural field in the area. In total 324 parameter combinations in spatial h_s , and range h_r , domains were tested $\{3,4,5,\dots,20\} \times \{3,4,5,\dots,20\}$ respectively, and effective parameter combinations were found for the fused Kompsat-2 data.

4.2.2 Quality Assessment of the Segments

In order to evaluate the segmentation results and define the optimum parameters, the segmentation results for different parameter combinations were evaluated in a wide perspective via multiple goodness measures. Two types of measures; (i) area-based and

(ii) location-based were utilized during the assessment of the segments. In total 11 measures namely; over segmentation, under segmentation, area fit index (AFI), count over, count under, relative area metric, similar size index, quality rate, under merge, over merge indices, qLoc, relative position indices and a number of weighted products of their variants were computed between the segments and the reference field boundaries to compute the similarities in area- and location-based manner. Specific formulas for each goodness measure used are given in Table 4.1 in which it was assumed that $X = \{x_i: i=1 \dots n\}$ is the set of n training objects (the selected reference polygons), and $Y = \{y_i: i=1 \dots m\}$ denotes the related subsets of the segments generated from the image data.

Table 4.1 The goodness measures used in this study

<u>Over/Under Segmentation</u> $1 - \frac{area(x_i \cap y_i)}{area(x_i)}$	<u>Under Merging</u> $\frac{(area(x_i) - area(x_i \cap y_i))}{area(x_i)}$
<u>Over Merging</u> $\frac{(area(x_i) - area(x_i \cap y_i))}{area(x_i)}$	<u>Area Fit Index (AFI)</u> $\frac{area(x_i) - area(y_{iMax})}{area(x_i)}$
<u>Similar Size Index (SimSize)</u> $\frac{\min(area(x_i), area(y_i))}{\max(area(x_i), area(y_i))}$	<u>Relative Area Index (RA)</u> $\frac{area(x_i \cap y_i)}{area(x_i)}$
<u>Quality Rate Index (QR)</u> $\frac{area(x_i \cap y_i)}{area(x_i \cup y_i)}$	<u>qLoc Distance Index</u> $dist(centroid(x_i), centroid(y_i))$
<u>Relative Position (RP) index</u> $\frac{dist(centroid(x_i), centroid(y_i))}{dist_{max}}$	

The measures of under merging and over merging are considered to compute area-based similarities between the reference polygons and the output segments. Based on the total over segmentation and total under segmentation of an image for p pixels and a training set of polygons, the minimum (min) and maximum (max) values of the under merging are 0 (zero) and $(p-1)$, respectively. The minimum value (zero, 0) means the reference polygons and the relevant segments have a perfect match or over merged. The min and max ranges of the over merging lies between 0 and $p(p-1)$, respectively, in which the min value indicates a perfect match or under merging. As its name implies the area fit index (AFI) is another measure that is utilized to compute the area-based similarities. The min value of the AFI is $(1-p)$, while the max value of this measure is $(p-1)/p$. If the AFI is smaller than zero ($AFI < 0$), which means under segmentation while the reverse case ($AFI > 0$) refers over segmentation. The relative area (RA) and quality rate (QR) indices were also used to evaluate the area-based similarities between the segments and the reference fields. The min and max values of these measures are $1/p$ and 1 , respectively. For each measure, one (1) indicates an optimum match. The min and max ranges of the over segmentation and under segmentation are defined 0 and $(p-1)/p$, respectively. Zero (0) means a perfect match for each index.

The indices mean distance (ModDb), relative position, and qLoc distance were utilized to compute the location-based similarities between the reference polygons and the related segments. The measure of ModDb is computed based on the distance between the reference polygon and the closest vertex in the output segment. The min value of this index is zero (0). If the distance increases, it indicates a worse matching in the segmentation. Similar to the ModDb, for the measures of relative position index, and qLoc distance index, an increase in the distance to nadir location indicates worse matching results.

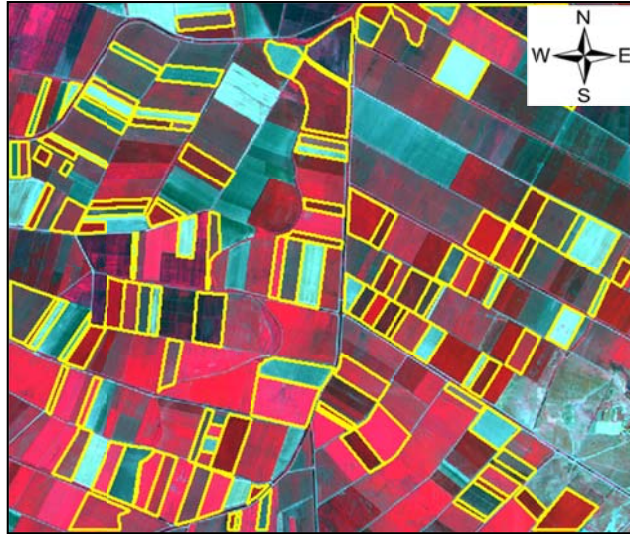


Figure 4.3 The selected reference polygons of the vector data

In order to compute the accuracies of the segments, a subset of representative 10% of all the fields, operator delineated agricultural fields, were selected from the reference vector data (ground truth) (Figure 4.3) and compared with the relevant segments by open source software called Alpha v 0.1 (http://nature.berkeley.edu/~nclinton/goodness0_1alpha.zip). After computing the goodness measures, the optimum parameters of the segments were determined based on a ranking process of the results in terms of one or more of the goodness measures followed by performing an optimization process. The evaluations indicated that the optimum parameter combinations of the fused Kompsat-2 image taken in July were found as $h_s = 12$, $h_r = 3$, respectively. The optimum segmentation result overlaid with the fused Kompsat-2 image and the computed goodness measure values are given in Figure 4.4.

After the segmentation, two post-processing operations; (i) buffering, and (ii) line simplification; were applied on the segments to generate more representative objects for the agricultural patches (Figure 4.5).

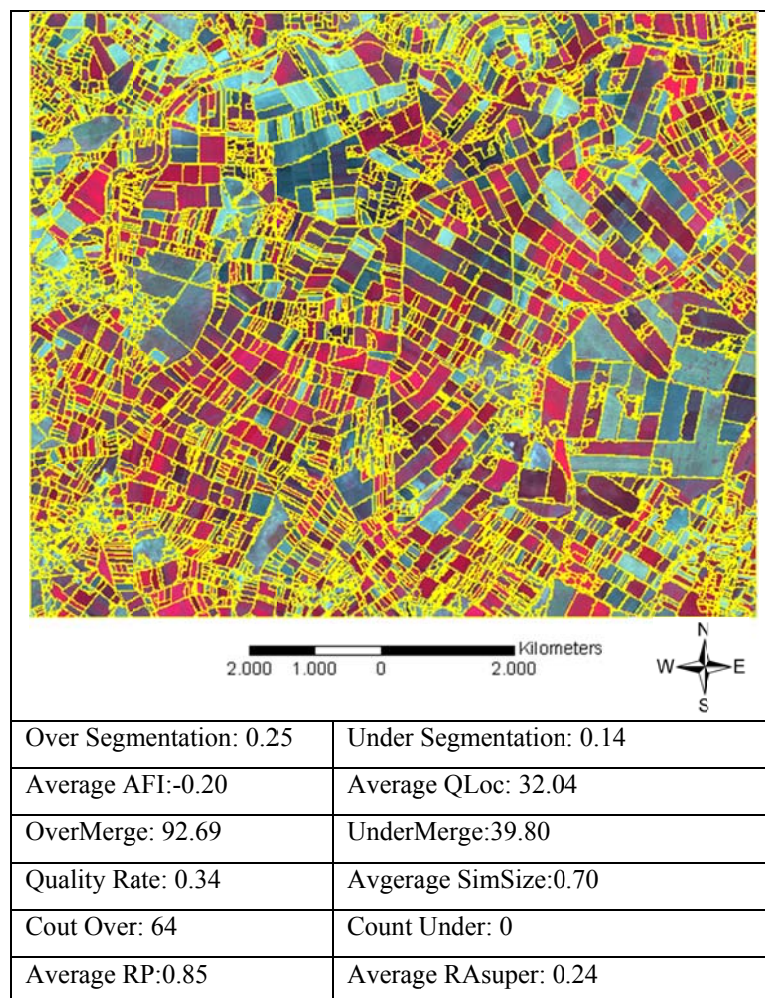


Figure 4.4 The optimum segmentation result and the results of the computed goodness measures for the fused Kompsat-2 image taken in July ($h_s: 5, h_r: 10$)

During the post-processing operation, first a buffer distance, 10 pixels, was applied inside the segment boundaries to eliminate the sprawling edges and to separate the segments from each other. Next, a new shorter buffer distance was applied on the outside of the segments to keep the distances among the segment edges around 3-4 pixels. In this way, the effects caused by mixed pixels on the field boundaries were also reduced significantly. Finally, a line simplification process was performed on the segments to remove redundant edges by preserving the main shapes of the polygons.

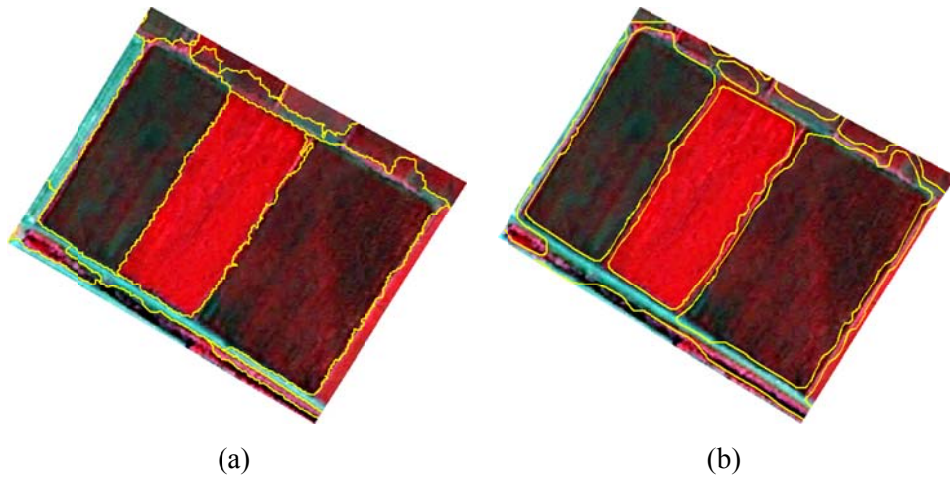


Figure 4.5 (a) The original segmentation result of the fused Kompsat-2 image (July) and (b) the post-processed segmentation result of a small part in the study area

4.3 Image Classification

In agricultural activities, quantitative analysis of remotely sensed data is necessary to provide reliable information about agricultural products. For this purpose, the most commonly used information extraction method from remotely sensed data is *image classification*. Through the image classification, the pixels in an image domain are automatically categorized into pre-determined land cover classes according to their spectral characteristics. In traditional remote sensing, image classification operations are performed based on three categories: (i) unsupervised, (ii) supervised, and (iii) hybrid (Lillesand et al. 2000). Although a significant number of different image classification studies is available in the literature, most of them benefit from the supervised approaches to obtain more reliable results (e.g. Lillesand and Kiefer, 2000, Lu and Weng, 2007, Turker and Ozdarici, 2011). In the supervised classification approach, sufficient number of samples called *training sample* are required as prior information to produce representative parameters for each class based on a selected supervised algorithm (Lillesand et al., 2004; De Wit and Clevers, 2004).

In this part, three types of supervised image classification approaches namely, (i) pixel-based, (ii) segment-based, and (iii) field-based applied on multi-temporal images are described.

- (i) In the pixel-based classification; first, each single-date Kompsat-2 images were classified separately by assigning the class label to the pixels. Then the classification operations were performed using the Kompsat-2 images along with the Envisat ASAR data.
- (ii) For the segment-based approach, the thematic maps generated with the pixel-based classifications were integrated with the segments. The frequencies of the pixel values in each segment were computed and the mode of the class id was assigned as label to the segments,
- (iii) In the field-based approach, the original agricultural field boundaries were overlaid with the thematic map and the majority class was assigned as label to the fields.

For a meaningful comparison between those three different types of classification approaches, the same training sites were automatically selected and utilized in the analyses. The details of the proposed training site selection strategy and the classification approaches are given below:

4.3.1 Training Site Selection

In supervised classification, sufficient number of samples is required as prior information to produce representative parameters for the pre-defined classes. On the other hand, defining training samples is a critical process since the quality of the samples directly affects the final accuracies of the thematic maps. Therefore, manual selection of the training samples not only needs qualified expert knowledge but also requires lots of time and money (Chen and Stow, 2002; Lu and Weng, 2007). In order to tackle those problems and eliminate possible bias that may occur during the training area selection, in this study, a new approach was proposed to automatically select and define homogenous training samples from a subset of segmentation results. First, the optimum segmentation output was overlaid with each band (blue, green, red, and NIR) of the MS Kompsat-2 data to find the best representative regions among all the available segments. Next, standard deviations of the pixels within the segments were computed and stored in a database. Next, mean values of the standard deviations of the segments computed for each band were then calculated. In the final step, the segments that have standard deviation smaller than 2 were extracted as training samples and labeled automatically

with the help of reference information. In this way, a representative 10% of all the pixels in the segments were automatically selected as training samples for each image. This process was performed for each Kompsat-2 MS data taken in three different dates. The ranges of the training sizes lie as 0.1-1.2 ha, 0.1-2.3 ha, and 0.1-2.2 ha for the images taken in June, July, and August, respectively. The selected training segments were then utilized as prior information to carry out the supervised classifications of the 4m MS Kompsat-2 images (blue, green, red, and near-infrared) and 15m Envisat ASAR data. The fused Kompsat-2 images (1m) along with the Envisat ASAR data were also classified in this study; however, the overall accuracies did not exceed 0.2%. Therefore, to increase the computational efficiency and save time, the MS Kompsat-2 (4m) data were used in the classification operations. The automatically selected training objects for the MS Kompsat-2 image taken in July is presented in Figure 4.6. The distribution of other training segments collected for the MS Kompsat-2 images taken in June and August can be found in Appendix F.

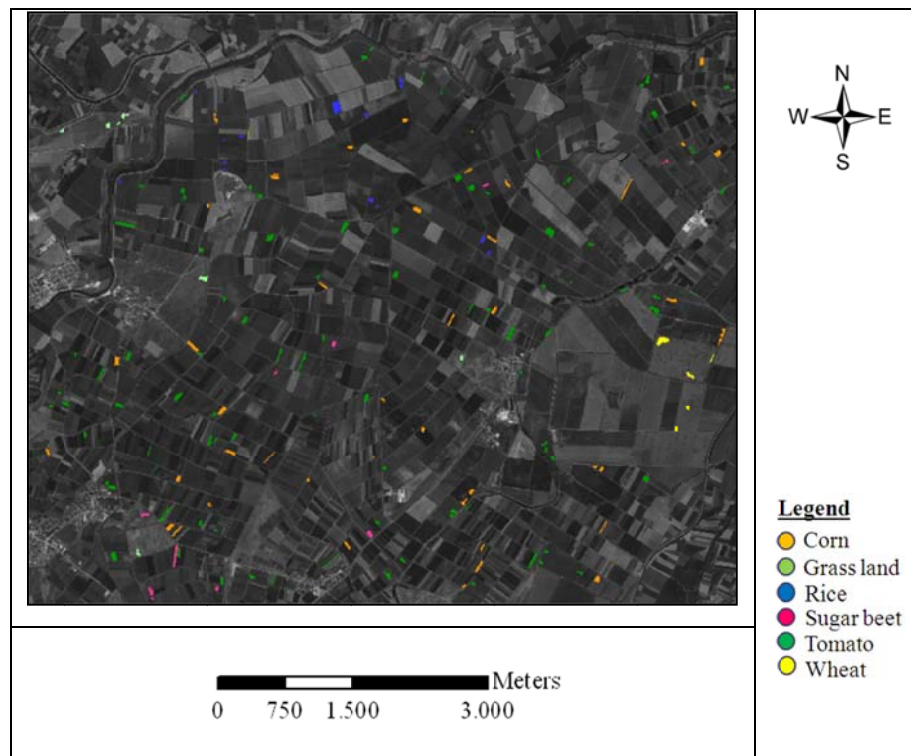


Figure 4.6 The automatically selected training samples of the MS Kompsat-2 image taken in July

Accuracies obtained for the resulting thematic maps not only depend on the quality of the training samples but also the optimum bands used in the classification operations (Jensen, 2005). Therefore, to assess the degree of statistical separability between the selected training class signatures based on the input bands, Bhattacharya Distance and Transformed Divergence separability indices were utilized.

Let say a and b are the classes that statistical separability is going to be calculated. Bhattacharya Distance is computed by the mean and covariance matrix of the classes (Eq.4.3).

$$Bhat_{ab} = \frac{1}{8} (M_a - M_b)^T \left(\frac{V_a + V_b}{2} \right)^{-1} (M_a - M_b) + \frac{1}{2} \log_e \left[\frac{\frac{|V_a + V_b|}{2}}{\sqrt{(|V_a| \cdot |V_b|)}} \right] \quad (\text{Eq.4.3})$$

Where;

M_a and M_b are the mean vectors of the classes a and b ,

V_a and V_b are the covariance matrices of the classes a and b .

The Transformed Divergence Index is implemented based on the Eq.4.4 and Eq. 4.5 below:

$$TDiver_{ab} = 2000 \left[1 - \exp \left(\frac{-Diver_{ab}}{8} \right) \right] \quad (\text{Eq.4.4})$$

Where;

$Diver_{ab}$ is computed as:

$$Diver_{ab} = \frac{1}{2} \text{tr}[(V_a - V_b)(V_b^{-1} - V_a^{-1})] + \frac{1}{2} \text{tr}[(V_a^{-1} - V_b^{-1})(M_a - M_b)(M_a - M_b)^T] \quad (\text{Eq.4.5})$$

$\text{tr}[\]$ is the trace of matrix (e.g. the sum of the diagonal elements),

M_a and M_b are the mean vectors of the classes a and b ,

V_a and V_b are the covariance matrices of the classes a and b .

The separability values are scaled between 0 and 2 for each index. The value of 2 indicates a complete separation between the classes and therefore, the larger the value the greater the statistical distance between the class a and b (Jensen, 2005). The separability values of each crop pairs computed for the Bhattacharya Distance and the Transformed Divergence Index of the four-band MS Komsat-2 images acquired in June, July, and August (a, b, c), and the same optical bands with Envisat-ASAR data (d, e, f) are given in Table 4.2 and Table 4.3.

Except for the matrix produced for the four-band Komsat-2 MS image taken in August, the average separability values were computed over 1.70 for other image combinations. The Komsat-2 MS image taken in August provided relatively poor separability values when compared with the other matrices. This can be explained by the inefficient training samples collected for the August image. The average separability value computed for the four-band Komsat-2 MS image taken in August was improved when the Envisat ASAR data was included in the analysis. The same case is also valid for the other images taken in June and July. This means an improvement was observed for the separability values of the four-band Komsat-2 MS images when the Envisat ASAR data was included.

Table 4.2 The matrices of Bhattacharya distance of the four-band Komsat-2 MS images taken in June, July, and August (a, c, e), with the Envisat ASAR data (b, d, f).

Four-band Komsat-2 MS image taken in June					
Class Names	Corn	Tomato	Rice	Sugar beet	Wheat
Tomato	1.94				
Rice	1.99	1.99			
Sugar beet	1.99	1.90	1.99		
Wheat	1.97	1.63	1.91	1.95	
Grass Land	1.51	1.40	1.97	1.80	1.51
Average Separability: 1.83					
Signature pair with Minimum Separability: Tomato, Grass Land					

(a)

Table 4.2 (Cont'd)

Four-band Kompsat-2 MS image with Envisat ASAR data taken in June

Class Names	Corn	Tomato	Rice	Sugar beet	Wheat
Tomato	1.94				
Rice	1.99	1.99			
Sugar beet	1.99	1.93	1.99		
Wheat	1.97	1.65	1.91	1.97	
Grass Land	1.55	1.58	1.98	1.95	1.54
Average Separability: 1.86					
Signature pair with Minimum Separability: Wheat, Grass Land					

(b)

According to the matrices, it was observed that the separability values improved when the Envisat ASAR data was included in the computation. For the matrix of four-band Kompsat-2 MS image and Envisat ASAR data taken in June, the major confusions were observed for the crop pairs of grass land -corn, grass land-tomato, and grass land-wheat as 1.55, 1.58, and 1.54, respectively. A moderate separability value of 1.65 was computed for the class pairs of wheat and tomato.

Four-band Kompsat-2 MS image taken in July

Class Names	Corn	Tomato	Rice	Sugar beet	Wheat
Tomato	0.90				
Rice	1.85	1.95			
Sugar beet	1.99	1.82	2.00		
Wheat	1.99	1.99	2.00	2.00	
Grass Land	1.91	1.95	1.99	1.99	1.58
Average Separability: 1.86					
Signature pair with Minimum Separability: Corn, Tomato					

(c)

Table 4.2 (Cont'd)

Four-band Kompsat-2 MS image with Envisat ASAR data taken in July

Class Names	Corn	Tomato	Rice	Sugar beet	Wheat
Tomato	1.04				
Rice	1.88	1.95			
Sugar beet	1.99	1.82	2.00		
Wheat	1.99	1.99	2.00	2.00	
Grass Land	1.93	1.98	1.99	1.99	1.59
Average Separability: 1.88					
Signature pair with Minimum Separability: Corn, Tomato					

(d)

The lowest separability value was computed as 1.04 for tomato and corn of the four-band Kompsat-2 MS image and Envisat ASAR data acquired in July. The classes grass land and wheat provided moderate result of about 1.59. The separability values of the other crop types exhibited relatively high results over 1.80. The max separabilities (2.00) were provided between the class pairs of sugar beet-rice, wheat-rice, and wheat-sugar beet.

Four-band Kompsat-2 MS image taken in August

Class Names	Corn	Tomato	Rice	Sugar beet	Wheat
Tomato	1.56				
Rice	1.51	1.30			
Sugar beet	1.82	1.04	0.96		
Wheat	1.99	1.92	1.99	1.99	
Grass Land	1.99	1.66	1.99	1.99	1.27
Average Separability: 1.67					
Signature pair with Minimum Separability: Rice, Sugar beet					

(e)

Table 4.2 (Cont'd)

Four-band Kompsat-2 MS image with Envisat ASAR data taken in August

Class Names	Corn	Tomato	Rice	Sugar beet	Wheat
Tomato	1.63				
Rice	1.53	1.47			
Sugar beet	1.84	1.07	1.27		
Wheat	1.99	1.97	1.99	1.99	
Grass Land	1.99	1.93	1.99	1.99	1.38
Average Separability: 1.74					
Signature pair with Minimum Separability: Tomato, Sugar beet					

(f)

The lowest separability values of the four-band Kompsat-2 MS image and Envisat ASAR data taken in August were computed for the class pairs of sugar beet-tomato (1.07), sugar beet-rice (1.27), grass land-wheat (1.38), and rice-tomato (1.47). A marginal result of about 1.53 was observed between the class rice and corn.

Separability values computed for the Transformed Divergence Index slightly improved the results of the Bhattacharya distance. The results are provided below:

Table 4.3 The matrices of Transformed Divergence Index for four-band Kompsat-2 MS images taken in June, July, and August (a, c, e), with the Envisat ASAR data (b, d, f).

Four-band Kompsat-2 MS image taken in June

Class Names	Corn	Tomato	Rice	Sugar beet	Wheat
Tomato	1.99				
Rice	1.99	1.99			
Sugar beet	1.99	1.95	1.99		
Wheat	1.99	1.94	1.99	1.99	
Grass Land	1.85	1.64	1.99	1.85	1.58
Average Separability: 1.92					
Signature Pair with Minimum Separability: Wheat, Grass Land					

(a)

Table 4.3 (Cont'd)

Four-band Kompsat-2 MS image with Envisat ASAR data taken in June

Class Names	Corn	Tomato	Rice	Sugar beet	Wheat
Tomato	1.99				
Rice	1.99	1.99			
Sugar beet	1.99	1.96	1.99		
Wheat	1.99	1.94	1.99	1.99	
Grass Land	1.88	1.76	1.99	1.97	1.62
Average Separability: 1.94					
Signature Pair with Minimum Separability: Wheat, Grass Land					

(b)

Four-band Kompsat-2 MS image taken in July

Class Names	Corn	Tomato	Rice	Sugar beet	Wheat
Tomato	0.98				
Rice	1.97	1.99			
Sugar beet	1.99	1.96	2.00		
Wheat	1.99	2.00	2.00	2.00	
Grass Land	1.96	1.98	2.00	2.00	1.80
Average Separability: 1.91					
Signature pair with Minimum Separability: Corn, Tomato					

(c)

Four-band Kompsat-2 MS image with Envisat ASAR data taken in July

Class Names	Corn	Tomato	Rice	Sugar beet	Wheat
Tomato	1.13				
Rice	1.98	1.99			
Sugar beet	1.99	1.97	2.00		
Wheat	1.99	2.00	2.00	2.00	
Grass Land	1.97	1.99	2.00	2.00	1.81
Average Separability: 1.92					
Signature pair with Minimum Separability: Corn, Tomato					

(d)

Table 4.3 (Cont'd)

Four-band Kompsat-2 MS image taken in August

Class Names	Corn	Tomato	Rice	Sugar beet	Wheat
Tomato	1.69				
Rice	1.70	1.92			
Sugar beet	1.86	1.51	1.09		
Wheat	2.00	1.98	2.00	2.00	
Grass Land	1.99	1.95	2.00	1.99	1.52
Average Separability: 1.81					
Signature pair with Minimum Separability: Rice, Sugar beet					

(e)

Four-band Kompsat-2 MS image with Envisat ASAR data taken in August

Class Names	Corn	Tomato	Rice	Sugar beet	Wheat
Tomato	1.75				
Rice	1.72	1.96			
Sugar beet	1.87	1.55	1.42		
Wheat	2.00	1.99	2.00	2.00	
Grass Land	1.99	1.99	2.00	1.99	1.60
Average Separability: 1.86					
Signature pair with Minimum Separability: Rice, Sugar beet					

(f)

In this study, manually collected training samples were also analyzed for each image and similar results were obtained with the results achieved from the proposed automated approach. Furthermore, due to the lower separability values, the optical band combinations less than four were not included in the analysis. The separability values computed for Bhattacharya Distance less than four band combinations are provided in Appendix G.

4.3.2 Pixel-Based Analysis

In this study, two different types of pixel-based image classification methods called; (i) Maximum Likelihood Classification (MLC) and (ii) Support Vector Machines (SVMs)

were examined to classify eight crop types by four-band Kompsat-2 MS images and Envisat ASAR data. When performing the classifications, other type of land classes such as villages, roads, and water canals were manually excluded. The flowchart of the pixel-based image classification is presented in Figure 4.7. Detailed explanations of the MLC and SVMs methods are provided in Section 4.3.2.1 and Section 4.3.2.2, respectively.

4.3.2.1 Maximum Likelihood Classification (MLC)

Maximum Likelihood Classification (MLC), a traditional supervised classification method, computes the probabilities of a pixel for a given number of training classes and assigns the class id to the pixel that has the highest probability value. The method assumes that the statistics of each class in the training data has a normal distribution. In order to obtain the most probable classes, a *probability density function* is computed. If the classification is performed on a single band image, the statistics mean and variance of each training class are computed as in Eq.4.6 (Jensen, 2005).

$$\hat{p}(x|w_i) = \frac{1}{(2\pi)^{\frac{1}{2}}\hat{\sigma}_i} \exp\left[-\frac{1}{2} \frac{(x - \hat{\mu}_i)^2}{\hat{\sigma}_i^2}\right] \quad (\text{Eq.4.6})$$

Where;

$\exp []$ is e (the base of the natural logarithms) raised to the computed power,

x is the brightness values of the pixel,

$\hat{\mu}_i$ is the estimated mean value of the pre-defined training class,

$\hat{\sigma}_i^2$ is the estimated variance of all measurements in this class.

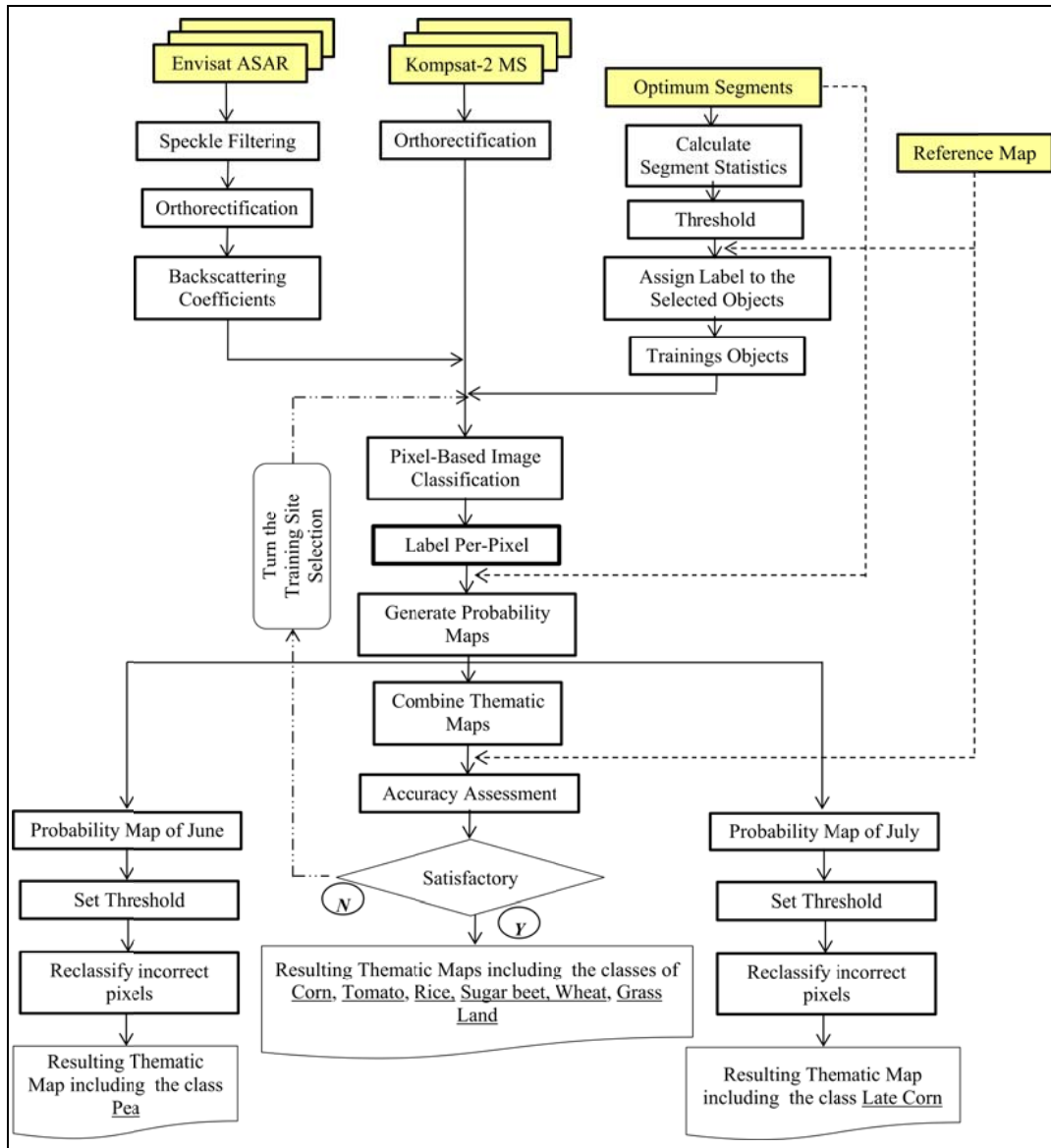


Figure 4.7 The flowchart of the pixel-based image classification process

If a multi-band classification problem of a given training data set is searched, there is a need to define an n -dimensional multivariate normal density function by computing the variance and covariance statistics of the training data used in the classification operation (Eq.4.7) (Jensen, 2005).

$$p(X|w_i) = \frac{1}{(2\pi)^{\frac{n}{2}} |V_i|^{\frac{1}{2}}} \exp \left[-\frac{1}{2} (X - M_i)^T V_i^{-1} (X - M_i) \right] \quad (\text{Eq.4.7})$$

M_i is the mean vector of each training class,
 V_i is the covariance matrix of each training class,
 $|V_i|$ is the determinant of the covariance matrix,
 V_i^{-1} is the inverse of the covariance matrix,
 $(X - M_i)^T$ is the transpose of the vector $(X - M_i)$.

The MLC method was tested on the study area based on two different data sets:

- (i) The four-band single-date Kompsat-2 images (June, July, and August) and,
- (ii) The four-band single-date Kompsat-2 images (June, July, and August) with the corresponding Envisat ASAR data.

First, the classification method was applied on the MS Kompsat-2 data by the automatically selected training samples and the resulting thematic maps for the six crop types (corn, tomato, rice, sugar beet, wheat, and grass land) having common growing period were produced separately for each date (June, July, and August) (Figure 4.8 (a, c, e)). The classification results of the fused Kompsat-2 products were also tested in the analyses. However, the overall accuracies did not exceed 0.2% to the classification results of the MS data. Hence, the MS Kompsat-2 data was used in the classification operations to increase the computational efficiency and save time. In order to make use of different characteristics of the microwave data, backscattering coefficients of the filtered Envisat ASAR data was included as additional band to the classification analyses. The resulting pixel-based classification results of the six crop types are given in Figure 4.8 (b, d, f).

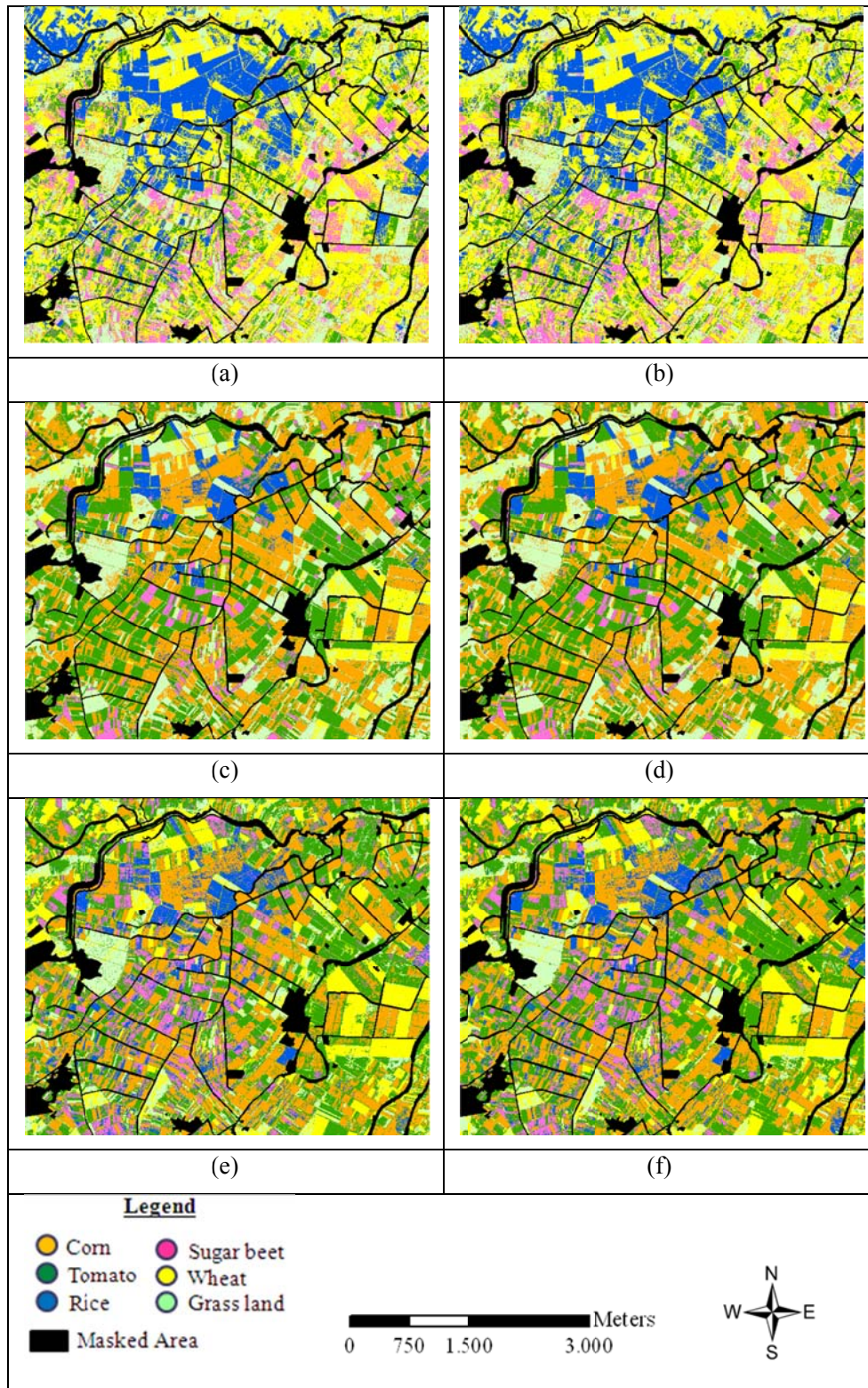


Figure 4.8 (a, c, e) The pixel-based results of the MLC for the four-band MS Kompsat-2 images acquired in June, July, and August (2008), respectively. (b, d, f). The classification results of the same optical images with Envisat-ASAR.

4.3.2.2 Support Vector Machines (SVMs) Classification

The Support Vector Machines (SVMs) approach has become an attractive supervised classification method in recent years due to the effective classification performance in the remote sensing analyses (e.g. Huang et al., 2002; Keuchel et al., 2003; Foody and Mathur, 2004; Pal and Mather, 2005; Foody and Mathur, 2006; Liu et al., 2006; Pal, 2006; Yang, 2011; Taskin Kaya et al., 2011) although it was proposed in the late 1970s (Vapnik, 1979). A recent and an extensive review of the SVMs method were performed by Mountrakis et al. (2011). Based on the studies conducted, the SVM method has several advantages compared to the other image classification algorithms: (i) The SVMs do not have any assumption about data distribution, because the distribution of remotely sensed images is usually unknown. This characteristic makes the SVMs method superior to the other image classification methods, especially MLC; because the MLC assumes that the data have a normal distribution. However, if the selected classes have different kind of distributions than the normal distribution, this may negatively affect the final performance of the classification. (ii) Other important characteristic of the SVMs method is the ability of classifying the data successfully using small numbers of training data set. The SVMs algorithm can be effectively applied on the data using a limited number of training samples which is a very important characteristic, especially for the studies analyzing large areas. This is because the collection of ground truth is very expensive and time consuming process for large test sites. Besides the advantages described above, the usage of an appropriate kernel type in the analysis provides further effective classification performance (e.g. Kavzoglu and Colkesen, 2009; Yang, 2011; Mountrakis et al., 2011). Detailed explanation about the SVMs algorithm is presented below:

In SVMs, a *structural risk minimization concept* is introduced to reduce the probability of misclassification of the data by defining a hyper plane (e.g. a decision boundary) based on the training samples (Vapnik, 1995, 1998). The method was originally developed to solve linear classification problems by assigning the labels +1 and -1, in which a hyper plane is constructed to classify the data with maximal distance, called '*margin*'. Figure 4.9 shows multiple hyper planes that separate the two classes, where the hyper plane b separates the classes with maximum margin, while the other hyper planes (a, c, and d) are very close to the training data points and do not provide an efficient separation. So, the logic of the SVMs classifier is to construct the optimum hyper plane that keeps the

distance between the hyper plane and the training samples as large as possible (Tso and Mather, 2009).

In a case of two linearly separable classes, the training data set is defined by $\{x_i, y_i\}$, $i = 1, \dots, n$, $y_i \in \{1, -1\}$, $x_i \in R^d$, where x_i is the training data value in d dimensional space and y_i is the class label of the training data.

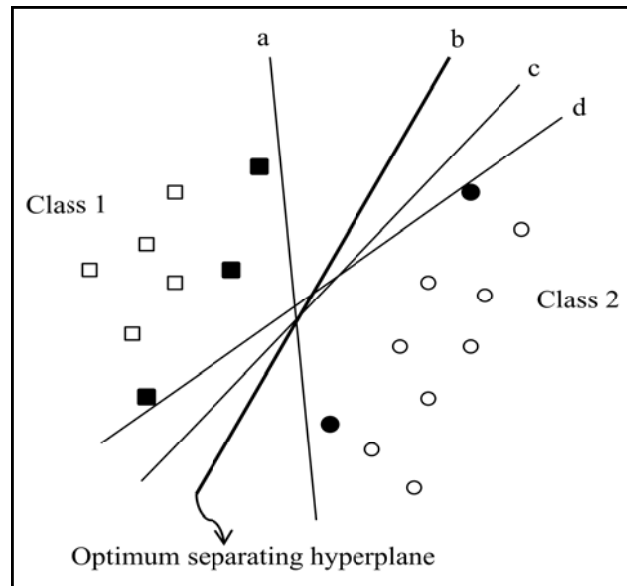


Figure 4.9 Examples of hyper planes and the optimum hyper plane (b) in the linear situation (Tso and Mather, 2009)

In this case, a decision function can be defined based on the equation below (Eq.4.8):

$$w^T x + b = 0 \tag{Eq.4.8}$$

Where;

x is a data point on the hyper plane,

w is normal to the hyper plane,

T means matrix transposition, and

b indicates bias.

If it is assumed that the constructed hyper plane is suitable for separating all training data, the equation can be written as $w^T x_i + b \geq +1$, $y_i = 1$, for the closest training points on one

side of the hyper plane with the perpendicular distance from the origin and $w^T x_i + b \leq -1$, $y_i = -1$, for the training points lying on the other side of the hyper plane. The training points on the hyper planes are called *support vectors*, which are used to construct the optimum hyper plane and classify the unknown data in the analyses. Hence, a small number of training samples could be sufficient to obtain high accuracies for the SVMs method. The two equations defined above can be combined as below (Eq.4.9);

$$y_i(w^T X x_i + b) - 1 \geq 0 \quad (\text{Eq.4.9})$$

The margin between two hyper planes is written as $2/\|w\|$. Depending on the restriction indicated in Eq.4.9, the maximization of the margin is formulated as (Eq. 4.10);

$$\min \left\{ \frac{w^2}{2} \right\} \quad (\text{Eq.4.10})$$

In order to make the Eq. 4.9 easy, a dual Lagrangian equation is utilized:

$$L_{dual} = \sum_{i=1}^n \alpha_i - \frac{1}{2} \sum_{i=1}^n \alpha_i \alpha_j y_i y_j x_i \times x_j \quad (\text{Eq.4.11})$$

Where;

α_i represents positive Lagrangian multipliers.

The hard margin SVM optimization problem is then defined using the Eq. 4.12.

$$f(x) = \text{sign} \left(\sum_{i=1}^{nsv} \alpha_i y_i (x \times x_i) + b \right) \quad (\text{Eq.4.12})$$

Where;

nsv means the number of support vectors.

Based on the formula, all the training samples are suitable to the inequality restriction and thus the points can be separated easily, which is called *hard margin* method. On the other hand, due to the nature of remotely sensed data, this situation does not always valid and

the linear boundaries do not provide a good separation to the data points. Therefore, a *soft margin* method was introduced to overcome this problem by defining the slack variables $\xi_i, i = 1, \dots, n$. When the slack variables are added to the basic formula of the SVM, the Eq.4.9 is updated as Eq. 4.13.

$$y_i(w^T X x_i + b) \geq 1 - \xi_i; \xi_i \geq 0, \quad (\text{Eq.4.13})$$

The optimal problem then computed as Eq.4.14 when the penalty parameter (C) is added into the analysis:

$$\min \left\{ \frac{\|w\|^2}{2} + C \sum_{i=1}^n \xi_i \right\} \quad (4.14)$$

Where;

C is a penalty parameter that is defined by the user prior to the classification. When the C increases, it means the degree of misclassification increases (Tso and Mather, 2009; ENVI Manual, 2007).

The first part of the equation (Eq. 4.14) is to increase the margin to its maximum level, while the second part is to search the training points positioned to the “wrong” side of the margin (Figure 4.10).

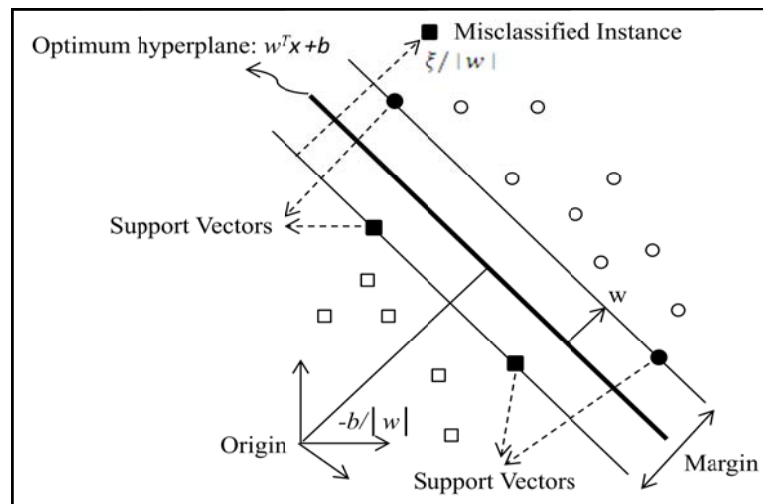


Figure 4.10 Linear hyper planes for two classes that do not totally separated (Tso and Mather, 2009)

The linear hyper planes are not suitable to separate the classes in most real-world problems; therefore the concept of *non-linear decision surface* is proposed. Based on this concept, to increase the separability between classes, the data points are mapped into a higher dimensional Euclidean space (called Hilbert Space).

In order to improve the computational performance of the SVMs performed in higher dimensional space, several kernel functions are presented (Vapnik 1995). Most of the recent remote sensing studies indicated that the definition of kernel function based on the study is a very critical step to obtain reliable outputs (e.g. Yang, 2011; Schölkopf et al., 1997). The mostly used kernel functions are given in Eq.4.15, Eq.4.16, Eq.4.17, and Eq.4.18.

Linear kernel:

$$K(x_i, x_j) = x_i^T \times x_j \quad (\text{Eq. 4.15})$$

Polynomial kernel:

$$K(x_i, x_j) = (\gamma(x_i \times x_j) + \delta)^d, \gamma > 0, \delta > 0 \quad (\text{Eq. 4.16})$$

Radial basis function:

$$K(x_i, x_j) = \exp(-\gamma \|x_i - x_j\|^2), \gamma > 0 \quad (\text{Eq. 4.17})$$

Sigmoid kernel:

$$K(x_i, x_j) = \tanh(\gamma(x_i \times x_j) - \delta), \gamma > 0, \delta > 0 \quad (\text{Eq. 4.18})$$

Where;

γ defines gamma term in the kernel function,

d is the polynomial degree for the polynomial kernel types,

δ means bias term (Tso and Mather, 2009).

In order to classify multiple classes, the method of SVMs is then extended (Vapnik, 1998; Crammer and Singer, 2002). There are three main approaches proposed for the problem of multiclass SVMs in the literature: (i) one-against-one, (ii) one-against-others, and (iii) directed acyclic graph (DAG).

The one-against-one method was applied on the MS Kompsat-2 images and Envisat ASAR data in this study, in which the training process is performed based on each couple of classes and the label is assigned to the pixel having the highest vote (Chang and Lin, 2001; Wu et al., 2004; Tso and Mather, 2009). Radial Basis Function (RBF) kernel that provides the improved classification accuracies in most of the studies (e.g. Yang, 2011; Kavzoglu and Colkesen, 2010, Pal and Mather, 2005) was utilized in the analyses. In order to perform a meaningful comparison, the same training samples were used when classifying the data with MLC and SVMs method (Section 4.2.1). Similar to the analyses of MLC, the Kompsat-2 images taken for each date were classified with the method of SVMs, and after that, Envisat ASAR data were also included in the analyses. The gamma functions (γ) and penalty parameters (C) utilized in the classifications of each image combinations are provided in Table 4.4. The resulting thematic outputs of the SVMs method are presented in Figure 4.11.

Table 4.4 Gamma functions (γ) and penalty parameters (C) used for the SVMs classification of the MS Kompsat-2 images and for the combined maps of Kompsat-2 MS and Envisat ASAR data

Data	Month	γ	C
Four-band Kompsat-2 MS image	June	0.25	2200
	July	0.25	200
	August	0.25	200
Four-band Kompsat-2 MS image and Envisat ASAR data	June	0.20	2200
	July	0.20	200
	August	0.20	200

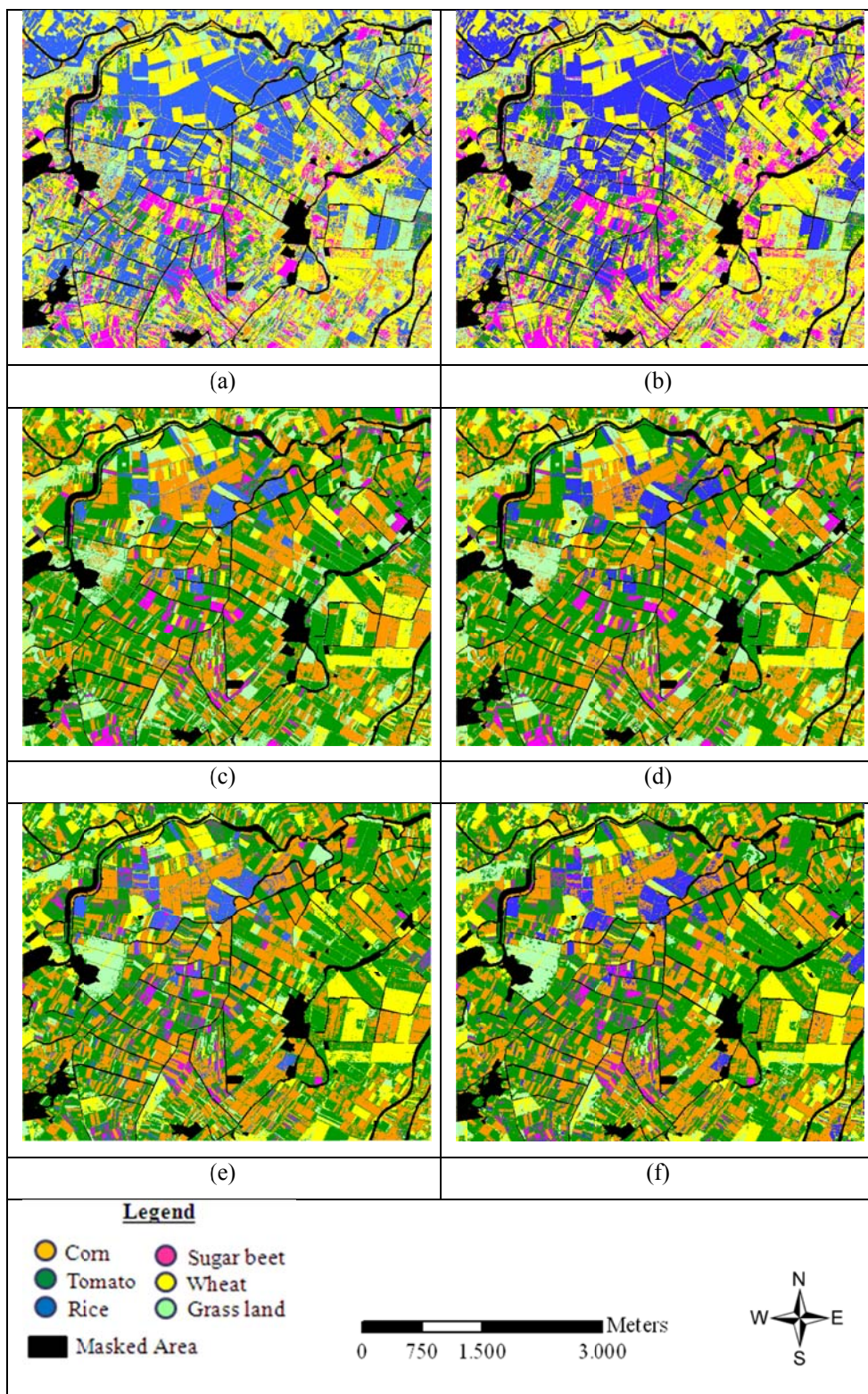


Figure 4.11 (a, c, e) The pixel-based results of the SVMs classification for the four-band MS Komsat-2 images acquired in June, July, and August, respectively. (b, d, f) The classification results of the same optical images with Envisat-ASAR data.

4.3.3 Probability Estimation

In multi-temporal applications, reliable methods are necessary to combine the information of the same objects taken in different images. This is generally performed based on multiple decision rules. Although the rule-based analysis may provide acceptable results in various remote sensing studies (e.g. Ban, et al., 2010), defining the rules require not only an efficient knowledge about the study area but also an accurate data analysis. Suitability of these rules to the study area and data directly affects the resulting accuracy of the thematic maps. Hence, much more effective methods are necessary to combine such multi-temporal data.

In this study, a new approach was proposed to combine the thematic information of optical and microwave images taken in different dates. The proposed approach is based on a hard classification strategy in which, first, probability maps were computed for each single-date image in pixel-based manner and the max membership value is then assigned as a class label to the pixels. The probabilities of the pixels were computed using two different approaches due to the different characteristics of the classifiers used. For the MLC, the probability membership function of the class a is computed by the following equations, Eq.4.19, Eq.4.20, Eq.4.21, and Eq.4.22:

$$f_a(x) = \frac{P_a^*(x)}{\sum_{i=1}^m P_i^*(x)} \quad (\text{Eq.4.19})$$

Where;

$$P_i^*(x) = \frac{1}{(2\pi)^{N/2} |V_i^*|^{\frac{1}{2}}} \times \exp[-0.5(x - \mu_i^*)^T V_i^{-1} (x - \mu_i^*)] \quad (\text{Eq.4.20})$$

N means the dimension of the pixel vectors,

m is the number of classes,

In the equation (Eq.4.20), fuzzy mean and covariance matrices are calculated as below, respectively:

$$\mu_a^* = \frac{\sum_{i=1}^n f_a(x_i) x_i}{\sum_{i=1}^n f_a(x_i)} \quad (\text{Eq.4.21})$$

n is the total number of sample pixel measurement vectors,
 f_a is the membership function of class a ,
 x_i is a sample pixel measurement vector ($1 \leq i \leq n$)

$$V_a^* = \frac{\sum_{i=1}^n f_a(x_i)(x - \mu_i^*)(x - \mu_i^*)^T}{\sum_{i=1}^n f_a(x_i)} \quad 1.4.22$$

In the equation Eq. 4.20, the term $(x - \mu_i^*)^T V_i^{-1} (x - \mu_i^*)$ defines the *Mahalanobis Distance* between the pixel x and the signature means. The membership function of class a and the distance value is inversely proportional. That means, if the distance between the pixel and the class mean is high, the membership function of the pixel is small and the pixel is most likely to be incorrectly classified (Pouncey and Swanson, 1999, Jensen, 2005). Figure 4.12 indicates the combined thematic map (June-July-August) of the four-band Kompsat-2 and Envisat ASAR data classified by the MLC method with the probability map.

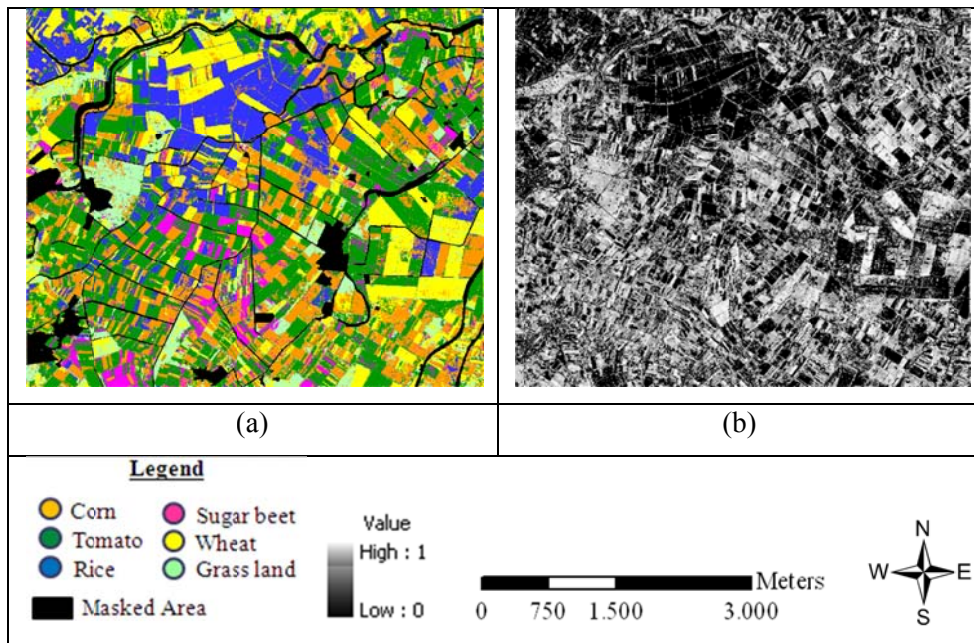


Figure 4.12 (a) The combined thematic map (June-July-August) of four-band Kompsat-2 and Envisat ASAR data computed for the MLC method (b) with the probability map (black areas represent the most correctly classified pixels)

In order to assess the probabilities of the thematic maps computed for the SVMs method, assume that an observation of x is provided with its label y . Based on the given observations; let say r_{ij} , which is the estimated pair wise class probabiliti (Eq.4.23) $P(y = i | y = i \text{ or } j, \mathbf{x})$, are exist. A model was constructed by i^{th} and j^{th} classes of a training set to compute r_{ij} for each new \mathbf{x} . After computing all r_{ij} , estimation of $p_i = P(y = i | \mathbf{x}), i = 1, \dots, k$. is performed for each pixel as follows (Wu et al., 2004):

$$p^{min} \sum_{i=1}^k \sum_{j:j \neq i} (r_{ji}p_i - r_{ij}p_j)^2$$

Subject to:

$$\sum_{i=1}^k p_i = 1, p_i \geq 0, \forall i. \quad (\text{Eq.4.24})$$

The classification rule is then defined by

$$\delta = \text{argmax}_i [p_i^2] \quad (\text{Eq.4.25})$$

Where;

p^2 denotes the solution of Eq. 4.24,

k is the number of classes.

Figure 4.13 indicates a combined SVMs classification result of the four-band Kompsat-2 images with Envisat ASAR data taken in June, July, and August with the computed probability map. Other probability maps produced for the MLC and SVMs methods with the corresponding thematic maps are given in Appendix H.

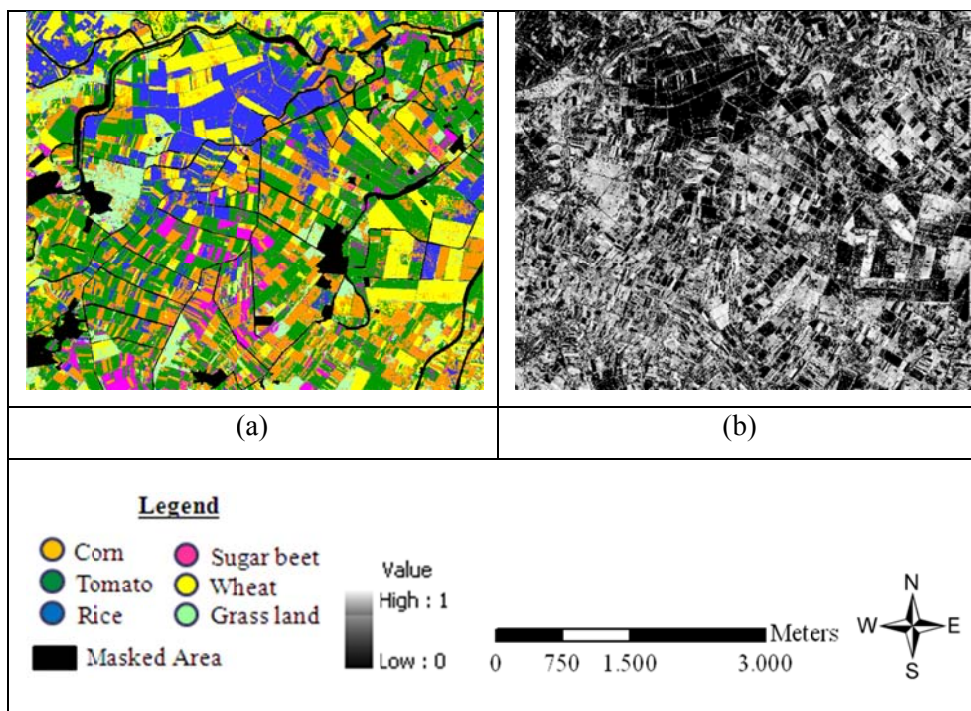


Figure 4.13 (a) The combined thematic map of SVMs method and (b) its probability map

In this study, the probability maps were generated for each single-date image. However, according to the field-works it was observed that a crop rotation occurs for the class pea and late corn in the test site. The images taken in June represent the late planting period of the pea. After June, a crop rotation occurs for the pea fields. A similar case is valid for the late corn cultivated in July. To find those regions, first, the Kompsat-2 and Envisat ASAR data taken in June and July were classified separately by including new training samples for the class pea and late corn into the classification. However, the produced maps did not provide satisfactory results for the crops. Hence, a histogram threshold was set on the probability maps of the single-date June and July to find out the pixels that were most likely to be incorrectly classified. The incorrectly classified pixels under the threshold (< 0.90) were then extracted from the thematic map and those regions were reclassified again (Figure 4.14).

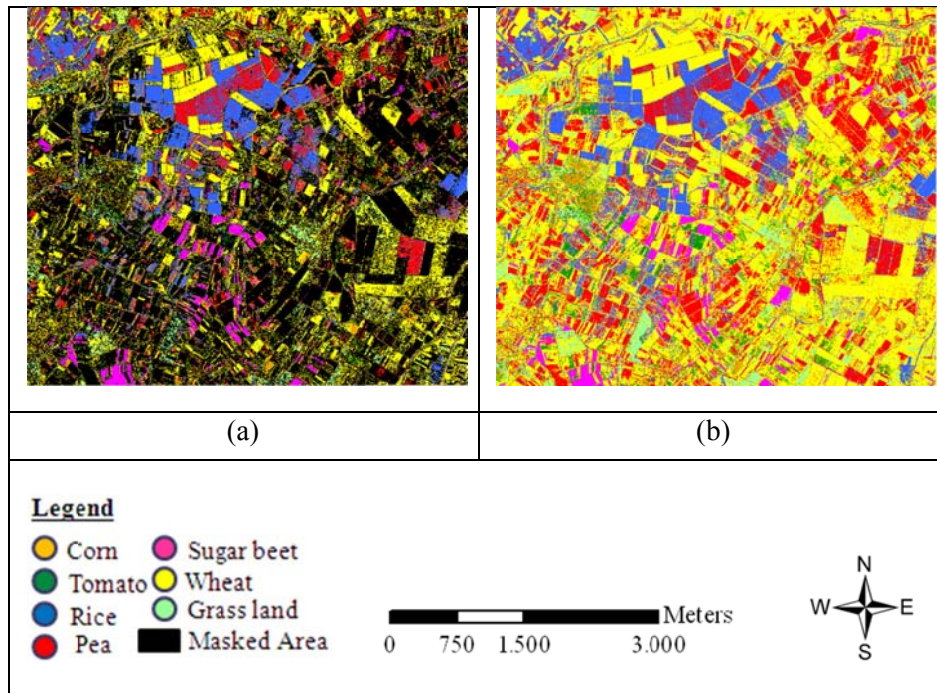


Figure 4.14 (a) Correctly classified pixels and (b) the new thematic map of June including pea

4.3.4 Segment-Based Analysis

With the recent advances in RS technology, high spatial resolution satellites (e.g. GeoEye-1, Worldview1-2, and QuickBird) have become available and provide an opportunity to obtain more detailed information from the earth surface. On the other hand, in the case of agricultural applications, with the improvement of high spatial resolution images, the traditional pixel-based analyses are negatively affected due to the misclassification problems caused by for example; the nutrient limitations, pests, disease, the variation in soil moisture conditions, and the mixed pixel effects on the agricultural boundaries (Smith and Fuller, 2001; De Wit and Clevers, 2004). Hence, in order to eliminate the misclassification problems, a segment-based strategy is proposed, in which the image is divided into homogenous segments and each pixel is assigned to a final class of the entire segment according to the statistical properties, instead of determining the class label for each pixel separately (De Wit and Clevers, 2004). In this case, quality of the segments generated for the homogenous regions play a critical role to determine the accuracy of the classification. In this study, the segment-based approach was applied on the thematic maps defined below (Figure 4.15):

- i. The optimum segmentation result was integrated to the classified map,
- ii. the frequency of the classified pixels (mode) in the segments were computed,
- iii. the label of majority class was assigned to the segments (Figure 4.16).

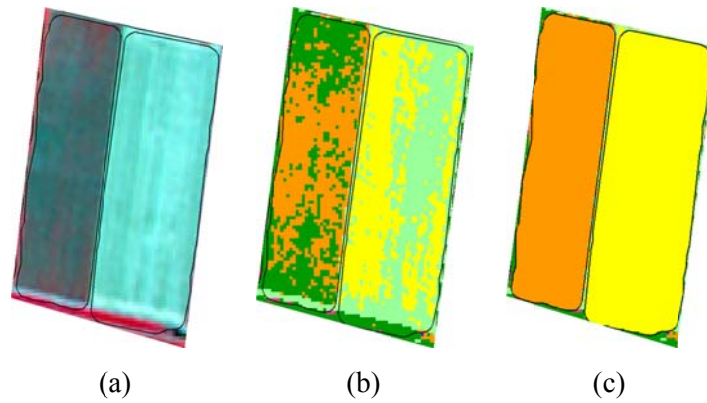


Figure 4.15 A small part of (a) false color composite MS Kompsat-2 image (taken in July), (b) the result of MLC classification (blue, green, red, NIR), and (c) the classification result of the segment-based approach overlaid with the produced segments.

The segment-based results of the combined image (June-July-August) generated for the MLC and SVMs method are presented in Figure 4.17 and Figure 4.18, respectively. The thematic maps of the segment-based approach produced for the single-date images and multiple image combinations are provided in Appendix H.

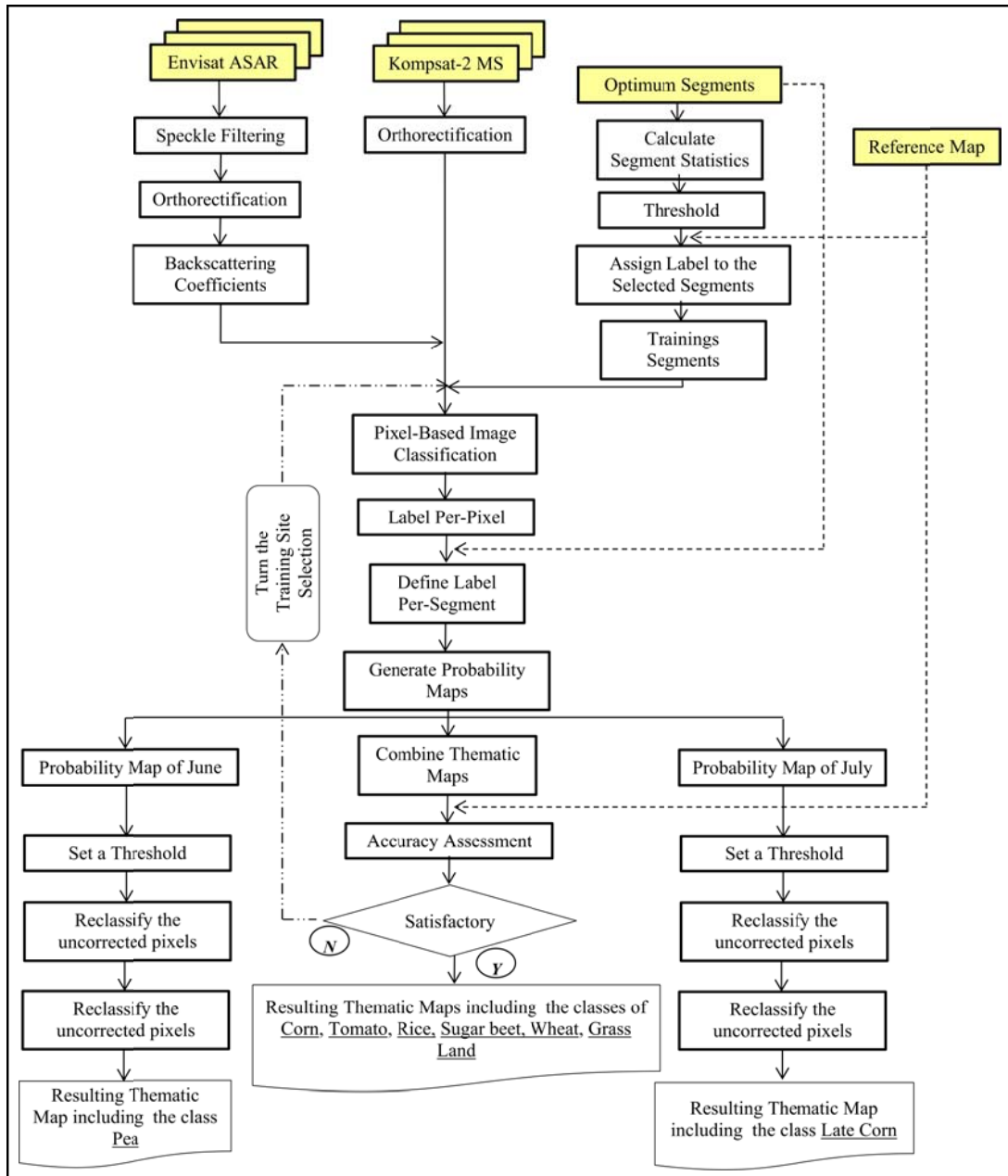


Figure 4.16 The flowchart of the segment-based image classification methodology

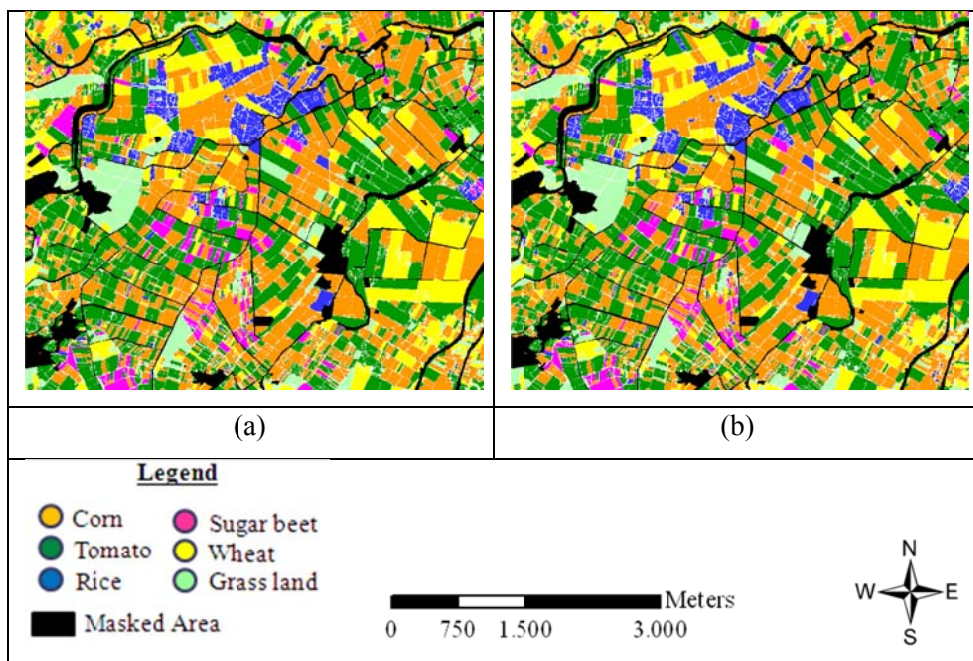


Figure 4.17 (a) The combined (June-July-August) thematic maps produced by the segment-based approach using MLC method of four-band Kompsat-2 MS images (b) with Envisat ASAR data.

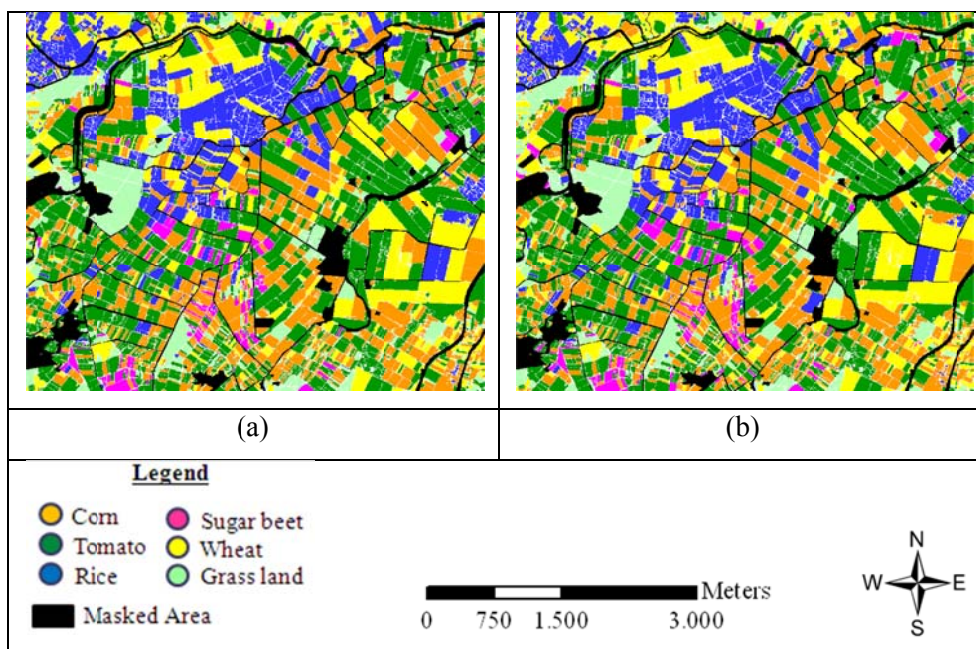


Figure 4.18 (a) The combined (June-July-August) thematic maps produced by the segment-based approach using SVMs method of four-band MS Kompsat-2 MS images (b) with Envisat ASAR data.

4.3.5 Field-Based Analysis

Besides the pixel-based and segment-based analyses, the thematic maps generated with the pixel-based approach were overlaid with the reference agricultural fields and the results were evaluated in a field-based manner, as well. To perform the field-based analyses, frequency of the pixels classified by MLC and SVMs was computed and the mode of the class id was assigned as label to the original fields. After that, to analyze the field size effect on the accuracies, the field agricultural fields were divided into three groups based on the field-sizes. The first group includes small agricultural fields with the field size range from 0.01 ha to 4.99 ha, the second group indicates the fields that have medium size (5.00 ha-9.99 ha), and the third group contains the large fields (10.00ha-38.31ha) (Figure 4.19). The resulting combined thematic maps (June-July-August) produced by the field-based approach of the MLC and SVMs methods are presented in Figure 4.20 and Figure 4.21, respectively. The field-based results computed for the MLC and SVMs method based on the field sizes are provided in Appendix I.

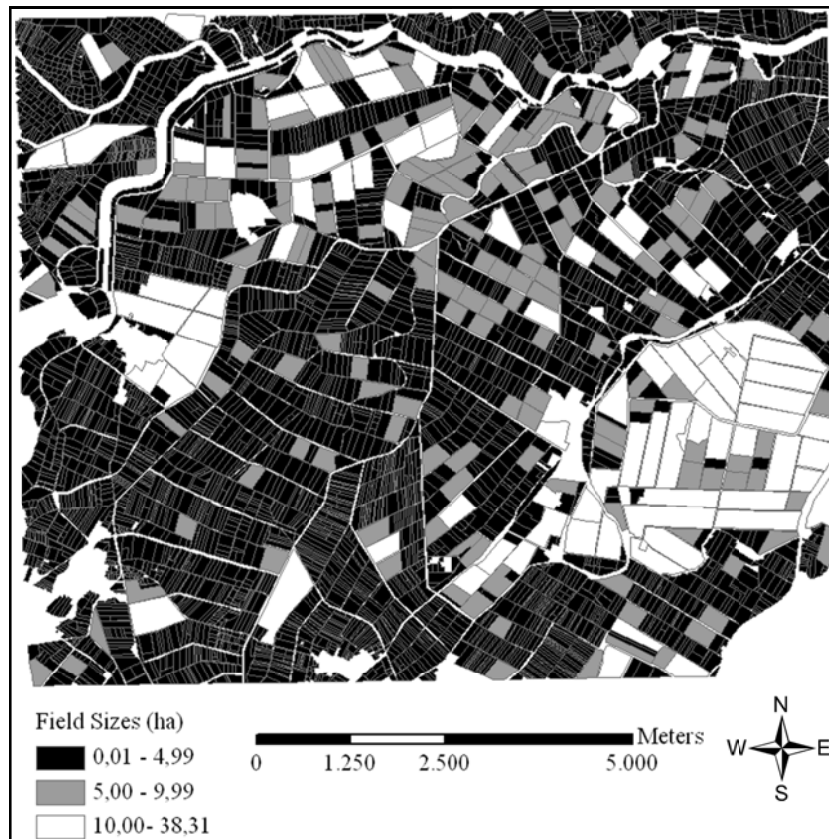


Figure 4.19 Agricultural fields classified based on the field-sizes

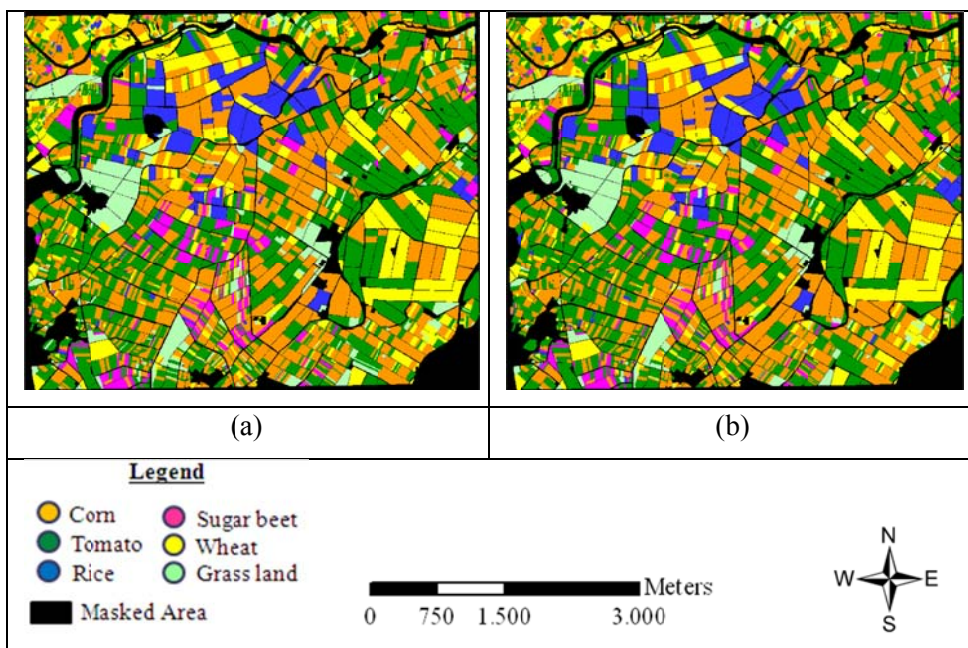


Figure 4.20 (a) The field-based results of the combined (June-July-August) thematic map of the MLC method for four-band Kompsat-2 MS images (b) with the Envisat-ASAR data.

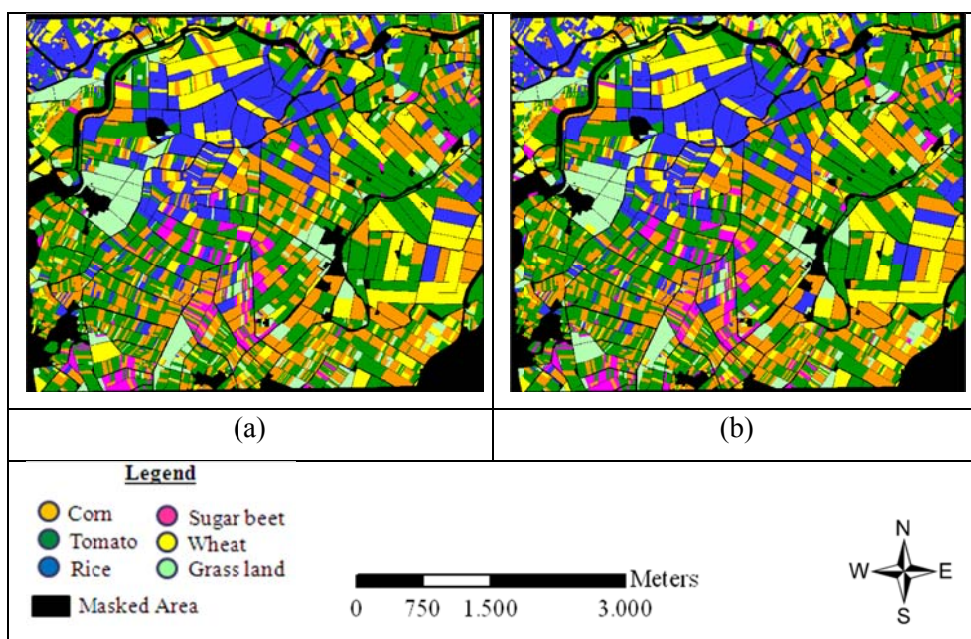


Figure 4.21 (a) The field-based result of the combined (June-July-August) thematic map of the SVMs method for four-band Kompsat-2 MS images with (b) the Envisat-ASAR data.

CHAPTER 5

RESULTS AND DISCUSSION

Evaluation of the thematic maps is a crucial process to image classification analyses to understand and interpret the quality of the final products produced. In this chapter, the evaluation strategy is explained in detail followed by an introduction of the reference data used in the accuracy assessment process. The computed accuracies of the pixel-based, segment-based and field-based analyses are then discussed.

5.1 Reference Data

The reference data was prepared by updating the database of the existing vector data (agricultural field boundaries) by the field works performed concurrently with the image acquisitions. Three visits were performed on the test site and crop information such as canopy developments, irrigation, fertilization activities were recorded into a database of the vector data. After transferring the vector data into a raster format based on the crop information, around 30% of all the pixels were utilized as a reference source in the accuracy assessment process. During the computations of the accuracy measures, to provide a reliable evaluation, the training areas were excluded from the reference data. The reference fields utilized in the accuracy assessment process of the six crop types that have a common development period are presented in Figure 5.1.

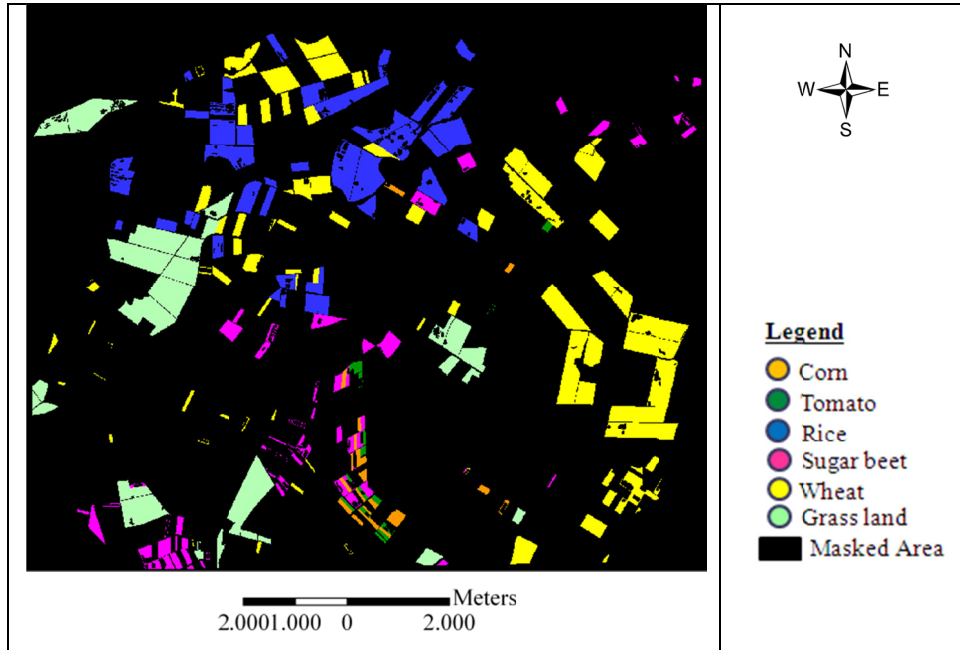


Figure 5.1 Reference map for six crop types (corn, tomato, rice, sugar beet, wheat, and grass land)

To evaluate the thematic maps, in total 567 sample points were scattered on the reference fields by a simple random sampling strategy, where the sample points were distributed to the reference fields based on its class percentages. The number of samples used in the evaluation was determined by Jensen (2005) in Eq.5.1:

$$N = \frac{B \prod_i (1 - \prod_i)}{b_i^2} \quad (\text{Eq.5.1})$$

Where

N refers to the sample size

\prod_i is the proportion of a population in the i^{th} class out of k classes that has the proportion closest to 50%,

b_i is the desired precession for this class (e.g. 5%),

B explains the upper $(\alpha/k) \times 100^{\text{th}}$ percentile of the chi square (χ^2) distribution with 1 degree of freedom,

k is the number of classes.

5.2 Evaluation Method

Accuracies of the thematic maps were computed by *confusion (error) matrices*, which is a very widely used accuracy assessment method in remote sensing studies. By the confusion matrix, the relationship between the known reference data (ground truth) and the corresponding results can be compared pixel-by-pixel basis on the defined categories (Lillesand, 2004). The matrix consists of three major accuracy measures: (i) *producer's accuracy (omission error)*, (ii) *user's accuracy (commission error)* and (iii) *overall accuracy*. The *producer's accuracy (omission error)* is computed by dividing the total number of correctly classified pixels by the total number of the given reference pixels, which indicates the probability of a reference pixel that is correctly classified. The *user's accuracy (commission error)* is defined by a ratio between the total number of correctly classified pixels in a category and the total number of pixels that were actually classified in that category. The user's accuracy of a class indicates the reliability of a pixel classified on a map actually represents that category on the ground. In order to provide a general accuracy for the results, the *overall accuracy* is computed by dividing the total number of correctly classified pixels, major diagonal elements of the matrix, by the total number of pixels in the error matrix (Jensen, 2005).

The overall accuracy includes the data along the major diagonal only and excludes the errors of omission and commission, therefore Kappa was also computed to evaluate the results. The Kappa value incorporates the non-diagonal elements of the error matrix, which removes the chance agreement. The Kappa statistics (k) are adapted from Lillesand (2004) in (Eq. 5.2):

$$k = \frac{N \sum_{i=-1}^r x_{ii} - \sum^r (x_{i+} \cdot x_{+i})}{N^2 - \sum_{i=-1}^r (x_{i+} \cdot x_{+i})} \quad (\text{Eq.5.2})$$

Where;

r = number of rows in the error matrix

x_{ii} = number of observations in row i and column i (on the major diagonal)

x_{i+} = total of observations in row i

x_{+i} = total of observations in column i

N = total number of observations include in matrix

Table 5.1 Summary table of the analyzed data

Data	Date	Class No	Methods	Approaches
Kompsat-2 MS	June	6	MLC	Pixel-Based, Segment-Based, Field-Based
	July			
	August			
Kompsat-2 MS &Envisat ASAR	June	6&8		
	July	6&8		
	August	6		
	June&July	6	MLC & Probabilistic Approach	
June&August				
July&August				
Kompsat-2 MS	June	6	SVMs	
	July			
	August			
Kompsat-2 MS &Envisat ASAR	June	6&8		
	July	6&8		
	August	6		
	June&July	6	SVMs & Probabilistic Approach	
June&August				
July&August				
Kompsat-2 MS &Envisat ASAR	June	6	SVMs & Probabilistic Approach	
	July			
	August			
	June&July	6		
June&August				
July&August				
Kompsat-2 MS &Envisat ASAR	June	6	SVMs & Probabilistic Approach	
	July			
	August			
	June&July	6		
June&August				
July&August				

According to Table 5.1, in total 64 different overall accuracy measures were computed for the image combinations based on pixel-based, segment-based, and field-based manner.

Table 5.2 and Table 5.3 provide a general overview about the results computed for the classification methods of the (a) MLC and (b) SVMs, respectively, based on the pixel-based and segment-based analyses for the six crop types having similar planting period. For each method, the highest accuracies in the results are examined by confusion matrices in Section 5.3 and Section 5.4 for pixel-based and segment-based analyses, respectively. The classification results computed for the MLC and SVMs method were evaluated based

on the field-based analyses, as well. The confusion matrices of the field-based results are provided in Section 5.5. Other confusion matrices generated for the produced thematic maps can be found in Appendix I.

Table 5.2 MLC results of the thematic maps computed for different image combinations based on pixel-based and segment-based manners

Data	Kompsat-2 MS (4 m)				Kompsat-2 MS (4 m) & Envisat ASAR (15 m)			
	Pixel-based results		Segment-based results		Pixel-based results		Segment-based results	
	Overall Accuracy (%)	Overall Kappa	Overall Accuracy (%)	Overall Kappa	Overall Accuracy (%)	Overall Kappa	Overall Accuracy (%)	Overall Kappa
June	45.67	0.34	51.85	0.41	54.32	0.44	63.66	0.56
July	74.25	0.69	76.36	0.71	75.13	0.70	80.42	0.76
August	71.95	0.66	78.13	0.73	79.18	0.75	82.71	0.79
June-July	75.66	0.70	84.30	0.81	77.07	0.72	87.47	0.84
June-August	72.66	0.67	84.48	0.81	78.83	0.74	88.71	0.86
July-August	76.01	0.71	82.71	0.79	78.66	0.74	85.36	0.82
June-July-August	75.66	0.70	85.18	0.82	79.18	0.75	88.71	0.86

Table 5.3 SVMs results of the thematic maps computed for different image combinations based on pixel-based and segment-based manner

Data	Kompsat-2 MS (4 m)				Kompsat-2 MS (4 m) & Envisat ASAR (15 m)			
	Pixel-based results		Segment-based results		Pixel-based results		Segment-based results	
	Overall Accuracy (%)	Overall Kappa	Overall Accuracy (%)	Overall Kappa	Overall Accuracy (%)	Overall Kappa	Overall Accuracy (%)	Overall Kappa
June	51.67	0.41	59.61	0.51	56.96	0.48	63.84	0.56
July	76.01	0.71	84.12	0.81	79.18	0.75	85.36	0.82
August	65.43	0.58	70.54	0.64	76.01	0.71	78.30	0.73
June-July	80.24	0.76	91.71	0.90	80.77	0.76	92.59	0.91
June-August	70.54	0.64	82.54	0.78	81.48	0.77	88.88	0.86
July- August	79.36	0.75	86.59	0.83	82.36	0.78	86.59	0.83
June-July-August	82.01	0.78	91.35	0.89	84.48	0.81	92.06	0.90

5.3 Results of the Pixel-Based Analysis

In this section, the results of the pixel-based classification of the MLC and SVMs methods are discussed in sections 5.3.1 and 5.3.2, respectively. In the pixel-based analysis the minimum spatial unit is a pixel that defines the minimum discernable object on the satellite image.

5.3.1 Results of the MLC Method

The overall accuracies and overall kappa results of the pixel-based MLC classification method computed for the single-date images and different image combinations are provided in Table 5.4.

Table 5.4 The overall accuracies of the pixel-based classifications for the thematic maps generated

Month	Kompsat-2 MS		Kompsat-2 MS & Envisat ASAR	
	Overall Accuracy (%)	Overall Kappa	Overall Accuracy (%)	Overall Kappa
June	45.67	0.34	52.20	0.42
July	74.25	0.69	75.13	0.70
August	71.95	0.66	79.18	0.75
June-July	75.66	0.70	77.07	0.72
June-August	72.66	0.67	78.83	0.74
July-August	76.01	0.71	78.66	0.74
June-July-August	75.66	0.70	79.18	0.75

Results indicated that an improvement was observed for the thematic maps when the Envisat ASAR data was included in the classification analyses. The highest improvement was observed around 8% for the Kompsat-2 and Envisat ASAR data taken in August. The overall accuracy and kappa values of the August image were computed as 79.18% and 0.75, respectively. The results computed for the combined thematic map of the images taken in June-July-August, and the thematic map produced for the single-date August images provided the best overall accuracies. Comparable results around 78% were obtained for the thematic maps of the dual image combinations. On the other hand, the

lowest overall accuracy (52.20%) and kappa value (0.42) were computed for the Kompsat-2 and Envisat ASAR data taken in June. These unsatisfactory performances can be explained by the acquisition date of the images, because the crops are in the first planting phase in June and the canopy development of the crops has not been completed yet. Thus, bare soil may substantially affect the spectral response of different crop types. The confusion matrix of the combined map of June-July-August can be seen in Table 5.5.

Table 5.5 Confusion matrix of the combined map of June-July-August

Classes	Corn	Grass Land	Rice	Sugar beet	Tomato	Wheat	Row T*	UA*** (%)
Corn	67	6	6	1	19	4	103	65.04
Grass Land	1	77	0	0	1	19	98	78.57
Rice	0	0	84	2	0	0	86	97.67
Sugar beet	1	0	3	63	6	0	73	86.30
Tomato	2	3	2	17	64	1	89	71.91
Wheat	1	23	0	0	0	94	118	79.66
Column T*	72	109	95	83	90	118	567	
PA ** (%)	93.05	70.64	88.42	75.90	71.11	79.66		
Overall A. (%): 79.18 Kappa: 0.75								

*: Total

** : Producer's Accuracy

***: User's Accuracy

According to the confusion matrix in Table 5.5, the highest producer's accuracy of 93.05% was obtained for the corn, which can be explained by significant spectral difference between the corn and other crop types because; only 5 of the 72 corn pixels for validation were misclassified as other cover types. The class rice also provided high producer's accuracy around 88%. Reasonable producer's accuracies over 70% were obtained for the classes grass land, sugar beet, and wheat.

User's accuracies of the crops indicated that the lowest accuracy (65.04%) was computed for the corn with the highest commission error although it provided the maximum producer's accuracy (93.05%). This is due to the fact that only 67 pixels of 113 reference pixels were classified as corn. The major confusion occurred for the class tomato with 19 pixels. On the other hand, the class rice yielded the best user's accuracy of 97.67%. The user's accuracy of the sugar beet was found as 86.30% while the user's accuracies of the grass land, tomato, and wheat exhibited acceptable results over 70%.

- *MLC Results of the Class Pea and Late Corn computed for the Kompsat-2 and Envisat ASAR data*

Owing to the crop rotation occurring in June and July, the class pea and late corn were classified separately by MS Kompsat-2 and Envisat ASAR data. However, marginal producer's and user's accuracies around 50% were observed for the class pea and late corn. Hence, to improve the classification accuracies, a histogram threshold (< 0.90) was applied on the probability maps of the images taken in June and July and mostly incorrectly classified pixels below the threshold was excluded from the images and the masked areas were then classified again. The resulting confusion matrices computed based on the pixel-based MLC are shown in Table 5.6.

Table 5.6 Confusion matrix of the map of June including the class pea

Classes	Corn	Grass Land	Rice	Sugar beet	Tomato	Wheat	Pea	Row T*	UA*** (%)
Corn	9	3	0	1	1	8	1	23	39.13
Grass Land	29	51	1	2	17	28	6	134	38.06
Rice	1	0	88	2	2	1	10	104	84.61
Sugar beet	3	2	2	63	7	3	2	82	76.82
Tomato	3	5	0	3	17	1	5	34	50
Wheat	5	18	4	2	6	76	25	136	55.88
Pea	6	2	1	0	4	6	35	54	64.81
Column T*	56	81	96	73	54	123	84	567	
PA ** (%)	16.07	62.96	91.66	86.30	31.48	61.78	41.66		
		Overall A (%): 59.78			Kappa: 0.52				

The classification of seven classes including the pea revealed a marginal classification performance, where the overall accuracy and overall kappa were calculated as 59.78% and 0.52, respectively (Table 5.6). For the class pea, of 54 pixels for validation, only 35 were correctly classified as pea and the producer's accuracy of that class was computed as 60.71%. The major confusions were observed for the class rice and wheat with 10 and 25 pixels, respectively. The user's accuracy of the pea indicated that only 35 pixels of 54 were classified as pea that was actually represents that category on the ground. The pea pixels were confused mostly with corn and wheat in the user's accuracy level. The results can be explained by the reason that the pea is in harvesting period, so most of the pea fields are old in June. Spectral response of the pea fields may be unhealthy in this period and this situation negatively affects the classification performance of the pea pixels.

Table 5.7 Confusion matrix for the map of July including the late corn

Classes	Corn	Grass Land	Rice	Sugar beet	Tomato	Wheat	Late Corn	Row T*	UA*** (%)
Corn	64	1	0	0	13	0	31	111	57.65
Grass Land	0	54	0	0	0	31	4	89	60.67
Rice	0	0	83	1	4	1	0	89	93.25
Sugar beet	0	0	4	71	1	0	0	76	93.42
Tomato	3	0	1	9	51	0	1	65	78.46
Wheat	0	14	2	0	0	63	9	88	71.59
Late Corn	1	9	0	0	6	3	30	49	61.22
Column T*	68	78	90	81	75	98	77	567	
PA ** (%)	94.11	69.23	92.22	87.65	68	64.28	38.96		
Overall A (%): 73.36				Kappa: 0.68					

Table 5.7 indicates the confusion matrix of the MLC for seven crop types including late corn computed for the Kompsat-2 and Envisat ASAR data. The overall accuracy and kappa values were computed to be 73.36% and 0.68, respectively, which means a moderate classification performance. The class corn provided the highest user's accuracy while its user's accuracy was poor (57.65%). On the other hand, the lowest producer's accuracy of 38.96% was obtained for the late corn. The major confusion was calculated for the class corn due to the similar spectral response characteristics. Of the 77 pixels of the late corn for validation, only 30 were correctly classified as late corn and 31 pixels were wrongly classified as corn in the matrix. Although the lowest producer's accuracy was computed for the late corn, a moderate user's accuracy of about 61.22% was obtained for the same class. The major confusion of the late corn was observed for the grass land. The highest user's accuracy was obtained for the rice and sugar beet above 90% in the matrix.

5.3.2 Results of the SVMs Method

Table 5.8 summarizes the overall accuracies of the pixel-based SVMs classifications for different image combinations. According to the Table 5.8, it was observed that except for the images taken in August, the method of SVMs improved the classification accuracies of the MLC method. This improvement indicates effective classification performance of the SVMs approach. Similar to the results computed for the MLC method, a certain improvement was observed when the Envisat ASAR data was included in the

classification framework. The highest improvement was around 11% for the thematic map of Kompsat-2 and Envisat ASAR data taken in August (overall accuracy: 76.01% and kappa: 0.71) and the combined map of the optical and microwave images acquired in June and August (overall accuracy: 81.48% and kappa: 0.77). While the highest improvement was observed for those images, the combined map of June-July- August provided the best performance with an overall accuracy of 84.48% and kappa value of 0.81 when the Envisat ASAR data was included in the classification. The error matrix of the combined map (June-July-August) is provided in Table 5.9.

Table 5.8 The overall accuracies of the pixel-based classifications for the thematic maps

Month	Kompsat-2 MS (4 m)		Kompsat-2 MS (4m) & Envisat ASAR (15 m)	
	Overall Accuracy (%)	Overall Kappa	Overall Accuracy (%)	Overall Kappa
June	51.67	0.41	56.96	0.48
July	76.01	0.71	79.18	0.75
August	65.43	0.58	76.01	0.71
June-July	80.24	0.76	80.77	0.76
June-August	70.54	0.64	81.48	0.77
July-August	79.36	0.75	82.36	0.78
June-July-August	82.01	0.78	84.48	0.81

The confusion matrix in the Table 5.9 revealed that the maximum producer's and user's accuracy were observed for the class rice around 93% and 95%, respectively. The high accuracies of the rice pixels can be explained by the dielectric properties of the microwave data due to the flooded rice fields and the multi-temporal optical response characteristics. Although the lowest producer's accuracy (71.08%) was computed for the class corn, which was mainly confused with the sugar beet, the corn pixels had fairly good user's accuracy around 86%. The other crop types also provided rather good results for the combined thematic map (June-July-August).

Table 5.9 Confusion matrix of the combined map of June-July-August

Classes	Corn	Grass Land	Rice	Sugar beet	Tomato	Wheat	Row T*	UA*** (%)
Corn	59	3	4	0	0	3	69	85.50
Grass Land	4	78	0	0	1	6	89	87.64
Rice	4	0	106	1	1	0	112	94.64
Sugar beet	11	2	0	81	10	1	105	77.14
Tomato	3	2	3	15	64	1	88	72.72
Wheat	2	9	1	1	0	91	104	87.50
Column T*	83	94	114	98	76	102	567	
PA ** (%)	71.08	82.97	92.98	82.65	84.21	89.21		
	Overall A (%): 84.48			Kappa: 0.81				

5.4 Results of the Segment-Based Analysis

This part examines the classification results of the segment-based analysis, where the minimum spatial unit is a segment. The segment-based results and discussions for the MLC and SVMs method are presented in Section 5.4.1 and Section 5.4.2, respectively.

5.4.1 Results of the MLC Method

Table 5.10 summarizes the overall accuracies of the thematic maps computed for the segment-based approach. It was observed that the segment-based approach improved the classification accuracies of the results computed for the pixel-based MLC. The highest overall accuracy 88.71% and kappa value of 0.86 were achieved for the combined thematic map of June-July-August of the classified Kompsat-2 and Envisat ASAR data, which were higher around 4% than the relevant classification results of the Kompsat-2 data. Similar results were obtained for the combined thematic map of June and July. Except for the June image (overall accuracy: 61.19, kappa: 0.53), other thematic maps provided rather good results over 80%. This improvement can be explained by the segments that define the textural information of the classes by overcoming the problem of within field spectral variability.

The confusion matrix of the combined thematic map of Kompsat-2 and Envisat ASAR data revealed that the highest producer's (94.73%) and user's accuracies (100%) were computed for the class rice (Table 5.11). This is due to the dielectric property of water sensed by microwave data. The rice fields appear dark during the early vegetative phase

when the fields are flooded, which makes the rice fields significantly different from that of the other land cover. The crops corn, grassland, sugar beet, tomato, and wheat yielded producer's accuracies over 85%, which denotes a good identification performance. Nevertheless, the user's accuracies of corn and tomato were around 77%, which demonstrates that the segment-based analysis of the combined images slightly overestimated the classification performance for those crops. The major confusion of the class corn was computed with 9 pixels for the class tomato. Tomato was mainly mixed with the sugar beet with 11 pixels. The confusions are due to the similar spectral response characteristics of those crop types.

Table 5.10 The overall accuracies of the segment-based MLC for the thematic maps generated

Month	Kompsat-2 MS		Kompsat-2 MS & Envisat ASAR	
	Overall Accuracy (%)	Overall Kappa	Overall Accuracy (%)	Overall Kappa
June	51.85	0.41	61.19	0.53
July	76.36	0.71	80.42	0.76
August	78.13	0.73	82.71	0.79
June-July	84.30	0.81	87.47	0.84
June-August	84.48	0.81	86.59	0.83
July- August	82.71	0.79	85.36	0.82
June-July-August	85.18	0.82	88.71	0.86

Table 5.11 Confusion matrix of the combined map of June-July-August

	Corn	Grass Land	Rice	Sugar beet	Tomato	Wheat	Row T	UA
Corn	63	0	2	1	9	6	81	77.77
Grass Land	0	93	0	0	0	2	95	97.89
Rice	0	0	90	0	0	0	90	100
Sugar beet	2	0	0	71	3	0	76	93.42
Tomato	7	0	3	11	78	2	101	77.22
Wheat	0	16	0	0	0	108	124	87.09
Column T	72	109	95	83	90	118	567	
PA	87.50	85.32	94.73	85.54	86.66	91.52		
Overall A (%): 88.71 Kappa: 0.86								

- **MLC Results of the Class Pea and Late Corn**

Table 5.12 provides the confusion matrix of the thematic map of June produced by the segment-based approach for seven crop types including class pea. An improvement around 5% was observed when the segment-based approach was applied on the thematic map, where the overall accuracy and kappa result were found as 64.72% and 0.58, respectively. Even an obvious improvement was observed with the segment-based approach; it was not sufficient to obtain high producer's accuracy of the class pea, which was computed as 45.23%. The lowest producer's accuracy around 23% was computed for the class corn with the highest omission error. Other classes provide reasonable producer's accuracies over 75% except for the class tomato and wheat. When the user's accuracies of the crops were examined, it was observed that the classes of corn, rice, sugar beet and tomato provided significant results over 85%. On the other hand, the lowest user's accuracy of 42.25% was obtained for the grass land. The classes of wheat and pea exhibited marginal results. The user's accuracy of pea was computed as 57.57%, where the major confusions were observed for the class corn and wheat.

Table 5.12 The confusion matrix of the reclassified map including pea

Classes	Corn	Grass Land	Rice	Sugar beet	Tomato	Wheat	Pea	Row T*	UA*** (%)
Corn	13	1	0	0	0	1	0	15	86.66
Grass Land	29	60	0	0	15	36	2	142	42.25
Rice	0	0	92	2	0	2	7	103	89.32
Sugar beet	4	0	0	62	3	0	1	70	88.57
Tomato	0	0	0	1	29	2	1	33	87.87
Wheat	2	17	1	5	5	73	35	138	52.89
Pea	8	2	3	3	2	9	38	66	57.57
Column T*	56	81	96	73	54	123	84	567	
PA ** (%)	23.21	74.07	95.83	84.93	53.70	59.35	45.23		
Overall A (%): 64.72					Kappa: 0.58				

The confusion matrix including the late corn is presented in Table 5.13, where the overall accuracy and kappa value were computed as 78.30% and 0.74, respectively. An improvement around 5% was observed for the overall accuracies of the segment-based approach compared with pixel-based results. The lowest producer's accuracy around 25% was computed for the late corn. The major confusion of the late corn was observed for the class corn. Only 19 pixels in 77 for validation were correctly classified as late corn due to

the spectral similarity and similar phenological characteristics of the crops. On the other hand the other crop types provided significant producer's accuracies over 85% while marginal result (65.30%) was observed for the class wheat. The user's accuracies of the classes indicated that except for the corn, acceptable results were obtained for the other crop types over 70%. The lowest accuracy around 50% was observed for the class corn, which denotes a marginal result. The user's accuracy of the late corn was computed as 73.07% though it provided an inefficient producer's accuracy (24.67%).

Table 5.13 The confusion matrix of the reclassified map including late corn

Classes	Corn	Grass Land	Rice	Sugar beet	Tomato	Wheat	Late Corn	Row T*	UA*** (%)
Corn	67	1	5	2	6	4	47	132	50.78
Grass Land	0	75	0	0	0	24	0	99	75.75
Rice	0	0	78	0	0	1	0	79	98.73
Sugar beet	0	0	3	72	0	0	0	75	96
Tomato	1	0	2	7	69	0	0	79	87.34
Wheat	0	0	2	0	0	64	11	77	83.11
Late Corn	0	2	0	0	0	5	19	26	73.07
Column T*	68	78	90	81	75	98	77	567	
PA ** (%)	98.52	96.15	86.66	88.88	92	65.30	24.67		
Overall A (%): 78.30					Kappa: 0.74				

5.4.2 Results of the SVMs method

The overall accuracies of the SVMs method computed for the segment-based strategy are presented in Table 5.14. According to the table, even the classifications were performed based on the Kompsat-2 data only, the segment-based approach of the SVMs method improved the classification accuracies of the MLC results. For the thematic maps produced using the Kompsat-2 image, the highest overall accuracies around 90% were computed for the dual and triple map combination of June and July, and the combined map of June-July-August, respectively. The computed accuracy was improved around 1% when the Envisat ASAR data was included in the classification analyses. For the thematic maps generated for the Kompsat-2 and Envisat ASAR data, the highest overall accuracy of 92% was obtained for dual image combination of June and July and the combined map of June-July-August. The kappa results of those images were computed around 90%, which means an outstanding classification performance for the crop types. The confusion

matrix of the dual combination of the images taken in June and July are given in Table 5.15.

Table 5.14 The overall accuracies of the segment-based SVMs classifications for the thematic maps

Month	Kompsat-2 MS		Kompsat-2 MS & Envisat ASAR	
	Overall Accuracy (%)	Overall Kappa	Overall Accuracy (%)	Overall Kappa
June	59.61	0.51	63.84	0.56
July	84.12	0.81	85.36	0.82
August	70.54	0.64	78.30	0.73
June-July	91.71	0.90	92.59	0.91
June-August	82.54	0.78	88.88	0.86
July- August	86.59	0.83	86.59	0.83
June-July-August	91.35	0.89	92.06	0.90

According to the confusion matrix of the combined map of June and July (Table 5.15), the producer's accuracies were computed significantly high (over 85%), which means a quite good classification performance. The maximum producer's accuracy of about 99% was achieved for the grass land, in which only 1 pixel of 94 were omitted as tomato. Promising results (97.89%) were achieved for the user's accuracy of the grass land, as well. The best user's accuracy was found for the class wheat around 99%, in which of the 93 pixels 92 were correctly classified as wheat. The lowest, but not actually low, user's accuracy was computed around 83% for tomato, which was mainly confused with sugar beet due to the spectral overlaps.

Table 5.15 Confusion matrix of the combined map of June-July

	Corn	Grass Land	Rice	Sugar beet	Tomato	Wheat	Row T	UA
Corn	75	0	0	1	6	7	89	84.27
Grass Land	0	93	1	0	0	1	95	97.89
Rice	4	0	111	1	1	0	117	94.87
Sugar beet	4	0	1	85	0	1	90	94.44
Tomato	0	1	1	11	69	1	83	83.13
Wheat	0	0	1	0	0	92	93	98.92
Column T	83	94	114	98	76	102	567	
PA	90.36	98.93	97.36	86.73	90.78	90.19		
Overall A (%): 92.59 Kappa: 0.91								

The class pea and late corn were also classified by the segment-based SVMs method without using a histogram threshold. This is because the reclassified thematic maps did not significantly improve the thematic accuracies of the classes when the masked areas were reclassified. The segment-based SVMs classification approach computed for the images taken in June improved the producer's and user's accuracies of the class pea around 10% and 5%, respectively, compared to the results of segment-based MLC method. A dramatic improvement around 50% was computed for the producer's accuracy of the late corn (76.62%) when a segment-based SVMs classification was applied on the June image. The user's accuracy of the late corn was found to be 75.64%, which was higher around 2% than the corresponding MLC result.

5.5 Results of the Field-Based Analysis

This part presents the results of field-based analyses of the Kompsat-2 and Envisat ASAR data computed for the MLC method. First, the analyses were performed on all the fields, thereafter the effects of field sizes were analyzed by dividing the fields into three groups: (i) small (0.1-4.9 ha), (ii) medium (5-9.9 ha), (iii) large fields (10-38 ha).

Table 5.16 presents the confusion matrix of the field-based classification computed for all reference fields. The overall accuracy and kappa values of the matrix were computed as 92.45% and 0.90, respectively, which indicates similar performance with the segment-based approach. In the producer's accuracy level, all the crop types provided high accuracies over 85%. The highest producer's accuracy was computed for the class rice with the minimum omission error. For sugar beet, all the reference pixels were correctly classified and the class had maximum user's accuracy (100%). The smallest user's accuracy of 57.14% was observed for the class tomato although producer's accuracy of tomato was relatively high (88.88%). The major confusion was observed as 5 pixels for sugar beet due to the similar spectral response characteristics.

Table 5.16 Confusion matrix of the field-based analysis

	Corn	Grass Land	Rice	Sugar beet	Tomato	Wheat	Row T	UA
Corn	26	0	1	0	1	6	34	76.47
Grass Land	0	25	0	0	0	2	27	92.59
Rice	0	0	48	0	0	1	49	97.95
Sugar beet	0	0	0	54	0	0	54	100
Tomato	1	0	0	5	8	0	14	57.14
Wheat	0	3	0	0	0	84	87	96.55
Column T	27	28	49	59	9	93	265	
PA	96.29	89.28	97.95	91.52	88.88	90.32		
Overall A (%): 92.45 Kappa: 0.90								

Table 5.17 indicates the results of field-based analysis based on the small fields between 0.1 and 4.9 ha. In total 195 agricultural fields were analyzed for that group. The overall accuracy and kappa values were computed as 90.76% and 0.81, respectively. Except for the grass land (70%), the producer's accuracies of all the other crop types were calculated over 85%. No confusion was observed for the class rice in the producer's accuracy level (100%). Similar result was computed for the class sugar beet in the user's accuracy level. On the other hand, the highest commission error (57.14%) was observed for tomato while it provided fairly acceptable producer's accuracy (88.88%).

Table 5.17 Confusion matrix of the small fields (0.1 ha and 4.9 ha)

	Corn	Grass Land	Rice	Sugar beet	Tomato	Wheat	Row T	UA
Corn	25	0	0	0	1	5	31	80.64
Grass Land	0	7	0	0	0	2	9	77.77
Rice	0	0	34	0	0	1	35	97.14
Sugar beet	0	0	0	48	0	0	48	100
Tomato	1	0	0	5	8	0	14	57.14
Wheat	0	3	0	0	0	55	58	94.82
Column T	26	10	34	53	9	63	195	
PA	96.15	70	100	90.56	88.88	87.30		
Overall A (%): 90.76 Kappa: 0.81								

The field-based analysis computed for the medium fields (5 ha-9.9 ha) include four crop types; grass land, rice, sugar beet, and wheat. The confusion matrix of the crops is given in Table 5.18, where the overall accuracy and kappa value were computed as 96.87% and 0.95, respectively. It was observed from the matrix that all the crops provided significantly high accuracies. The major confusion was computed for the sugar beet in the

user's accuracy level. This is due to the reason that 1 sugar beet field out of 2 was classified as rice, where the number of samples is not adequate for validation.

Table 5.18 Confusion matrix of the medium fields (5 ha and 9.9 ha)

	Grass Land	Rice	Sugar beet	Wheat	Row T	UA
Grass Land	6	0	0	0	6	100
Rice	0	12	0	0	12	100
Sugar beet	0	1	1	0	2	50
Wheat	0	0	0	12	12	100
Column T	6	13	0	0	32	
PA	100	92.30	100	100		
Overall A (%): 96.87 Kappa: 0.95						

Table 5.19 indicates the confusion matrix of the large fields (10-38 ha), which includes grass land, rice, and wheat. The overall accuracy and kappa value for the large fields were computed as 100%, where all the classes were classified in its maximum accuracy level. Based on the results, it is quite evident that the larger the fields, the higher the classification performances reached.

Table 5.19 Confusion matrix of the large fields (10 ha and 38 ha)

	Grass Land	Rice	Wheat	Row T	UA
Grass Land	9	0	0	9	100
Rice	0	1	0	1	100
Wheat	0	0	12	12	100
Column T	9	1	12	22	
PA	100	100	100	100	
Overall A (%): 100 Kappa: 100					

Similar results were obtained for the field-based analyses of the SVMs method. Confusion matrix of the field-based analysis for the SVMs method is provided in Appendix I.

CHAPTER 6

CONCLUSIONS AND RECOMMENDATIONS

In this part the conclusions derived from this study are presented along with the recommendations for further studies.

6.1 Conclusions

Based on the results, the following conclusions are drawn from this study:

- The Least Square Fusion was found to be the most effective method compared to the other image fusion methods that provided high spatial resolution (1 m) MS Kompsat-2 images for the study,
- It was observed that the Lee filter with 5x5 window size was an appropriate method to minimize the speckle effect of the Envisat ASAR data,
- For all the image combinations used, the separability values between the classes and also the classification accuracies were improved when the C-band Envisat ASAR data was included in the classification framework,
 - Based on the Transformed Divergence Index, major confusions were observed between wheat/grass land, corn/tomato, and tomato/sugar beet for the MS Kompsat-2 and Envisat ASAR data acquired in June, July, and August 2008, respectively. Using less than four optical bands caused low separability values. Additional images based on the development periods of the crops might be a good way to increase the separabilities between the classes,

- For the segment-based MLC method, an improvement of 13% was observed for the combined thematic map of June-July-August when the Envisat ASAR data was included into the classification framework.
- In terms of the segment-based SVMs method of the combined thematic map of June-July-August, an improvement around 10% was achieved when the Envisat ASAR data was included into the classification.
- The classification accuracies are strongly affected from the quality of the segments. In this study, for the segmentation task, the goodness measures computed for 324 different parameter combinations of the Mean-Shift were evaluated and the optimum segments were provided for the classification operations,
- The proposed training site selection strategy was found to be effective to prevent possible bias on the classification performance and save time during the collection of training sample,
- Segment-based approach was found to be an effective way compared to the pixel-based method during the classification of images by overcoming the problem of misclassification due to the within field internal spectral variability,
 - For the segment-based MLC method, the highest accuracies were obtained for the combined map of June-July-August classified with MS Kompsat-2 and Envisat ASAR data, which improved the overall accuracy of the pixel-based classification around 10% and computed to be 88.71%.
 - The best results around 92% were obtained for the segment-based SVMs method of the combined thematic maps of the June-July and June-July-August classified with MS Kompsat-2 and Envisat ASAR data, which is better around 10% than the corresponding pixel-based results.

- It was observed that multi-temporal classification approach is essential to provide reliable results in agricultural classification studies. For this study, higher accuracies were obtained for the classification of multi-date data compared to the single-date satellite images,
- Selection of the optimum growing dates of different crop types is a key factor to improve the classification performance. In this study, based on the results, the images taken in June, July, and August were found to be effective to classify the crop types,
 - It was observed that high accuracies were computed around 89% for the segment-based MLC results of the combined thematic maps of June-August, and June-July-August.
 - For the segment-based SVMs method, the highest accuracies were computed around 92% for the combined map of June-July and June-July-August.
- Results indicated that the SVMs method provided better classification accuracies compared to the results obtained from MLC method except for the images taken in August:
 - The segment-based SVMs improved the maximum overall accuracy of the segment-based MLC method around 4% and it was computed as 92.06%.
 - A significant drop around 3% was observed for the map of August classified with the segment-based MLC and SVMs methods. This can be explained by unrepresentative training samples that provide inefficient classification performance for the image taken in August, which can be explained by the low separability index values of the August image.

- Multi-temporal segment-based approach along with the probabilistic approach was found to be effective to combine the information of multi-date data and improved the classification accuracies of the agricultural crop types,
- To set a histogram thresholds on the probability maps to classify pea and late corn improved the classification accuracies of the single-date images of June and July but the improvement was not enough to achieve the high classification accuracies computed for the multi-temporal data sets,
 - For the pixel-based MLC of the optical and microwave data taken in June and July, marginal user's accuracies over 60% were observed for the class pea and late corn while low producer's accuracies were computed around 40%. For the class pea, this can be explained by the acquisition dates of the images because the pea fields are in harvesting period in June and bare soil may affect the spectral response of this crop type. The major confusion of late corn was observed for the class corn because each crop type exists in July on the study area, which causes spectral overlaps between these classes.
- It was observed that the segment-based approach provided similar results based on the field-based analyses, which is a good indicator of reliability for the segments produced,
 - The maximum overall accuracy for the segment- and field-based approaches was computed around 92% for the combined thematic map (June-July-August) of the MLC and SVMs classifications of the MS Kompsat-2 and Envisat ASAR data,
- It was revealed that field sizes of the agricultural parcels directly affects the classification accuracies, hence, it can be stated that the higher the field-size, the higher the classification performance,

6.2 Recommendations

The following items are recommended for further studies:

- To detect more precise agricultural fields, satellite images (e.g. Geoeye and Worldview-2) or aerial photographs that provide higher spatial resolutions might be utilized in the segmentation process.
- Further research should be performed to classify land cover types by microwave images that have spatial resolution higher than 15m (TerraSAR, Radarsat etc.),
- Besides VV polarizations, HH and other cross polarized microwave data should be analyzed in further studies to understand the polarization effect of the microwave data on the classification results. On the other hand, phase information of Envisat ASAR data might be included in the analysis in order to understand the potential of the phase information on the classification performance,
- In order to classify the crop types more reliably, additional images and also ground truth taken on early-, mid-, and late-season of each month might be helpful.
- Evaluation of the segment-based classification results is still a challenging process. This is because the produced segments generally do not represent actual fields on the ground; therefore an appropriate segment-based evaluation method is necessary to further assess the segments.
- The proposed methodology should be tested on rough terrains and the effects of topography on the results should be evaluated,
- In order to see the effect of red and near infrared bands on the segmentation performance, Normalized Difference Vegetation Index (NDVI) may be tested in the study,

- Soil condition (e.g. clay, fertilizer, water content) directly affects the spectral response characteristics of the satellite imagery and also classification accuracies, therefore more detailed ground truth data and further researches are necessary to understand the crop conditions,
- As a future application area, the resulting products (thematic maps, statistics, graphs, etc.) can provide valuable information to various departments; hence this information should be shared with the relevant departments to assess the crop diversity in agricultural communities, to compute water consumption in large regions, etc.

REFERENCES

Alpha Software. http://nature.berkeley.edu/~nclinton/goodness0_1alpha.zip.

Aplin, P., Atkinson, P.M. and Curran, P.J., 1999, Fine spatial resolution simulated satellite sensor imagery for land cover mapping in the United Kingdom. *Remote Sensing of Environment*, Vol.68, pp.206-216.

Baghdadi, N., Holah, N., and Zribi, M., 2006. Soil moisture estimation using multi-incidence and multi-polarization ASAR data. *International Journal of Remote Sensing*, Vol. 27, pp. 1907-1920.

Ban Y., 2003. Synergy of multitemporal ERS-1 SAR and Landsat TM data for classification of agricultural crops. *Can. J. of Remote Sensing*, Vol. 29, pp. 518-526.

Ban Y., Hu, H., and Rangel, I.M., 2010. Fusion of QuickBird MS and RADARSAT SAR data for urban land-cover mapping: object-based and knowledge-based approach. *International Journal of Remote Sensing*, Vol. 31, pp. 1391-1410.

Ban, Y., Hu, H. and Rangel, I. M., 2010. Fusion of QuickBird MS and RADARSAT SAR data for urban land-cover mapping: object-based and knowledge-based approach. *International Journal of Remote Sensing*, Vol. 31, pp. 1391-1410.

Blaes, X., Vanhalle, L., and Defourny, P., 2005. Efficiency of crop identification based on optical and SAR image time series. *Remote Sensing of Environment*, Vol. 96, pp. 352-365.

Chang, C.-C. and Lin C.-J., 2001. LIBSVM: a library for support vector machines.

Chen, D., and Stow, D., 2002. The effect of training strategies on supervised classification at different spatial resolutions. *Photogrammetric Engineering and Remote Sensing*, Vol. 68, pp. 1155-1161.

Cheng Y., 1995. Mean shift, mode seeking, and clustering, *IEEE Transactions on Pattern Analysis and Machine Intelligence*, Vol. 17, pp. 790-799.

Chen Z., Zhao Z., Gong P. and Zeng B., 2006. A new process for the segmentation of high resolution remote sensing imagery. *International Journal of Remote Sensing*, Vol. 27, pp. 4991-5001.

Chen, E., Li, Z., Pang, Y., and Tian X., 2007. Quantitative evaluation of polarimetric classification for agricultural crop mapping”, *Photogrammetric Engineering and Remote Sensing*, Vol. 73, pp. 279-284.

Cheng, H. D., Jiang, X. H., Sun, Y., Wang, J., 2001. Color image segmentation: advances and prospects. *The Journal of the Pattern Recognition*, Vol. 34, pp.2259-2281.

Clinton N., Holt A., Scarborough J., Yan Li., and Gong P., 2010. Accuracy assessment measures for object-based image segmentation goodness. *Photogrammetric Engineering & Remote Sensing*, 76, pp. 289-299.

Comaniciu D., and Meer P., 1997. Robust analysis of feature spaces: Color image segmentation. In: IEEE Conference on Computer Vision and Pattern Recognition, San Juan, June 1997, Puerto Rico, pp. 750-755.

Comaniciu D. and Meer P., 1999. Mean shift analyses and applications. In: Proceeding of 7th International Conference on Computer Vision, Kerkyra, Greece, pp. 1197-1203.

Comaniciu D. and Meer P., 2002. Mean shift: a robust approach toward feature space analysis. *IEEE Transactions on Pattern Analysis and Machine Intelligence*, Vol. 24, pp. 603-619.

Congalton, R. G., Balogh, M., Bell, C., Green, K., Milliken, J. A., and Ottmann, R. 1998. Mapping and monitoring agricultural crops and other land cover in the Lower Colorado River Basin, *Photogrammetric Engineering and Remote Sensing*, pp. 1107-1113.

Corcoran P., Winstanley A. and Mooney P., 2010. Segmentation performance evaluation for object-based remotely sensed image analysis. *International Journal of Remote Sensing*, Vol. 31, pp. 617-645.

Crammer, K. and Singer, Y., 2002. On the learnability and design of output codes for multi-class problems. *Machine Learning*, Vol. 47, pp. 201-233.

Dabrowska-Zielinska, K., Inoue, Y., Gruszczynska, M., Kowalik, W., Stankiewicz, K., 2001. Various Approaches for Soil Moisture Estimates Using Remote Sensing, In: Proceeding of IEEE, pp. 261-263

De Wit A. J. W. and J. G. P. W. Clevers, 2004. Efficiency and accuracy of per-field classification for operational crop mapping. *International Journal of Remote Sensing*, Vol. 25, pp. 4091-4112.

Dronova, I., Gong, P., and Wang, L., 201X. Object-based analysis and change detection of major wetland cover types and their classification uncertainty during the low water period at Poyang Lake, China. *Remote Sensing of Environment*, In Press.

Du, L., Grunes, M.R., and Lee, J.S, 2002 “Unsupervised segmentation of dual-polarization SAR images based on amplitude and texture characteristics”, *International Journal of Remote Sensing*, Vol. 23, pp. 4383-4402.

EDISON software: <http://www.caip.rutgers.edu/riul/research/code.html> (Last Access: 10/05/2009).

ENVI Manual, 2007.

Euroimage, 2009. <http://www.eurimage.it/products/docs/envisat.pdf> (Last Access: 12/09/2011).

FAOSTAT, 2005. FAO (Food and Agriculture Organization of United Nations) Statistics.

Foody, G.M., 1996. Approaches for the production and evaluation of fuzzy land cover classification from remotely-sensed data. *International Journal of Remote Sensing*, Vol. 17, pp. 1317–1340.

Foody, G.M. and Mathur, A., 2004. Towards intelligent training of supervised image classifications: Directing training data acquisition for SVM classification. *Remote Sensing of Environment*, Vol.93, pp.107-117.

Foody, G.M. and Mathur, A., 2006. The use of small training sets containing mixed pixels for accurate hard image classification: Training on mixed spectral responses for classification by a SVM, *Remote Sensing of Environment*, Vol. 103, pp.179-189.

Franklin, S.E. and Wulder, M.A., 2002. Remote sensing methods in medium spatial resolution satellite data land cover classification of large areas, *Progress in Physical Geography*, Vol. 26, pp. 173–205.

Friedman, L., Netanyahu, N. S., and Shoshany, M., 2003. Mean-Shift based clustering of remotely sensed data. Geosciences and Remote Sensing Symposium, IGARSS'03 In: Proceedings, IEEE International, pp.3432-3434.

Frost, V. S., Stiles J. A., Shanmugan K. S. and Holtzman J. C., 1982. A model for radar images and its application to adaptive digital filtering of multiplicative noise. *IEEE Transactions on Geosciences and Remote Sensing*, Vol. 4, pp. 157-166.

Fukunaga, K. and Hostetler, L.D, 1975. The estimation of the gradient of a density functions with applications in pattern recognition, *IEEE Transactions on Information Theory*, Vol. 21, pp. 32-40.

Gallego, F.J., 2004. Remote sensing and land cover area estimation. *International Journal of Remote Sensing*, Vol. 25, pp. 3019–3047.

Gao, Y., Mas, J. F., Kerle, N., and Pacheco, J. A. N., 2011. Optimal region growing segmentation and its effect on classification accuracy. *International Journal of Remote Sensing*, Vol. 32, pp. 3737-3763.

Gong, P. and Howarth P. J., 1990. The use of structural information for improving land-cover classification accuracies at the rural-urban fringe. *Photogrammetric Engineering and Remote Sensing*, Vol. 56, pp. 67-73.

Gong P. and Howarth P. J., 1992. Frequency-based contextual classification and grey-level vector reduction for land-use identification. *Photogrammetric Engineering and Remote Sensing*, Vol. 58, pp. 423-437.

Gong, P., Marceau D., and Howarth P. J., 1992. A comparison of spatial feature extraction algorithms for land-use mapping with SPOT HRV data. *Remote Sensing of Environment*, Vol. 40, pp.137-151.

Haack, B. N., Herold N. D., Nathaniel, and Bechdol M. A., 2000. Radar and optical data integration for land-use/land-cover mapping. *Photogrammetric Engineering and Remote Sensing*, Vol. 66, pp. 709-716.

Henderson, F. M., and Lewis, A. J., 1998. Principles & Applications of Imaging Radar, Manual of Remote Sensing, 3th Edition, pp. 67-68.

Herold, N. D., Haack, B. N., and Solomon, E., 2005. Radar spatial consideration for land cover extraction. *International Journal of Remote Sensing*, Vol. 26, pp. 1383-1401.

HGK, 2007. General Command of Mapping, Turkey, http://www.hgk.msb.gov.tr/urunler/pafta_sorgu/pafta_sorgu.asp

Huang, C., Davis, L.S., and Townshend J.R.G., 2002. An assessment of support vector machines for land cover classification. *International Journal of Remote Sensing*, Vol.23, pp.725-749.

Jensen, J. R., 2005. Introductory Digital Image Processing, 3th Edition, (USA: Pearson, Prentice Hall), pp. 175, 198-202.

Kavzoglu, T. and Colkesen, I., 2010. Destek vector makineleri ile uydu görüntülerinin sınıflandırılmasında kernel fonksiyonlarının etkilerinin incelenmesi (Investigation of the effects of kernel functions in satellite image classification using support vector machines). In: *Harita Dergisi*, Vol. 144, pp. 73-82.

Kaya, G. T., Ersoy, O. K., and Kamasak, M. E., 2011. Support vector selection and adaptation for remote sensing classification. *IEEE Transactions on Geoscience and Remote Sensing*, Vol. 49, pp.2071-2079.

Keuchel, J., Nauman S., Heiler, M., and Siegmund, A., 2003. Automatic land cover analysis for Tenerife by supervised classification using remotely sensed data, *Remote Sensing of Environment*, Vol.86, pp.530-541.

Kontoes, C., Wilkinson, G.G., Burrill, A., Goffredo, S. and Megier, J., 1993. An experimental system for the integration of GIS data in knowledge-based image analysis for remote sensing of agriculture, *International Journal of Geographical Information Systems*, Vol. 7, pp. 247–262.

Krishnaswamy, J., Kiran, M.C., and Ganeshaiyah, K. N., 2004. Tree model based eco-climatic vegetation classification and fuzzy mapping in diverse tropical deciduous ecosystems using multi-season NDVI. *International Journal of Remote Sensing*, Vol. 25, pp. 1185-1205.

Kuan D. T., Sawchuck A. A., Strand T. C., and Chavel P., 1985. Adaptive noise smoothing filter for images with signal-dependent noise, *IEEE Transactions on Pattern Analysis and Machine Intelligence*, Vol. 7, pp. 165 -177.

Lee, J. S., 1980. Digital image enhancement and noise filtering by use of local statistics. *IEEE Transactions on Pattern Analysis and Machine Intelligence*, Vol. 2, pp. 65-168.

Lee, J-S., Grunes, M. R., and Pottier, E., 2001. Quantitative comparison of classification capability: fully polarimetric versus dual and single-polarization SAR. *IEEE Transactions on Geo-Science and Remote Sensing*, Vol. 39, pp. 2343-2351.

Lee, J. Y., and Warner T. A., 2006. Segment based image classification, *International Journal of Remote Sensing*, Vol. 27, pp. 3403-3412.

Li P. and Xiao X. 2007. Multispectral image segmentation by a multichannel watershed-based approach. *International Journal of Remote Sensing*, Vol. 28, pp. 4429-4452.

Li P. and Xiao X. 2007. Multispectral image segmentation by a multichannel watershed-based approach. *International Journal of Remote Sensing*, Vol. 28, pp. 4429-4452.

Lillesand, T. M. and Kiefer, R. W., 2000. Remote Sensing and Image Interpretation. New York: John Wiley and Sons.

Lillesand, M., Kiefer R. W., Chipman J. W., 2004. Remote Sensing and Image Interpretation, 5th Edition, USA: John Wiley and Sons, Inc., .pp.638.

Liu, D., Kelly, M., and Gong, P., 2006. A spatial temporal approach to monitoring forest disease spread using multi-temporal high spatial resolution imagery. *Remote Sensing of Environment*, 101:167-180.

Liu, L., Wang, J., Bao, Y., Huang, W., Ma, Z., and Zhao, C., 2006. Predicting winter wheat condition, grain yield and protein content using multi-temporal Envisat-ASAR and Landsat TM satellite images. *International Journal of Remote Sensing*, Vol. 27, pp. 737-753.

Lloyd, C. D, Berberoglu, S., Curran, P. J., and Atkinson, P. M., 2004. A comparison of texture measures for the per-field classification of Mediterranean land cover. *International Journal of Remote Sensing*, Vol. 25, 3943-3965.

Lu, D. and Weng Q. 2007. A survey of image classification methods and techniques for improving classification performance. *International Journal of Remote Sensing*, Vol. 28, pp. 823-870.

Manual of Mini MAX, 2004. Manual of Mini MAX, CSI Wireless Inc.

Manual of PCI Geomatica, 2009. PCI Geomatics Enterprises.

Manual of Photogrammetry, 2004. 5th Edition.

Martin D., Fowlkes C., Tal D., Malik J., 2004. Learning to detect natural image boundaries using local brightness, color and texture. *IEEE Transaction on Pattern Analysis and Machine Intelligence*, Vol. 26, pp. 530-549.

McNairn, H., Champagne, C., Shang, J. Holmstorm, D., and Reichert, G., 201X. Integration of optical and synthetic aperture radar (SAR) imagery for delivering operational annual crop inventories. *ISPRS Journal of Photogrammetry & Remote Sensing*, InPress.

Mountrakis, G., Im, J., and Ogole, C., 2011. Support vector machines in remote sensing: a review. *ISPRS Journal of Photogrammetry and Remote Sensing*, Vol 66, pp. 247-259.

Mueller M., Segl K. and Kaufmann H. 2003. Extracting characteristic segments in high-resolution panchromatic imagery as basic information for objects-driven image analysis. *Can. J. Remote Sensing*, Vol. 29, pp. 453-457.

Ozdarici A. and Akyurek Z., 2009. Evaluating the contribution of image fusion methods into the classification accuracies of agricultural lands. In: Türkiye Ulusal Fotogrammetri ve Uzaktan Algılama Birliği V. Teknik Sempozyumu (TUFUAB), February 2009, Turkey.

Ozdarici A. And Akyurek Z., 2010a. A comparison of SAR filtering techniques on agricultural area identification. In: Proceedings of ASPRS 2010 Annual Conference, 26-30 April, San Diego, California, USA.

Ozdarici A. And Akyurek Z., 2010b., 2010. Ortalama kaydırma ve Berkeley görüntü segmentasyon yöntemlerinin çok zamanlı Kompsat-2 görüntüleri kullanılarak değerlendirilmesi. In: Uzaktan Algılama ve Coğrafi Bilgi Sistemleri Sempozyumu (UZALCBS).

Ozdarici Ok A. and Akyurek Z., 2011, Evaluation of Image Fusion Methods on Agricultural Lands, *Journal of Earth Science and Engineering*, Vol.1, pp.107-113.

Pal, M. and Mather, P.M., 2003. An assessment of the effectiveness of decision tree methods for land cover classification. *Remote Sensing of Environment*, Vol. 86, pp. 554–565.

Pal, M. and Mather, P.M., 2005. Support vector machines for classification in remote sensing. *International Journal of Remote Sensing*, Vol. 26, pp.1007-1011.

Pal, M., 2006. Support vector machine-based feature selection for land cover classification: A case study with DAIS hyperspectral data. *International Journal of Remote Sensing*, Vol. 27, pp. 2877-2894.

Panigrahy, S. and Sharma, S. A., 1997. *ISPRS Journal of Photogrammetry and Remote Sensing*, Vol. 52, pp. 85-91.

Panigrahy, S., Manjunath, K. R., and Ray, S. S., 2005. Deriving cropping system performance indices using remote sensing data and GIS. *International Journal of Remote Sensing*, Vol. 26, pp. 2595-2606.

Parmuchi, M. G., Karszenbaum, H., and Kandus, P., 2002. Mapping wetlands using multi-temporal RADARSAT-1 data and a decision-based classifier, *Can. J. Remote Sensing*, Vol. 28, pp. 175-186.

Pedley, M. I., and Curran, P. J. 1991. Per-field classification: an example using SPOT HRV imagery. *International Journal of Remote Sensing*, Vol.12, pp.2181 -2192.

Penã-Barragán M. J., Ngugi, M.K., Plant, R. E., Six, J., 2011. Object-based crop identification using multiple vegetation indices, textural features and crop phenology. *Remote Sensing of Environment*, Vol. 115, pp. 1301-1316.

Pohl, C. and Van Genderen, J. L., 1988. Multisensor image fusion in remote sensing: concepts, methods and applications. *International Journal of Remote Sensing*, Vol. 19, pp. 823-854.

Pouncey R., Swanson K., 1999. ERDAS Manual, 5th Edition, USA: ERDAS., p.540,

Richter R., 1990. A fast atmospheric correction algorithm applied to LANDSAT TM images. *International Journal of Remote Sensing*, Vol. 11, pp. 159-166.

Rydberg A. and Borgefors G. 2001. Integrated method for boundary delineation of agricultural fields in multispectral satellite images. *IEEE Transactions on Geoscience and Remote Sensing*, Vol. 39, pp. 2514-2520.

Schoenmakers, R.P.H.M., Van Leeuwen., H.J.C., Lemoine, G.G., and Nezry, E., 1994. Segmentation of combined high resolution optical and radar imagery for the determination of field inhomogenities. In: Proceeding of IEEE, pp. 2137-2139.

Schölkopf, B., Sung, K. K., Burges, C., Girosi, F., Niyogi, P., Poggio, T., and Vapnik V., 1997. Comparing support vector machines with Gaussian kernels to radial basis function classifiers. *IEEE Transactions on Signal Processing*, Vol.45, pp.2758-2765.

Serkan, M, Musaoglu N., Kirkici H., and Ormeci C., 2008. Edge and fine detail preservation in SAR images through speckle reduction with an adaptive mean filter. *International Journal of Remote Sensing*, Vol. 29, p.6727-6738.

Schoenmakers, R.P.H.M., van Leeuwen., H.J.C., Lemoine, G.G., and Nezry, E., 1994. Segmentation of combined high resolution optical and radar imagery for the determination of field inhomogenities, In: Proceeding of IEEE, pp. 2137-2139.

Skriver, H., Mattia, F., Satalino, G., Balenzano, A., Pauwels, V.R.N., Verhoest, N.E.C, and Davidson, M., 2011. Crop classification using short-revisit multitemporal SAR data. *IEEE Journal of Selected Topics in Applied Earth Remote Sensing*, Vol.4, pp.423-431.

Slazar, L., Kogan, F., and Roytman, L., 2008. Using vegetation health indices and partial least squares method for estimation of corn yield. *International Journal of Remote Sensing*, Vol. 29, pp. 175-189.

Smith.G.M. and Fuller R. M. 2001. An integrated approach to land cover classification: an example in the Island of Jersey. *International Journal of Remote Sensing*, Vol.22, 3123-3142.

Spot Image, 2008, <http://www.spot.com/web/SICORP/2378-kompsat-2-images.php> (Last Access: 15/12/2011).

Stankiewicz, K.A., 2006. The efficiency of crop recognition on ENVISAT ASAR images in two growing season, *IEEE Transactions on Geosciences and Remote Sensing*, Vol. 44, pp. 806-814.

Tso, B. and Mather, P. M., 1999. Crop discrimination using multi-temporal SAR imagery. *International Journal of Remote Sensing*, Vol.20, 2443-2460.

Tso, B. and Mather, P. M., 2001. *Classification Methods for Remotely Sensed Data*, Taylor & Francis Group, LLC. USA.

Tso, B. and Mather, P. M., 2009. *Classification Methods for Remotely Sensed Data*, 2nd Edition, Taylor & Francis Group, LLC. USA, pp.11-12.

Turker, M. and Arıkan, M., 2005. Sequential masking classification of multi-temporal Landsat7 ETM+ images for field-based crop mapping in Karacabey, Turkey. *International Journal of Remote Sensing*, Vol.26 pp. 3813-3830.

Turker, M. and Ozdarici A., 2011. Field-based crop classification using SPOT4, SPOT5, IKONOS, and QuickBird imagery for agricultural areas: A comparison study. *International Journal of Remote Sensing*, Vol.32 pp. 9735-9768.

Vapnik, V., 1979 Estimation of dependences based on empirical data (in Russian). Moscow (English translation: Springer-Verlag, New York).

Vapnik, V., 1995, The Nature of Statistical Learning Theory. New York: Springer-Verlag.

Vapnik, V., 1998, Statistical Learning Theory. New York: Springer-John Wiley.

Wang, L., Sousa, W.P., and Gong, P. 2004. Integration of object-based and pixel-based classification for mapping mangroves with IKONOS imagery. *International Journal of Remote Sensing*, Vol. 25, pp.5655-5668.

Wang L., P. Gong, Q. Ying, Z. Yang, X. Cheng and Q. Ran, 2010. Settlement extraction in the north china plain using Landsat and Beijing-1 multispectral data with an improved watershed segmentation algorithm. *International Journal of Remote Sensing*, 31, pp.1411-1426.

Waring, R. H., Way, J. B., Hunt, E. R., Morrissey, L., Ranson, K. J., Weishampel, J. F., Oren, R., and Franklin, S. E., 1995. Imaging radar for ecosystem studies *BioScience* 45 (10):715–723.

Watanachaturaporn, P., Arona, M. K., and Varshney, P. K., 2008. Multisource classification using support vector machines: An empirical comparison with decision tree and neural network classifiers. *Photogrammetric Engineering and Remote Sensing*, Vol. 74, pp. 239-346.

Wilkinson, G. G., 2005. Results and implications of a study of fifteen years of satellite image classification experiments, *IEEE Transactions on Geosciences and Remote Sensing*, Vol. 43, pp. 433-440.

Wu, T.-F., Lin, C.-J. and Weng R. C., 2004. Probability estimates for multi-class classification by pairwise coupling. *Journal of Machine Learning Research*, 5:975-1005. <http://www.csie.ntu.edu.tw/~cjlin/papers/svmprob/svmprob.pdf>.

Xiao P., Feng X., An R. and Zhao S. 2010. Segmentation of multispectral high-resolution satellite imagery using log Gabor filters. *International Journal of Remote Sensing*, Vol. 31, pp. 1427-1439.

Xu, W., Wu, B., Huang, J., and Zhang, Y., 2004. Synergy of multi-temporal Radarsat SAR and Landsat ETM data for extracting agricultural crops structure. In: Proceeding of IEEE, pp. 4073-4076.

Yang, X., 2011. Parameterizing support vector machines for land cover classification. *Photogrammetric Engineering & Remote Sensing*, Vol. 77, pp.27-37.

Yu, Q., Gong P., Clinton N., Biging G., SchirokaueR D., 2006. Object-based detailed vegetation mapping using high spatial resolution imagery. *Photogrammetric Engineering and Remote Sensing*, Vol. 72, pp.799-811.

Zhan Q., Molenaar M., Tempfli K. and Shi W. 2005. Quality assessment for geo-spatial objects derived from remotely sensed data. *International Journal of Remote Sensing*, Vol. 26, pp. 2953-2974.

Zhang, Y., Wang, C., Wu, J., and Qi, J., 2009. Mapping paddy rice with multitemporal ALOS/PALSAR imagery in southern China. *International Journal of Remote Sensing*, Vol. 30, pp.6301-6315.

APPENDIX A

PHOTOGRAPHS OF THE CROP TYPES CULTIVATED IN THE STUDY AREA



Figure A.1 A wheat field in the test site (April 2008)



Figure A.2 A wheat field in the test site (April 2008)



Figure A.3 A wheat field in the test site (April 2008)



Figure A.4 A wheat field in the test site (June 2008)



Figure A.5 A wheat field in the test site (June 2008)



Figure A.6 A sugar beet field in the test site (June 2008)



Figure A.7 A tomato field in the test site (June 2008)



Figure A.8 A tomato field in the test site (June 2008)



Figure A.9 A tomato field in the test site (June 2008)



Figure A.10 An irrigated rice field in the test site (June 2008)



Figure A.11 An irrigated rice field in the test site (June 2008)



Figure A.12 A rice field in the test site (June 2008)



Figure A.13 A corn field in the test site (June 2008)



Figure A.14 A corn field in the test site (June 2008)



Figure A.15 A corn field in the test site (June 2008)

APPENDIX B

GÖRÜNTÜ ZENGİNLEŞTİRME YÖNTEMLERİNİN TARIMSAL ÜRÜN SINIFLANDIRMASI ÜZERİNDEKİ ETKİLERİNİN DEĞERLENDİRİLMESİ

Proceeding: Published in “Türkiye Ulusal Fotogrametri ve Uzaktan Algılama Birliği V. Teknik Sempozyumu (TUFUAB 2009)”, Ankara, Turkey

A. Ozdarici^a, Z. Akyurek^b

^a ODTÜ Jeodezi ve Coğrafi Bilgi Teknolojileri EABD, Orta Doğu Teknik Üniversitesi
Ankara, Türkiye - ozdarici@metu.edu.tr

^b ODTÜ İnşaat Mühendisliği Bölümü, Orta Doğu Teknik Üniversitesi, Ankara, Türkiye -
zakyurek@metu.edu.tr

ANAHTAR KELİMELEER: Görüntü Zenginleştirme, Görüntü Sınıflandırması, Tarım,
Doğruluk Değerlendirme, QuickBird

ÖZET

Görüntü zenginleştirme, farklı mekânsal, spektral ve zamansal görüntü özellikleri biraraya getirilerek bu görüntülerden yüksek mekânsal ve spektral özelliklere sahip yeni bir görüntü elde etme yöntemidir. Yöntemin ana amacı, görüntü analizlerine (görüntü sınıflandırması, bölütleme, değişim belirleme vb.) detaylı girdi sağlamaktır.

Çalışmada literatürde sıkça karşılaşılan dokuz farklı görüntü zenginleştirme yöntemi test edilmiş ve bu yöntemlerin tarımsal ürün sınıflandırması üzerindeki etkileri incelenmiştir. Çalışma alanı olarak Bursa'da yer alan Karacabey Ovası seçilmiştir. Karacabey Ovası, alanda yetiştirilen ürün çeşitliliği bakımından Türkiye'nin en verimli ovaları arasında yer almaktadır. Tarımsal alanlarda yetiştirilen ürünlerin güvenilir bir şekilde haritalanabilmesi için son yıllarda yüksek mekânsal çözünürlük sağlayan uydular önem kazanmıştır. Bu çalışmada 13 Ağustos 2004 tarihli QuickBird siyah-beyaz (0.61m) ve renkli (2.44 m) görüntüleri kullanılmıştır. Hesaplamalarda kolaylık sağlamak amacıyla analizler görüntünün yaklaşık 5 km² lik bölümü üzerinde uygulanmıştır. Görüntüler üzerinde ilk olarak, Gram-Schmidt, En Küçük Kareler, Yüksek Frekans Filtreleme yöntemi, Ana Bileşenler Spektral görüntü zenginleştirme yöntemi, Renk-Doygunluk-Parlaklık dönüşümü (RDP), İyileştirilmiş Yoğunluk-Renk-Doygunluk (YoRD) dönüşümü, Brovey, Dalgaboyu tabanlı Ana Bileşenler Yöntemi ve Dalgaboyu tabanlı YoRD görüntü zenginleştirme yöntemleri uygulanmıştır. Zenginleştirilmiş görüntüler üzerinde yer alan beş ürün sınıfı (Mısır, Buğday, Anız, Domates ve Şeker Pancarı) En Büyük Olasılık Sınıflandırma yöntemi yardımıyla sınıflandırılmıştır. Görüntü zenginleştirme yöntemleri sonucunda üretilen zenginleştirilmiş görüntülerin spektral kalitesinin gerçek renkli görüntü ile karşılaştırılabilmesi için görüntüler, gerçek renkli görüntü çözünürlüğü olan 2.44 m ye dönüştürülerek sınıflandırılmıştır. Sınıflandırma süresince tüm görüntüler için aynı örnek alanlar kullanılmıştır. Sınıflandırma sonuçları gerçek renkli görüntüye ait sınıflandırma sonucu ile karşılaştırılmış ve referans harita yardımıyla değerlendirilmiştir. Kullanılan referans harita, ürün bilgilerinin alana gidilerek toplanması yoluyla üretilmiştir. Referans harita üretimi, görüntü çekim tarihiyle eş zamanlı olarak gerçekleştirilmiştir. Referans harita yardımıyla sınıflandırılmış görüntüler için hata matrisleri oluşturulmuş ve genel hata, Kappa değeri ve ürün sınıflarına ait doğruluk oranları bu matrisler yardımıyla hesaplanmıştır. Değerlendirmeler sonucunda gerçek renkli görüntüye ait en yüksek genel hata oranı %84,2 olarak hesaplanmıştır. Gram-Schmidt görüntü zenginleştirme yöntemi gerçek renkli görüntüden elde edilen sınıflandırma doğruluğunu yaklaşık %4 arttırarak %88 olarak hesaplanmıştır. Bu oranı yaklaşık %86 ile En Küçük Kareler yöntemi, Ana Bileşenler Spektral görüntü zenginleştirme yöntemi, Yüksek Frekans Filtreleme Yöntemi ve İyileştirilmiş YoRD dönüşümü yöntemleri izlemiştir. Brovey ve

Dalgaboyu tabanlı YoRD dönüşümlerine ait doğruluk oranları yaklaşık %85 olarak hesaplanmış ve bu iki yonteme ait sonuçlar da kabul edilebilir bulunmuştur. Diğer taraftan Dalgaboyu tabanlı Ana Bileşenler yöntemi ve RDP yöntemlerine ait doğruluk oranlarının gerçek renkli görüntü için hesaplanan orandan düşük olduğu gözlenmiştir. Bu iki yonteme ait genel doğruluk oranları yaklaşık %81 olarak hesaplanmıştır. Elde edilen sonuçlar, Gram-Schmidt, En Küçük Kareler, Ana Bileşenler Spektral, Yüksek Frekans Filtreleme Yöntemi, İyileştirilmiş YoRD dönüşümü, Brovey dönüşümü ve Dalgaboyu tabanlı YoRD görüntü zenginleştirme yöntemlerinin tarım alanlarındaki ürün çeşitliliğinin sınıflandırılmasında sınıflandırma doğruluğunu arttırmak için kullanılabileceğini göstermiştir.

**EVALUATING THE CONTRIBUTION OF IMAGE FUSION METHODS
INTO THE CLASSIFICATION ACCURACIES OF AGRICULTURAL CROPS**

A. Ozdarici^a, Z. Akyurek^b

^a METU Geodetic and Geographic Information Technologies Department, Middle East
Technical University

Ankara, Turkey - ozdarici@metu.edu.tr

^b METU Civil Engineering Department, Middle East Technical University, Ankara, Turkey -
zakyurek@metu.edu.tr

KEY WORDS: Image Fusion, Image Classification, Agriculture, Accuracy, QuickBird

ABSTRACT:

Image fusion is a process to generate a new image by integrating different spatial, spectral and/or temporal resolution images. The main goal of image fusion is to provide detail input to the later image analyses (image classification, segmentation, change detection, etc.).

This study focuses on evaluating the influence of nine different image fusion methods, mostly encountered in the literature, on the accuracies of the agricultural crop classification. The study site selected is on the Karacabey Plain, one of the most productive and valuable agricultural regions, located in Bursa in Turkey. A new trend for the agricultural crop classification is to utilize high resolution satellite products in order to extract the crop types more reliably. Therefore, a QuickBird panchromatic (0.61m) and multispectral (2.44m)

images acquired on 13 August 2004 were used in this study. A small part of QuickBird (~5 km²) image was used in order to improve computational efficiency in the analyses. Nine different fusion methods, namely Gram-Schmidt, Least Square Fusion (LSF), High Pass Filter Resolution Merge (HPF), Principle Component (PC) Spectral Sharpening, Hue-Saturation-Value (HSV), Modified Intensity-Hue-Saturation (IHS) Resolution Merge, Brovey, Wavelet-based PCA (Principle Component Analysis), and Wavelet-based IHS were used to combine the panchromatic and multispectral data. The fused images were classified into number of five classes (Corn, Wheat, Residue, Tomato and Sugar beet) as a supervised manner using Maximum Likelihood Classification method. Before the classification, the fused images were resized to 2.44m, the size of the original multispectral image, in order to understand the radiometric quality of the fused products. During the classification the same training areas were used for each image. The classification results were then compared with the classification of the original multispectral image. The accuracies of the classified thematic maps were tested using a reference map. The reference map was produced by collecting information about crop types from the study area. Producing reference map and image acquisition were performed simultaneously. Based on the reference map, the overall accuracy, overall kappa and individual class accuracies were computed using error matrices. The overall accuracy of the original multispectral image, was computed as 84,2%. The classified images fused by the Gram-Schmidt method provided the highest overall accuracy of about 88%. The Gram-Schmidt method was followed by the methods of LSF, PC Spectral Sharpening, HPF, and Modified IHS Resolution Merge and their accuracies were computed around 86%. The accuracies of Brovey and Wavelet IHS Resolution Merge also revealed acceptable result, which was around 85%. On the other hand, the results obtained from the Wavelet PCA and HSV methods were found lower than the accuracy of the classified original image. The accuracies of these methods were computed as around 81%. The results revealed that the methods of the Gram-Schmidt, LSF, PC Spectral Sharpening, HPF, and Modified IHS Resolution Merge, Brovey, and Wavelet IHS Resolution Merge can be used to fuse the images before the classification of the agricultural crops to increase the classification accuracy.

1. GİRİŞ

Uzaktan Algılama, arařtırmacılara mekânsal, spektral ve zamansal çözünlükte çeşitli ürünler sağlayarak elektromanyetik spektrumun büyük bir bölümüne ait bilgi çıkarımına katkıda bulunmaktadır. Uzaktan algılama teknolojisinin sağladığı bu geniş çaplı veri, bir takım problemleri de beraberinde getirmektedir. Bu problemlerden başlıcaları; verilerin birbirleri ile uyumu, yüksek kalitede bilgi elde etmek ve gereksiz bilgilerin ayıklanması olarak sayılabilir. En önemli problemlerden bir tanesi, renkli görüntüye ait spektral bilgi ile siyah-beyaz görüntüye ait mekânsal bilginin nasıl etkili bir şekilde kullanılacağına yöneliktir. Bu problemlerin çözümünde kullanılan en etkili yöntem ‘görüntü zenginleştirme’ olarak adlandırılmaktadır. Görüntü zenginleştirme, farklı mekânsal, spektral ve zamansal çözünlükteki görüntülerin birleştirilmesi ve bu sayede yüksek spektral ve mekânsal özelliklerde yeni bir görüntü elde edilmesi işlemi olarak tanımlanabilir. Daha genel bir ifade ile görüntü zenginleştirme, farklı kaynaklardan elde edilen uydu verilerinin birleşimi, korelasyonu ve kombinasyonu olarak ifade edilebilir. Bu yaklaşım sadece görsel yönden kaliteli görüntüler üretmekle kalmaz daha sonra görüntü üzerine uygulanacak analizlere de detaylı girdi sağlar. Pohl ve van Genderen tarafından 1998 yılında görüntü zenginleştirme yöntemlerinin değerlendirilmesine yönelik geniş çaplı bir çalışma yapılmıştır. Çalışmada, görüntü zenginleştirme yöntemleri; piksel tabanlı, nesne tabanlı ve karar ağacı düzeyinde olmak üzere 3 gruba ayrılmaktadır. Piksel düzeyinde gerçekleştirilen yöntemler veriyi oluşturan en küçük nesnelere (piksel) üzerinde uygulanmaktadır. Nesne düzeyinde uygulanan yöntemler, görüntüyü oluşturan nesnelere zenginleştirilmesine yönelik olarak yapılmaktadır. Karar ağacı düzeyinde gerçekleştirilen zenginleştirme yöntemlerinde görüntüler üzerinde zenginleştirme işlemini gerçekleştirecek uygun kuralların (kararların) belirlenmesi gerekmektedir (Pohl ve van Genderen, 1998). Bu çalışmada piksel düzeyinde uygulanan görüntü zenginleştirme yöntemlerine yer verilecektir. Görüntü zenginleştirme yöntemleri ile ilgili problemler ve kısıtlamalar bugüne kadar bir çok arařtırmacı tarafından incelenmiştir (Chavez vd., 1991, Pellemans vd., 1993, Zhang, 2002). Bu arařtırmacılardan Zhang (2002), görüntü zenginleştirme yöntemlerine ait sorunları Landsat 7 ve IKONOS görüntüleri üzerinde inceleyerek bu problemlere neden olan aksaklıkların belirlenmesi için çeşitli tespitlerde bulunmuştur. Colditz vd. (2006) Landsat 7 görüntüsü üzerinde 5 farklı görüntü zenginleştirme yöntemi uygulamış ve sonuçları 3 farklı sınıflandırma yöntemi yardımıyla

sınıflandırılarak değerlendirilmiştir. Elde edilen bulgular, Brovey ve RDP dönüşümlerinin görüntülerin zenginleştirilmesi ve daha sonra bu görüntülere uygulanacak sınıflandırma işlemi için uygun yöntemler olmadığını göstermiştir. Benzer bir çalışma Karathanassi vd. tarafından gerçekleştirilmiştir (Karathanassi vd., 2007). Çalışmada görüntü zenginleştirme yöntemlerini incelemek amacıyla çeşitli değerlendirme yöntemleri kullanılmıştır. Değerlendirmeler sonucunda en yüksek sonuçların Lokal Ortalama ve Dağılım Uyuşması, En Küçük Kareler ve Gram-Schmidt görüntü zenginleştirme yöntemlerinin sağladığı gözlemlenmiştir. Yukarıda sözü edilen çalışmalara benzer bir diğer çalışma Konstantinos (2008) tarafından gerçekleştirilmiştir. Çalışmada zenginleştirme yöntemi uygulanmış görüntüler görsel ve istatistiksel olarak değerlendirildikten sonra kontrolsüz bir sınıflandırma yöntemi kullanılarak yöntemlerin sınıflandırma doğruluğu üzerindeki etkileri incelenmiştir.

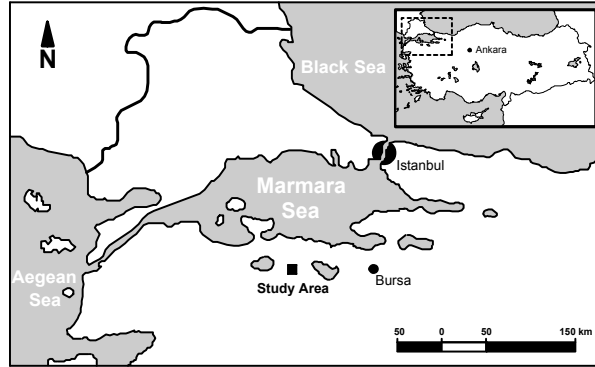
Bu çalışmada dokuz (9) farklı görüntü zenginleştirme yöntemi sonucu üretilmiş görüntüler kontrollü bir sınıflandırma yöntemi yardımıyla sınıflandırılarak görüntü zenginleştirme yöntemlerinin ürün sınıflandırması üzerindeki etkileri incelenmiştir. Analizler 13 Ağustos 2004 tarihli QuickBird renkli (2.44m) ve siyah-beyaz (0.60m) görüntüleri üzerinde uygulanmıştır. İlk olarak Gram-Schmidt, En Küçük Kareler, Yüksek Frekans Filtreleme yöntemi, Ana Bileşenler Spektral görüntü zenginleştirme yöntemi, Renk-Doygunluk-Parlaklık dönüşümü (RDP), İyileştirilmiş Yoğunluk-Renk-Doygunluk (YoRD) dönüşümü, Brovey, Dalgaboyu tabanlı Ana Bileşenler Yöntemi ve Dalgaboyu tabanlı YoRD görüntü zenginleştirme yöntemleri kullanılarak QuickBird görüntüleri zenginleştirilmiştir. Yukarıda sayılan yöntemler yoluyla üretilen görüntüler beş (5) farklı istatistiksel değerlendirme yöntemi yardımıyla değerlendirilerek üretilen yüksek çözünürlükteki görüntülerin gerçek renkli görüntüye ait spektral değerlere yakınlığı ölçülmüştür. Bu amaç için kullanılan değerlendirme yöntemleri; *Görelî Ortalama ve Varyans farkları*, *Korelasyon*, *En Yüksek Sinyal Hata Oranı* ve *Genel Kalite İndeksidir*. Zenginleştirilmiş görüntülerin istatistiksel ve görsel olarak değerlendirilmelerinin ardından görüntüler üzerinde yer alan beş (5) farklı ürün sınıfı (mısır, domates/biber, buğday, anız ve şeker pancarı) *En Büyük Olasılık* sınıflandırma yöntemi yardımıyla sınıflandırılmıştır. Sınıflandırmalarda kullanılan örnek alanlar gerçek renkli görüntü üzerinden toplanmış ve aynı alanlar zenginleştirilmiş ve gerçek renkli görüntülerin sınıflandırılmasında kullanılmıştır. Sınıflandırma sonrasında tematik haritalar

üzerinde Sieve filtresi uygulanmış ve belli bir eşik değerinin altında kalan poligonları oluşturan pikseller birbirine komşu olan en yakın poligonların içine düşen piksel değerine atanmıştır. Elde edilen sonuçlar hata matrisleri yardımıyla değerlendirilmiş ve genel hata oranları, kappa değerleri ve ürünlere ait doğruluklar hesaplanarak sonuçlar gerçek renkli görüntüden elde edilen sınıflandırma sonucu ile karşılaştırılmıştır.

2. ÇALIŞMA ALANI VE VERİ SETİ

2.1 Çalışma Alanı

Analizleri gerçekleştirmek için seçilen çalışma alanı, Türkiye'nin kuzeybatısında bulunan Marmara bölgesindeki Bursa ilinde yer almaktadır (Şekil 1). Karacabey Ovası olarak bilinen alan, ikliminin üretime elverişli olması ve zengin ürün çeşitliliği bakımından Türkiye'nin en verimli ve en değerli ovaları arasında yer almaktadır. Alanda yetiştirilen başlıca ürünler; mısır, domates, biber, soğan, pirinç, şeker pancarı, buğday ve bezelye olarak sayılabilir (Özdarıcı, 2005).



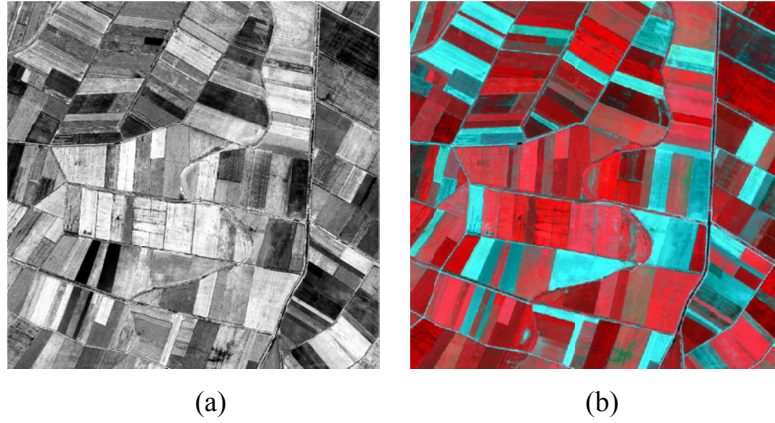
Şekil 1. Çalışma alanı

2.2 Veri Seti

Çalışmada uydu görüntüsü ve referans veri olmak üzere iki farklı veri tipi kullanılmıştır. Görüntü zenginleştirme yöntemleri, 0.61 m siyah-beyaz ve 2.44 m renkli QuickBird uydu görüntüleri üzerinde uygulanmıştır (Şekil 2). Kullanılan QuickBird görüntüleri ürün

dağılımının ve gelişiminin en üst düzeyde olduğu Ağustos 2004 tarihinde elde edilmiştir. Görüntüler, standart ürün formatındadır. Standart ürün formatına sahip olan görüntülerde sensör ile ilgili düzeltmeler yapılmış, radyometrik ve geometrik hatalar düzeltilmiş ve görüntüler kartografik projeksiyon sistemine uygun hale getirilmiştir. Hesaplamalarda kolaylık sağlamak için 8 bitlik QuickBird görüntüsünün yaklaşık 5 km² lik bir bölümü kullanılmıştır. Renkli QuickBird görüntüsü mavi, yeşil, kırmızı ve yakın kızıl ötesi olmak üzere dört banttandır. Çalışmada kullanılan Brovey, RDP, İyileştirilmiş YoRD dönüşümü, Dalgaboyu tabanlı YoRD dönüşümü yöntemleri üç bant ile sınırlıdır. Bu nedenle karşılaştırma işlemi için çalışmada yeşil, kırmızı ve yakın kızıl ötesi bantları kullanılmıştır. Kullanılan yeşil, kırmızı ve yakın kızıl ötesi bantlar alandaki ürün çeşitliliğini açıklamada mavi banttandır daha etkilidir (Özdarıcı, 2005).

Analizlerde kullanılan bir diğer veri alanda yetiştirilen ürünlere ait parsel bilgilerini içeren vektör veridir. Vektör veri 2002 yılında Arıkan tarafından yapılan bir çalışma sonucunda kadastr bilgileri kullanılarak üretilmiş ve 2005 yılında Özdarıcı tarafından yapılan bir çalışma ile güncellenerek bu çalışmaya girdi sağlamıştır (Arıkan, 2003; Özdarıcı, 2005). Sözü edilen çalışmalar yoluyla elde edilen vektör veri çalışmanın görüntü sınıflandırması ve doğruluk analizi aşamasında kullanılmıştır.



Şekil 2. (a) 13 Ağustos 2004 tarihine ait siyah-beyaz (a) ve renkli (b) QuickBird görüntüleri

3. YÖNTEM

Bu bölümde çalışmada kullanılan yöntemler açıklanmıştır. İlk bölümde görüntü zenginleştirme yöntemleri incelenecektir. İkinci bölümde, zenginleştirilmiş görüntüler üzerinde uygulanan görüntü sınıflandırma yöntemi anlatılacaktır. Son olarak sınıflandırma işlemi sonunda üretilen tematik haritalara ait sonuçlar ortaya koyulacaktır.

3.1 Görüntü Zenginleştirme Yöntemleri

Başarılı bir görüntü zenginleştirme, görüntülerin birbirine göre geometrik olarak hassas bir şekilde yönelimlerini gerektirir. Analizlerde kullanılan QuickBird görüntüleri birbirlerine göre düzeltilmiş olarak elde edilmiştir. Görüntüler aynı tarihte ve zamanda çekildikleri için iki veri arasında zaman farkı yoktur. Çalışmada literatürde sıkça karşılaşılan Renk-Doygunluk-Parlaklık dönüşümü (RDP), Brovey, İyileştirilmiş Yoğunluk-Renk-Doygunluk (YoRD) dönüşümü, Ana Bileşenler Spektral görüntü zenginleştirme yöntemi, Gram-Schmidt, En Küçük Kareler, Yüksek Frekans Filtreleme yöntemi, Dalgaboyu tabanlı Ana Bileşenler Yöntemi ve Dalgaboyu tabanlı YoRD görüntü zenginleştirme yöntemleri değerlendirilmiştir. Yöntemlere ait açıklamalar aşağıda yer almaktadır.

3.1.1 Renk-Doygunluk-Parlaklık (RDP) Dönüşümü

RDP dönüşümü Yoğunluk-Renk-Doygunluk (YoRD) dönüşümü ile benzer özellikler göstermektedir. Yöntem, Kırmızı-Mavi-Yeşil (KMY) uzayının RDP uzayına dönüştürülmesi ile başlar. Bu dönüşüm, görüntü zenginleştirme sürecinde renkler üzerinde yüksek kontrol olanağı sağlar. Dönüşümü, parlaklık (P) ve yüksek mekânsal çözünürlüğe sahip bantların yer değiştirmesi izler. Bu işlem, renk R ve Doygunluk (D) bantlarına ait piksellerin yüksek mekânsal çözünürlüğe dönüştürülmesi (resampling) ile devam eder. Son aşamada, RDP uzayı RGB uzayına tekrar dönüştürülerek görüntü zenginleştirme işlemi tamamlanır (ENVI kılavuzu). RDP dönüşümü 3 banta sahip görüntüler üzerinde uygulanabilmektedir.

3.1.2 Brovey Dönüşümü

Brovey dönüşümünde yüksek ve düşük mekânsal çözünürlüklü veri özellikleri 139'ar araya getirilerek bu görüntülerden yeni bir görüntü elde etmek için basit bir oran kullanılır. Bu oran, düşük mekânsal çözünürlüğe sahip bantların yüksek mekânsal çözünürlüğe sahip bant ile çarpılması ve sonucun düşük mekânsal çözünürlüklü bantların toplamına bölünmesi şeklinde olmaktadır (Eşitlik 1). Bu işlem düşük mekânsal çözünürlüklü bantların uygun bir yeniden örnekleme yöntemi (örn. En yakın komşuluk, bilinear, cubic convolution) yardımıyla yüksek mekânsal çözünürlüğe dönüştürülmesi ile son bulmaktadır (ENVI kılavuzu). Brovey dönüşümü 3 bant ile sınırlıdır.

$$DN_{fused}_i = \frac{DN_i \times DN_{pan}}{\sum_{i=1}^N DN_i} \quad (1)$$

Eşitlikte;

DN_i renkli görüntüye ait bantların piksel değerleri i ($i=1,2,3$), DN_{pan} yüksek mekansal çözünürlüklü veriye ait piksel değeri;

N renkli görüntüdeki bant sayısı ($Bant1+Bant2+Bant3$).

3.1.3 İyileştirilmiş YoRD Dönüşümü

YoRD dönüşümü, zenginleştirme işlemi uygulanacak görüntüleri RGB uzayından YoRD uzayına dönüştürerek bantlar arasındaki mekânsal korelasyonu algılamada kolaylık sağlar. YoRD uzayını oluşturan yoğunluk değeri; parlaklığı, renk değeri baskın olan rengi, doygunluk ise gri değere göre olan saflığı ifade eder (Lillesand, 2005). Renkli görüntünün YoRD uzayına dönüştürülmesini dönüşüm sonucunda elde edilen yoğunluk değeri ile yüksek mekânsal çözünürlüklü görüntünün yer değiştirmesi takip eder. Ardından renk ve doygunluk, siyah-beyaz görüntünün sahip olduğu mekânsal çözünürlüğe dönüştürülür. Bu işlemi YoRD

uzayından KYM uzayına geçmeyi sağlayan ters dönüşüm işlemi takip eder ve zenginleştirme işlemi tamamlanır (Siddiqui, 2003).

YoRD dönüşümü, yüksek mekânsal çözünürlüğe sahip görüntüye ait detayların korunmasında etkili bir yöntem olmasına rağmen bu yöntem ile üretilecek zenginleştirilmiş görüntüler sadece siyah-beyaz görüntü ile yoğunluk değerinin benzerlik gösterdiği durumlarda geçerlidir. Fakat renkli görüntüye ait yoğunluk değeri her zaman yüksek mekânsal çözünürlüklü görüntüler ile benzer özellikler göstermeyebilir. Bu nedenle daha güvenilir sonuçlar elde etmek için alternatif olarak iyileştirilmiş YoRD dönüşümü geliştirilmiştir.

İyileştirilmiş YoRD dönüşümünde amaç görüntünün KYM uzayına dönüştürülmesinden önce yüksek mekânsal çözünürlüklü görüntüye ait istenmeyen piksellerin filtrelenmesidir. Yöntem, basit bir oran hesabına dayanır. Amaç, yüksek mekânsal çözünürlüklü görüntünün renkli görüntüye ait yoğunluk değerine benzetilmesidir (Eşitlik 2) (ERDAS Kılavuzu). İyileştirilmiş YoRD dönüşümü 3 banta sahip görüntüler üzerinde uygulanabilmektedir.

$$r_i = \frac{\alpha_r d_r + \alpha_g d_g + \alpha_b d_b}{\sum_j \beta_j d_j} \quad (2)$$

eşitlikte

r_i = yoğunluk iyileştirme oranı

α_r = kırmızı banttaki piksel değerine ait katsayı payı

d_r = kırmızı banta ait piksel değeri

α_g = yeşil banttaki piksel değerine ait katsayı payı

d_g = yeşil banta ait piksel değeri

α_b = mavi banttaki piksel değerine ait katsayı payı

d_b = mavi banta ait piksel değeri

β_j = j bantındaki piksel değerine ait katsayı payı

$d_j = j$ bantına ait piksel değeri

j bantı, yüksek mekansal çözünürlüğe sahip verinin kapsadığı spektral aralığı temsil eden düşük mekansal çözünürlüklü bantları ifade eder.

3.1.4 Ana Bileşenler Görüntü Zenginleştirme Yöntemi

Renkli görüntülere ait bantlar birbirlerine göre genellikle benzer bilgiler içerir. Ana Bileşenler görüntü zenginleştirme yönteminin amacı, bu bantlardan birbirinden bağımsız doğrusal kombinasyonlar üretmek ve bu sayede bantlar arasında tekrarlanan bilgiyi en aza indirmektir. Bu dönüşüm sonucunda birbirine dik akslar üretilir. İşlem, görüntünün gerçek uzayına (RGB uzayı) dönüştürülmesi ile son erer.

Ana Bileşenler görüntü zenginleştirme yöntemi, düşük ve yüksek mekansal çözünürlüklü görüntülerin zenginleştirilmesi için kullanılan etkili bir yöntemdir. İlk olarak, görüntüye Ana Bileşenler dönüşümü uygulanır. Bir sonraki işlem, bu dönüşüm sonucunda üretilen ilk bantın (Ana Bileşen 1) yüksek mekansal çözünürlüklü veri ile yer değiştirmesidir. Bu aşamada, üretilen ilk ana bileşenin yüksek mekansal çözünürlüklü veri özelliklerine yakın olduğu varsayımından yola çıkılır. Bu işlemi, spektral bilgi üzerinde olabilecek hataları önlemek amacıyla siyah-beyaz görüntünün ilk ana bileşen bandına göre ölçeklenmesi takip eder. Ardından ters dönüşüm uygulanarak görüntü gerçekte bulunduğu uzaya (KYM) dönüştürülür. Son aşama, renkli görüntüye ait bantların yüksek mekansal çözünürlüğe dönüştürülmesi işlemidir (ENVI Kılavuzu). Ana Bileşenler görüntü zenginleştirme yöntemi 3 ve 3'ten fazla banta sahip görüntüler için uygulanabilmektedir.

3.1.5 En Küçük Kareler Görüntü Zenginleştirme Yöntemi

En Küçük Kareler görüntü zenginleştirme yöntemi iki temel problemi çözmeyi hedeflemiştir. Bu problemlerden biri renk bozulmaları, diğeri kullanıcı ve veri bağımlılığıdır. Diğer görüntü zenginleştirme yöntemlerinde olduğu gibi En Küçük Kareler görüntü zenginleştirme yöntemi de gerçek renkli görüntü ve zenginleştirilmiş görüntü arasında en iyi etkileşimi kurmayı hedefler. Bu amaç doğrultusunda görüntü zenginleştirme işlemini standart ve otomatik hale getirmek için bir takım istatistiksel yöntemlere başvurur. En Küçük Kareler görüntü

zenginleştirme yönteminin uygulanmasında kullanılan istatistiksel yöntemlere ilişkin literatürde net bir bilgi bulunmamaktadır (PCI Geomatica Kılavuzu). Gram-Schmidt görüntü zenginleştirme yöntemi 3 ve daha fazla banta sahip görüntüler üzerinde uygulanabilmektedir.

3.1.6 Gram-Schmidt Görüntü Zenginleştirme Yöntemi

Gram-Schmidt görüntü zenginleştirme yöntemi ismini matematik biliminde sıkça karşılaşılan Gram-Schmidt teoreminden almıştır. Gram-Schmidt, doğrusal cebirde kullanılan önemli bir yöntemdir ve bir uzayı oluşturan vektörlerin birbirine göre dik hale getirilmesi için kullanılır. Bu işlem, veri üzerinde daha fazla kontrol imkanı sağlar.

Yöntemde ilk olarak, yüksek mekansal çözünürlüğe sahip veriyi düşük mekansal çözünürlüğe dönüştürmek için siyah-beyaz görüntünün simülasyonu yapılır. Ardından simülasyon işlemi uygulanmış siyah-beyaz veriye ve renkli görüntüye ait spektral bantlara Gram-Schmidt dönüşümü uygulanır. Bu dönüşümde simülasyon işlemi uygulanmış yüksek çözünürlüklü bant, sıralamada ilk sırada yer alır. Gerçek yüksek mekansal çözünürlüklü banta ait istatistikler Gram-Schmidt dönüşümü uygulanmış ilk banta adapte edilir ve gerçek yüksek mekansal çözünürlüklü bant Gram-Schmidt dönüşümü sonucu elde edilen ilk bantın yerini alır. Yüksek mekansal çözünürlüğe sahip yeni bantlar üretmek için ters dönüşüm işlemi uygulanarak zenginleştirme işlemi tamamlanır (Laben ve ark. 2000; ENVI Kılavuzu).

3.1.7 Yüksek Frekans Filtreleme Yöntemi

Yüksek Frekans Filtreleme yöntemi yüksek ve düşük mekansal çözünürlüklü görüntüleri filtreleme tekniği yardımıyla zenginleştirmektedir. Yöntem, görüntüleri oluşturan piksellerin okunması ve R değerinin hesaplanması ile başlar. R değeri, renkli görüntüdeki piksel boyutunun siyah-beyaz görüntüdeki piksel boyutuna oranıdır. Bu oran QuickBird görüntüsü için 4 olarak hesaplanmıştır. R değeri hesaplandıktan sonra filtre boyutu belirlenerek yüksek mekansal çözünürlüğe sahip görüntü filtrelenir. Çalışmada kullanılan QuickBird görüntüsü için görüntü özellikleri ve R değeri dikkate alınarak 9×9 boyutunda bir filtre kullanılmıştır. Renkli görüntüye ait piksel boyutunun filtrelenmiş görüntünün piksel boyutuna

dönüştürülmesi için renkli görüntü üzerinde yeniden örnekleme işlemi uygulanır. Ardından filtrelenmiş görüntü renkli görüntüye ait bantlara eklenir. İşlem, üretilen görüntünün gerçek renkli görüntüye ait istatistiksel değerlere benzetilmesi ile sona erer (ERDAS Kılavuzu). Yöntem, 3 ve daha fazla banta sahip görüntüler üzerinde uygulanabilmektedir.

3.1.8 Dalgaboyu Tabanlı Görüntü Zenginleştirme Yöntemi

Dalgaboyu tabanlı görüntü zenginleştirme yöntemi, Fourier dönüşümü ile benzer özellikler göstermektedir. Fourier dönüşümünde uzun dalga boyları (sinüs ve kosinüs) kullanılırken dalgaboyu tabanlı dönüşümlerde birbirinden farklı kısa dalgaboyları kullanılmaktadır. Bu nedenle yöntem, daha lokal işlemler üzerinde uygulanabilmektedir. Yöntemin en önemli noktalarından bir tanesi, temel dalga boylarının belirlenmesi aşamasıdır. Dönüşüme girdi olacak sinyale (görüntü) birbirinin ardı sıra filtreleme işlemi uygulanır ve önemli parçalar belirlenerek görüntü temsil edilir. Bu işlem sayesinde farklı çözünürlükte birden fazla görüntü elde edilmektedir. Üretilen görüntülerdeki farklılıklar görüntüye ait detayları temsil eder. Çoklu mekansal çözünürlüğe sahip görüntüler KYM uzayına dönüştürülerek gerçek renkli görüntü elde edilebilir (Ranchin vd., 2003; ERDAS Manual). Aşağıda dalgaboyu tabanlı iki farklı görüntü zenginleştirme yöntemi açıklanmaktadır.

3.1.8.1 Dalgaboyu tabanlı YoRD Dönüşümü

Dalgaboyu tabanlı YoRD dönüşümü, görüntünün KYM uzayından YoRD uzayına dönüştürülmesi ve yoğunluk değerinin elde edilmesi ile başlar. Bu aşamayı, yüksek mekânsal çözünürlüğe sahip görüntüye dalgaboyu dönüşümünün uygulanması takip eder. Dalgaboyu dönüşümü uygulanmış görüntü daha sonra yoğunluk bantı ile yer değiştirir. Son olarak ters dönüşüm işlemi uygulanarak görüntü KYM uzayına getirilir. Dalgaboyu tabanlı YoRD dönüşümü üç bant ile sınırlıdır.

3.1.8.2 Dalgaboyu tabanlı Ana Bileşenler Görüntü Zenginleştirme Yöntemi

Dalgaboyu tabanlı ana bileşenler görüntü zenginleştirme yönteminde görüntüye ilk olarak Ana Bileşenler dönüşümü uygulanır. Ana Bileşenler görüntü zenginleştirme yöntemi sonucunda üretilen ilk bileşen yüksek mekânsal çözünürlüğe sahip görüntü ile yer değiştirir ve KYM uzayına geri dönüşüm gerçekleştirilir. Ana Bileşenler yöntemi üç ve daha fazla banta sahip görüntüler üzerinde uygulanabilmektedir.

Yukarıda açıklanan görüntü zenginleştirme yöntemleri yoluyla üretilen görüntüler *Görelî ortalama ve Varyans farkları, Korelasyon, En Yüksek Sinyal Hata Oranı ve Genel Kalite İndeksi* yardımıyla incelenmiştir. Değerlendirme yöntemleri zenginleştirilmiş görüntü çözünürlüğü olan 2.44m ye düşürülerek gerçekleştirilmiştir (Özdarıcı ve Akyürek, 2008).

3.2 Görüntü Sınıflandırması

Görüntü zenginleştirme yöntemlerinin ana amacı, görüntü üzerinde uygulanacak analizlere detaylı girdi sağlamak ve bu sayede güvenilir bilgi elde etmektir.

Bu aşamada, görüntü zenginleştirme yöntemi sonucunda elde edilen yüksek mekânsal çözünürlüğe sahip renkli görüntüler gerçek renkli görüntü çözünürlüğü olan 2.44 m ye dönüştürülerek En Büyük Olasılık sınıflandırma yöntemi yardımıyla sınıflandırılmıştır. Görüntü zenginleştirme işlemi sonucunda elde edilen çözünürlük olan 0.60 m nin gerçek renkli görüntü çözünürlüğüne dönüştürülmesinin nedeni üretilen görüntülerin spektral olarak gerçek renkli görüntü ile karşılaştırılabilmesi ve bu sayede zenginleştirilmiş görüntüler üzerindeki spektral hataların bulunabilmesidir. Görüntülerin sınıflandırılmasında kullanılan yöntem, *En Büyük Olasılık* sınıflandırma yöntemi, görüntü üzerindeki bilinmeyen pikselleri bilgisayara tanıtılan örnek alanlara bağlı kalarak varyans ve kovaryans değerlerine göre gruplandırmaktadır (Lillesand et.al, 2004). *En Büyük Olasılık* sınıflandırma yöntemi yardımıyla mısır, buğday, anız, domates ve şeker pancarı olmak üzere beş ürün türü sınıflandırılmıştır. Sınıflandırma öncesinde uygun bir eşik değeri (2 piksel) atanarak parsel kenarlarına düşen pikseller gerçek renkli ve zenginleştirilmiş görüntülerden çıkarılmıştır. Parsel kenarlarına düşen piksellerin görüntülerden çıkarılmasının ardından sınıflandırma

işlemi için gerçek renkli görüntü üzerinde örnek alanlar belirlenmiştir. Örnek alan seçimi homojen parseller üzerinden yapılmıştır. Bu alanların seçiminde görüntü üzerindeki spektral farklılıklar ve fenolojik olaylar dikkate alınmıştır. Toplanan alanlar, ayrılabilirlik indeksleri yardımıyla değerlendirilmiştir. Bu incelemeler sonucunda domates ve biberin ayrılma oranlarının düşük olduğu gözlenmiş ve bu iki ürün, domates sınıfı altında birleştirilmiştir. Sınıflandırma işlemi tamamlandıktan sonra bu görüntüler üzerinde Sieve filtresi uygulanmış ve bu sayede tematik haritalama sonucu ortaya çıkan istenmeyen büyüklükteki piksellerden oluşan poligonlar elimine edilmiştir. Filtre büyüklüğü bu çalışma için 20 piksel olarak belirlenmiştir. Filtreleme işleminin ardından tematik haritalar üzerinde doğruluk analizi yapılarak sonuçlar değerlendirilmiştir.

3.3 Doğruluk Analizi

Üretilen tematik haritaların gerçeğe yakın olup olmadığı hata matrisleri yardımıyla değerlendirilmiştir. Hata matrisi oluşturmak için alanın görüntü çekim tarihi ile eş zamanlı olarak elde edilen parsel bilgisini içeren referans veriden yararlanılmıştır. Sonuçlar üzerinde olabilecek önyargıyı önlemek için sınıflandırma işlemi için toplanan örnek alanlar doğruluk analizine dahil edilmemiştir. Sınıflandırılmış görüntülerin doğruluklarını test etmek için alan üzerinde rastgele örnekleme yöntemi kullanılarak (*simple random sampling*) 557 nokta belirlenmiştir. Bu noktalar referans verideki gerçek bilgiler ile karşılaştırılarak hata matrisleri oluşturulmuştur. Doğruluk analizleri için belirlenen nokta sayısı, aşağıda verilen eşitliğe dayanmaktadır (Eşitlik 3) (Jensen, 2005).

$$N = \frac{B \prod_i (1 - \Pi_i)}{b_i^2} \quad (3)$$

Eşitlikte yer alan;

N : örnek boyutu

Π_i : alanda bulunan k sınıf içinde toplam alanın %50'sini kapsamaya en yakın olan i sınıfının tüm alana oranını

b_i : i sınıfı için hedeflenen hassasiyet düzeyini (örn. %5),

B : 1 serbestlik derecesinde ve $(\alpha / k) \times 100$ formülüyle hesaplanan Ki kare (χ^2) tablosundaki değeri,

k : alanda bulunan toplam sınıf sayısını göstermektedir.

Ratgele örnekleme işlemi doğruluk analizi için on defa tekrarlanmış ve tüm görüntüler için aynı örnek noktalar kullanılmıştır. Bu sayede doğruluk analizi üzerinde olabilecek ön yargı en aza indirilmeye çalışılmıştır. Doğruluk analizleri sonucunda tematik haritalara ait genel hata ve kappa oranları ve ürünlere ait doğruluklar elde edilmiştir.

4. TARTIŞMA

Üretilen tematik haritalar için hata matrisleri oluşturulmuş, en küçük ve en büyük genel hata ve kappa oranları ile sınıflara ait doğruluk oranları hesaplanmıştır. Hata matrisleri sonucu ulaşılan genel hata ve Kappa sonuçlarına ait ortalama değerler tablo 2 de verilmektedir. Tablo 2 de verilen değerler Kappa sonuçlarına göre büyükten küçüğe doğru sıralanmıştır.

Sınıflandırma sonuçları Gram-Schmidt, İyileştirilmiş YoRD dönüşümü, Dalgaboyu tabanlı YoRD dönüşümü, En Küçük Kareler yöntemi, Ana Bileşenler Spektral görüntü zenginleştirme yöntemi, Yüksek Frekans Filtreleme yöntemi, Brovey dönüşümü ve Dalgaboyu tabanlı Ana Bileşen dönüşümünün gerçek renkli görüntüye ait sınıflandırma doğruluğunu arttırdığını göstermiştir. Buna karşılık RDP yönteminin gerçek renkli görüntüye ait sınıflandırma sonucunu yaklaşık %3 oranında düşürdüğü gözlenmiştir. Sınıflandırma sonuçlarına ait en yüksek oran, %83,4 genel doğruluk ve %79,2 Kappa değerleri ile Gram-Schmidt görüntü zenginleştirme yöntemi tarafından sağlanmıştır. Gram-Schmidt görüntü zenginleştirme yöntemi, gerçek renkli görüntüye ait sınıflandırma doğruluğunu yaklaşık %3 oranında arttırmıştır. Gram-Schmidt yöntemine en yakın sonucu %83,4 genel doğruluk ve %79,14 Kappa oranları ile İyileştirilmiş YoRD dönüşümü sağlamıştır. Bu yöntemleri, gerçek renkli görüntü sonucuna yaklaşık %2 lik artış sağlayan Dalgaboyu tabanlı YoRD dönüşümü, En Küçük Kareler yöntemi, Ana Bileşenler Spektral görüntü zenginleştirme yöntemi, Yüksek Frekans Filtreleme yöntemi ve Brovey dönüşümleri izlemiştir. Dalgaboyu tabanlı Ana Bileşenler görüntü zenginleştirme yöntemi %79,69 genel doğruluk ve % 77,49 Kappa sonucuyla gerçek renkli görüntü sonucunu yaklaşık %1 oranında arttırmıştır.

Table 2. Görüntü sınıflandırması sonuçları

<i>Image Classification Methods</i>	<i>Avg. Overall Accuracy (%)</i>	<i>Avg. Overall Kappa (%)</i>
<i>Gram Schmidt</i>	83,4	79,2
<i>İyileştirilmiş YoRD dönüşümü</i>	83,4	79,14
<i>Dalgaboyu tabanlı YoRD dönüşümü</i>	82,99	78,63
<i>En Küçük Kareler</i>	82,95	78,55
<i>Ana Bileşenler Spektral</i>	82,84	78,36
<i>Yüksek Frekans Filtreleme y.</i>	82,41	77,9
<i>Brovey</i>	82,77	78,3
<i>Dalgaboyu tabanlı PCA</i>	79,69	77,49
<i>Renkli QuickBird görüntüsü</i>	81,03	76,2
<i>RDP dönüşümü</i>	78,97	73,35

Ürünlere ait en yüksek hata oranları şekil 3 de verilmektedir. Şekil 3a da yer alan siyah kutucuklar, görüntüler üzerinden toplanan örnek alanları göstermektedir. Gerçek renkli görüntüye ait sonuçlar, en düşük üretici doğruluğunun %78,26 ile mısır bitkisi tarafından sağlandığını göstermektedir. Diğer taraftan en düşük kullanıcı doğruluğu yaklaşık %75 ile domates ve şeker pancarı bitkileri için hesaplanmıştır.



(a)

Genel Doğruluk Oranı	84.2%	
Genel Kappa Oranı	80.2%	
	Üretici	Kullanıcı
	Doğruluğu	Doğruluğu
	(%)	(%)
<i>Anız</i>	81.65	92.70
<i>Buğday</i>	92	86.79
<i>Mısır</i>	78.26	91.52
<i>Domates</i>	89.28	75.18
<i>Ş.Pancarı</i>	81.63	76.92

Gram-Schmidt görüntü zenginleştirme yöntemi bütün ürünler için %80 in üzerinde üretici doğruluğu ortaya koymuştur. En düşük kullanıcı doğruluğu bu yöntem ile sınıflandırılmış görüntü için %76,57 doğruluk ile şeker pancarı tarafından sağlanmıştır.



(b)

Genel Doğruluk Oranı	87.61%	
Genel Kappa Oranı	84.5%	
	Üretici	Kullanıcı
	Doğruluğu	Doğruluğu
	(%)	(%)
<i>Anız</i>	82.59	95.74
<i>Buğday</i>	94	89.52
<i>Mısır</i>	85.50	91.47
<i>Domates</i>	90.17	85.59
<i>Ş.Pancarı</i>	86.73	76.57

En Küçük Kareler yöntemi de Gram-Schmidt yöntemine yakın sonuçlar göstermiştir. En düşük üretici ve kullanıcı doğrulukları bu yöntem için %79,16 ile şeker pancarı bitkisi için hesaplanmıştır



(c)

Genel Doğruluk Oranı		86.35%
Genel Kappa Oranı		82.8%
	Üretici Doğruluğu (%)	Kullanıcı Doğruluğu (%)
<i>Anız</i>	84.69	95.40
<i>Buğday</i>	87.37	87.37
<i>Mısır</i>	85.29	89.23
<i>Domates</i>	93.54	82.27
<i>Ş.Pancarı</i>	79.16	79.16

Ana Bileşenler görüntü zenginleştirme yöntemine ait üretici ve kullanıcı doğrulukları incelendiğinde bu yöntemine ait en düşük üretici doğruluğunun %67,70 ile şeker pancarı bitkisi tarafından sağlandığı görülmektedir. Yönteme ait en düşük kullanıcı doğruluğu %75,32 ile domates bitkisi için hesaplanmıştır.



(d)

Genel Doğruluk Oranı		86.35%
Genel Kappa Oranı		82.8%
	Üretici Doğruluğu (%)	Kullanıcı Doğruluğu (%)
<i>Anız</i>	84.69	93.25
<i>Buğday</i>	91.26	86.23
<i>Mısır</i>	90.44	91.79
<i>Domates</i>	93.54	75.32
<i>Ş.Pancarı</i>	67.70	91.54

Yüksek Frekans Filtreleme yöntemi yardımıyla üretilen görüntüler için bulunan sonuçlar, mısır ve şeker pancarı bitkisine ait üretici doğruluklarının yaklaşık %79 ile en düşük seviyede olduğunu göstermiştir. Bu ürünler için bulunan kullanıcı doğrulukları yaklaşık %90 olarak hesaplanmıştır. En düşük kullanıcı doğruluğu %74,51 ile domates bitkisi tarafından sağlanmıştır.



(e)

Genel Doğruluk Oranı	86.17%	
Genel Kappa Oranı	82.6%	
	Üretici	Kullanıcı
	Doğruluğu	Doğruluğu
	(%)	(%)
<i>Anız</i>	91.83	92.78
<i>Buğday</i>	89.32	86.79
<i>Mısır</i>	79.41	90.75
<i>Domates</i>	91.93	74.51
<i>Ş.Pancarı</i>	79.16	92.68

İyileştirilmiş YoRD dönüşümü kullanılarak elde edilen sonuçlar en düşük üretici ve kullanıcı doğruluklarının şeker pancarı bitkisi için yaklaşık %75 olarak hesaplanmıştır.



(f)

Genel Doğruluk Oranı	85.99%	
Genel Kappa Oranı	82.4%	
	Üretici	Kullanıcı
	Doğruluğu	Doğruluğu
	(%)	(%)
<i>Anız</i>	90.81	90.81
<i>Buğday</i>	86.40	91.75
<i>Mısır</i>	88.23	93.75
<i>Domates</i>	87.09	80.59
<i>Ş.Pancarı</i>	76.04	73

Brovey dönüşümü sonucu elde edilen görüntü üzerinde uygulanan doğruluk analizi sonuçları, en düşük üretici doğruluğunun %65,93 doğruluk payı ile anız için, en düşük kullanıcı doğruluğunun ise %79,03 ile buğday bitkisi için hesaplandığını göstermiştir. Brovey dönüşümü sonucunda elde edilmiş bulgular, bu yöntem ile elde edilmiş görüntünün diğer yöntemlerden farklı sınıflandırma sonuçları olduğunu ortaya koymuştur.



(g)

Genel Doğruluk Oranı	85.4%	
Genel Kappa Oranı	81.7%	
	Üretici	Kullanıcı
	Doğruluğu	Doğruluğu
	(%)	(%)
<i>Anız</i>	65.93	96.77
<i>Buğday</i>	87.50	79.03
<i>Mısır</i>	86.89	86.89
<i>Domates</i>	92.79	83.06
<i>Ş.Pancarı</i>	90.81	87.25

Dalgaboyu tabanlı görüntü zenginleştirme yöntemi de üretici doğrulukları açısından Brovey dönüşümü ile benzer özellikler göstermiştir. Bu yöntem sonucu üretilen en düşük üretici doğruluğu %65,93 ile anız bitkisi için hesaplanmıştır. Diğer taraftan en düşük kullanıcı doğruluğu %72,32 ile şeker pancarı bitkisi tarafından sağlanmıştır.



(h)

Genel Doğruluk Oranı	85.1%	
Genel Kappa Oranı	81.3%	
	Üretici	Kullanıcı
	Doğruluğu	Doğruluğu
	(%)	(%)
<i>Anız</i>	79.09	93.54
<i>Buğday</i>	89.65	82.97
<i>Mısır</i>	83.80	90.84
<i>Domates</i>	88.61	85.82
<i>Ş.Pancarı</i>	85.26	72.32

Genel doğruluk oranları incelendiğinde Dalgaboyu tabanlı Ana Bileşenler görüntü zenginleştirme yönteminin gerçek renkli görüntüye ait sınıflandırma sonucunu yaklaşık %1 (genel hata) oranında düşürdüğü gözlenmiştir. Bu yöntem sonucunda üretilen tematik haritanın genel Kappa oranı gerçek renkli görüntü sonucunu aynı oranda arttırmıştır. En küçük üretici ve kullanıcı doğrulukları bu yöntem için sırasıyla 70,33% ve 77,93% olarak anız ve mısır ürünleri için hesaplanmıştır. En düşük kullanıcı doğruluğu gerçek renkli

görüntü ile benzerlik gösterecek şekilde %75 olarak domates ve şeker pancarı bitkilerinden elde edilmiştir.



(i)

Genel Doğruluk Oranı		82.22%
Genel Kappa Oranı		77.6%
	Üretici	Kullanıcı
	Doğruluğu	Doğruluğu
	(%)	(%)
<i>Anız</i>	70.33	98.46
<i>Buğday</i>	89.28	81.96
<i>Mısır</i>	77.93	86.26
<i>Domates</i>	88.28	74.24
<i>Ş.Pancarı</i>	84.69	77.57

En düşük sınıflandırma sonuçları RDP dönüşümü uygulanmış görüntüden elde edilmiştir. RDP dönüşümü uygulanan görüntüye ait en düşük üretici doğrulukları sırasıyla %72,47 ve %63 ile anız ve buğday bitkileri için hesaplanmıştır. En düşük kullanıcı doğruluğu yaklaşık %75 doğruluk payı ile buğday ve mısır bitkilerinden sağlanmıştır.



(j)

Genel Doğruluk Oranı		81.6%
Genel Kappa Oranı		76.9%
	Üretici	Kullanıcı
	Doğruluğu	Doğruluğu
	(%)	(%)
<i>Anız</i>	72.47	90.80
<i>Buğday</i>	63	75.90
<i>Mısır</i>	90.58	73.09
<i>Domates</i>	91.96	83.06
<i>Ş.Pancarı</i>	86.73	92.39

Figure 6 (a) Renkli QuickBird görüntüsü (b) Gram-Schmidt, (c) En Küçük Kareler, (d) Ana Bileşenler Spektral, (e) Yüksek Frekans Filtreleme, (f) İyileştirilmiş YoRD, (g) Brovey, (h) Dalgaboyu tabanlı YoRD, (i) Dalgaboyu tabanlı Ana Bileşenler, (j) RDP dönüşümü

Sonuçlar, Brovey ve RDP dönüşümleri dışında kalan görüntü zenginleştirme yöntemlerinin alanda yetiştirilen ürünleri güvenilir bir şekilde ayırabildiğini göstermiştir. En düşük ayrılabilirlik domates ve şeker pancarı ürünleri arasında gözlenmiştir. Diğer taraftan, gerçek renkli görüntü ile Brovey ve RDP dönüşümleri sonucu üretilen görüntüler arasında spektral açıdan farklılıklar olması bu yöntemler sonucunda üretilen görüntüler üzerine düşen örnek alanların diğer görüntülerden farklı olmasına ve ürünlerin farklı sınıflara atanmasına yol açmıştır.

QuickBird görüntülerine uygulanan zenginleştirme yöntemlerinden, Brovey, RDP, Dalgaboyu tabanlı YoRD ve İyileştirilmiş YoRD dönüşümleri 3 bant ile sınırlıdır. Bu özellik, görüntü zenginleştirme yöntemlerine katkı sağlayacak bilgi miktarını kısıtlamakta ve zenginleştirme sonrasında uygulanacak analizlerin performansını olumsuz yönde etkilemektedir. Bunun nedeni geniş spektral aralığa sahip olan görüntülerin dar aralığa sahip olanlardan daha fazla bilgi sunma kapasitesine sahip olmasıdır.

Ana Bileşenler Spektral ve Dalgaboyu tabanlı Ana Bileşenler görüntü zenginleştirme yöntemleri görüntülere Ana Bileşen dönüşümünün uygulanması ile gerçekleştirilebilmektedir. Fakat görüntüye Ana Bileşen dönüşümünün uygulanması bir takım problemleri de beraberinde getirmektedir. Ana Bileşen dönüşümünün doğrusallık mantığı ile çalışması ve Gaussian dağılımını esas alması bu dağılıma uymayan çoklu moda sahip veriler üzerinde güvenilir sonuçlar ortaya koymada olumsuz yönde etkili olabilmektedir. Bu nedenle yöntemin uygulanacağı görüntü özelliklerinin dikkate alınması gerekmektedir.

5. SONUÇLAR

Çalışmada 9 farklı görüntü zenginleştirme yöntemi incelenmiş ve bu yöntemlerin görüntü sınıflandırması üzerindeki etkileri değerlendirilmiştir. Kullanılan görüntü zenginleştirme yöntemleri; Gram-Schmidt, En Küçük Kareler, RDP, Brovey, İyileştirilmiş YoRD, Ana Bileşenler Spektral, Yüksek Frekans Filtreleme Yöntemi, Dalgaboyu tabanlı YoRD dönüşümü ve Dalgaboyu tabanlı Ana Bileşenler görüntü zenginleştirme yöntemleridir. Yöntemler, hesaplamalarda kolaylık sağlamak amacıyla yaklaşık 5 km² lik QuickBird görüntüleri üzerinde uygulanmıştır. Analizlerde siyah-beyaz ve yeşil, kırmızı ve yakın kızıl

ötesi bantlarından oluşan QuickBird renkli görüntüleri kullanılmıştır. Zenginleştirilmiş görüntüler, *Görelî ortalama ve varyans farkları, Korelasyon, En Yüksek Sinyal Hata Oranı ve Genel Kalite İndeksi* kullanılarak spektral açıdan değerlendirilmiştir. Sonuçların istatistiksel olarak değerlendirilmesinin ardından gerçek renkli görüntü ve zenginleştirilmiş görüntüler En Büyük Olasılık sınıflandırma yöntemi yardımıyla sınıflandırılmıştır. Görüntü sınıflandırması için gerekli örnek alanlar renkli QuickBird görüntüsü üzerinden toplanmıştır. Üretilen zenginleştirilmiş görüntüler ve renkli QuickBird görüntüsü daha sonra örnek alanlar yardımıyla sınıflandırılmış ve sonuçlar hata matrisleri yardımıyla değerlendirilmiştir. Hata matrisleri sonucunda hesaplanan kappa değerleri %79,2 doğrulukla en yüksek doğruluğu Gram-Schmidt görüntü zenginleştirme yönteminin sağladığını göstermiştir. Gram-Schmidt yöntemi, gerçek renkli görüntünün sınıflandırılması sonucu üretilen tematik haritanın doğruluğunu yaklaşık %3 oranında arttırmıştır. İyileştirilmiş YoRD dönüşümü, Dalgaboyu tabanlı YoRD dönüşümü, En Küçük Kareler, Ana Bileşenler Spektral, Keskinleştirilmiş Filtreleme Yöntemi, Brovey ve Dalgaboyu tabanlı Ana Bileşenler yöntemlerinin de gerçek renkli görüntüye ait tematik harita doğruluğunu belli oranlarda arttırdığı gözlenmiştir. Diğer taraftan RDP dönüşümü kullanılarak üretilen tematik harita doğruluğu gerçek renkli görüntüye ait doğruluğu %1 oranında düşürmüştür.

Sonuçlar Gram-Schmidt, İyileştirilmiş YoRD dönüşümü, Dalgaboyu tabanlı YoRD ve Ana Bileşenler Zenginleştirme yöntemi, En Küçük Kareler, Ana Bileşenler Spektral, Yüksek Frekans Filtreleme Yöntemi ve Brovey dönüşümü kullanılarak elde edilmiş görüntülerin tarımsal alanlarda yetiştirilen ürün çeşitliliğini ayırmada etkili olduğunu göstermiştir. Görüntü zenginleştirme yöntemlerinin tarım alanlarında yetiştirilen ürün deseninin tesbit edilmesine olan katkısının belirlenebilmesi için yöntemlerin ürün çeşitliliğinin temsil edildiği farklı çalışma bölgelerine uygulanması yapılan çalışmanın güvenilirliğini arttıracaktır.

Kaynaklar

Arıkan, M., 2003, A multitemporal masking classification method for field-based agricultural crop mapping. *Yüksek Lisans Tezi, Jeodezi ve Coğrafi Bilgi Teknolojileri EABD, Orta Doğu Teknik Üniversitesi, Ankara, Türkiye.*

Chavez, P. S., Sides, S. C., Anderson, J. A., 1991, Comparison of three different methods to merge multiresolution and multispectral data: Landsat TM and SPOT panchromatic, *Photogrammetric Engineering & Remote Sensing*, Vol. 57, pp. 295-303.

Colditz, R. R., Wehrmann, T., bachmann, M., Steinnocher, K., Schmidt, M., Strunz, G., and Dech, S., 2006, Influence of image fusion approaches on classification accuracy: a case study, *International Journal of Remote Sensing*, Vol. 27, pp. 3311-3335.

ENVI Kılavuzu v. 4.4

ERDAS Kılavuzu v. 9.1

Jensen, J., 2005, “*Introductory Digital Image Processing: A Remote Sensing Perspective*”, University of South Carolina, p. 501.

Karathanassi, V., Kolokousis, P., and Ioanniduo, S., A comparison study on fusion methods using evaluation indicators, *International Journal of Remote Sensing*, Vol. 28, pp. 2309-2341.

Konstantinos, G. N., 2008, Comparison of nine fusion techniques for very high resolution data, *Photogrammetric Engineering & Remote Sensing*, Vol. 74, pp. 647-659.

Laben, E.A., 2000, Process for enhancing the spatial resolution of multispectral imagery using pan-sharpening (Gram-Schmidt). US Patent: USA, Eastman Kodak Company.

Lillesand, M., Kiefer, R. W., Chipman, J. W., 2004, Remote Sensing and Image Interpretation, *Fifth Edition*, John Wiley and Sons, Inc., USA.

Ozdarici, A., 2005, Comparison of Different Spatial Resolution Images for Polygon-Based Crop Mapping, *Yüksek Lisans Tezi, Jeodezi ve Coğrafi Bilgi Teknolojileri EABD, Orta Doğu Teknik Üniversitesi, Ankara, Türkiye.*

Özdarıcı ve Akyürek, 2008, Tarım Alanlarının Uydu Görüntülerinden Görsel Belirlenmesinde Görüntü Zenginleştirme Yöntemlerinin Etkileri, *Uzaktan Algılama ve Cğrefi Bilgi Sistemleri (UZAL CBS) Sempozyumu*, 13-15 Ekim, Kayseri, Türkiye.

PCI Geomatica Kılavuzu v. 10.1.3

Pellemans, A., Jordans, R., Allewijn, R., 1993, Merging multispectral and panchromatic SPOT images with respect to the radiometric properties of the sensor, *Photogrammetric Engineering & Remote Sensing*, Vol. 59, pp. 81-87.

Pohl, C., and Van Genderen, J. L., 1998, Multisensor image fusion in remote sensing: concepts, methods and applications, *International Journal of Remote Sensing*, Vol. 19, pp. 823-854.

Ranchin, T., Aiazzi, B., Alparone, L., Baronti, S., Wald, L., 2003, Image fusion-the ARSIS concept and some successful implementation schemes, *ISPRS Journal of Photogrammetry&Remote Sensing*, V. 58, pp. 4-18.

Siddiqui, Y., 2003, The modified IHS method for fusing satellite imagery, *ASPRS Annual Conference Proceedings*, Anchorage, Alaska.

Zhang, Y., 2002, Problems in the fusion of commercial high-resolution satellite as well as Landsat7 images and initial solutions, *Symposium on Geospatial Theory, Processing and Applications*, Ottawa.

APPENDIX C

EVALUATION OF IMAGE FUSION METHODS ON AGRICULTURAL LANDS

Article: Published in Journal of Earth Science and Engineering, November 20, 2011.

A. Ozdarici Ok¹ and Z. Akyurek²

*1. Department of Geodetic and Geographic Information Technologies, Middle East
Technical University (METU), Ankara 06800, Turkey*

*2. Civil Engineering Department, Middle East Technical University (METU), Ankara
06800, Turkey*

Received: July 16, 2011 / Accepted: August 22, 2011 / Published: November 20, 2011.

Abstract: This study focuses on evaluating four different image fusion methods on an agricultural land of Turkey. Two subsets of QuickBird images having almost 5 km² are used as test sites in the analyses. Panchromatic and multispectral QuickBird data are fused and a high resolution colour images are generated by the image fusion methods namely: Gram-Schmidt, Least Square Fusion, Principle Component Spectral Sharpening, and Wavelet-integrated Principle Component Analysis. In order to examine the spectral properties of the fused images, the fused products are resampled to spatial resolution of multispectral image first, and then several statistical evaluation methods called: Relative Mean Difference (RMD), Relative Variation Difference (RVD), Correlation (C), Peak Signal to Noise Ratio (PSNR), Universal Image Quality Index (UQI) and Erreur Relative

Globale Adimensionnelle Desynthèse (ERGAS) are computed. Based on the results, it is observed that the Gram-Schmidt method provides the best performance for each test site.

Key words: Image fusion, agriculture, QuickBird, evaluation.

1. Introduction

Image fusion is a process to generate a new image by integrating different spatial and spectral characteristics of the images. It is used to generate not only visually appealing images but also provide detailed input to the later image analyses like image classification, change detection, landslide hazard detection etc. [1]. A review article was presented by Pohl and Van Genderen in 1998 [2] about image fusion methods, in which concepts, methods and applications of image fusion were examined. Various pixel-level fusion methods were applied on QuickBird images by Karathanassi et al. in 2007 [3] and fused outputs were evaluated using some statistical evaluation indicators. Another assessment was performed on nine different image fusion methods by Konstantinos in 2008 [4], in which the fused products were evaluated both visually and statistically. Results indicated that the Local Mean and Variance Matching, Local Mean Matching, PANsharp and the Modified IHS algorithms produced better outputs. A similar study was conducted by Colditz et al. in 2006, where five image fusion methods on Landsat 7 ETM+ images were examined [5]. Acceptable results were obtained with the Wavelet, multi-sensor multi-resolution image fusion and the method of principle component analysis. Problems and limitations of image fusion methods were examined by some other studies (Refs. [6-8]). Although several researches about evaluating the performance of image fusion methods are available in the literature, general view is that more studies are needed to examine the fusion methods on different data sets to make a generalization.

Corresponding author: A. Ozdarici Ok, research assistant, main research fields: remote sensing, image classification, object-based image analysis, GIS. E-mail: aozdarici@gmail.com.

In this study we focused on four image fusion methods namely: Principle Component (PC) Spectral Sharpening, Least Square Fusion (LSF), Gram-Schmidt, and Wavelet-integrated PCA, mostly encountered in the literature, on an agricultural land. QuickBird panchromatic (PAN) and four band (blue, green, red and near-infrared) multispectral (MS) images were utilized in the analyses. The fused results acquired by the fusion methods were resampled from 0.60 m to 2.44 m in order to compare them with the original MS image (2.44 m) by utilizing multiple evaluation indicators called: Relative Mean Difference (RMD), Relative Variation Difference (RVD), Correlation (C), Peak Signal to Noise Ratio (PSNR), Universal Quality Index (UQI) and Erreur Relative Globale Adimensionnelle Desynthèse (ERGAS).

2. Methodology

2.1 Study Area and Data

The study area was selected from Karacabey Plain (Bursa) which is located in Marmara region in northwest of Turkey. The Karacabey Plain is a representative region of agricultural structure and it is characterized by rich, loamy soils having good weather conditions. The main crops can be listed as corn, tomato, pepper, wheat, pea, sugar beet and rice among twelve crop types cultivated in the area [9].

QuickBird PAN (0.61 m) and MS (2.44 m) images were used to test the image fusion methods in the study. The spectral range of QuickBird PAN image lies between 0.44-0.90 μm . The multispectral image consists of four channels including blue (0.45-0.52 μm), green (0.52-0.60 μm), red (0.63-0.69 μm), and near-infrared (0.76-0.89 μm). The images were taken on 13 August 2004 in which crop variation is in its maximum level in the area. The images used in the study correspond to the standard imagery product, where corrections for sensor, radiometric and geometric distortions are performed and the images are mapped to a cartographic projection. For the computational efficiency, two

small parts of 8 bit QuickBird image ($\sim 5 \text{ km}^2$) selected from the area were used in the study. The first test site composes of five classes namely corn, wheat, residue, tomato and sugar beet and the second test site includes rice fields instead of the class of sugar beet.

2.2 Methods

In this part, the characteristics of image fusion methods used in the study are examined.

2.2.1 Image Fusion Methods

2.2.1.1 Principle Component (PC) Spectral Sharpening Method

Principle Component Analysis (PCA) is used to reduce redundancy between image bands by generating a set of new uncorrelated linear combinations of the original variables. The technique is used to fuse low spatial resolution multispectral bands and a corresponding high spatial resolution PAN band. To do that, first, a PC transformation is applied on the multispectral data. Second, the PC band 1 is replaced with the high spatial resolution data. This is based on an assumption that the first PC and the PAN data which have similar spectral characteristics. Next, a scaling process is performed to match the PC band 1 to remove distortions of the spectral information. Next, an inverse transform is applied to return the RGB space. Final step is to perform a resampling process on the multispectral data to conform it to the high resolution pixel size [10].

2.2.1.2 Least Square Fusion (LSF) Method

LSF aims to achieve a best color relationship between the original multispectral and fused images while improving the spatial resolution of the image fused. The main objectives of this technique are to prevent color distortions and operator/data dependency. To do this, some statistical approaches are used to standardize the fusion process [3, 11].

2.2.1.3 Gram-Schmidt Method

In the method of Gram-Schmidt spectral sharpening, first, a simulation of PAN band is performed using lower resolution spectral bands. In the simulation process, the high

resolution PAN band is blurred by appropriate factor, sub-sampled and interpolated up to an appropriate scale. Second, the Gram-Schmidt orthogonalization transformation, which provides to remove the redundant information in the data, is applied on the simulated PAN band and the spectral bands. The simulated lower spatial resolution PAN image is used as the first band in the Gram-Schmidt transformation. Third, the statistics of the higher spatial resolution PAN image are adjusted to the statistics of the first transform band resulting from the Gram-Schmidt transformation. Next, the higher spatial resolution PAN image having adjusted statistics is replaced with the band of the first transform. Finally, an inverse transform is applied to produce higher resolution spectral bands [10].

2.2.1.4 Wavelet-Integrated PCA Method

The wavelet transform is applied on the images by producing a set of low resolution PAN images from the high resolution PAN image using wavelet coefficients for each level. After decomposing the PAN band, the resulting low resolution PAN band is replaced with a multispectral band at the same resolution level. Then, a reverse wavelet transform is performed to convert the data to the original resolution level of PAN [12].

In the Wavelet-integrated PCA method, PCA is applied on the multispectral image prior to the wavelet analysis. After applying a histogram match between the first PC and the PAN image, the first PC is replaced with the PAN band. The inverse transform is applied on the image to construct a fused RGB image.

2.2.2 Evaluation Methods

In order to understand the spectral effects of the image fusion methods, the fused products (0.60 m) were examined relative to the multispectral image (2.44 m). Six different evaluation indicators called Relative Mean Difference (RMD), Relative Variation Difference (RVD), Correlation, Peak Signal to Noise Ratio (PSNR), Universal Image Quality Index (UQI) and Erreur Relative Globale Adimensionnelle Desynthèse (ERGAS) were computed for the fused products of each image in Matlab environment.

Before the computations there is a need to decrease the spatial resolution of the fused products to the spatial resolution of low resolution image in order to examine the spectral quality of the fused products. Hence the spatial resolutions of the fused images were resampled to the multispectral image resolution (2.44 m). In this paper, the fused image with reduced resolution is called as “fused image”. The assessment criterion is based on preserving the spectral quality of the multispectral data for the fused products. Based on the results, if spectral quality of the multispectral and fused images is similar to each other, it can be stated that their global statistical parameters should be very similar [8]. The evaluation indicators used in this study are explained below:

2.2.2.1 Relative Mean Difference (RMD)

The RMD refers to the difference of means between the fused products and the low resolution image (Eq. (1)). It is computed as follows:

$$\frac{(\overline{F} - \overline{LR})}{\overline{LR}} \quad (1)$$

where, \overline{F} refers to the mean value of the fused image, \overline{LR} is the mean value of the low resolution image.

2.2.2.2 Relative Variation Difference (RVD)

The objective of RVD is to find the variation difference between the fused product and the low spatial resolution image (Eq. (2)). It is computed using the following equations:

$$\frac{(\hat{\sigma}_F^2 - \hat{\sigma}_{LR}^2)}{\hat{\sigma}_{LR}^2} \quad (2)$$

where, $\hat{\sigma}_F^2$ is the variation of the fused product and, $\hat{\sigma}_{LR}^2$ is the variation of the low resolution image.

2.2.2.3 Correlation (C)

This evaluation criterion is used to compute the correlation between the fused product and the low spatial resolution image (Eq. (3)).

$$\delta_{F_i.LR_i} = \frac{\mathbf{COV}_{F_i.LR_i}}{\partial_{F_i} \times \partial_{LR_i}} \quad (3)$$

F_i means the fused image and LR_i refers to the low spatial resolution image.

2.2.2.4 Peak Signal to Noise Ratio (PSNR) Index

The PSNR index is used to reveal radiometric distortions of the final product after applying an image fusion method (Eq. (4-5)). The computation is performed between the fused image and the low resolution image [3]. It is calculated as:

$$MSE = \frac{1}{N} \sum_{i=1}^N (F_i - LR_i)^2 \quad (4)$$

$$PSNR = 20 \log_{10} \frac{Peak}{\sqrt{MSE}} \quad (5)$$

where, F_i is the pixel value i of the fused image, LR_i is the pixel value i of the low resolution image, N refers to the number of non-null image pixels, Peak is the maximum possible pixel value which is equal to 255 for 8 bit images.

2.2.2.5 Universal Image Quality Index (UQI)

The UQI has the capability of modeling any distortions as a combination of three different factors: (i) loss of correlation, (ii) luminance distortion, and (iii) contrast distortion (Eq. (6)). The dynamic range of Q is between -1 and 1. The possible highest value is provided if the spectral quality of the fused product and the low resolution image are identical [13].

$$Q = \frac{\partial_{F.LR}}{\partial_F \partial_{LR}} \frac{2\overline{F.LR}}{(\overline{F})^2 + (\overline{LR})^2} \frac{2\partial_F \partial_{LR}}{\partial_F^2 + \partial_{LR}^2} \quad (6)$$

where, \overline{F} refers to the mean value of the fused product, \overline{LR} is the mean value of the low spatial resolution image, ∂_F and ∂_{LR} means the variation of the fused and the low

resolution image, respectively, $\hat{\sigma}_{F.LR}$ is the variance value of the fused and the low resolution images.

2.2.2.6 ERGAS

ERGAS (erreur relative globale adimensionnelle desynthèse), relative dimensional global error in synthesis, is used to compare the spectral characteristics of the fused and reference image for identity. The ERGAS value exhibits a strong tendency to decrease when the quality of the fused product increases. If the ERGAS value is less than 3, it can be said that the resulting fused image has a “good quality” [14] (Eq. (7)).

$$ERGAS = 100 \frac{h}{l} \sqrt{\frac{1}{N} \sum_{k=1}^N \frac{RMSE(B_k)^2}{(M_k)^2}} \quad (7)$$

where, h , l refers to the high and low spatial resolution, N is the number of bands, $RMSE(B_k)$ means the root mean square error between the fused image and the low resolution image, M_k is the mean value of the low resolution image for the k^{th} band [14].

If the conditions of these evaluation indicators provide the smallest possible RMD, RVD, ERGAS and the maximum C, PSNR, UQI values with the MS image, it can be stated that the fused image better preserves the spectral information of the low resolution image [3].

3. Results and Discussion

The images fused were assessed both visually and statistically in the study. The visual interpretation of the outputs revealed that except for the method of Wavelet-integrated PCA, the visual quality of the other methods was found relatively good. Some spectral distortions were obtained through visual interpretation of the products of wavelet-integrated PCA. The reason could be explained by the changes of the wavelength ranges of the new satellite products (e.g. QuickBird and Kompsat-2) in respect to the available

fusion methods, which can be solved by updating the existing fusion methods [11, 15]. The visual qualities of the methods based on the photo interpretation of the authors are given in Table 1.

The statistical results were ranked based on the ERGAS values (Tables 2 and 3). Statistical evaluation of the first test site indicated that the Gram-Schmidt image fusion method better preserved the spectral quality of the MS image (Table 2). The results of Gram-Schmidt method was followed by the LSF method. It was observed that the methods of Wavelet-integrated PCA and PC Spectral Sharpening exhibited relatively poor results with the highest ERGAS and the lowest UQI values. The image fusion results can be seen for a small part of study area in Fig. 1 to make a visual comparison.

Results obtained for the second test site indicated that similar to the first test site, the Gram-Schmidt method provided the best performance with the smallest RMD (-0.00) and ERGAS values (0.76) and the highest C, PSNR and UQI values when compared with the results of other image fusion methods (Table 3). The LSF method exhibited similar results with the Gram-Schmidt except for its ERGAS value, which was computed relatively high when compared with the Gram-Schmidt method. The method of Wavelet-integrated PCA also exhibited high results although the PSNR index of it was too small (14), the poorest value among the others.

Table 1 Visual quality of the image fusion methods.

	Gram-Schmidt	LSF	PC Spectral S.	Wavelet-PCA
Very Good		X		
Good	X			
Medium			X	
Poor				X

Table 2 Statistical result of image fusion methods of the first test site.

Methods	RMD	RVD	C	PSNR	UQI	ERGAS
Gram-Schmidt	-0.01	0.10	0.98	29.6	0.90	2.30
LSF	0.00	-0.01	0.89	23	0.72	7.39
Wavelet PCA	0.70	1.59	0.92	8.6	0.53	35.14
PC Spectral S.	0.00	-0.20	0.91	15.4	0.39	18.24





Table 3 Statistical results of image fusion methods of the second test site.

Methods	RMD	RVD	C	PSNR	UQI	ERGAS
Gram-Schmidt	-0.00	0.06	0.98	34.8	0.97	0.76
LSF	-0.00	0.00	0.90	32	0.96	3.18
Wavelet PCA	-0.01	0.00	0.93	14	0.92	2.22
PC Spectral S.	0.00	-0.23	0.86	26.4	0.97	4.24



5. Conclusions

Image fusion is an important step for agricultural areas for the later image analyses like sensing agricultural patches and predicting undesirable agricultural issues like plant diseases, drought, and wrong agricultural practices etc. Hence, utilizing effective image fusion methods could provide researchers to improve the quality of the interpretation. The focus of this study was to evaluate four different image fusion methods in a statistical and visual manner on two test sites in an agricultural land. Visual evaluation revealed that the methods of Gram-Schmidt and LSF had better performance than other methods for each test site. In order to evaluate the results in a statistical manner, some basic evaluation indicators called RMD, RVD, C, PSNR, UQI and ERGAS were utilized. It was observed that better statistical results were achieved for the Gram-Schmidt method on both test sites. That means the results obtained for the Gram-Schmidt method better preserved the spectral characteristics of the QuickBird MS image. Similar results were observed for the

LSF methods while the other methods exhibited relatively poor outputs. The method of the Wavelet-integrated PCA provided acceptable spectral values although the visual quality of it was relatively poor. The PC Spectral Sharpening provided the worst results when compared with the other image fusion methods although the values of RMD, RVD and C were acceptable. A small part of fused images of the second test site can be seen in Fig. 2.

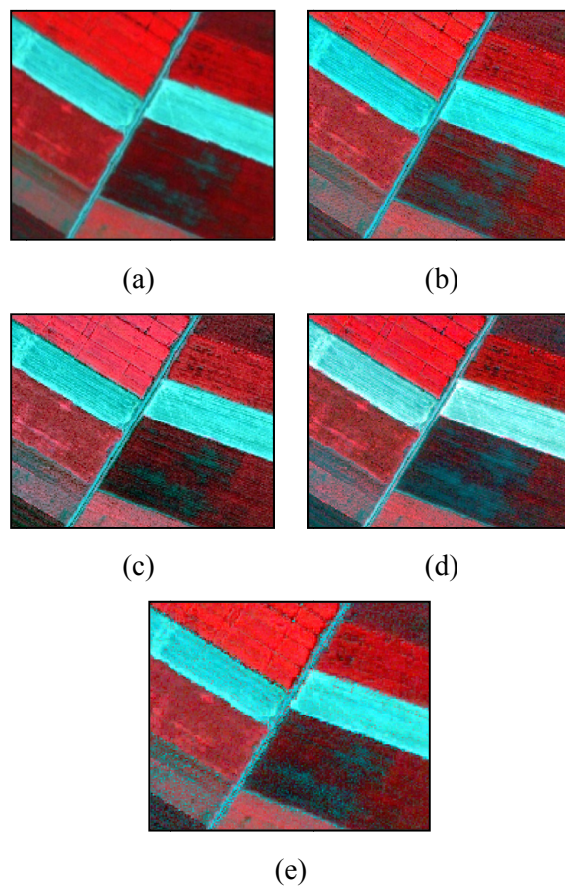


Fig. 1 (a) A part of original multispectral image from the first test site and results of (b) Gram-Schmidt method, (c) LSF method, (d) PC Spectral Sharpening method, (e) Wavelet-integrated PCA.

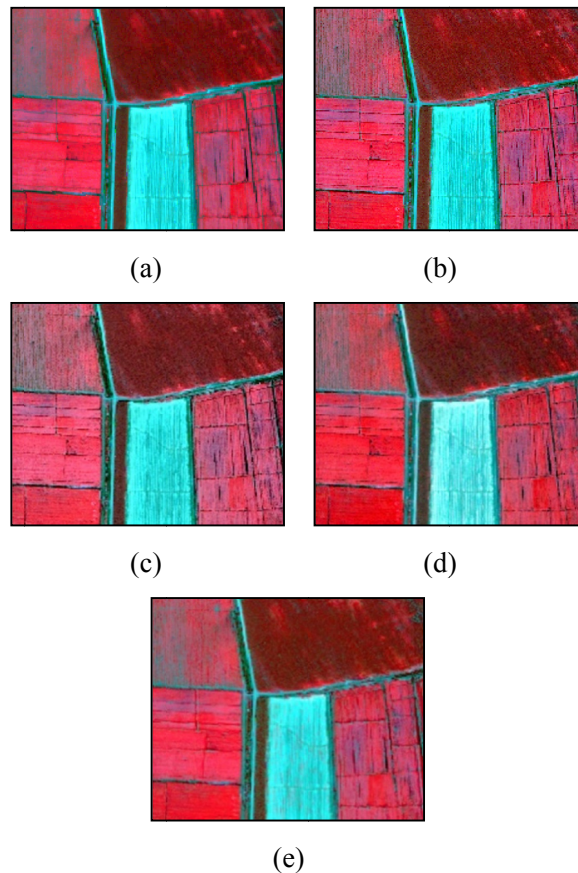


Fig. 2 (a) A part of original multispectral image from the second test site and results of (b) Gram-Schmidt method, (c) LSF method, (d) PC Spectral Sharpening method, (e) Wavelet-integrated PCA.

References

- [1] M. Kim, J.B. Holt, M. Madden, Comparison of global- and local-scale pansharpening for rapid assessment of humanitarian emergencies, *Photogrammetric Engineering and Remote Sensing* 77 (2011) 51-63.
- [2] C. Pohl, J.L. Van Genderen, Multisensor image fusion in remote sensing: concepts, methods and applications, *International Journal of Remote Sensing* 19 (1998) 823-854.

- [3] V. Karathanassi, P. Kolokousis, S. Ioannidou, A comparison study on fusion methods using evaluation indicators, *International Journal of Remote Sensing* 28 (2007) 2309-2341.
- [4] G.N. Konstantinos, Comparison of nine fusion techniques for very high resolution data, *Photogrammetric Engineering & Remote Sensing* 74 (2008) 647-659.
- [5] R.R. Colditz, T. Wehrmann, M. Bachmann, K. Steinnocher, M. Schmidt, G. Strunz, et al., Influence of image fusion approaches on classification accuracy: A case study, *International Journal of Remote Sensing* 27 (2006) 3311-3335.
- [6] P.S. Chavez, S.C. Sides, J.A. Anderson, Comparison of three different methods to merge multiresolution and multispectral data: Landsat TM and SPOT PAN, *Photogrammetric Engineering & Remote Sensing* 57 (1991) 295-303.
- [7] A. Pellemans, R. Jordans, R. Allewijn, Merging multispectral and PAN SPOT images with respect to the radiometric properties of the sensor, *Photogrammetric Engineering & Remote Sensing* 59 (1993) 81-87.
- [8] Y. Zhang, Problems in the fusion of commercial high-resolution satellite as well as Landsat7 images and initial solutions, Ottawa, in: *Symposium on Geospatial Theory, Processing and Applications*, 2002.
- [9] M. Turker, A. Ozdarici, Field-based crop classification using SPOT4, SPOT5, IKONOS, and QuickBird imagery for agricultural areas: A comparison study, *International Journal of Remote Sensing* (In Press).
- [10] E.A. Laben, Process for enhancing the spatial resolution of multispectral imagery using PAN-sharpening (Gram-Schmidt), available online at: <http://www.freepatentsonline.com/6011875>.
- [11] Y. Zhang, Problems in the fusion of commercial high-resolution satellite as well as Landsat 7 images and initial solutions, *ISPRS* 34 (2002) 4.
- [12] R. Pouncey, K. Swanson, *ERDAS Manual*, in: K. Harth (ed.), fifth ed., ERDAS, USA, 1999, p. 193.
- [13] Z. Wang, A.C. Bovik, A universal image quality index, *IEEE Signal Processing Letters* 20 (2002) 1-4.

- [14] L. Wald, Data Fusion, Definitions and Architectures-Fusion of Images of Different Spatial Resolutions, ISBN 2-911762-38-X (2002), (Presses de l'Ecole, Ecole des Mines de Paris), Paris, France, pp. 161-162.
- [15] Y. Zhang, Understanding image fusion, Photogrammetric Engineering and Remote Sensing 6 (2004) 657-661.

APPENDIX D

A COMPARISON OF SAR FILTERING TECHNIQUES ON AGRICULTURAL AREA IDENTIFICATION

Proceeding: Published in ASPRS Annual Conference, 2010, San Diego, California, USA

Asli Ozdarici, Research Assistant

Zuhal Akyurek, Associated Professor

Geodetic and Geographic Information Technologies Department

Civil Engineering Department

Middle East Technical University

Ankara, 06531

ozdarici@metu.edu.tr, zakyurek@metu.edu.tr

ABSTRACT

This study presents a comprehensive evaluation of the most frequently used non-adaptive and adaptive Synthetic Aperture Radar (SAR) filtering techniques called; Mean, Median, Lee, Lee-sigma, Local Region, Frost and Gamma- MAP. Envisat ASAR Precision Image (PI) mode data acquired on August 2008 is used to examine the filtering techniques. Three test sites (~ 4 km²), located in Karacabey of Bursa in northwest of Turkey are selected. Two of them consist of homogenous agricultural fields and the third one is selected from lake. One of the agricultural test sites has 143 fields where seven different crop types namely; corn, pasture, pepper, sugar beet, tomato, wheat, and watermelon exist. The other agricultural test site contains relatively smaller agricultural fields and it has 386 fields where corn, rice, sugar beet, tomato, wheat, and watermelon are cultivated

in it. After correcting the images geometrically, the filtering operations are applied on the amplitude data using 5x5 windows. The filtering performances are evaluated by computing difference of means (MeanDif), difference of standard deviation (StdDif), correlation, and quality factor (Q). If the conditions of these evaluation indicators provide the smallest possible means, standard deviation and the maximum correlation and Q, it can be stated that the filtered image preserves the spectral information of the original image while reducing the speckle effect. Based on this evaluation the most reliable outputs are achieved by applying the Lee filter when compared with the original data. This technique is followed by the results of the Mean, Median, Gamma-MAP and Frost filters.

INTRODUCTION

Microwave signals backscattered from the earth's surface can be in phase or out of phase when received by the satellite sensor. This stage causes random pattern of brighter and darker pixels in the microwave image called *speckle*. This characteristic reduces the interpretability of the microwave images. One of the most widely used method of reducing this limitation is image filtering. Image filtering is a local operation which modifies the original image with the neighboring pixels on the image (Lillesand et.al, 2004). This operation is applied using a window called *kernel*. There are several well-known researchers developing filtering algorithms for the SAR images (Lee 1980; Frost et.al, 1982 and Kuan et.al, 1985). In addition to this, there are also several researchers to examine the results of the filtered products and to evaluate the effectiveness of these methods (Lopes et.al, 1990; Shi and Fung, 1994; Serkan et.al, 2008). Shi and Fung (1994) compare the most widely used filtering methods called Kuan and Frost Filter, Enhanced Lee Filter, Enhanced Frost Filter and Gamma Map filter based on the preservation of point targets, linear features and angular structures. Two water bodies extracted from the ERS-1 image are filtered using the filtering methods in the study. The methods were applied on both the original SAR image and the computer simulated data. Results of the study indicate that the Kuan filter was found to be more accurate for determining point targets of the images. The results point out that the linear features could be separated better than the other filtering methods using the Frost filter. The Frost filter also provided the best results in term of the preservation of the angular structures in the image. Lopes et. al. (1990) also compares the most well-known adaptive filters called Frost, Kuan, Lee and Homomorphic filters on a SAR data and its simulation products. In order to improve the efficiency of the filter, some criteria are included in the filters. It is indicated that the filters reduce the speckle while better preserve the textural information. Herold et.al (2005) aims to improve the classification accuracy of the radar images. They examine various spatial components like speckle reduction while trying to improve the classification accuracy. Five different speckle filters (mean, median, local region, Frost and Lee) are applied on the image using 3x3 and 5x5 windows. They find that the mean and median filters increased the classification accuracy better than the other methods with the 5x5 window size. Serkan et al. (2008) propose a new adaptive speckle filter called Edge Map-Directed Adaptive Mean (ENDAM) and compare it with the other filtering methods (Mean, Median, Kuan, Lee, Lee-Sigma, Frost, Crimmins, Martin, Nagao and

Dong). The filtering operations were performed on a JERS-1 SAR image of Tuzla, Istanbul and a simulated SAR data. The ENDAM filtering method uses a wavelet edge detection algorithm while performing the filtering process, which is the main difference between the proposed method and the other filtering methods. Results indicate that the proposed method provided near results compared with the other filtering results. The objective of this study is to compare the most widely used SAR filtering methods called Mean, Median, Lee, Lee-Sigma, Frost, Gamma-Map and Local Region filters. Envisat ASAR precision image (I) mode is used to this purpose. The filters are tested on three different sites having almost 5 km² extracted from the data. Two out of three belongs to an agricultural area and third one is taken from a lake site. The kernel size of 5x5 is applied on the test sites and results are evaluated four statistical evaluation indicators namely; mean, Std, correlation and Q.

STUDY AREA AND DATA

Three study sites are selected from Marmara Region in Turkey (Figure 1). The sizes of these areas are approximately 5 km². Two out of three are selected from one of the most valuable agricultural area called Karacabey Plain in Turkey. Most of the fields in the areas have rectangular shape. The sizes of the fields ranged from 0.1 ha to 9.5 ha and from 0.1 to 13.7 ha for the first and second areas, respectively. There are six crop types filtered in the first region including, pasture, pepper, sugar beet, tomato, wheat, and watermelon. The land cover of the second agricultural region comprises six crop types including corn, rice, sugar beet, tomato, wheat, and watermelon. The third site is selected from the Ulubat Lake near the Karacabey Plain. The study area and the locations of the test sites on the whole area can be seen in figure 1 and 2.

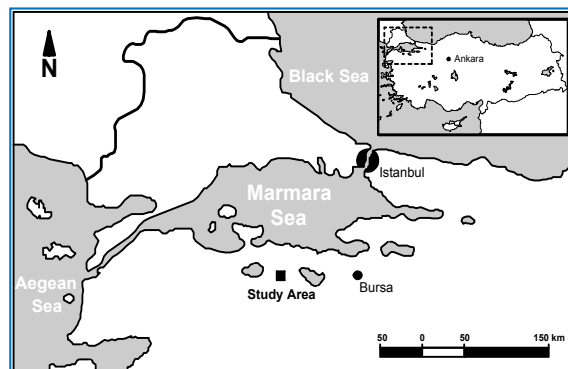


Figure 1 Study Area

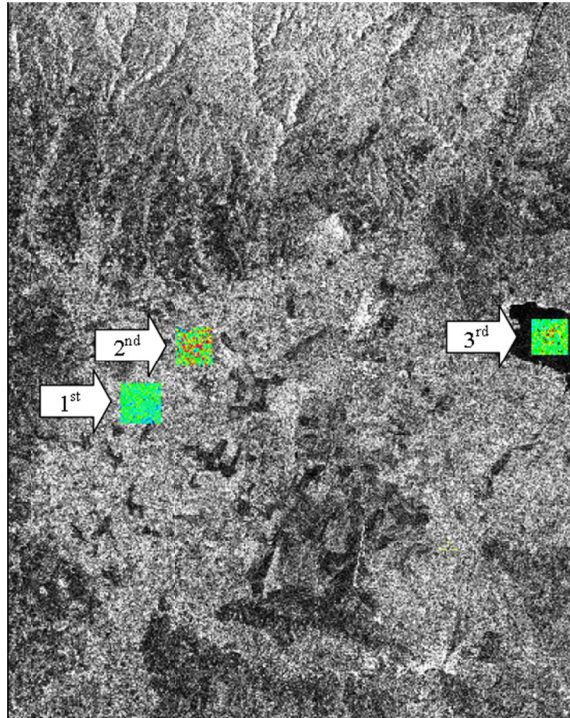


Figure 2 Envisat ASAR data and selected locations

The Envisat ASAR Precision Image mode used for the filtering operations acquired on 03 August 2008. Table 1 shows the technical summary of the data.

Table 1 Technical summary of the Envisat ASAR data

	Envisat ASAR
Image Type	Image Mode
Processing Level	Level 1b
Spatial Resolution	12.5 m
Wavelength Range	C-band
Frequency Range	5.331 GHz
Polarization	VV
Image Swath	IS7
Swath Width	70km and 56km
Datum	WGS 84
Map Projection	UTM
Zone Number	35

The image was obtained by an ESA Category 1 User project proposed by Akyurek and Ozdarici in 2007. The acquired model provides HH and VV polarization image data with a spatial resolution between 12.5 m and 150 m and coverage of 56x105 km². In this

study, the VV polarization image is used. Envisat ASAR operates in the C band and has various incidence angles between 15.0 and 45.20. Seven acquisition configurations are available for the Envisat ASAR. The technical characteristics of these configurations can be seen in table 2. Among the seven configuration category, the image used was acquired as IS7 acquisition configuration. The incident angles of the IS7 image vary from 42.5⁰ to 45.2⁰

Table 2 The configurations types of the Envisat ASAR data

<i>Image Swath</i>	<i>Swath Width (km)</i>	<i>Ground Position (km)</i>	<i>Incidence Angle Range</i>
IS1	105	187-292	15.0-22.9
IS2	105	242-347	19.2-26.7
IS3	82	337-419	26.0-31.4
IS4	88	412-500	31.0-36.3
IS5	64	490-555	35.8-39.4
IS6	70	550-620	39.1-42.8
IS7	56	615-671	42.5-45.2

SPECKLE FILTERING

Speckle, a grainy appearance caused by the interference between waves reflected from microscopic scattering through the terrain, reduces the interpretability of the images therefore it must be balanced with the amount of detail required for the spatial scale and the nature of the particular applications (Medeiros et. al., 2003; CCRS, 2000). There are two methods to reduce the speckle: (i) image filtering, (ii) multi look processing. In this study image filtering processes are examined. Image filtering is a local operation in which pixel values of an original image are modified using the gray values of the neighboring pixels. It can be categorized two main groups: (i) Non-adaptive speckle filters and (i) adaptive speckle filters. Non-adaptive filters use the same set of weights to smooth the image over the entire image (e.g. Mean and Median etc.). On the other hand, adaptive filters use weights based on the degree of speckle in the image (Lee, Frost, Kuan, Gamma-Map, Local Region etc.). The smoothing is dependent on the local statistics for the adaptive filters. Therefore, adaptive filters have more capability of preserving the details than the non-adaptive filters (Tso and Mather, 2001). Some of the adaptive filters like Lee, Lee-Sigma and Frost assume a Gaussian distribution while the Gamma-MAP filter assumes a Gamma distribution to decrease the speckle (Lopes et.al. 1990). In addition to the characteristics of the filtering methods, the window size is also one of the

most important factors for smoothing an image. The larger the window size means the larger smoothing. Therefore, it should be decided before smoothing the images based on the analyses.

Mean Filter

The mean filter is a simple filtering method that slides its window (kernel) on the image and replaces the center value in the window with the average (mean) of all the pixel values in the window. It has a speckle reduction capability but it also removes high frequency information in the image. It is one of the most popular non-adaptive filtering methods. Mean filter uses the same set of smoothing for the whole image. Due to the characteristics it ignores the differences in image texture, contrast, etc.

Median Filter

The median filtering procedure is based on ranking the pixel values in the specified window and assigning the median pixel to the center value of the window. Median filtering is another mostly used non-adaptive filtering method. It is more effective than the mean filter. This is because it suppresses the speckle while preserving the characteristics of sharp edges.

Lee Filter

Lee filter is an adaptive speckle filter. It is based on three assumptions:

- (i) SAR speckle is modeled as a multiplicative noise that means the brighter the area the noisier it is.
- (ii) The noise and the signal are statistically independent to each other.
- (iii) The sample mean and sample variance of a pixel is equal to its local mean and local variance found calculated within a window (Lee, 1980; Tso and Mather, 2001).

The assumptions above define the noise model of the Lee filter. In order to apply the filter, two main steps should be performed. The first one is approximating a multiplicative model by a linear model specified by the mean and the standard deviation. The other step is applying minimum mean square error criterion to this model. The filtering procedure

can be summarized as follows in a detail manner. First, a window size is determined. Second, the speckle noise mean μ_v and standard deviation σ_v are determined based on the speckle model. If window i has N_{pi} pixels, estimates of $\hat{\mu}_v$ and $\hat{\sigma}_v^2$ are computed as follows:

$$\hat{\mu}_v = \frac{1}{N_{pi}} \sum_j z_{ij}, \quad \hat{\sigma}_v^2 = \frac{1}{N_{pi}} \sum_j (z_{ij} - \mu_{li})^2 \quad [1]$$

Where;

z_{ij} is the return from pixel i in a window i ,

$\hat{\mu}_v$ refers to estimate mean intensity of pixels within the window,

N_{pi} means number of pixels in the window

Third, local noise fading mean μ_z and standard deviation σ_z of the pixels within the window are computed. Fourth, noise-free signal standard deviation σ_x is determined.

Next, weight coefficient k is determined. Finally, the computed \hat{x} value is assigned \hat{x} to the central pixel of the window. The formula of the Lee filter can be seen in Equation 2.

$$\hat{\chi} = \left(\frac{z}{\mu_v} \right) \left(\frac{C_z^2 - C_v^2}{C_z^2 + C_v^4} \right) + \left(\frac{\mu_z}{\mu_v} \right) \left(\frac{C_v^2 + C_v^4}{C_z^2 + C_v^4} \right) \quad [2]$$

Where

z is the noise effected image pixel,

μ_v is mean of the noise,

μ_z , mean of the noise affected pixel,

C_z and C_v refer to the coefficient of variations of the noise effected pixel and the noise, respectively.

Lee-sigma Filter

Lee-sigma filter is an adaptive speckle filter. As its name implies, the Lee-sigma filter uses the standard deviation (sigma) to suppress the speckle on an image window. The procedure of the Lee-sigma filter is similar to the Lee filter. It estimates the noise-free signal within the predefined window. The basic difference is that the Lee sigma filter uses two sigma ranges of the pixels within the window. In this way, the pixels lying outside this range are excluded from the averaging process. The formula of the Lee-sigma filter can be seen in equation 3.

$$\hat{\mu} X_{ij} = \left(\sum_{k=i-n}^{n+1} \sum_{l=j-n}^{n+j} \delta_{kl} z_{kl} \right) / \left(\sum_{k=i-n}^{n+i} \sum_{l=j-n}^{n+j} \delta_{kl} \right) \quad [3]$$

Where;

$$\delta_{kl} = 1 \text{ if } z_{ij} - 2\sigma_v z_{ij} \leq z_{kl} \leq z_{ij} + 2\sigma_v z_{ij}$$

$$\delta_{kl} = 0 \text{ otherwise}$$

Frost Filter

The basic idea of the Frost filter is to minimize the mean square error based on the multiplicative noise assumption so that an optional filtering model is to be constructed (Tso and Mather, 2001). It is based on the assumptions of the multiplicative and stationary noise. The pixel of interest is replaced with a weighted sum of the values within the predefined window. The weighting factor is inversely proportional with the distance from the pixel of interest (ERDAS Manual). Its calculation is performed based on the formula below (Equation 4, 5 and 6).

$$DN = \sum_{n \times n} K \alpha e^{-\alpha|r|} \quad [4]$$

Where;

$$\alpha = \left(\frac{4}{n\sigma^2} \right) \left(\frac{\sigma^2}{\mu^2} \right) \quad [5]$$

K is a normalization constant

$\bar{\mu}$ is a local mean

σ means local variance

$\bar{\sigma}$ refers to image coefficient of variation value

n is the moving window size

$$|t| = |x - x_0| + |y - y_0| \quad [6]$$

Gamma Map Filter

The Gamma- Map filter assumes that the scene reflectivity of an image has a Gaussian distribution. Therefore, this filter uses a priori knowledge of the probability density function (PDF) of the scene when suppressing the speckle of the image (Shi and Fung, 1994). Under this assumption the computation of the Gamma Map filter can be performed as follows (Equation 7).

$$\hat{\mu}^3 - \mu \hat{\mu}^2 + \sigma \left(\mu - \hat{DN} \right) = 0 \quad [7]$$

Where;

μ is the original image variance

$\hat{\mu}$ is the expected value

σ refers to original image variance

DN is the input value

Local Region Filter

The Local Region filter compares the variance values of the regions surrounding the pixel of interest (Equation 8). While doing this, it divides the moving window into eight regions based on angular position. The central pixel of the window is then replaced with the mean values within the region with the lowest variance (Sheng and Xia, 1996).

$$\sigma^2 = \sum (DN_{xy} - \mu) / n - 1 \quad [8]$$

EVALUATION INDICATORS

Quality of all the filtered products (3x3, 5x5, 7x7, and 9x9) was evaluated quantitatively using mean, standard deviation, correlation and quality factor. When evaluating the filtered products, preserving the radiometric quality of the data was taken into consideration. That means if the radiometric quality of the original and fused images is similar to each other, it can be stated that their global statistical parameters should be very similar (Karathanassi et al., 2007). If the conditions of these evaluation indicators provide the smallest possible means, standard deviation and the maximum correlation, the filtering performance can be thought as good. The computations of the correlation and Q measures can be seen in equation 9, 10 and 11.

Correlation

Correlation values were computed between the original and filtered products based on the equation below.

$$\delta_{f.o} = \frac{\mathbf{COV}_{f.o}}{\hat{\sigma}_f \hat{\sigma}_o} \quad [9]$$

where

$\mathbf{COV}_{f.o}$ refers to covariance of the original and filtered image

$\hat{\sigma}_o$ and $\hat{\sigma}_f$ are the standard deviations of the original and filtered images, respectively.

Quality Factor (Q)

On the other hand the Q is an important test measures which is used to reduce the standard deviation to decrease the variations in the uniform areas. The computation of the quality factor is given in equation 10 and 11.

$$Q = \frac{|\mu_{shift}|}{L_0 \times (\sigma^2)_f} \quad [10]$$

Where;

$$\mu_{shift} = \mu_o - |\mu_0 - \mu_f|$$

μ_o is the mean value of the original image

μ_f is the mean value of the filtered image

$(\sigma^2)_f$ is the variance of the filtered image

L_0 is the equivalent number of looks value of the original image which is computed as:

$$L_0 = \frac{\mu_0^2}{\sigma_0^2} \quad [11]$$

where

μ mean value,

σ is the variance of the image data,

The Q value is always equal to 1 for the original image. Any change in the mean value will reduce the Q. This can be evaluated as reduction in filter capability. A decrease in the variation for the filtered image will increase the value of Q. That means the higher the Q value, the stronger the speckle reduction (Serkan et.al, 2008).

RESULTS AND DISCUSSION

Seven different filtering methods called Mean, Median, Lee, Lee-sigma, Frost, Gamma-Map and Local Region were examined in the study. The filters with 5x5 kernels were

applied on three scenes extracted from an Envisat ASAR image taken on August 2008. Six criteria namely mean, Std, mean difference (MeanDif), Std difference (StdDif), correlation and Q were selected to evaluate the effectiveness of the results. Based on the table 3, it was indicated that the Lee filtered image provided similar mean value with the original image and it was reduced Std value of the original image around 1.19. Its correlation value was found relatively high (0.73) when compared with the Mean, Median, Frost, Local Region and Gamma-Map filters. The highest Q value was computed for the Lee filter for the first test site. These numerical indicators showed that the Lee filter yielded the best results in the other filtering methods. Although the Mean and Median filters exhibited closer results to the mean value of the original image and high StdDif values, the correlation and Q values were found relatively low when compared with the Lee filter. The Gamma-MAP filter also revealed satisfactory results although its mean values is low (5.34) than the original image. The Lee-Sigma filter exhibited relatively low results but unexpectedly it has the highest correlation value (0.81). The poorest results were obtained for the Local Region filter. Although the mean and median value of the image filtered by the Local Region filter were high enough, the correlation and Q value of this filter is very low.

Table 3 Filtering results for the first test site

	5x5 Window			
	<i>MeanDif</i>	<i>StdDif</i>	<i>Correlation</i>	<i>Q</i>
Original (FirstSite)	-	-	-	1
Mean	0	0.98	0.64	2.97
Median	0.09	0.92	0.64	2.65
Lee	0.01	1.19	0.73	2.8
Lee-Sigma	0.3	0.82	0.81	2.15
Frost	0.01	0.9	0.74	2.64
Local Region	0.13	0.63	0.53	1.8
Gamma-MAP	0.84	1.1	0.8	2.67

When the second agricultural test site was examined, it was observed that the Lee and Gamma-MAP filters provided the highest results relative to the other filtering methods (Table 4). The Lee filter preserves the mean of the original image while the mean value of the Gamma-MAP filter was rather low (5.34) from the original value. The highest Q values of 2.46 and 2.67 were computed for the Gamma-MAP and Lee filters, respectively. The results of the Lee and Gamma-MAP filters were followed by the Mean

and the Median filters. Except for the mean values of the filters, the other indicators were provided similar results. The mean value of the Mean filter was exhibited similar result with the original image (6.02) while the result of the mean value (5.92) for the Median filter was found low. Acceptable results were achieved by the Frost filter. The values of the Lee-Sigma filter were found to be less efficient. Similar to the first agricultural test site, the worst results were found for the Local Region filtering method. The correlation and the Q values were computed as 0.58 and 2.67, respectively.

Table 4 Filtering results for the second test site

	5x5 Window			
	<i>MeanDif</i>	<i>StdDif</i>	<i>Correlation</i>	<i>Q</i>
Original (Second Site)	-	-	-	1
Mean	0	0.91	0.68	2.25
Median	0.1	0.87	0.68	2.35
Lee	0.01	0.88	0.76	2.46
Lee-Sigma	0.28	0.78	0.81	1.97
Frost	0.01	0.83	0.77	2.03
Local Region	0.17	0.6	0.58	1.46
Gamma-MAP	0.68	1.19	0.81	2.67

The third site consists of pixels that are located on the Ulubat Lake which represents a more homogenous area than the other test sites. Therefore, the comparison of the filters using this site can be more realistic than the others. When the third site was examined, it was observed that similar to the first and the second agricultural test sites the Lee filter was superior to the other filtering methods (Table 5). It was provided a better preservation of the mean value (1.99) and a high StdDif (0.31) value. While the correlation value of the Lee filtered image was computed as 0.56, the Q value of it was found rather high (2.82). Acceptable results were obtained for the Mean and the Median filters although their correlation values were computed low (0.45). The Frost and the Gamma-MAP filters were also found effective. The Lee-Sigma and Local Region filters exhibited the poorest results when compared with the other filtering methods. The Lee-Sigma filter provided relatively high correlation value (0.71) and its Q value was found to be 1.67. The correlation value of the Local Region filter was computed as 0.41 while the Q value of this filter was 1.71.

Table 5 Filtering results for the third test site

	5x5 Window			
	<i>MeanDif</i>	<i>StdDif</i>	<i>Correlation</i>	<i>Q</i>
Original (Lake Site)	-	-	-	1
Mean	-0.03	0.34	0.44	3.17
Median	-0.01	0.33	0.45	3.09
Lee	-0.01	0.31	0.56	2.82
Lee-Sigma	0.16	0.12	0.76	1.67
Frost	-0.01	0.27	0.65	2.38
Local Region	0.03	0.19	0.41	1.72
Gamma-MAP	0.09	0.32	0.56	2.71

CONCLUSION

Aim of this paper is to examine the most widely used filtering methods and to decide the best method for agricultural areas. Three different test sites consisting of two agricultural areas and a small part of lake were selected to apply the filtering performances. The filtered products were evaluated based on the MeanDif, StdDif, Correlation, and Q indicators. The numerical results indicated that the Lee filter performs much better for preserving the spectral characteristics of the original image while reducing the speckle. The results of the Mean, Median, Gamma-MAP and Frost filters were found satisfactory. The Lee-Sigma filter could not provide similar results with the Lee filter and the results of those filters were found low. The poorest results were obtained for the Local Region filter. Although the analyses exhibited consistent results for three test sites, further quantitative evaluations (e.g. edge preserve, texture) should be added to the analyses in order to examine the filtering methods more reliably.

REFERENCES

- Frost, V. S., J. A. Stiles, K. S. Shanmugan and J. C. Holtzman, 1982. A model for radar images and its application to adaptive digital filtering of multiplicative noise, *IEEE Transactions on Geosciences and Remote Sensing*.
- Herold, N. D., B. N. Haack and E. Solomon, 2005. Radar spatial considerations for land cover extraction, *International Journal of Remote Sensing*, 26(7):1383-1401.

Karathanassi, V., P. Kolokousis, and S. Ioannidou, 2007. A comparison study on fusion methods using evaluation indicators, *International Journal of Remote Sensing*, 28, 2309-2341.

Kuan D. T., A. A. Sawchuck, T. C. Strand, and P. Chavel, 1985. Adaptive noise smoothing filter for images with signal-dependent noise, *IEEE Transactions on Pattern Analysis and Machine Intelligence*, 7(2):165 -177.

Lee, J. S., 1980. Digital image enhancement and noise filtering by use of local statistics, *IEEE Transactions on Pattern Analysis and Machine Intelligence*, 2(2):165-168.

Lillesand, M., R. W. Kiefer, J. W. Chipman, 2004, Remote Sensing and Image Interpretation, *Fifth Edition, John Wiley and Sons, Inc., USA*.

Lopes, A., R. Touzi and E. Nezry, 1990. Adaptive speckle filters and scene heterogeneity, *IEEE Transactions on Geosciences and Remote Sensing*, 28(6):992-1000.

Serkan, M, N. Musaoglu, H. Kirkici, and C. Ormeci, 2008. Edge and fine detail preservation in SAR images through speckle reduction with an adaptive mean filter, *International Journal of Remote Sensing*, 29(23):6727- 6738.

Tso, B. and P. Mather, 1999. Crop discrimination using multi-temporal SAR imagery, *International Journal of Remote Sensing*, 20():2443-2460.

APPENDIX E

ORTALAMA KAYDIRMA VE BERKELEY GÖRÜNTÜ SEGMENTASYON (BIS) YÖNTEMLERİNİN ÇOK ZAMANLI KOMPSAT-2 GÖRÜNTÜLERİ KULLANILARAK DEĞERLENDİRİLMESİ

Proceeding: Published in UZAL CBS 2010, Kocaeli, Turkey

A. Özdarıcı¹, N. Clinton², Z. Akyürek³

¹Orta Doğu Teknik Üniversitesi, Jeodezi ve Coğrafi Bilgi Teknolojiler Bölümü EABD,
06531, Çankaya, Ankara. ozdarici@metu.edu.tr

²NASA Ames Araştırma Merkezi, Moffett Field, California.
nicholas.clinton@gmail.com

³Orta Doğu Teknik Üniversitesi, İnşaat Mühendisliği Bölümü, 06531, Çankaya, Ankara.
zakyurek@metu.edu.tr

ÖZET

Bu çalışmada iki önemli görüntü segmentasyon yöntemine, Ortalama Kaydırma (Mean-Shift) ve Berkeley Görüntü Segmentasyon (Berkeley Image Segmentation – BIS), ait sonuçlar vektör tabanlı çok sayıda ölçüm tekniği kullanılarak değerlendirilmiş ve bu anlamda oluşan boşluğun doldurulmasına katkı sağlanması hedeflenmiştir. Bu amaçla Bursa’da yer alan Karacabey Ovası üzerinde Haziran, Temmuz ve Ağustos 2008 tarihlerinde çektilen keskinleştirilmiş Kompsat-2 uydu görüntüleri kullanılmıştır. Segmentasyon işlemi öncesinde çok zamanlı görüntülere ait bantlara Ana Bileşenler Dönüşümü uygulanmıştır. Analizlerde Ortalama Kaydırma ve BIS yöntemleri için çeşitli parametre bileşenleri kullanılmıştır. Elde edilen segmentlerin değerlendirme işlemi sırasında önceden belirlenmiş örnek alanlar sayesinde her bir segment üzerinde alan ve konum tabanlı 14 farklı doğruluk ölçme tekniği kullanılarak örnek alanlar ve segmentler arasında konum ve şekil benzerliği bulmaya yarayan hesaplamalar yapılmıştır. Bu hesaplamalara bağlı

olarak her iki yöntem için de en yüksek doğruluğa sahip olan görüntü segmentasyon sonuçları karşılaştırılarak değerlendirilmiştir. Elde edilen bulgular, her iki yöntem için belli parametre bileşenleri ile elde edilen sonuçların görüntüleri oluşturan nesnelere saptamakta uygun olduğunu bunun yanında Ortalama Kaydırma görüntü segmentasyon yönteminin BIS yönteminden daha etkili sonuçlar sergilediğini göstermiştir.

Anahtar Sözcükler: Görüntü Segmentasyonu, Ortalama Kaydırma Yöntemi, Berkeley Görüntü Segmentasyonu, Yüksek Mekânsal Çözünürlük, Doğruluk Analizi

AN EVALUATION OF MEAN-SHIFT AND BERKELEY IMAGE SEGMENTATION METHODS USING MULTI-TEMPORAL KOMPSAT-2 IMAGES

This study focuses on examining the results of two image segmentation methods, Mean-Shift and Berkeley Image Segmentation (BIS), by comparing it based on both area-based and location-based measures on an agricultural site. The test site (~10 km²) was selected from an important agricultural area, Karacabey Plain (Bursa), located in north-west of Turkey. Three Kompsat-2 images taken on June, July and August (2008) were used in the analyses by applying a Principle Component Analysis technique on the image bands. Multiple parameter combinations for Mean-Shift and BIS were tested and the resulting segments were evaluated using goodness measures that measure the shape similarity between the segments and training polygons. Results indicated that although some parameter combinations of each method provide efficient outputs based on the computations of goodness measures, Mean-Shift segmentation method provided more superior results than BIS.

Keywords: *Image Segmentation, Mean-Shift, BIS, High Spatial Resolution, Accuracy Assessment*

1.GİRİŞ

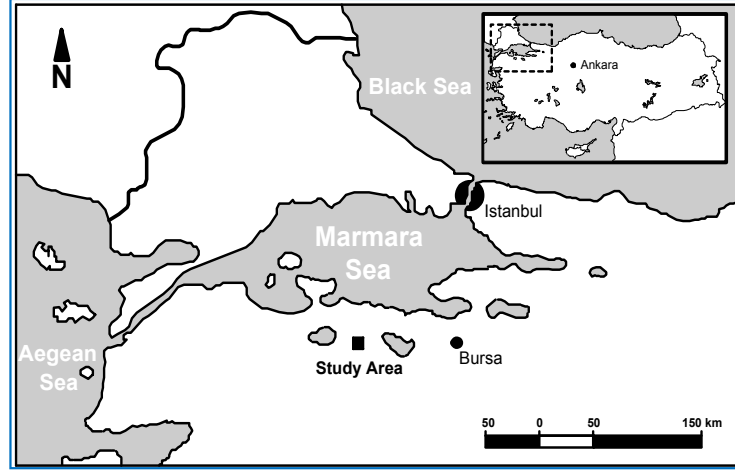
Uydu teknolojilerindeki gelişmelere paralel olarak elde edilen görüntülere ait mekânsal çözünürlüğün artması, nesne içine düşen piksel değerlerindeki çeşitliliği arttırmış ve bu etki, geleneksel piksel tabanlı görüntü analizlerini negatif yönde etkilemiştir. Bu durum, uzaktan algılama çalışmalarında nesne tabanlı görüntü analizlerine olan önemin artmasına neden olmuştur (örn. De Wit ve Clever 2004). Nesne tabanlı görüntü analizlerinin ilk basamağını *görüntü segmentasyonu* oluşturur. Görüntü segmentasyonu, birbirine komşu olan pikseller arasındaki homojenlik bilgisini araştırarak görüntüyü anlamlı parçalara bölme işlemidir (Cheng vd. 2001). Bu işlem sonucunda elde edilen her bir segment, görüntüyü oluşturan nesnelere tanımlanmasında kullanılır. Görüntü segmentasyonu yöntemiyle görüntüye ait nesnelere elde etme işlemi nesne tabanlı görüntü analizlerinin önemli bir basamağını oluşturur. Bu konuda algoritma geliştirme ve bu algoritmaların çeşitli amaçlara yönelik kullanımıyla ilgili çok sayıda çalışmaya rastlamak mümkündür (örn. Schoenmakers vd., 1994; Cheng, 1995; Rydberg and Borgefors, 2001; Mueller vd., 2003; Martin vd., 2004; Zhan vd., 2005; Lee and Warner 2006; Chen vd., 2006; Li and Xiao., 2007; Lu vd., 2007; Wang vd., 2010; Xiao vd., 2010; Corcoran vd., 2010).

Literatürde bu amaca yönelik birçok çalışma bulunmasına rağmen hala etkili yöntemlere ve ek analizlere ihtiyaç olduğu gözlenmektedir. Bunun nedeni segmentasyon algoritmaları sonucunda üretilen segmentlere ait doğruluk analizlerinin tek bir kritere dayandırılarak yapılmasıdır (Liu and Yang, 1994; Zhang, 1996; Zhang, 2001; Martin vd., 2001; Ge vd., 2006; Chabrier vd., 2006; Li and Xiao, 2007). Fakat üretilen segmentlerin referans nesnelere göre her yönden etkili bir şekilde değerlendirilebilmesi için tek değerlendirme kriterinin yeterli olmadığı (Zhang, 2001, Clinton et al. 2010) ve bu nedenle farklı değerlendirme yöntemlerine ihtiyaç olduğu açıktır (örn. Zhang 1996; Chabrier vd. 2006; Radoux and Defourny, 2007; Corcoran vd. 2010).

Segmentasyon sonuçlarının değerlendirilmesinde kullanılan istatistiksel yöntemler nesne tabanlı görüntü analizlerinin önem verdiği bir konudur. Bu nedenle çalışmada, Ortalama Kaydırma ve Berkeley Görüntü Segmentasyon yöntemi adıyla anılan iki farklı segmentasyon sonucunun bir tarım alanı üzerinde farklı doğruluk ölçüm teknikleri kullanılarak incelenmesi konu edilmiştir. İlk olarak; uydu görüntüsü ve çalışma alanının tanıtılmasının ardından Ortalama Kaydırma ve Berkeley Görüntü Segmentasyon yöntemleri açıklanmaktadır. İkinci aşamada elde edilen segmentasyon sonuçlarını değerlendirme yöntemleri tanıtılmaktadır. Tartışma ve sonuç bölümlerinde çalışma alanı için bulunan segmentasyon sonuçları, değerlendirme yöntemleri yardımıyla test edilerek tartışılmaktadır. Son olarak çalışmanın içeriği ile birlikte genel sonuçlar verilmektedir.

1.1 Çalışma Alanı

Çalışma alanı, Türkiye'nin kuzeybatısına düşen Marmara bölgesindeki Karacabey Ovası (Bursa) olarak belirlenmiştir (Şekil 1). Bu çalışma için Karacabey Ovası'nın yaklaşık 10 km² lik bir kısmı kullanılmıştır. Alan, zengin toprak yapısı ve ikliminin tarıma elverişli olması nedeniyle Türkiye'nin en verimli ovaları arasında yer almaktadır. Alanda başta mısır, biber, bezelye, buğday, pirinç ve şeker pancarı olmak üzere çeşitli ürünler yetiştirilmektedir (Özdarıcı, 2005).



Şekil 1. Çalışma alanı

1.2 Veri Seti

Çalışma alanında yetiştirilen ürünlere ait segmentleri bulmak için Haziran, Temmuz ve Ağustos (2008) tarihlerinde çekilmiş pankromatik (1m) ve renkli (4m) Komsat-2 uydu görüntüleri kullanılmıştır. Görüntülerin farklı aylarda çekilmesinin nedeni ürünlere ait ekim, büyüme, olgunlaşma ve hasat dönemleri ile ilgili bilgiler elde ederek segmentasyon işlemini kolaylaştırmaktır. Komsat-2 uydusu 1 m çözünürlükte pankromatik ve 4m çözünürlükte renkli görüntü sağlamaktadır. Renkli görüntü; mavi, yeşil, kırmızı ve yakın kızıl ötesi olmak üzere dört banttan oluşmaktadır. Bu bantlara ait spektral aralık sırasıyla 0.45-0.52, 0.52-0.60, 0.63-0.69 ve 0.76-0.90 μm değerleri arasındadır. Pankromatik görüntüye ait spektral aralık ise 0.50-0.90 μm dır. Komsat-2 görüntüsüne ait işlem düzeyi 2A dır. Bu düzeyde görüntü radiometrik olarak düzeltilmiş ve yer kontrol noktası (YKN) kullanılmaksızın geometrik düzeltme işlemi standart harita projeksiyonu (UTM WGS 84) na göre yapılmıştır.

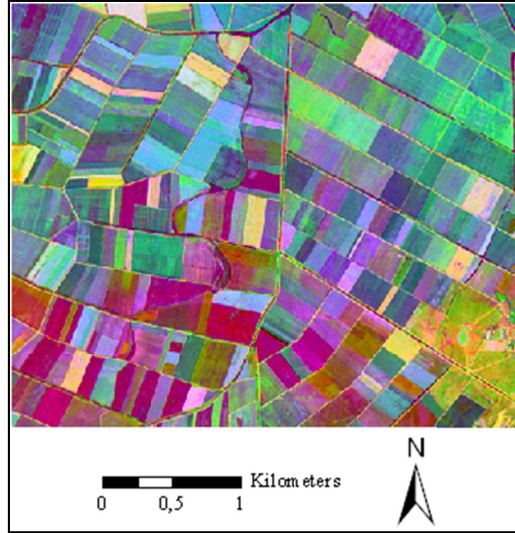
Elde edilen segmentlere ait doğruluk analizlerinin yapılabilmesi için referans olacak bir veri setine ihtiyaç vardır. Bu veri alanda bulunan parsel sınır bilgilerini içeren vektör veridir. Veri tabanında her bir parsel için ayrı numaralar verilerek aylara ait ürün bilgileri tanımlanmıştır. Vektör veri, alana ait 1:5.000 ölçekli kadastral haritalar kullanılarak Gauss-Kruger (Zone-5) ve Avrupa Datumu (1950) na göre sayısallaştırılmıştır (Turker ve Arıkan 2005). Vektör veri bu çalışmada, elde edilen segmentler ile gerçek parseller

arasındaki şekil benzerliklerini ölçmek amacıyla görüntü çekim tarihleri ile eş zamanlı olarak güncellenmiştir.

2. YÖNTEM

2.1 Ön İşlemler

Çalışmada kullanılacak verilerin birbirleri ile uyumunu sağlamak amacıyla verilere bir dizi ön işlem uygulanmıştır. İlk olarak, aynı aya ait pankromatik ve renkli Kompsat-2 görüntüleri ‘*En Küçük Kareler*’ görüntü keskinleştirme algoritması kullanılarak üç farklı yüksek çözünürlüklü renkli görüntü elde edilmiştir (Özdarıcı ve Akyürek 2009). İkinci aşamada 1:25.000 ölçekli sayısal haritalardan elde edilen Sayısal Arazi Yükseklik Modeli (SYM) yardımıyla keskinleştirilmiş görüntülerin hassas geometrik düzeltme işlemi gerçekleştirilmiştir. Bu amaçla üç görüntü için belirgin noktalardan toplanmış YKN ler kullanılmıştır. Bu işlemler sonucunda ortalama hata bir pikselin altında hesaplanmıştır. Bir sonraki aşamada farklı aylara ait keskinleştirilmiş renkli görüntülere ait bantlar bir araya getirilerek tüm bantlar üzerinde ‘*Ana Bileşenler Dönüşümü*’ uygulanmıştır (Şekil 2).



Şekil 2. Ana Bileşenler Dönüşümü uygulanmış Kompsat-2 görüntüsü

2.2 Ortalama Kaydırma Yöntemi

Ortalama Kaydırma yönteminin temeli, filtre yardımıyla yoğunluk tahmini yapmaya dayanır. Yöntem, filtre içine düşen piksellere ait ortalama değeri hesaplayarak filtreye ait gerçek merkezin hesaplanan yoğunluk merkezine kaydırılmasını içerir ve özetle şu şekilde tanımlanabilir:

“d” boyutlu R^d uzayında bulunan n nokta için x_i vektörü ($i = 1 \dots n$) verilsin. Herhangi bir K kerneli kullanılarak çok değişkenli Ortalama Kaydırma vektörü - $m_K(x)$ aşağıdaki formülle hesaplanır (Comaniciu ve Meer, 2002):

$$m_K(x) \equiv \frac{\sum_{i=1}^n x_i K\left(\frac{x-x_i}{h}\right)}{\sum_{i=1}^n K\left(\frac{x-x_i}{h}\right)} - x \quad (1)$$

Formülde kullanılan x , K filtresinin merkez noktası, h ise kullanılan filtrenin boyutunu tanımlamaktadır. Önemli modların bulunabilmesi için formülün (1), segmentasyonu yapılacak uzayı kapsayana kadar birden çok defa tekrarlanması gerekmektedir.

$$m_K(x) = h^2 \frac{\hat{\nabla} f_K(x)}{\hat{f}_K(x)} \quad (2)$$

Ortalama Kaydırma vektörü her zaman öznitelik uzayında var olan dağılımın en çok artan yönünü göstermektedir. Yine aynı formülden anlaşılabilceği üzere, filtrenin merkezi, yine aynı filtrenin içine düşen noktaların yoğun olduğu bölgeye doğru kaydırılmaktadır. Ortalama Kaydırma vektörü yerel eğim (gradient) tahmini ile uyduğu sürece, öznitelik uzayında var olan dağılımın durağan noktalarına (*stationary points*) kadar bir yol izleyebilir. Öznitelik uzayının modları ise bu durağan noktalardır. Dolayısıyla Ortalama Kaydırma işlemi iki basamaklı bir tekrar olduğu söylenebilir:

- $m_K(x)$ vektörün hesaplanması
- $K(x)$ kernelinin $m_K(x)$ kadar ötelenmesi

Bu yöntem ile hesaplanan vektörler her zaman yoğunluğun en fazla olduğu yere doğru hareket eder. Formül 2 deki eşitlik, hesaplanan vektörün filtre yardımıyla elde edilen yoğunluk ile daima doğru orantılı olduğunu göstermektedir.

Yöntemin renkli görüntüler üzerinde de uygulanabilmesi amacıyla *ortak alan (joint domain)* kavramı geliştirilmiştir. Bu kavrama göre her örnek, hem mekânsal uzayda (h_s) hem de renk uzayı (h_r) nda tanımlanır. Ortak alanda mekân ve renk vektörlerine ait farklılıkları gidermek için uygun bir normalizasyon işlemi gerekmektedir. Bu nedenle iki ışımsal simetrik filtre ürünü olan *çok değişkenli filtre (multivariate kernel)* öklid uzayında bant genişliği parametresi olarak kullanılmaktadır.

$$K_{h_s, h_r}(x) = \frac{C}{h_s^2 h_r^p} k\left(\left\|\frac{x^s}{h_s}\right\|^2\right) k\left(\left\|\frac{x^r}{h_r}\right\|^2\right). \quad (3)$$

Formül (3) de; x^s uzaysal kısmı, x^r spektral kısmı, h_s ve h_r uzaysal ve spektral kısımlar için uygulanan filtre boyutlarını ve C ise tanımlanacak olan normalizasyon katsayısını belirtmektedir (Comaniciu ve Meer, 2002).

Bu çalışmada segmentasyon işlemi, görüntülere *Ana Bileşenler Dönüşümü* uygulandıktan sonra gerçekleştirilmiştir. Segmentasyon işlemlerinde mekansal (h_s) değişkeni için {2, 3, 4, 5, 6, 7, 8, 9, 10} ve renk (h_r) değişkeni için {0.5, 1, 1.5, 2, 2.5, 3, 3.5, 4, 4.5, 5} değerleri kullanılmıştır. En küçük alan parametresi bu çalışma için 1000 piksel olarak belirlenmiştir. En küçük alan değişkeni, alanda bulunan en küçük parsel içine düşen piksel sayısını ifade etmektedir. Bu sayede Ortalama Kaydırma yöntemi ile segment edilecek görüntü üzerinde toplam 90 parametre bileşimi test edilmiştir. Tüm bantlara ait segmentleri tek bir katmanda toplamak için segmentasyon işlemi sonucunda elde edilen raster formatındaki katmanlar birbirleri ile çarpılarak 32 bit olarak kaydedilmiştir. Ardından en küçük parsel büyüklüğünden daha küçük alana sahip segmentler uygun işlemlerle elimine edilmiştir. Son olarak, raster formatındaki bant, vektöre dönüştürülerek doğruluk analizlerine hazır hale getirilmiştir.

2.3 Berkeley Görüntü Segmentasyon Yöntemi

Berkeley görüntü segmentasyon yöntemi, Benz vd. (2004) tarafından ortaya çıkarılan alan birleştirme mantığına dayanır. Yöntemin ilk aşamasında her piksel bir alan olarak düşünülür. Pikseller, spektral homojenlik ve şekil kriterlerine bağlı olarak birleştirilir veya farklı nesnelere olarak tanımlanır. Yöntemde her bir nesne (piksel) birbirinin sürekli komşusu olarak düşünülmektedir. a ve b şeklinde birbirine komşu olan iki nesne düşünüldüğünde bu iki nesnenin olası bileşimi ab birleşik (*merged*) nesne olarak kabul edilir. Birleşik nesneye ait spektral heterojenlik (h_p) aşağıdaki eşitlikle ifade edilir.

$$\Delta h_p = \sum_I w_i (n_{ab} \sigma_{i,ab} - (n_{ab} \sigma_{i,a} + n_b \sigma_{i,b})) \quad (4)$$

Eşitlikteki,

I bant ağırlığını,

n bir pikselin kapladığı alanı,

σ_i görüntüye ait bantlardaki nesnelere için standart sapmayı ifade etmektedir.

Nesnelere ait yumuşaklık (Δh_s) ve yoğunluk (Δh_p) farkı aşağıdaki şekilde hesaplanmaktadır:

$$\Delta h_c = \frac{n_{ab} l_{ab}}{\sqrt{n_{ab}}} - \frac{n_a l_a}{\sqrt{n_a}} - \frac{n_b l_b}{\sqrt{n_b}}$$

$$\Delta h_s = \frac{n_{ab} l_{ab}}{b_{ab}} - \frac{n_a l_a}{b_a} - \frac{n_b l_b}{b_b}$$

Eşitlikteki;

l nesnenin çevre uzunluğunu,

b nesneyi çevreleyen poligon çevresinin uzunluğunu ifade etmektedir.

Nesnelere arasındaki biçim farklılıklarına ait heterojenlik bilgisi aşağıdaki şekilde açıklanmaktadır:

$$\Delta h_t = w_c \Delta h_c + w_s \Delta h_s,$$

$$0 < w_c, w_s \leq 1, w_c + w_s = 1$$

Eşitlikteki

w_c değeri kullanıcı tarafından seçilen sıklık parametresini,

w_t ise yine kullanıcı tarafından belirlenen yumuşaklık parametresini ifade eder.

Berkeley Görüntü Segmentasyon yönteminde kullanılan ölçek oranı ise aşağıdaki eşitlik yardımıyla hesaplanmaktadır:

$$r = w_p \Delta h_p + w_t \Delta h_t,$$

$$0 < w_p, w_t \leq 1, w_p + w_t = 1$$

Eşitlikte görülen w_t kullanıcı tarafından belirlenen biçim parametresini ifade etmektedir.

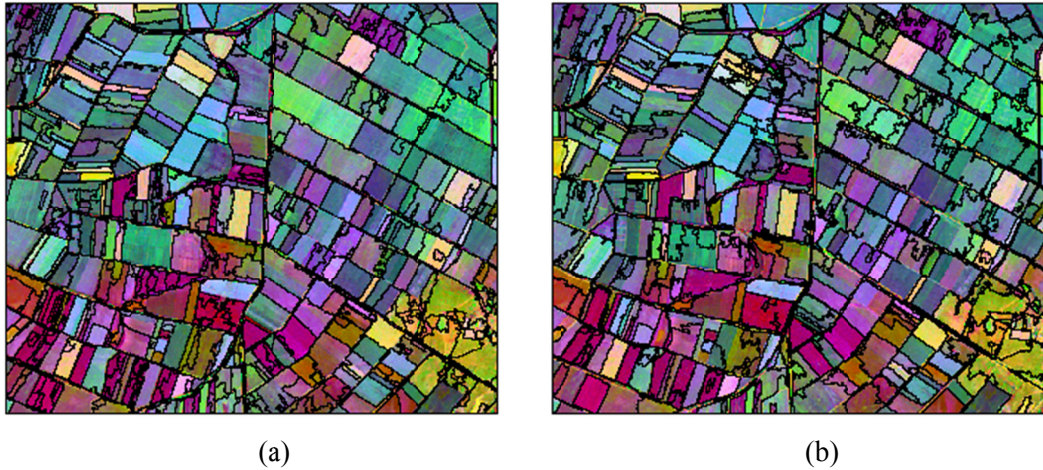
Nesne birleştirme işlemi önceden belirlenmiş ölçek eşik değeri kriteri (T) karşılanana kadar devam eder ($t = 0,1,2,\dots,T$).

2.4 Doğruluk Analizi

Her iki segmentasyon yöntemine ait sonuçların güvenilirliğinin araştırılabilmesi için segmentlere ait çeşitli kriterleri değerlendiren doğruluk testleri yapılmıştır (Clinton vd. 2010). Üretilen segmentlere uygulanan testler Clinton vd. (2010)' ne ait çalışmada detaylı olarak açıklanmaktadır. Bu kriterlerin amacı, elde edilen segmentler ve belirlenmiş örnek alanlar arasında konum ve şekil benzerliklerini çeşitli yönlerden araştırmaktır. Bu amaçla ilk olarak çalışma alanının %10 u kapsayan örnek poligonlar titizlikle belirlenmiş ve örnek poligonlar ile elde edilen segmentler doğruluk analizleri yardımıyla karşılaştırılmıştır. Son olarak, hesaplanan sonuçlar sıralanmış ve en çok kritere sahip segmentasyon sonucu çalışma alanı için en ideal sonuç olarak belirlenmiştir.

3. TARTIŞMA

Çalışmada iki farklı segmentasyon sonucu, örnek alanlara bağlı olarak değerlendirilmiştir. Elde edilen segmentler doğruluk kriterleri yardımıyla örnek alanlar ile karşılaştırılarak segmentler ve örnek alanlar arasında şekil benzerliği aranmıştır. Berkeley Görüntü Segmentasyon yöntemi segmentasyon esnasında çok sayıda parametre bileşimi kullanılarak üretilmiş segmentasyon sonuçlarını örnek alanlara benzerliğine göre otomatik olarak sıralayabilmektedir. Berkeley Görüntü Segmentasyon yöntemi bu işlem için Hsu vd. (2008) ne ait çalışmada adı geçen ‘grid araştırma’ yöntemini kullanmaktadır. Ortalama Kaydırma Segmentasyon yöntemi sonuçları için bu işlem elle yapılmıştır. Bu sayede iki yöntem için elde edilen en iyi sonuçlar birbirleri ile karşılaştırılarak test alanı için hangi segmentasyon yönteminin daha güvenilir olduğuna karar verilmiştir. Elde edilen sonuçlar ve kullanılan parametreler şekil 3’ de verilmektedir.



Şekil 3. (a) Ortalama Kaydırma Segmentasyon Yöntemi ve (b) Berkeley Görüntü Segmentasyon Yöntemi Sonuçları

Doğruluk analizleri sonucunda Ortalama Kaydırma yönteminin Berkeley Görüntü Segmentasyon yöntemine göre daha iyi sonuçlar sergilediği gözlenmiştir. Ortalama kaydırma yöntemi için kullanılan en uygun mekân ve renk değişkenleri sırasıyla h_s : 9 ve h_r : 3 olarak belirlenmiştir. Otomatik sıralama işlemi sonrasında Berkeley Görüntü Segmentasyonu için en ideal parametreler şekil, yoğunluk ve ölçek eşik değeri için sırasıyla s : 0.1, c : 0.9 ve T : 175 olarak belirlenmiştir. Bu değişkenler kullanılarak

ortalama kaydırma yöntemi için segment sayısı 562 olarak hesaplanırken Berkeley Görüntü Segmentasyon işlemi için bu sayının 293 olduğu gözlenmiştir.

Tüm sonuçlar genel olarak incelendiğinde Berkeley Görüntü Segmentasyon yöntemine ait ölçek eşik değerinin artmasıyla elde edilen segment sayısının ters orantılı olarak düştüğü gözlenmiştir. Diğer bir ifade ile ölçek eşik değerinin artması iki ya da daha fazla parselde ait segmentlerin birbirleri ile birleşmesine neden olmaktadır (*over-segmentation*). Diğer taraftan segmentasyon işleminde çok küçük mekânsal ve renk değişkenleri (h_s , h_r) kullanılmasının gereğinden fazla küçük segmentlere yol açtığı gözlenmiştir (*under-segmentation*).

4. SONUÇLAR

Segmentasyon sonuçlarının örnek alanlara göre detaylı olarak değerlendirilmesi sadece güvenilir segmentasyon sonuçları üretmeye yardımcı olmakla kalmayıp aynı zamanda var olan segmentasyon algoritmalarının iyileştirilmesinde önemli bir süreçtir (Zhang 1996; Clinton vd. 2010). Bu çalışmada çeşitli parametrelerle elde edilen segmentasyon sonuçlarının örnek alanlar ile olan konum ve alan tabanlı uyumu geniş bir çerçevede incelenmiştir. Segmentasyon sonuçlarının birden çok doğruluk ölçüm tekniği ile değerlendirilmesinin nedeni üretilen segment kalitesinin çeşitli faktörlerden etkilenmesidir (Zhan vd. 2005).

Üretilen segmentler doğruluk ölçütlerine göre sıralandıktan sonra her iki yönteme ait en uygun segmentasyon sonuçları doğruluk ölçütlerine göre birbirleri ile de karşılaştırılmıştır. Bu incelemeler ışığında Ortalama Kaydırma Yönteminin çalışma alanı için en ideal segmentasyon sonucunu ürettiğini göstermiştir. Ortalama Kaydırma Yöntemi en ideal sonucu sağlamasına rağmen üretilen bazı segmentlerde hala hatalar (*over-segmentation* ve *under-segmentation*) olduğu gözlenmiştir.

Tarım ürünlerinin uydu görüntülerinden tespit edilmesinde çok zamanlı görüntü kullanımı analizlerde daha güvenilir sonuçlar almak açısından önemlidir (De Wit ve Clevers 2004). Bununla birlikte segmentasyon işlemi öncesinde ve sonrasında yapılacak analizlerin de kaliteli segmentler üretmedeki başarısı da göz ardı edilmemesi gereken diğer bir noktadır (Zhang 1996).

Segmentasyon işlemi sonucunda üretilen sonuçların doğruluk kriterlerine göre otomatik olarak sıralanması doğruluk analizlerindeki olası insan faktörünü büyük ölçüde azaltacaktır. Bu nedenle yeni geliştirilecek segmentasyon yöntemlerinde bu durumun göz önünde bulundurulması araştırmacılara yarar sağlayacaktır.

Teşekkür

Bu çalışma Türkiye Bilimsel ve Teknolojik Araştırma Kurumu (TÜBİTAK) tarafından desteklenmiştir. Çalışmada kullanılan Kompsat-2 uydu görüntüleri Orta Doğu Teknik Üniversitesi (ODTÜ), Jeodezi ve Coğrafi Bilgi Teknolojileri EABD tarafından ODTÜ'ye sunulan DAP-2008-07-02-07 proje bütçesinden temin edilmiştir.

KAYNAKLAR

Benz U.C., Hofmann P., Willhauck G., Lingenfelder I., ve Heynen M., 2004, Multi-resolution, object-oriented fuzzy analysis of remote sensing data for GIS-ready information, *ISPRS Journal of Photogrammetry & Remote Sensing*, (58), 239-258.

Chabrier S., Emile B., Rosenberg C. ve Laurent H., 2006, Unsupervised performance evaluation of image segmentation. *EURASIP Journal on Applied Signal Processing*, article id:96306, pp.1-12.

Chen Z., Zhao Z., Gong P. ve Zeng B., 2006, A new process for the segmentation of high resolution remote sensing imagery, *International Journal of Remote Sensing*, 27 (22), 4991-5001.

Cheng, H.D., Jiang X. H., Sun Y., Wang J., 2001, Color image segmentation: advances and prospects, *Pattern Recognition*, (34), 2259-2281.

Cheng Y. 1995, Mean shift, mode seeking, and clustering, *IEEE Transactions on Pattern Analysis and Machine Intelligence*, 17(8),790-799.

Clinton N., Holt A., Scarborough J., Yan Li., ve Gong P.. 2010, Accuracy assessment measures for object-based image segmentation goodness, *Photogrammetric Engineering & Remote Sensing*, 76(3), 289-299.

Comaniciu D. ve Meer P., 2002, Mean shift: a robust approach toward feature space analysis, *IEEE Transactions on Pattern Analysis and Machine Intelligence*, 24(5),603-619.

Corcoran P., Winstanley A. ve Mooney P., 2010, Segmentation performance evaluation for object-based remotely sensed image analysis. *International Journal of Remote Sensing*, 31(3),617-645.

De Wit A. J. W. ve Clevers J. G. P. W., 2004, Efficiency and accuracy of per-field classification for operational crop mapping, *International Journal of Remote Sensing*, 25 (20), 4091-4112.

Hsu, Chih-Wei, Chih-Chung Chang, ve Chih-Jen Lin, 2008, A Paractical Guide to Support Vector Classification. URL: <http://www.csie.ntu.edu.tw~cjlin/papers/guide.pdf> (10.05.2010).

Ge F., Wang S. ve Liu T., 2006, Image-segmentation evaluation from the perspective of salient object extraction, *Proceedings of the Computer Society Conference on Computer Vision and Pattern Recognition (CVPR'06)*.

Lee, J.Y., ve Warner T.A., 2006, Segment based image classification, *International Journal of Remote Sensing*, 27(16),3403-3412.

Li P. and Xiao X., 2007, Multispectral image segmentation by a multichannel watershed-based approach, *International Journal of Remote Sensing*, 28(19),4429-4452.

Liu J. ve Yang Y-H., 1994, Multi-resolution color image segmentation, *IEEE Transactions on Pattern Analysis and Machine Intelligence*, 16(7),689-700.

Lu, S., Oki K., Shimizu Y. ve Omasa K., 2007, Comparison between several feature

extraction methods for mapping complicated agricultural land patches using airborne hyperspectral data, *International Journal of Remote Sensing*, 28(5), 963-984.

Martin D., Fowlkes C., Tal D., Malik J., 2004, Learning to detect natural image boundaries using local brightness, color and texture, *IEEE Transaction on Pattern Analysis and Machine Intelligence*, 26(5),530-549.

Mueller M., Segl K. ve Kaufmann H., 2003, Extracting characteristic segments in high-resolution panchromatic imagery as basic information for objects-driven image analysis, *Can. J. Remote Sensing*, 29(4), 453-457.

Özdarıcı, A. 2005, “Comparison of Different Spatial Resolution Images for Polygon-Based Crop Mapping”, MSc. Thesis, Middle East Technical University, Turkey.

Özdarıcı A. ve Akyürek Z., 2009, Evaluating the contribution of image fusion methods into the classification accuracies of agricultural lands. *Proceeding of Türkiye Ulusal Fotogrammetri ve Uzaktan Algılama Birliği V. Teknik Sempozyumu (TUFUAB)*, Turkey.

Radoux J. ve Defourny P., 2007, A quantitative assessment of boundaries in automated forest stand delineation using very high resolution imagery, *Remote Sensing of Environment*, (110),468-475.

Rydberg A. ve Borgefors G., 2001, Integrated method for boundary delineation of agricultural fields in multispectral satellite images, *IEEE Transactions on Geoscience and Remote Sensing*, 39(11), 2514-2520.

Schoenmakers, R.P.H.M., van Leeuwen H.J.C., G.G. Lemoine ve E. Nezry., 1994, Segmentation of combined high resolution optical and radar imagery for the determination of field inhomogenities, *Proceeding of IEEE*, pp.2137 – 2139.

Türker M. ve Arıkan M., 2005, Sequential masking classification of multi-temporal landsat7 ETM+ images for field-based crop mapping in Karacabey, Turkey, *International Journal of Remote Sensing*, 26 (17),3813-3830.

Xiao P., Feng X., An R. ve Zhao S., 2010, Segmentation of multispectral high-resolution satellite imagery using log gabor filters. *International Journal of Remote Sensing*, 31 (6),1427-1439.

Wang L., Gong P., Ying Q., Yang Z., Cheng X. and Ran Q.. 2010, Settlement extraction in the north china plain using landsat and Beijing-1 multispectral data with an improved watershed segmentation algorithm, *International Journal of Remote Sensing*, 31 (6),1411-1426.

Zhan Q., Molenaar M., Tempfli K. ve Shi. W., 2005, Quality assessment for geo-spatial objects derived from remotely sensed data. *International Journal of Remote Sensing*, 26(14), 2953-2974.

Zhang Y.J.1996. A survey on evaluation methods for image segmentation, *Pattern Recognition*, 29(8), 1335-1346.

Zhang Y. J. 2001. A review of recent evaluation methods for image segmentation, *International Symposium on Signal Processing and its Applications (ISSPA)*, Kuala Lumpur, Malaysia, 13-16 August.

APPENDIX F

SIGNATURE SEPARABILITY VALUES

Table F.1 The matrices of Bhattacharya distance for three-band, *blue, green, red*, of the Kompsat-2 MS images taken in June, July, and August (a, c, e), with the Envisat ASAR data (b, d, f).

Three-band Kompsat-2 MS image (blue, green, red) taken in June

Class Names	Corn	Tomato	Rice	Sugar beet	Wheat
Tomato	1.91				
Rice	1.32	1.62			
Sugar beet	1.99	1.87	1.83		
Wheat	1.89	1.50	1.45	1.94	
Grass Land	1.32	0.90	0.50	1.71	1.16
Average Separability: 1.53					
Signature pair with Minimum Separability: Rice, Grass Land					

(a)

Three-band Kompsat-2 MS image (blue, green, red) with Envisat ASAR data taken in June

Class Names	Corn	Tomato	Rice	Sugar beet	Wheat
Tomato	1.92				
Rice	1.44	1.67			
Sugar beet	1.99	1.92	1.89		
Wheat	1.90	1.52	1.51	1.96	
Grass Land	1.37	1.26	0.66	1.94	1.24
Average Separability: 1.61					
Signature pair with Minimum Separability: Rice, Grass Land					

(b)

Table F.1 (Cont'd)

Three-band Kompsat-2 MS image (blue, green, red) taken in July

Class Names	Corn	Tomato	Rice	Sugar beet	Wheat
Tomato	0.78				
Rice	1.73	1.82			
Sugar beet	1.96	1.74	1.95		
Wheat	1.89	1.99	1.99	2.00	
Grass Land	1.65	1.91	1.99	1.99	1.46
Average Separability: 1.79					
Signature pair with Minimum Separability: Corn, Tomato					

(c)

Three-band Kompsat-2 MS image (blue, green, red) with Envisat ASAR data taken in July

Class Names	Corn	Tomato	Rice	Sugar beet	Wheat
Tomato	0.93				
Rice	1.78	1.83			
Sugar beet	1.96	1.74	1.96		
Wheat	1.94	1.99	1.99	2.00	
Grass Land	1.76	1.96	1.99	1.99	1.47
Average Separability: 1.82					
Signature pair with Minimum Separability: Corn, Tomato					

(d)

Three-band Kompsat-2 MS image (blue, green, red) taken in August

Class Names	Corn	Tomato	Rice	Sugar beet	Wheat
Tomato	1.45				
Rice	1.20	1.25			
Sugar beet	1.76	0.99	0.85		
Wheat	1.99	1.89	1.99	1.99	
Grass Land	1.99	1.46	1.99	1.99	1.06
Average Separability: 1.59					
Signature pair with Minimum Separability: Rice, Sugar beet					

(e)

Table F.1 (Cont'd)

Three-band Kompsat-2 MS image (blue, green, red) with Envisat ASAR data taken in August

Class Names	Corn	Tomato	Rice	Sugar beet	Wheat
Tomato	1.56				
Rice	1.23	1.42			
Sugar beet	1.79	1.02	1.18		
Wheat	1.99	1.96	1.99	1.99	
Grass Land	1.99	1.90	1.99	1.99	1.20
Average Separability: 1.68					
Signature pair with Minimum Separability: Tomato, Sugar beet					

(f)

Table F.2 The matrices of Bhattacharya distance for three-band, *green, red, NIR* of the Kompsat-2 MS images taken in June- July-August (a, c, e), with Envisat ASAR data (b, d, f).

Three-band Kompsat-2 MS image (green, red, NIR) taken in June

Class Names	Corn	Tomato	Rice	Sugar beet	Wheat
Tomato	1.89				
Rice	1.99	1.99			
Sugar beet	1.99	1.89	1.98		
Wheat	1.97	1.46	1.90	1.95	
Grass Land	1.47	1.17	1.97	1.80	1.49
Average Separability: 1.79					
Signature pair with Minimum Separability: Tomato, Grass Land					

(a)

Table F.2 (Cont'd)

Three-band Kompsat-2 MS image (green, red, NIR) with Envisat ASAR data taken in August

Class Names	Corn	Tomato	Rice	Sugar beet	Wheat
Tomato	1.90				
Rice	1.99	1.99			
Sugar beet	1.99	1.93	1.99		
Wheat	1.97	1.49	1.91	1.97	
Grass Land	1.51	1.38	1.98	1.95	1.52
Average Separability: 1.83					
Signature pair with Minimum Separability: Tomato, Grass Land					

(b)

Three-band Kompsat-2 MS image (green, red, NIR) taken in July

Class Names	Corn	Tomato	Rice	Sugar beet	Wheat
Tomato	0.89				
Rice	1.73	1.88			
Sugar beet	1.99	1.80	2.00		
Wheat	1.99	1.99	2.00	2.00	
Grass Land	1.91	1.95	1.99	1.99	1.38
Average Separability: 1.83					
Signature pair with Minimum Separability: Corn, Tomato					

(c)

Three-band Kompsat-2 MS image (green, red, NIR) with Envisat ASAR data taken in July

Class Names	Corn	Tomato	Rice	Sugar beet	Wheat
Tomato	1.03				
Rice	1.78	1.89			
Sugar beet	1.99	1.81	2.00		
Wheat	1.99	1.99	2.00	2.00	
Grass Land	1.93	1.98	1.99	1.99	1.41
Average Separability: 1.85					
Signature pair with Minimum Separability: Corn, Tomato					

(d)

Table F.2 (Cont'd)

Three-band Kompsat-2 MS image (green, red, NIR) taken in August

Class Names	Corn	Tomato	Rice	Sugar beet	Wheat
Tomato	1.49				
Rice	1.41	0.91			
Sugar beet	1.78	0.62	0.82		
Wheat	1.99	1.87	1.99	1.99	
Grass Land	1.99	1.63	1.99	1.99	0.88
Average Separability: 1.56					
Signature pair with Minimum Separability: Tomato, Sugar beet					

(e)

Three-band Kompsat-2 MS image (green, red, NIR) with Envisat ASAR data taken in August

Class Names	Corn	Tomato	Rice	Sugar beet	Wheat
Tomato	1.58				
Rice	1.43	1.19			
Sugar beet	1.81	0.68	1.14		
Wheat	1.99	1.96	1.99	1.99	
Grass Land	1.99	1.92	1.99	1.99	0.99
Average Separability: 1.64					
Signature pair with Minimum Separability: Tomato, Sugar beet					

(f)

Table F.3 The matrices of Bhattacharya distance for three-band, *blue*, *red*, *NIR* of the Kompsat-2 MS data taken in June-July-August (a, c, e), with Envisat ASAR data (b, d, f).

Three-band Kompsat-2 MS image (blue, red, NIR) taken in June

Class Names	Corn	Tomato	Rice	Sugar beet	Wheat
Tomato	1.93				
Rice	1.99	1.99			
Sugar beet	1.85	1.51	1.98		
Wheat	1.63	1.60	1.83	1.91	
Grass Land	1.40	1.39	1.92	1.28	1.49

Average Separability: 1.74
Signature pair with Minimum Separability: Sugar beet, Grass Land

(a)

Three-band Kompsat-2 MS image (blue, red, NIR) with Envisat ASAR data taken in June

Class Names	Corn	Tomato	Rice	Sugar beet	Wheat
Tomato	1.94				
Rice	1.99	1.99			
Sugar beet	1.96	1.67	1.99		
Wheat	1.97	1.63	1.84	1.95	
Grass Land	1.44	1.56	1.93	1.84	1.52

Average Separability: 1.81
Signature pair with Minimum Separability: Corn, Grass Land

(b)

Three-band Kompsat-2 MS image (blue, red, NIR) taken in July

Class Names	Corn	Tomato	Rice	Sugar beet	Wheat
Tomato	0.76				
Rice	1.38	1.87			
Sugar beet	1.94	1.40	2.00		
Wheat	1.99	1.99	1.99	2.00	
Grass Land	1.91	1.95	1.99	1.99	1.57

Average Separability: 1.78
Signature pair with Minimum Separability: Corn, Tomato

(c)

Table F.3 (Cont'd)

Three-band Kompsat-2 MS image (blue, red, NIR) with Envisat ASAR data taken in July

Class Names	Corn	Tomato	Rice	Sugar beet	Wheat
Tomato	0.93				
Rice	1.53	1.88			
Sugar beet	1.95	1.42	2.00		
Wheat	1.99	1.99	2.00	2.00	
Grass Land	1.93	1.97	1.99	1.99	1.58

Average Separability: 1.81
Signature pair with Minimum Separability: Corn, Tomato

(d)

Three-band Kompsat-2 MS image (blue, green, NIR) taken in August

Class Names	Corn	Tomato	Rice	Sugar beet	Wheat
Tomato	1.54				
Rice	1.44	1.26			
Sugar beet	1.82	1.01	0.87		
Wheat	1.99	1.89	1.99	1.99	
Grass Land	1.99	1.59	1.99	1.99	1.25

Average Separability: 1.64
Signature pair with Minimum Separability: Rice, Sugar beet

(e)

Three-band Kompsat-2 MS image (blue, red, NIR) with Envisat ASAR data taken in August

Class Names	Corn	Tomato	Rice	Sugar beet	Wheat
Tomato	1.49				
Rice	1.28	1.41			
Sugar beet	1.59	0.96	1.19		
Wheat	1.99	1.97	1.99	1.99	
Grass Land	1.99	1.92	1.99	1.99	1.33

Average Separability: 1.67
Signature pair with Minimum Separability: Tomato, Sugar beet

(f)

Table F.4 The matrices of Bhattacharya distance for three-band, *blue, green, NIR*, of the Kompsat-2 MS images taken in June, July, and August (a, c, e), with the Envisat ASAR data (b, d, f).

Three-band Kompsat-2 MS image (blue, green, NIR) taken in June

Class Names	Corn	Tomato	Rice	Sugar beet	Wheat
Tomato	1.93				
Rice	1.99	1.99			
Sugar beet	1.96	1.38	1.98		
Wheat	1.93	1.24	1.28	1.45	
Grass Land	1.42	1.34	1.88	1.02	1.26

Average Separability: 1.60
Signature pair with Minimum Separability: Sugar beet, Grass Land

(a)

Three-band Kompsat-2 MS image (blue, green, NIR) with Envisat ASAR data taken in June

Class Names	Corn	Tomato	Rice	Sugar beet	Wheat
Tomato	1.94				
Rice	1.99	1.99			
Sugar beet	1.99	1.59	1.99		
Wheat	1.94	1.27	1.32	1.64	
Grass Land	1.47	1.53	1.89	1.77	1.31

Average Separability: 1.71
Signature pair with Minimum Separability: Tomato, Wheat

(b)

Three-band Kompsat-2 MS image (blue, green, NIR) taken in July

Class Names	Corn	Tomato	Rice	Sugar beet	Wheat
Tomato	0.84				
Rice	1.64	1.88			
Sugar beet	1.97	1.57	1.99		
Wheat	1.94	1.96	1.99	2.00	
Grass Land	1.76	1.82	1.98	1.99	1.07

Average Separability: 1.76
Signature pair with Minimum Separability: Corn, Tomato

(c)

Table F.4 (Cont'd)

Three-band Kompsat-2 MS image (blue, green, NIR) with Envisat ASAR data taken in July

Class Names	Corn	Tomato	Rice	Sugar beet	Wheat
Tomato	1.00				
Rice	1.71	1.89			
Sugar beet	1.98	1.58	1.99		
Wheat	1.97	1.99	1.99	2.00	
Grass Land	1.84	1.94	1.99	1.99	1.14
Average Separability: 1.80					
Signature pair with Minimum Separability: Corn, Tomato					

(d)

Three-band Kompsat-2 MS image (blue, green, NIR) taken in August

Class Names	Corn	Tomato	Rice	Sugar beet	Wheat
Tomato	1.54				
Rice	1.44	1.26			
Sugar beet	1.82	1.01	0.87		
Wheat	1.99	1.89	1.99	1.99	
Grass Land	1.99	1.59	1.99	1.99	1.25
Average Separability: 1.64					
Signature pair with Minimum Separability: Rice, Sugar beet					

(e)

Three-band Kompsat-2 MS image (blue, green, NIR) with Envisat ASAR data taken in August

Class Names	Corn	Tomato	Rice	Sugar beet	Wheat
Tomato	1.62				
Rice	1.47	1.44			
Sugar beet	1.84	1.03	1.21		
Wheat	1.99	1.96	1.99	1.99	
Grass Land	1.99	1.92	1.99	1.99	1.37
Average Separability: 1.72					
Signature pair with Minimum Separability: Tomato, Sugar beet					

(f)

APPENDIX G

THE COLLECTED TRAINING SAMPLES

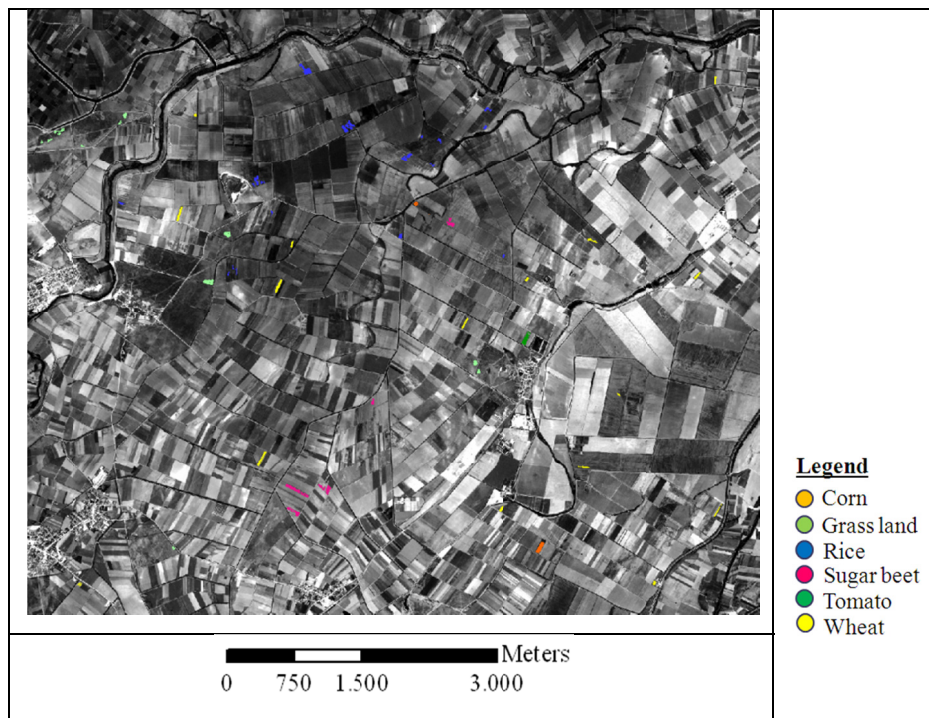


Figure G.1 The collected training sites of the MS Kompsat-2 image (green band) taken in June

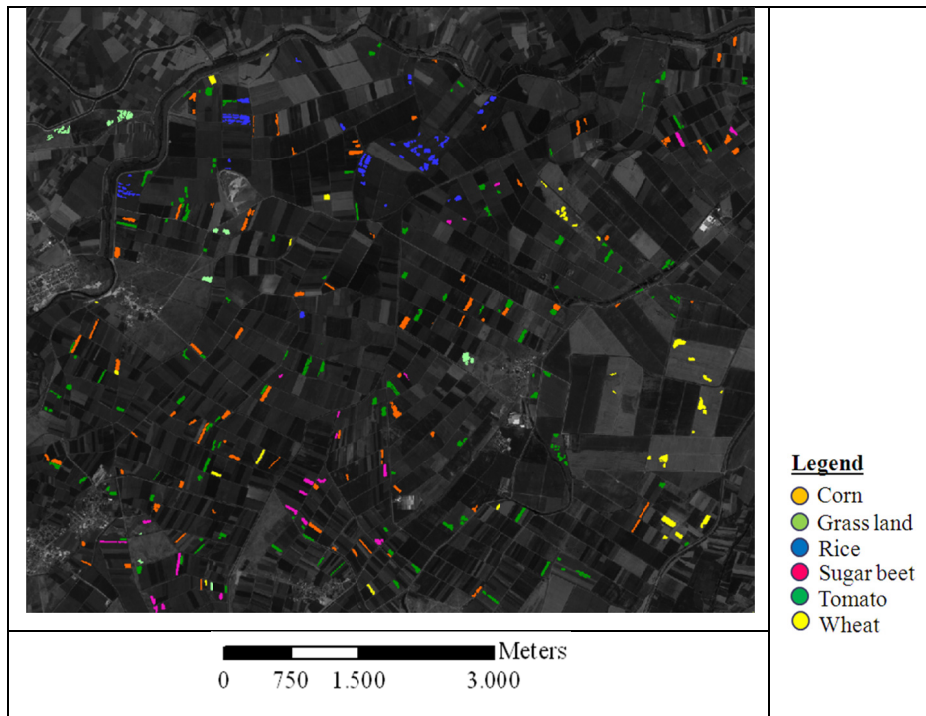


Figure G.2 The collected training sites of the MS Kompsat-2 image (green band) taken in August

APPENDIX H

THE PRODUCED THEMATIC MAPS

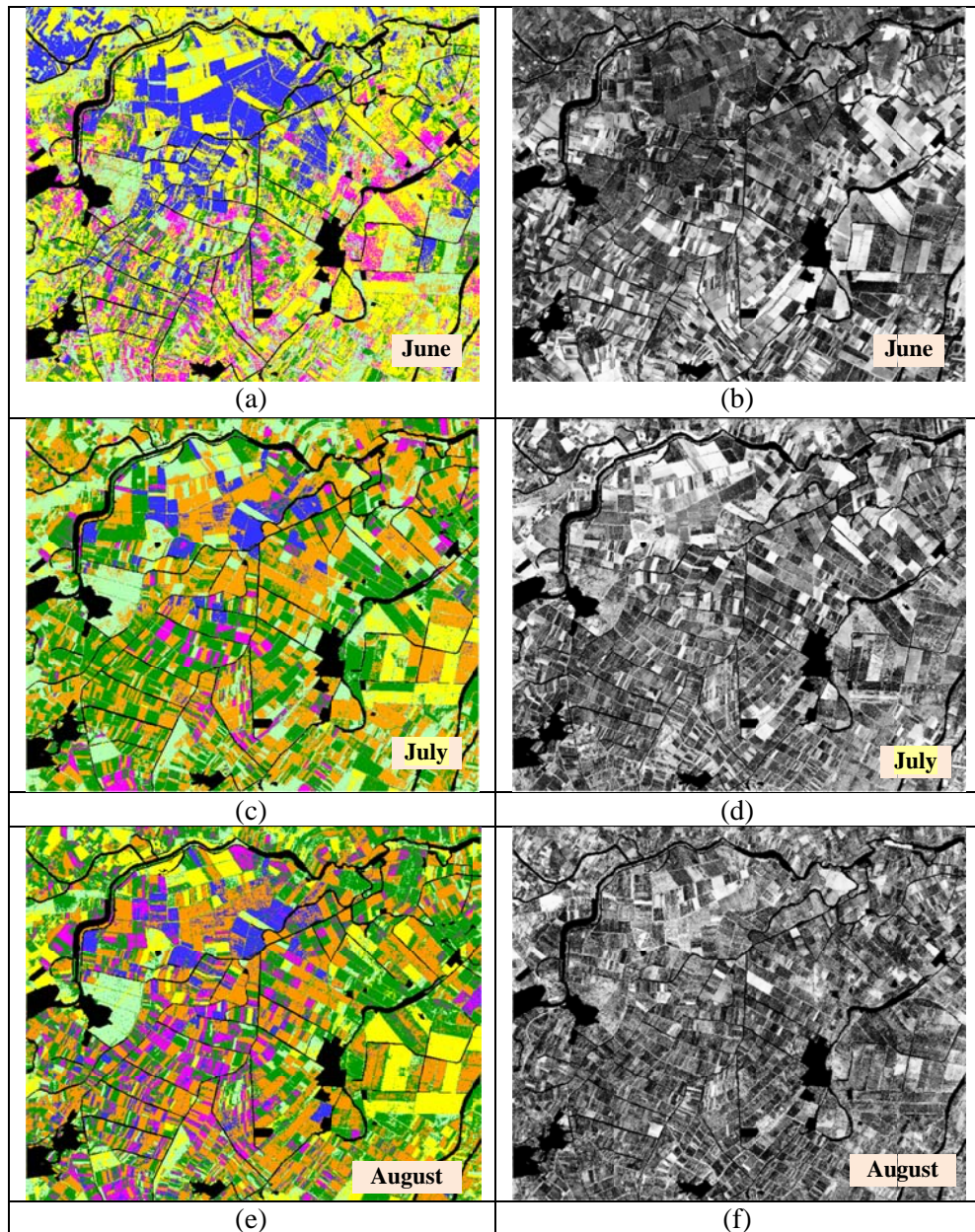


Figure H.1 Results of the pixel-based MLC of the four-band Kompsat-2 data (a, c, e, g, i, k, m) with the probability maps (b, d, f, h, j, l, n)

Figure H.1 (Cont'd)

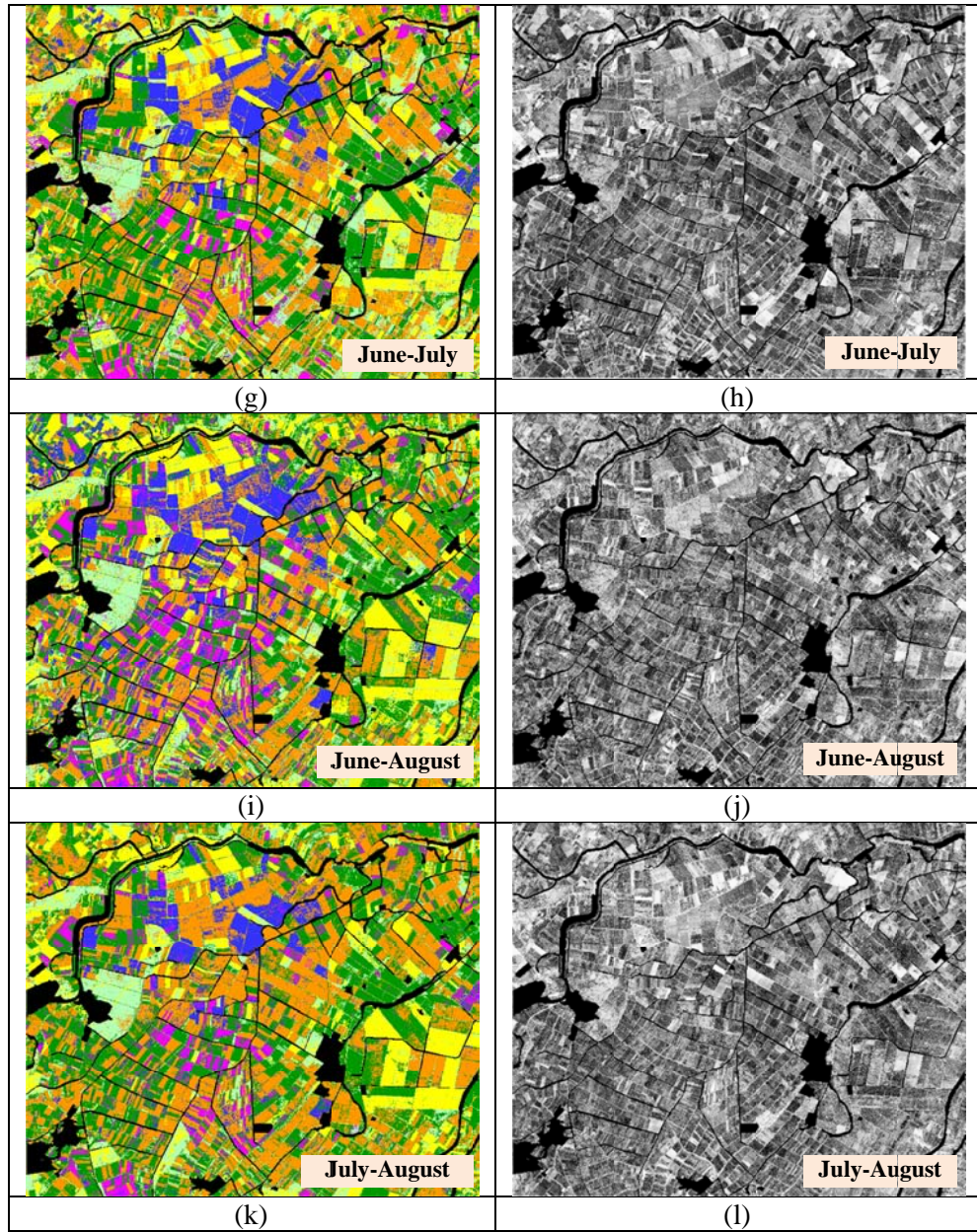


Figure H.1 (Cont'd)

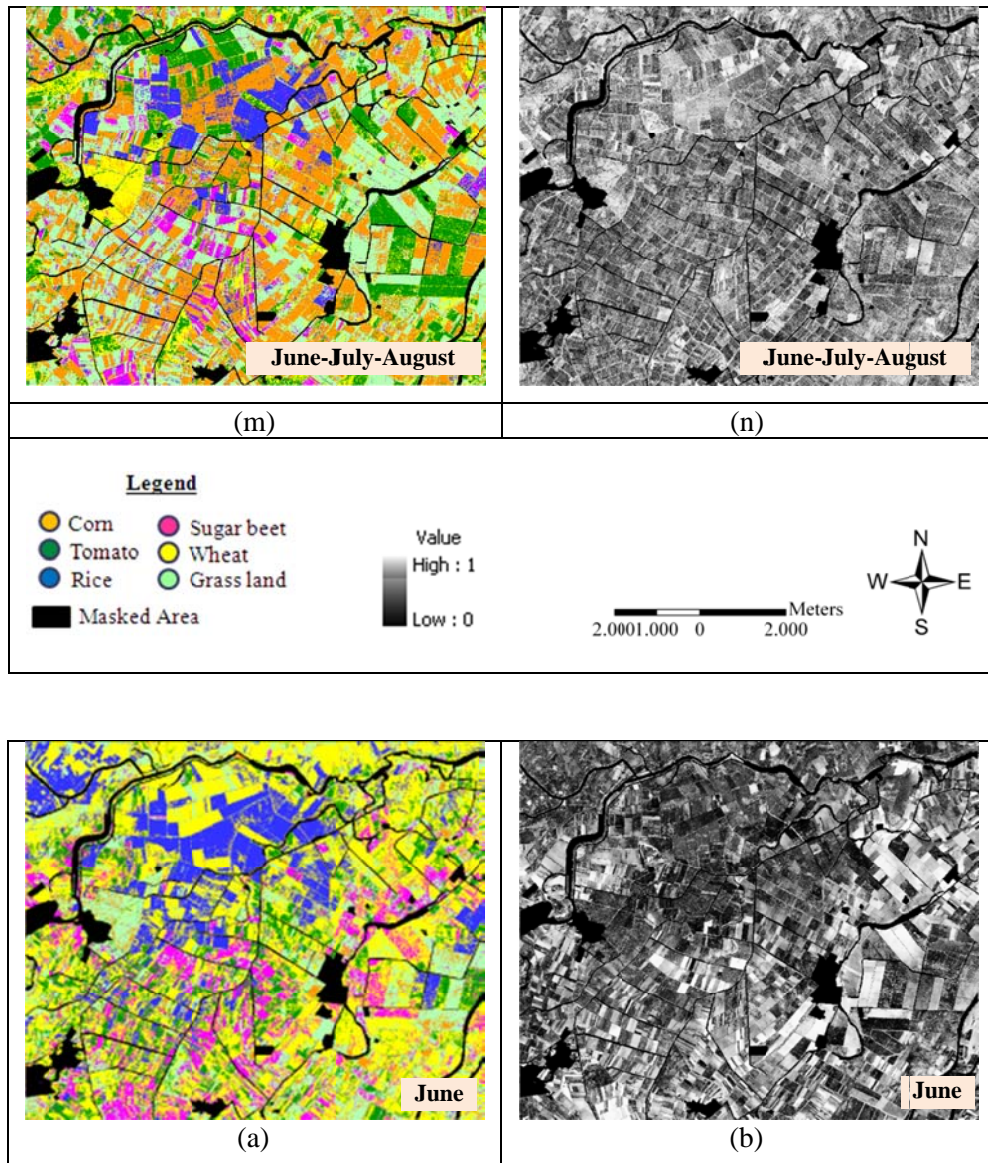


Figure H.2 Results of the pixel-based MLC of the four-band Kompsat-2 and Envisat ASAR data (a, c, e, g, i, k, m) with the probability maps (b, d, f, h, j, l, n)

Figure H.2 (Cont'd)

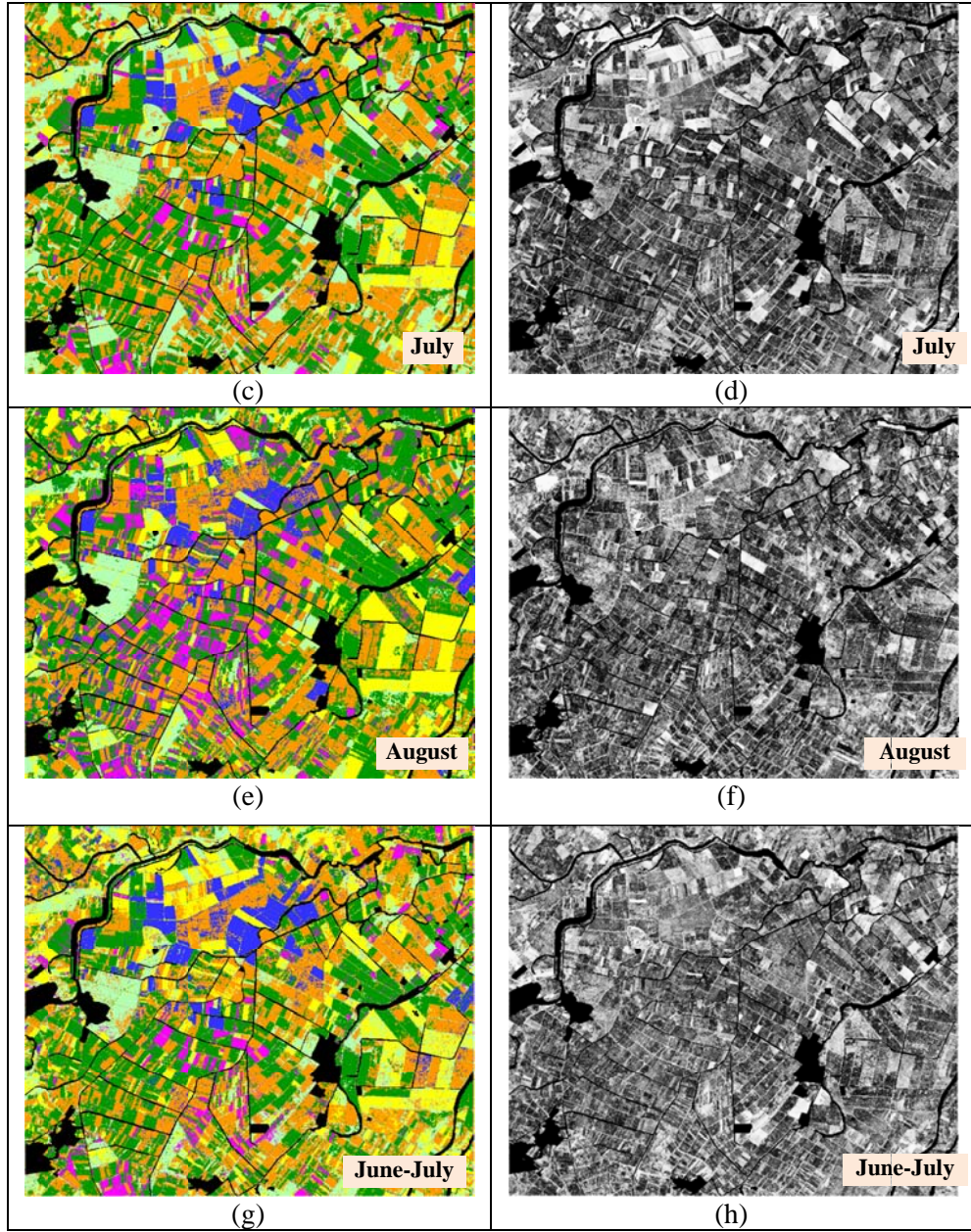
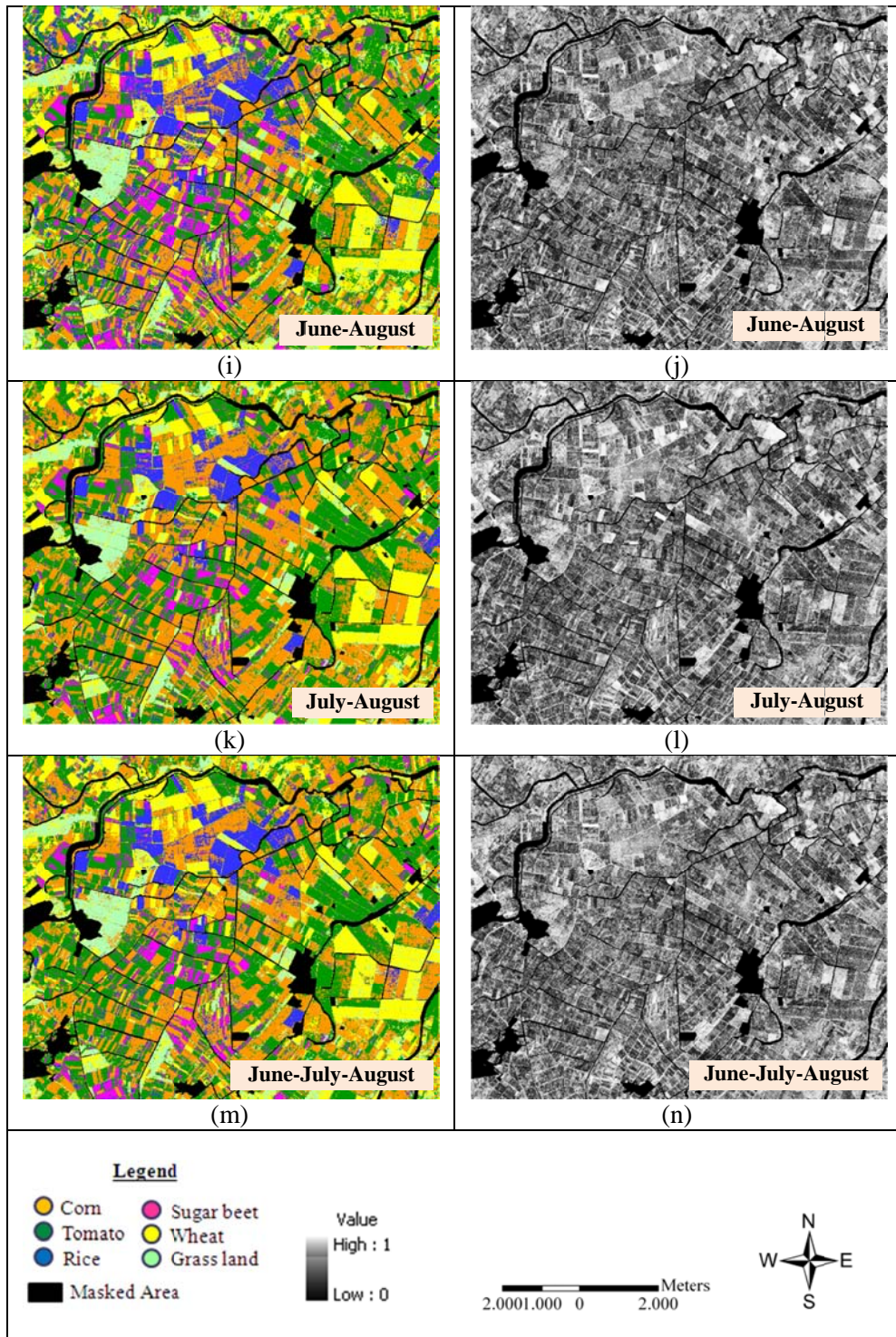


Figure H.2 (Cont'd)



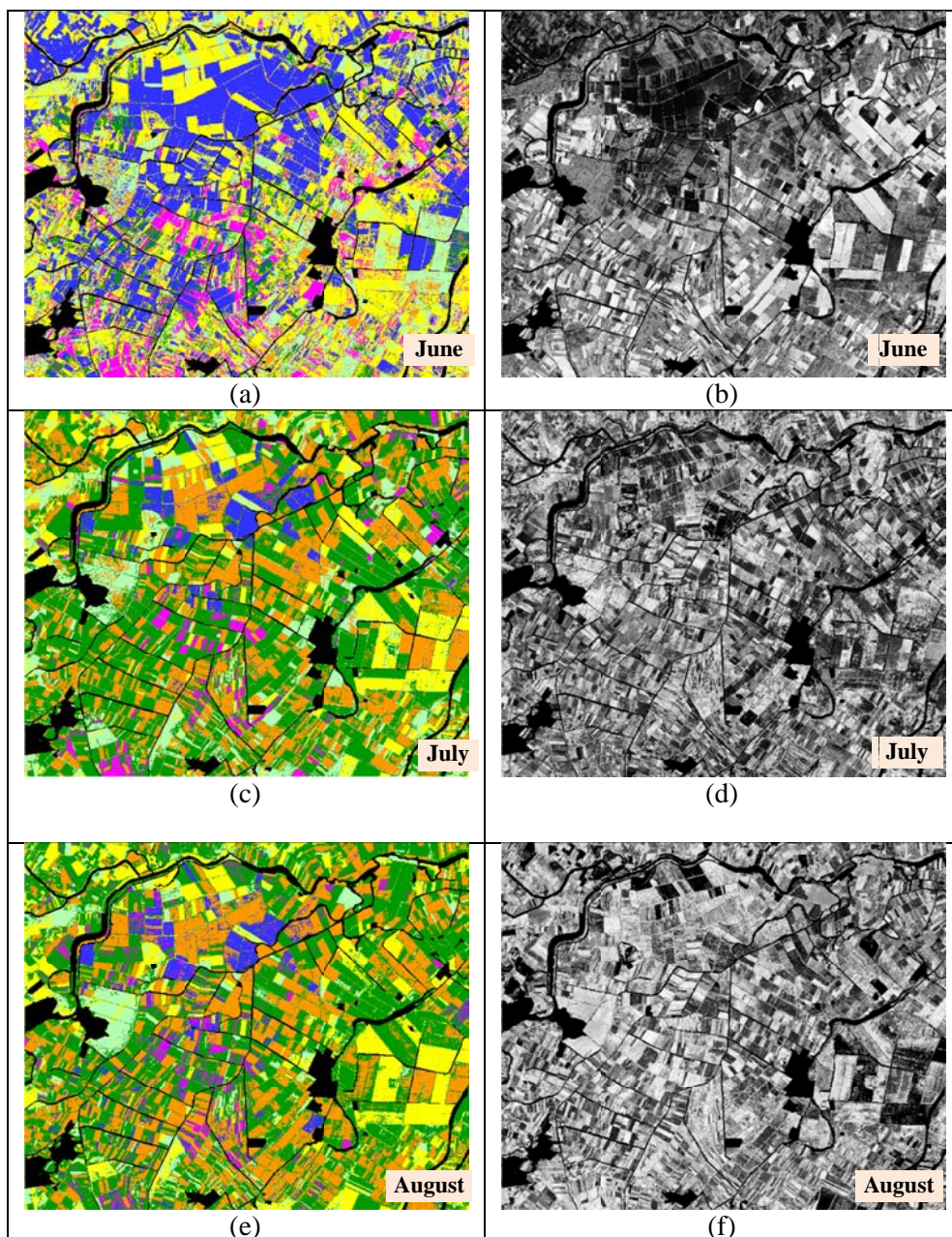


Figure H.3 Results of the pixel-based SVMs of the four-band Kompsat-2 data (a, c, e, g, i, k, m) with the probability maps (b, d, f, h, j, l, n)

Figure H.3 (Cont'd)

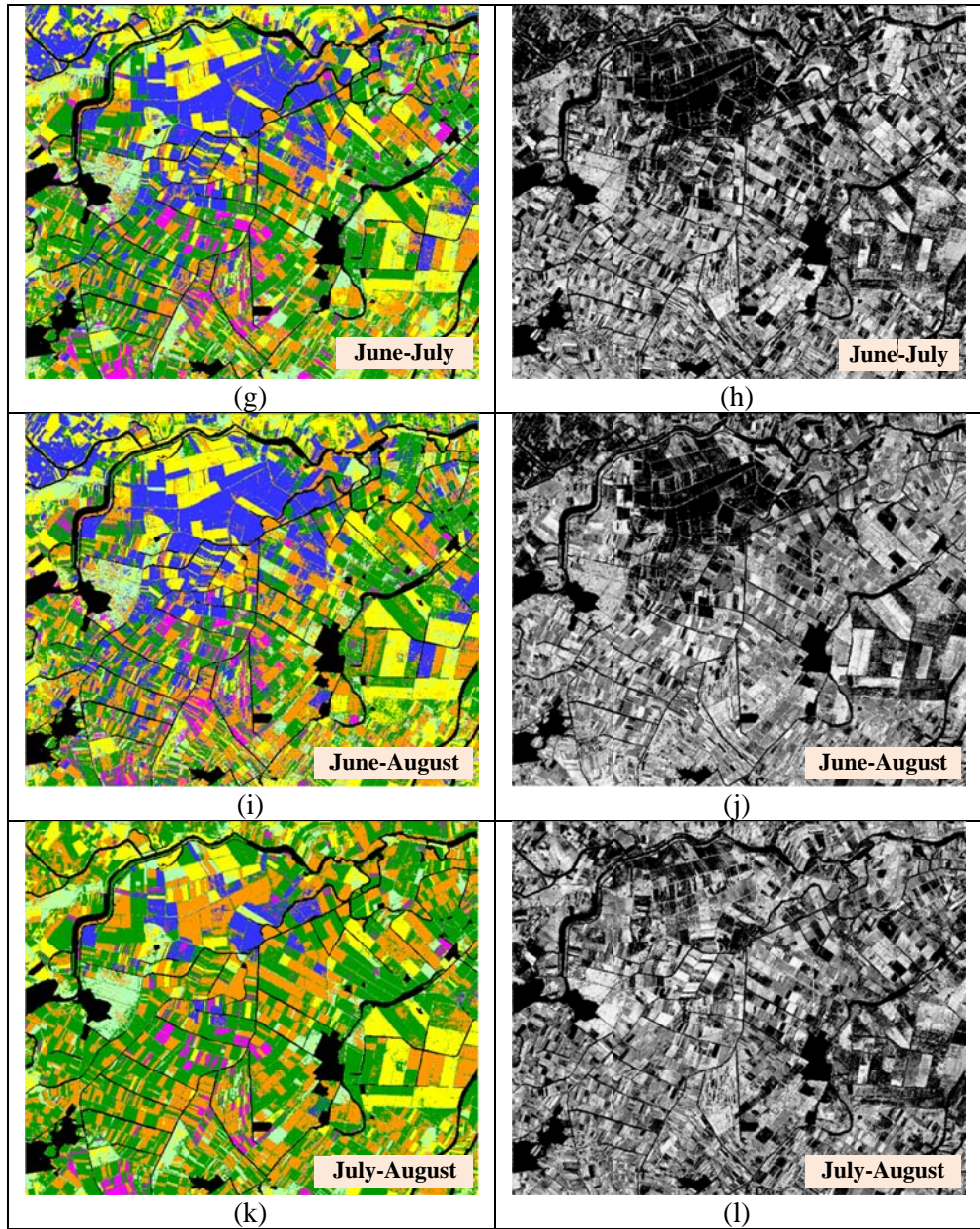


Figure H.3 (Cont'd)

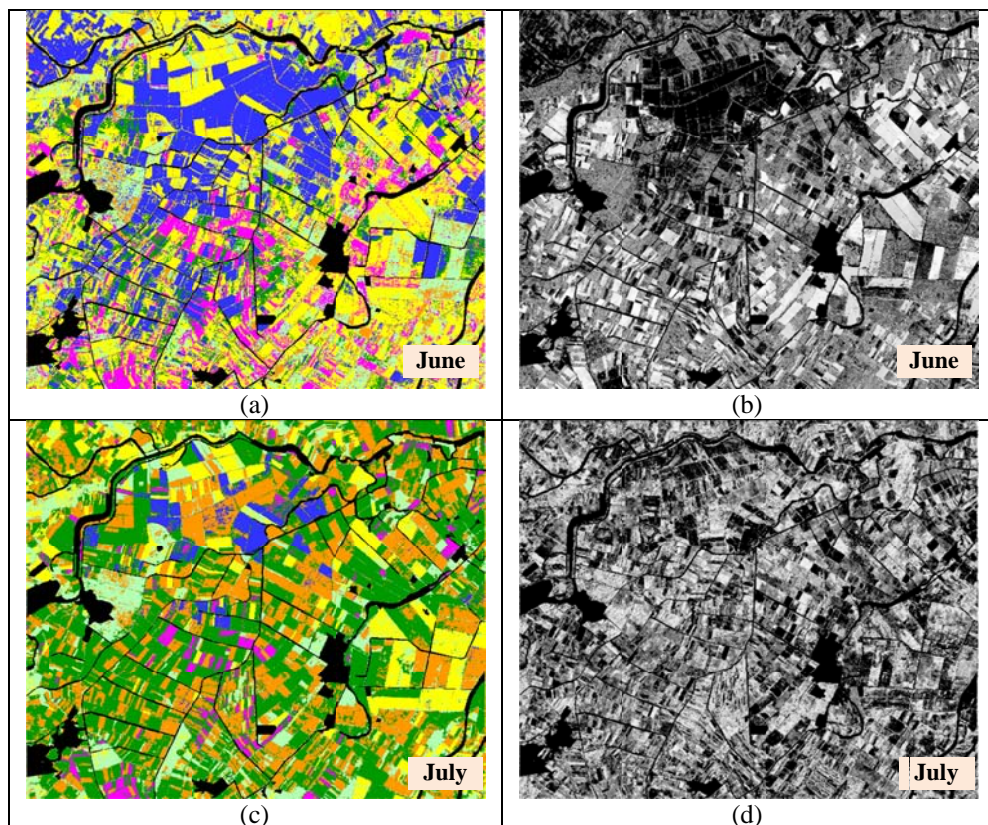
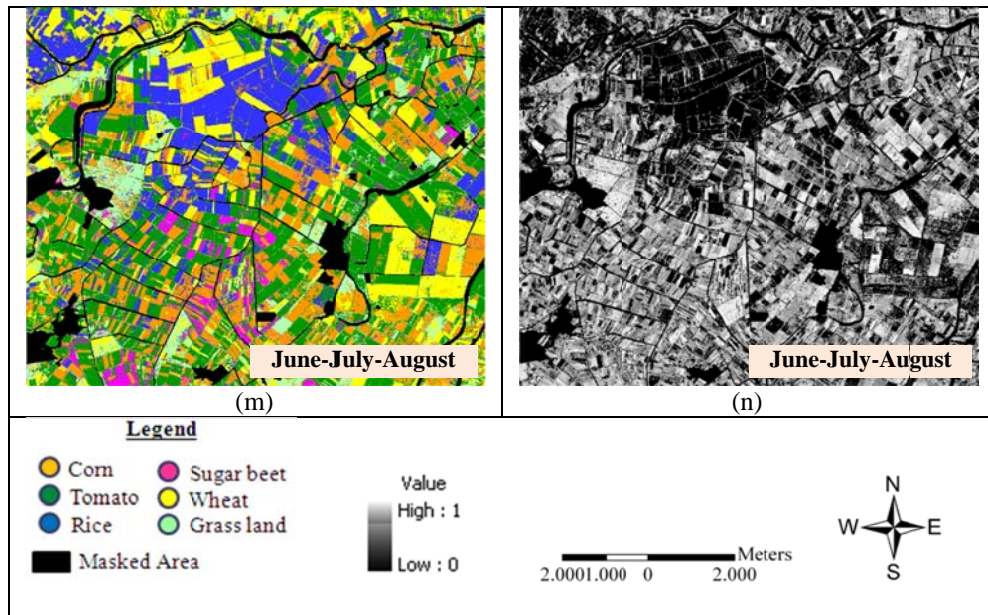
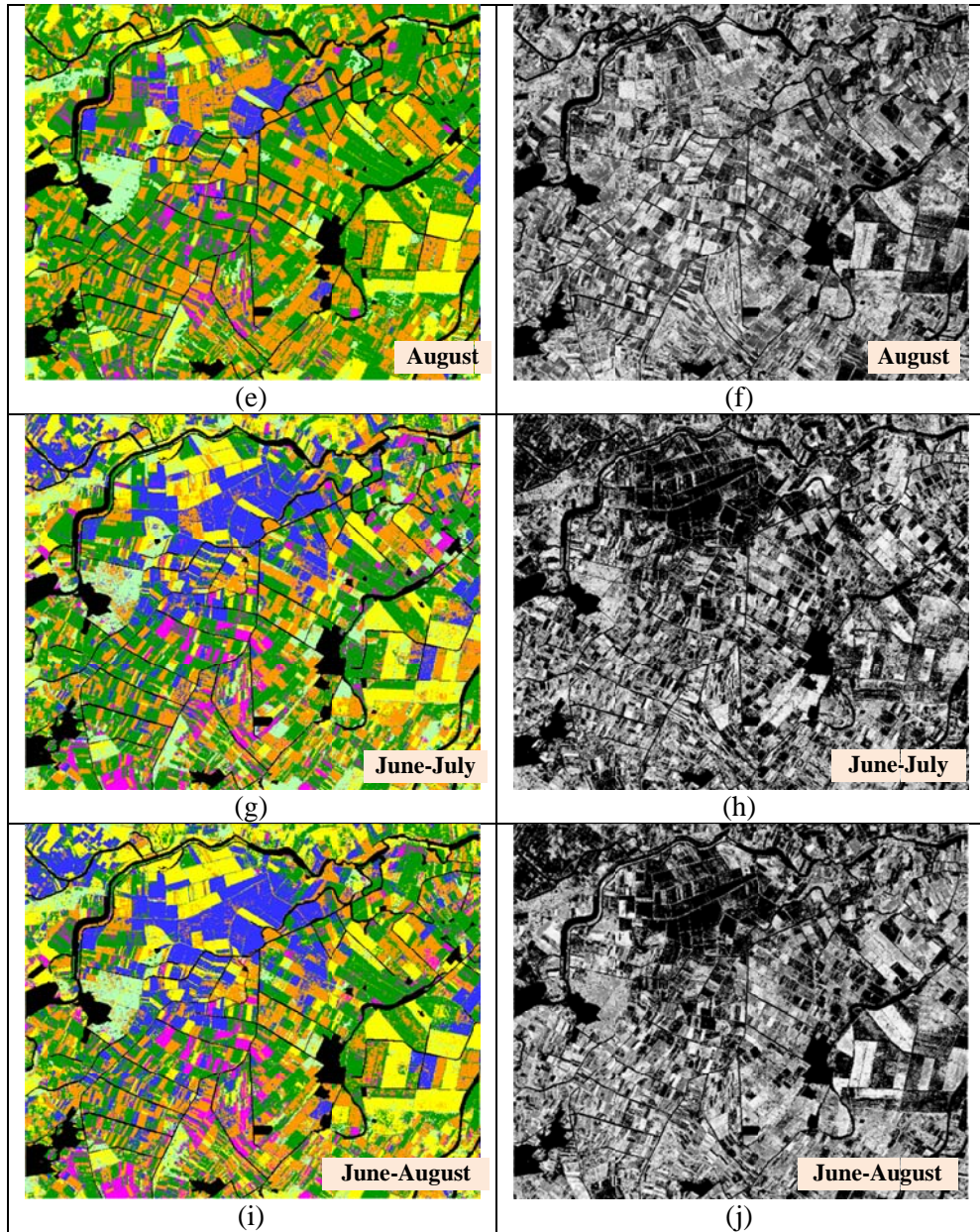
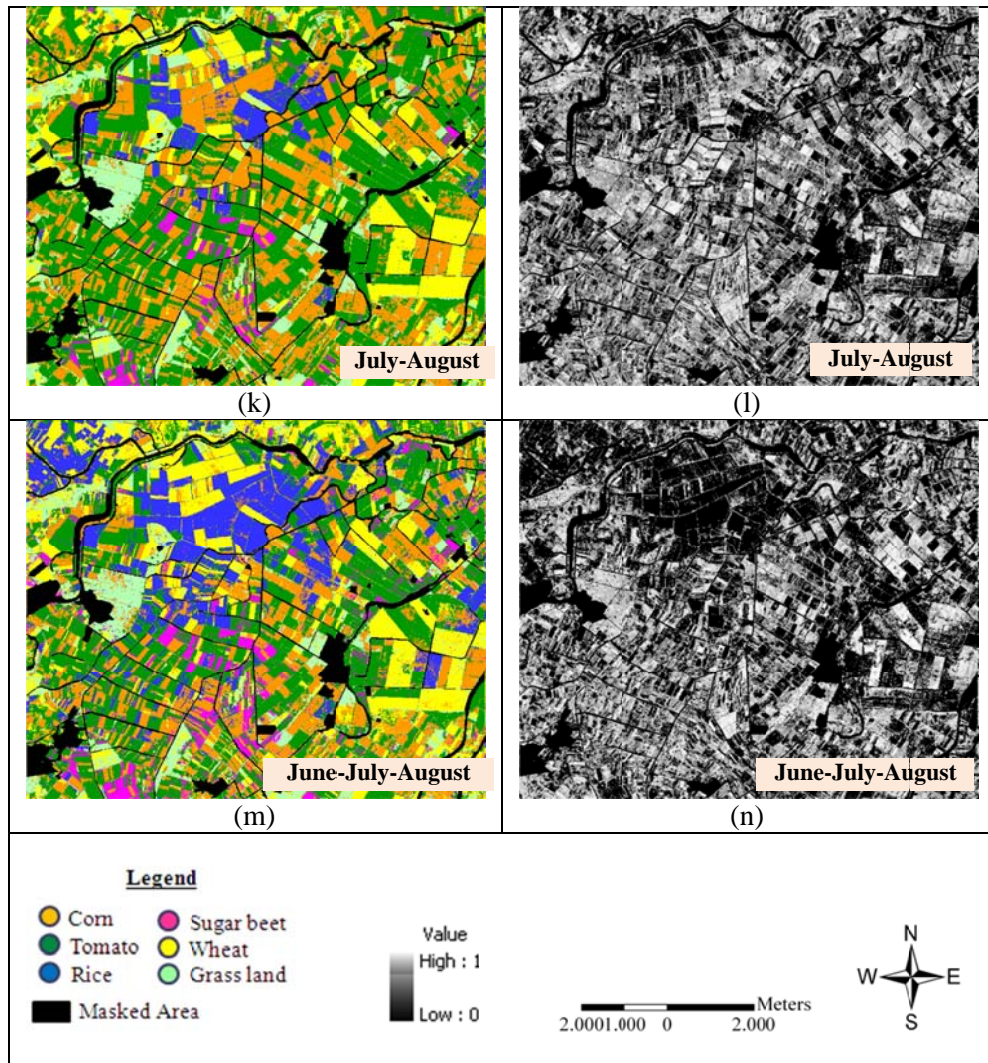


Figure H.4 Results of the pixel-based SVMs of the four-band Kompsat-2 and Envisat ASAR data (a, c, e, g, I, k, m) with the probability maps (b, d, f, h, j, l, n)

Figure H.4 (Cont'd)



(Figure H.4 Cont'd)



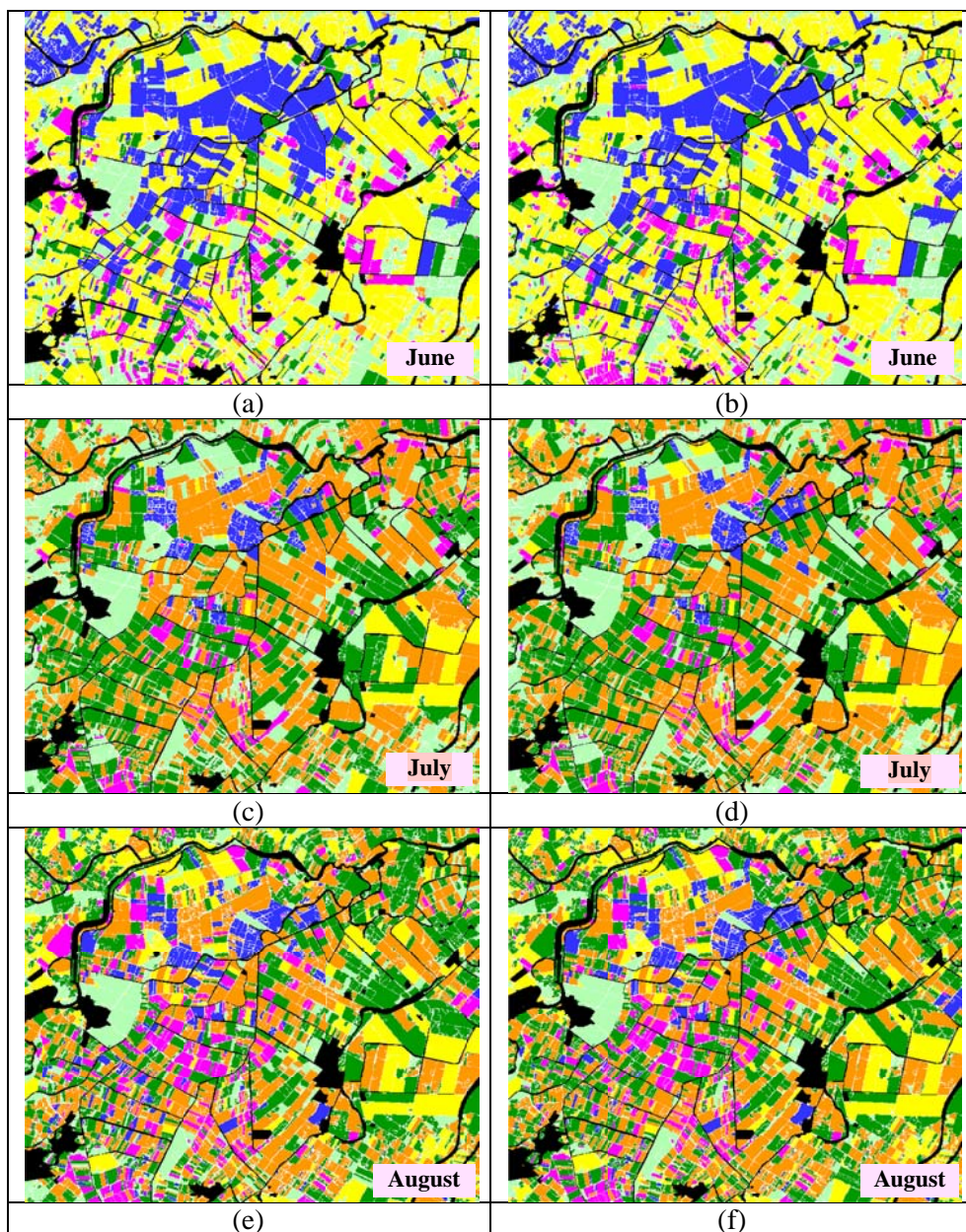


Figure H.5 (a, c, e, g, i, k, m) The segment-based results of the MLC for the four-band MS Kompsat-2 images. (b, d, f, h, j, l, n) The classification results of the same optical images with the Envisat-ASAR data.

Figure H.5 (Cont'd)

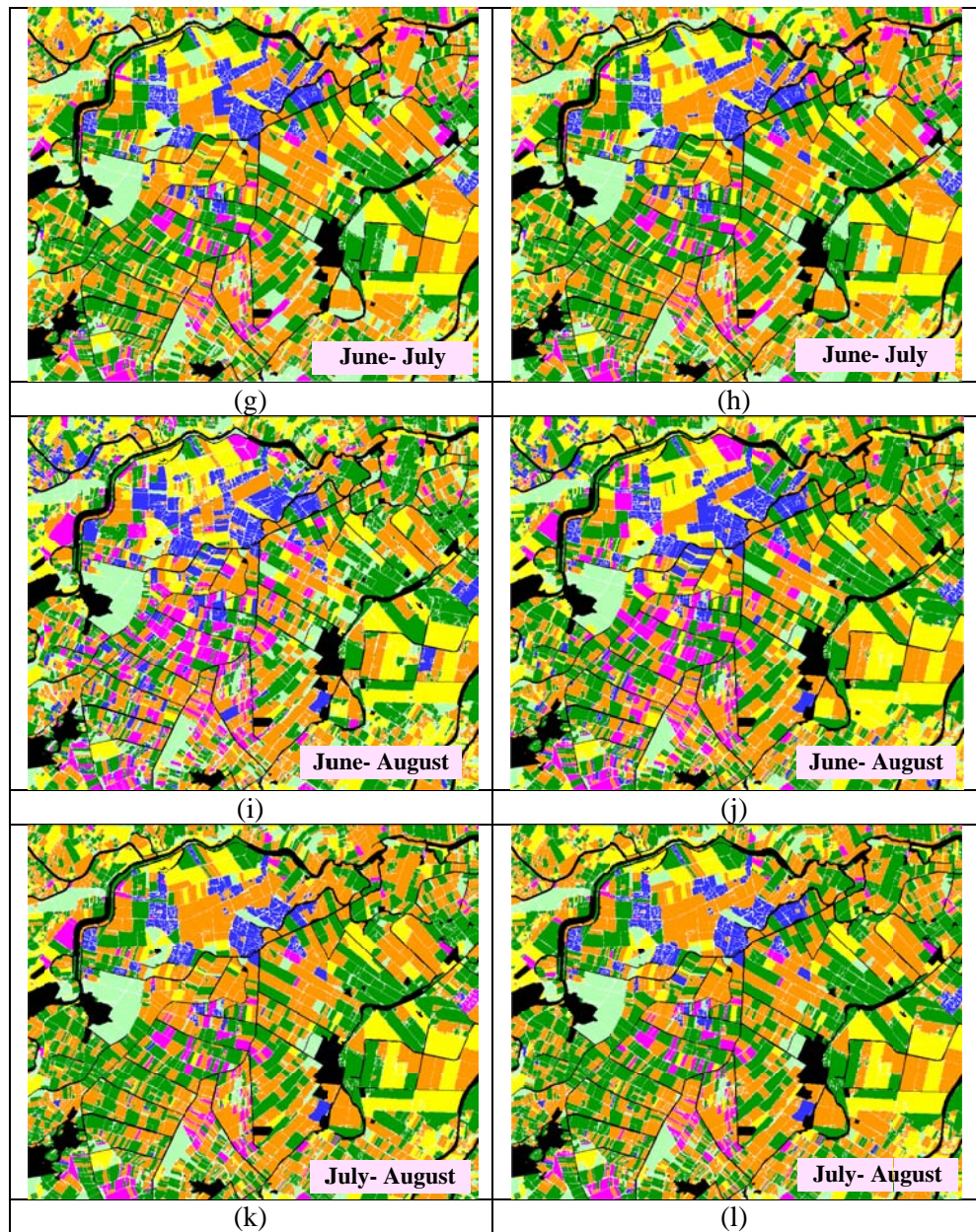


Figure H.5 (Cont'd)

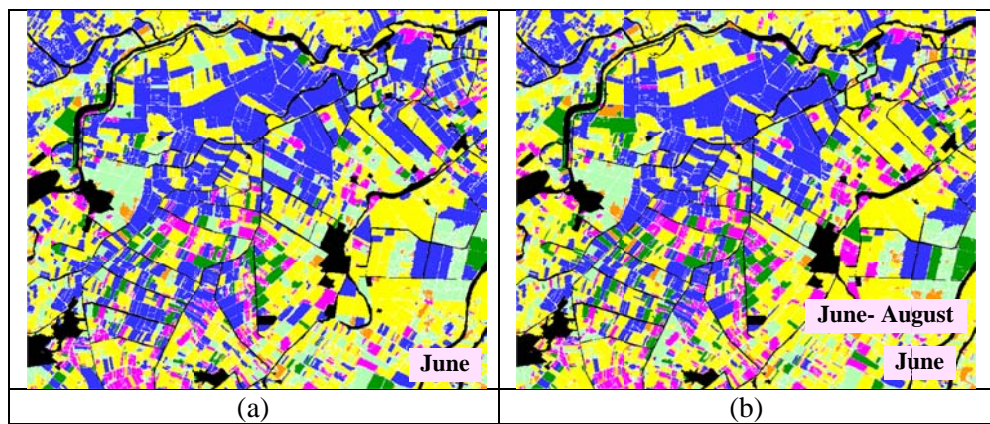
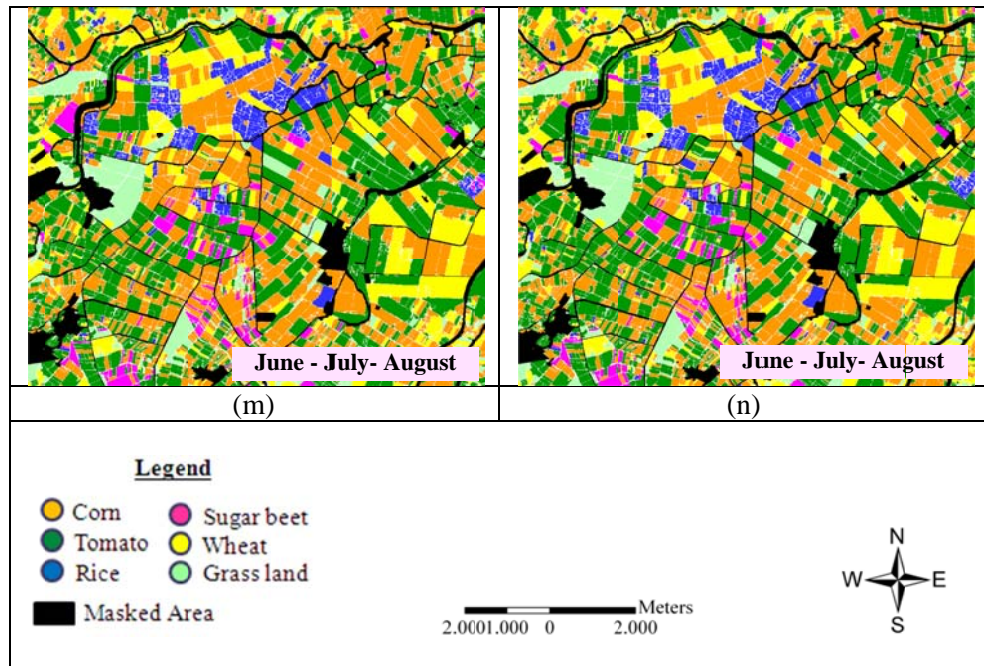


Figure H.6 (a, c, e, g, i, k, m) The segment-based results of the SVMs classification for the four-band MS Kompsat-2 images. (b, d, f, h, j, l, n). The classification results of the same optical images with Envisat-ASAR data.

Figure H.6 (Cont'd)

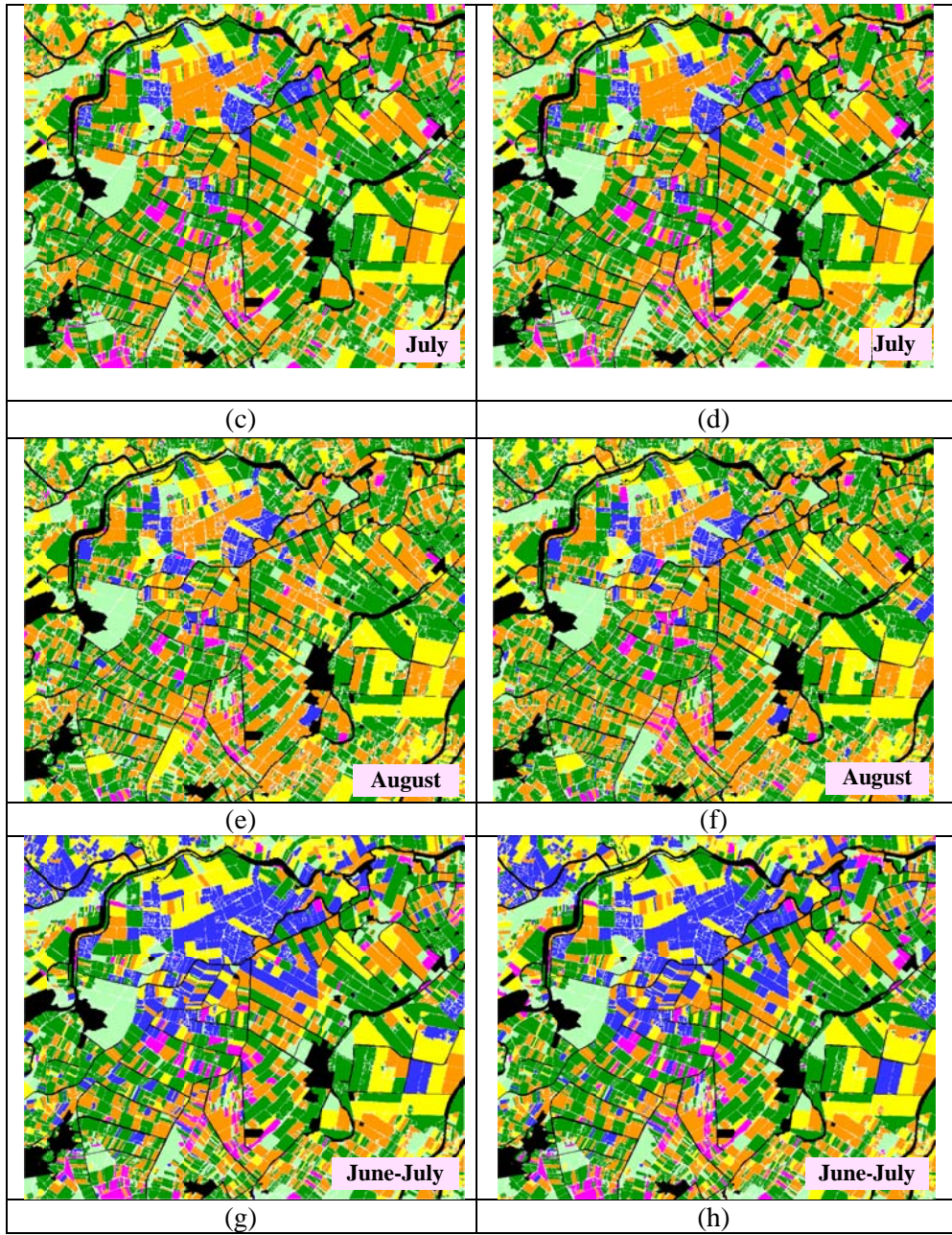
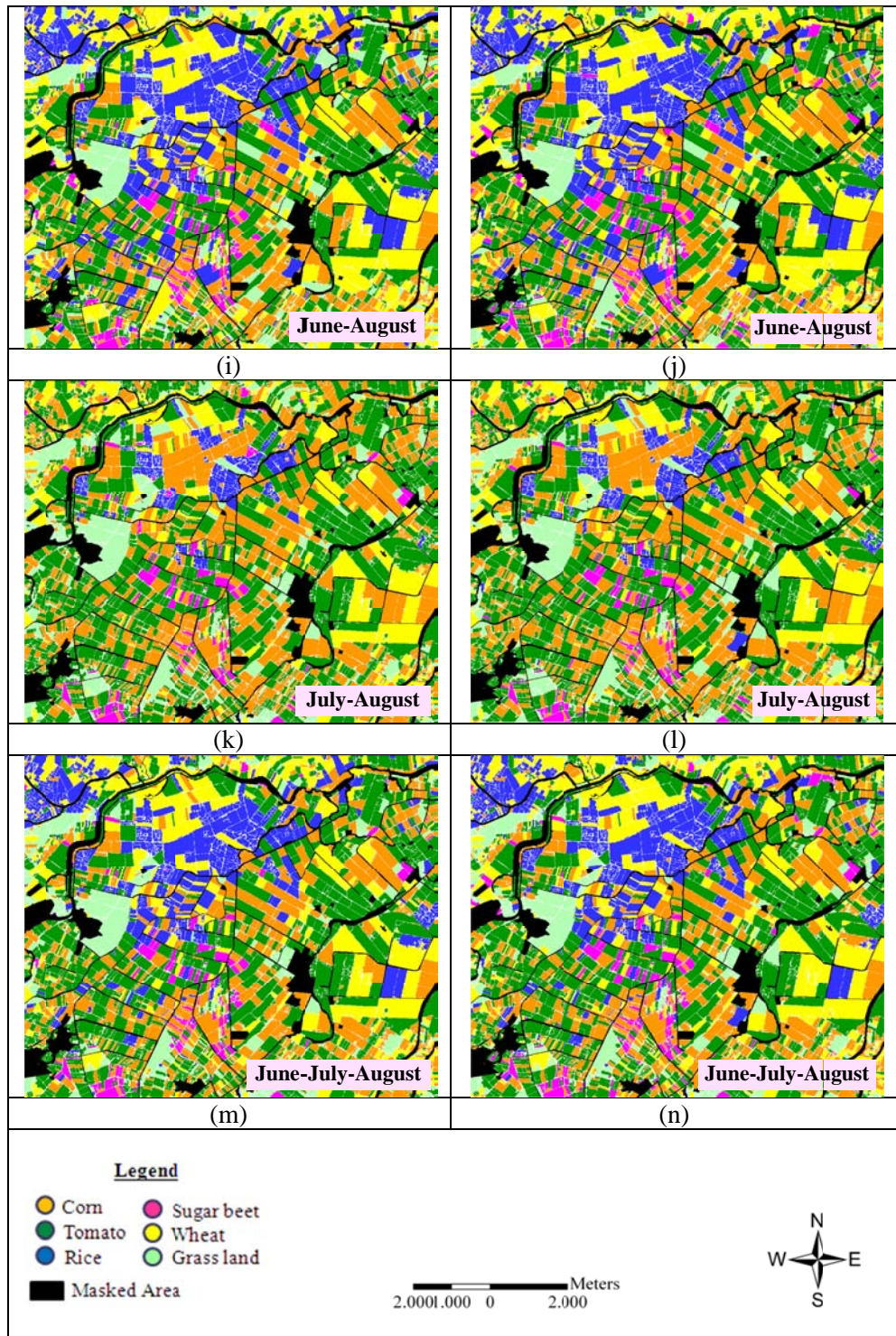


Figure H.6 (Cont'd)



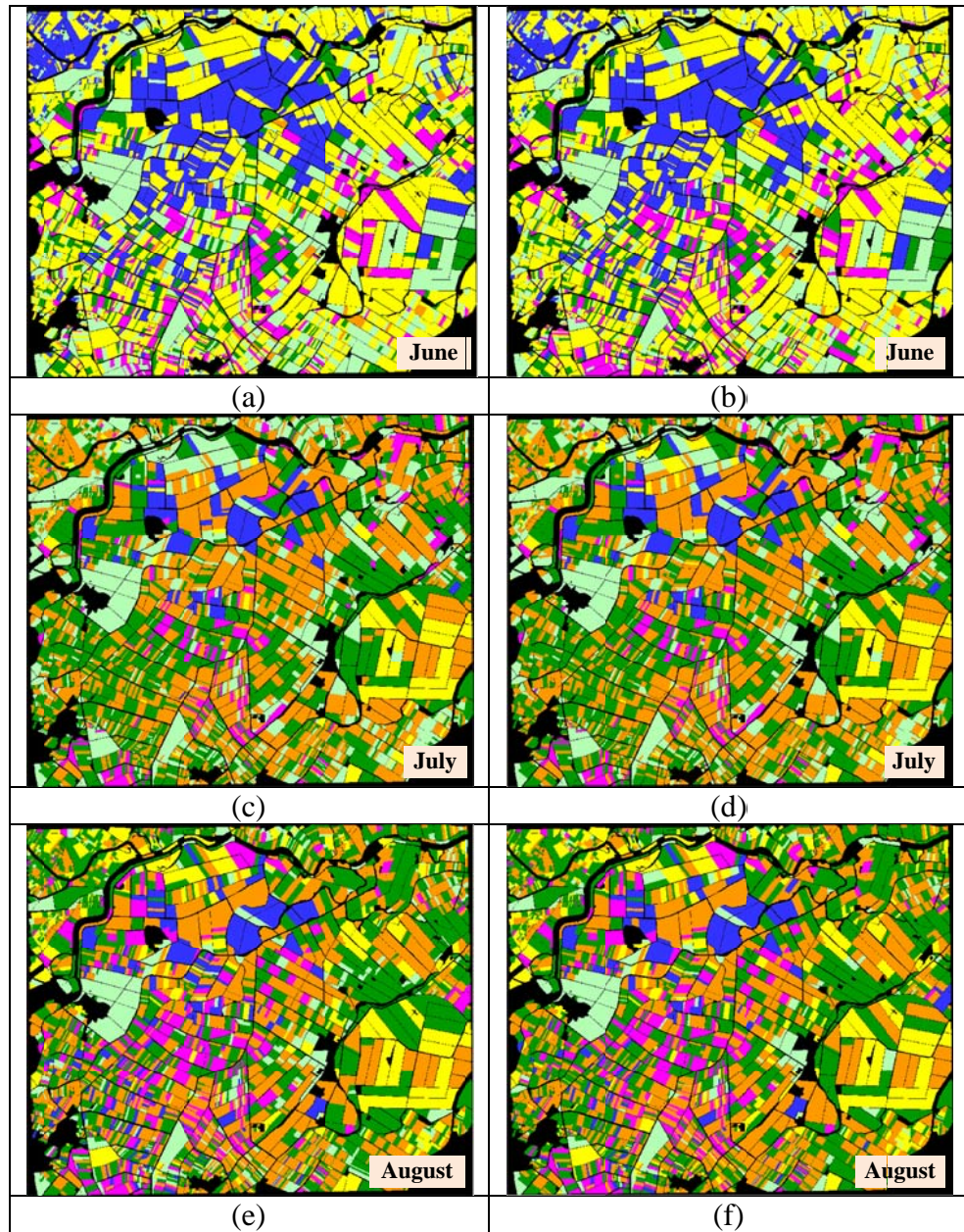


Figure H.7 (a, c, e, g, i, k, m) The field-based results of the MLC method for the MS Kompsat-2 images, (b, d, f, h, j, l, n) The classification results of the same optical images with Envisat ASAR data.

Figure H.7 (Cont'd)

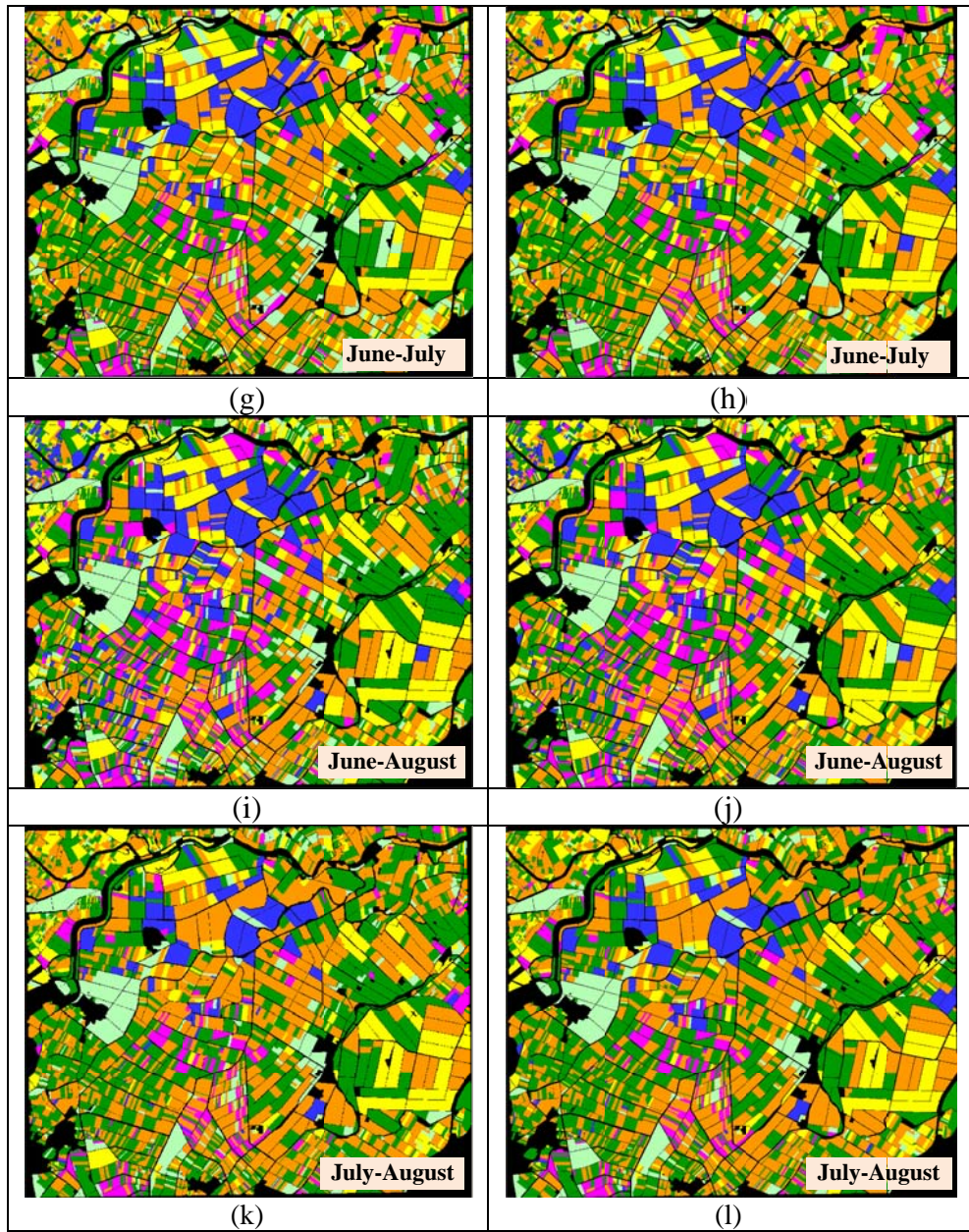


Figure H.7 (Cont'd)

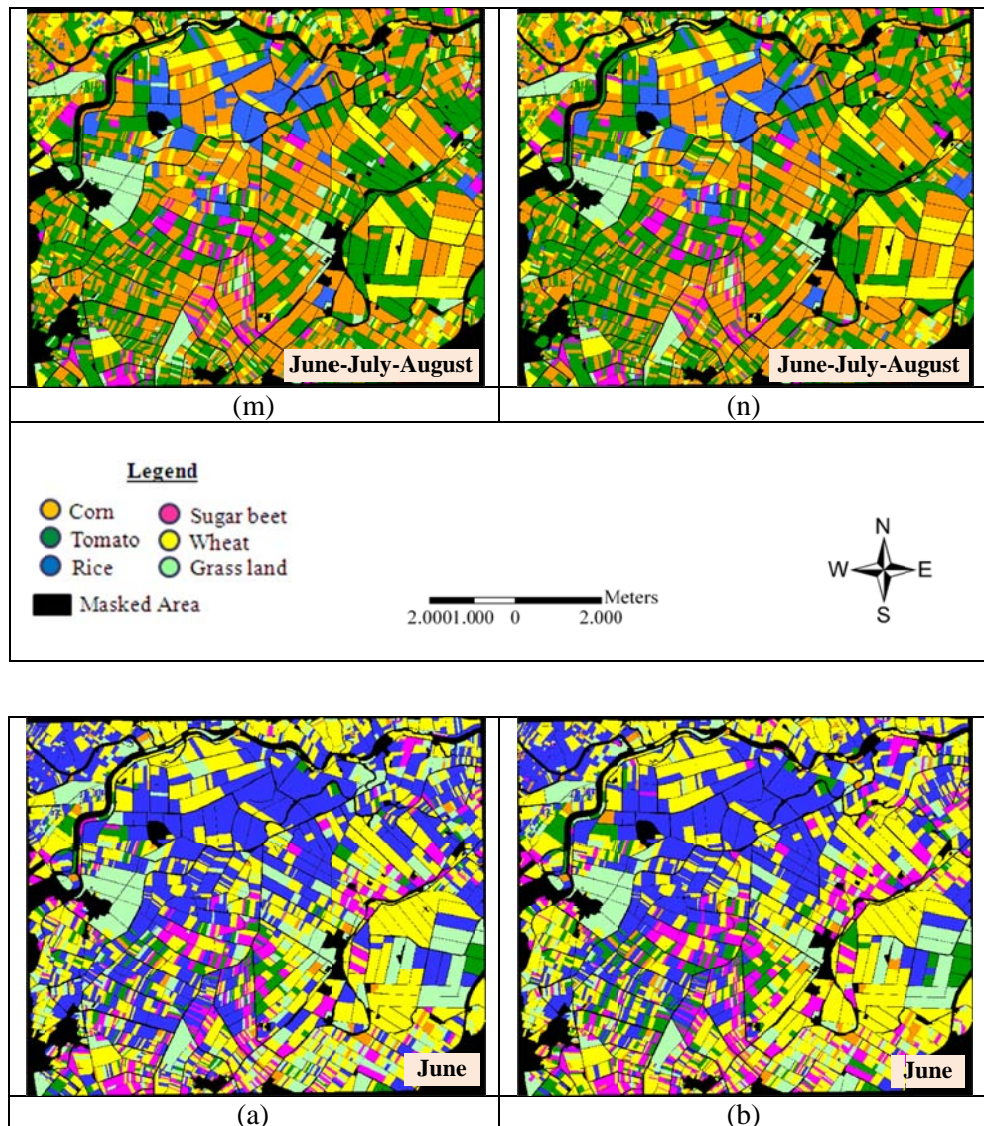


Figure H.8 (a, c, e, g, i, k, m) The field-based results of the SVMs method for the MS Kompsat-2 images acquired in June, July, and August, respectively. (b, d, f, h, j, l, n). The classification results of the same optical images with Envisat-ASAR data.

Figure H.8 (Cont'd)

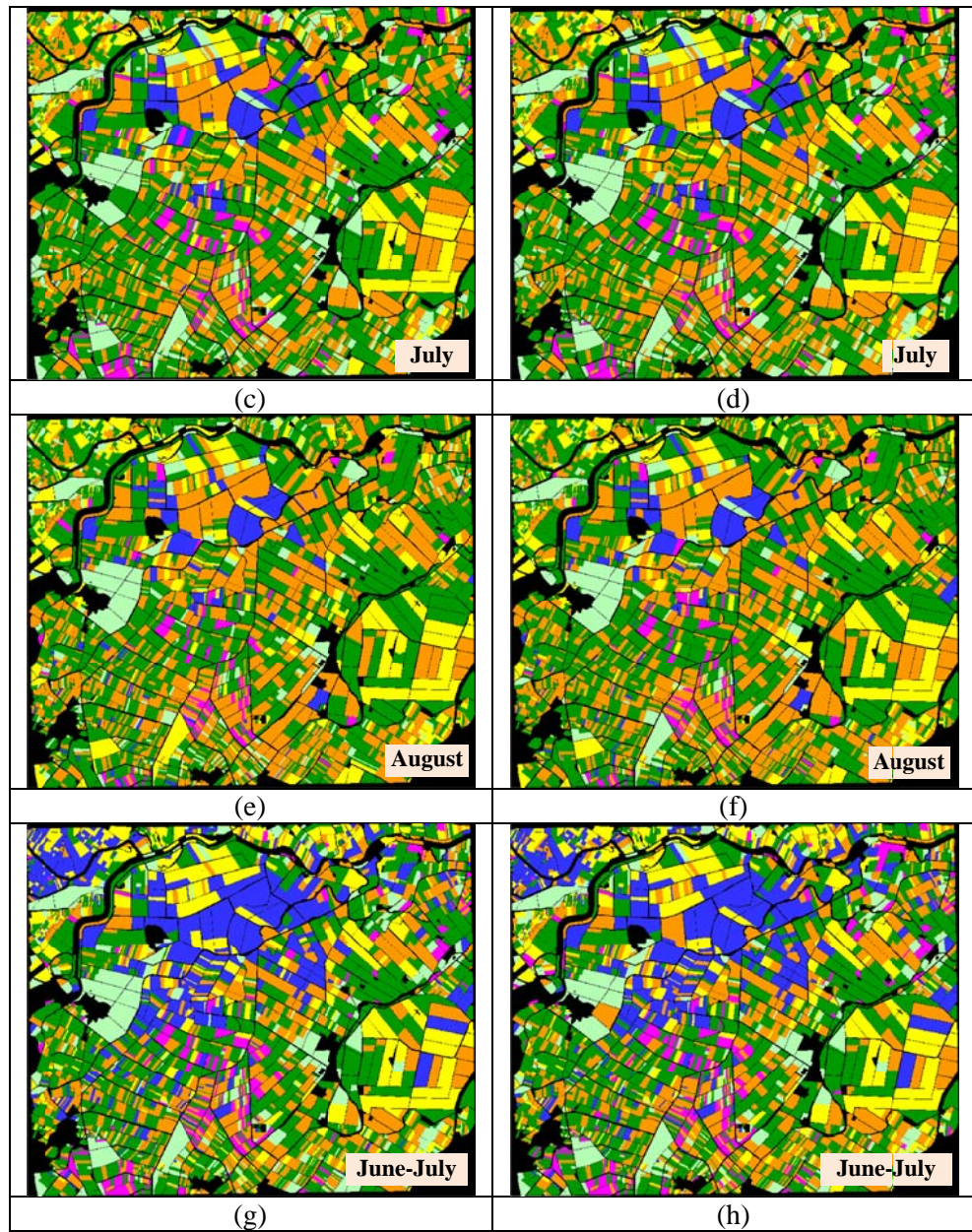
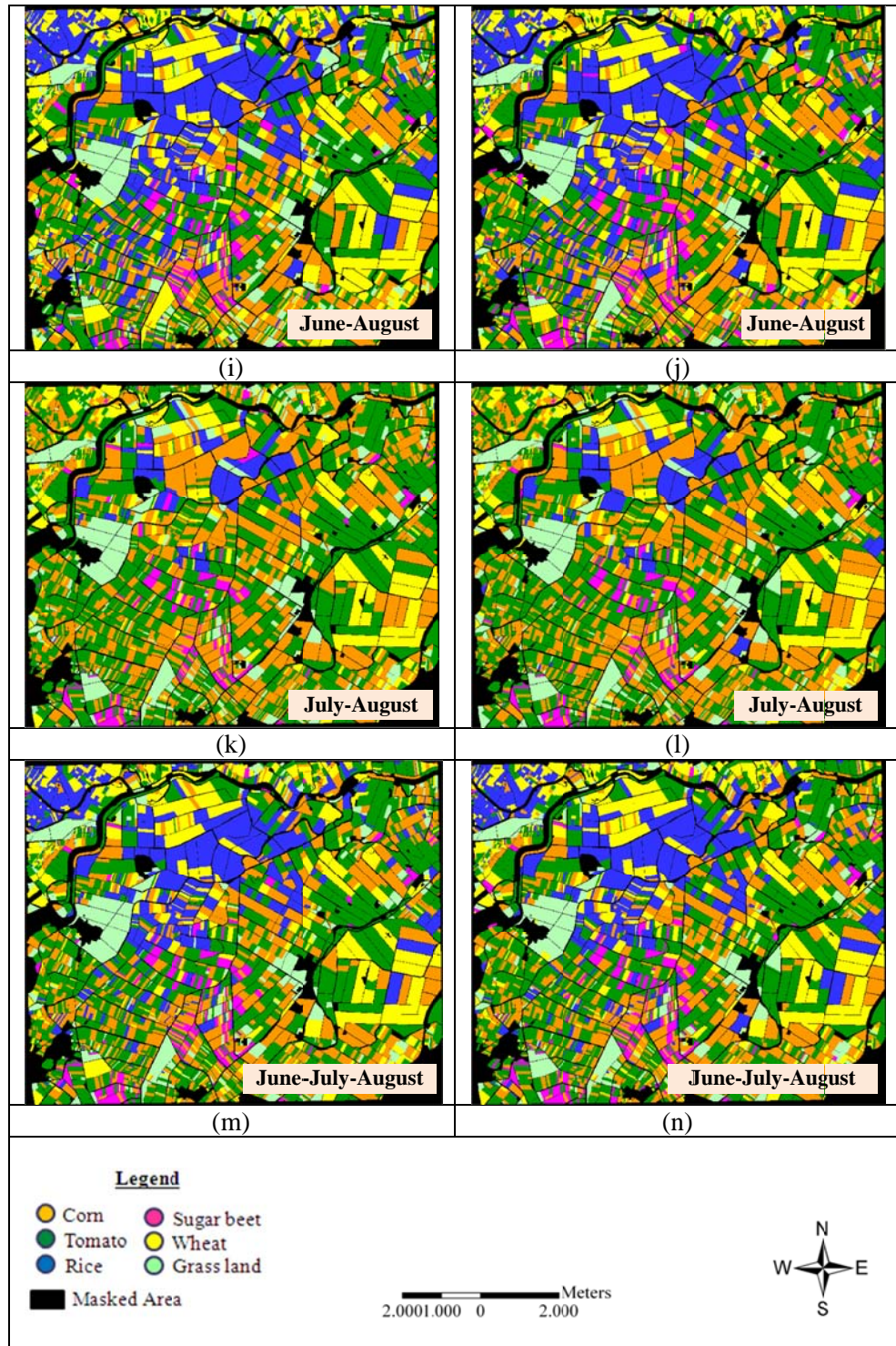


Figure H.8 (Cont'd)



APPENDIX I

CONFUSION MATRICES OF THE PRODUCED THEMATIC MAPS

Table I.1 Confusion matrix of the (a) pixel-based and (b) segment-based MLC, respectively, for the map of June classified with Kompsat-2 data.

Classes	Corn	Grass Land	Rice	Sugar beet	Tomato	Wheat	Row T*	UA*** (%)
Corn	13	6	0	1	7	7	34	38.23
Grass Land	34	51	0	54	21	45	45	24.87
Rice	3	2	88	0	5	0	98	89.79
Sugar beet	20	7	3	28	18	1	77	36.36
Tomato	1	8	3	5	28	0	108	62.22
Wheat	8	23	7	5	14	51	205	47.22
Column T*	79	97	101	93	93	97	567	
PA ** (%)	16.45	52.57	87.12	30.10	30.10	49.03		
Overall A (%): 45.67 Kappa: 0.34								

(a)

Classes	Corn	Grass Land	Rice	Sugar beet	Tomato	Wheat	Row T*	UA*** (%)
Corn	12	0	0	0	3	0	15	80
Grass Land	33	67	0	53	26	46	225	29.77
Rice	3	0	98	0	0	2	103	95.14
Sugar beet	22	5	2	30	13	1	73	41.09
Tomato	0	7	0	2	33	1	43	76.74
Wheat	9	18	1	8	18	54	108	50
Column T*	79	97	101	93	93	104	567	
PA ** (%)	15.19	69.07	97.03	32.25	35.48	51.92		
Overall A (%): 51.85 Kappa: 0.41								

(b)

Table I.2 Confusion matrix of the (a) pixel-based and (b) segment-based MLC, respectively, for the map of July classified with Kompsat-2 data.

Classes	Corn	Grass Land	Rice	Sugar beet	Tomato	Wheat	Row T*	UA*** (%)
Corn	73	6	16	0	19	6	120	60.83
Grass Land	2	83	0	1	3	51	140	59.28
Rice	0	0	84	0	0	0	84	100
Sugar beet	0	0	8	85	2	0	95	89.47
Tomato	8	2	5	12	52	1	80	65
Wheat	0	3	1	0	0	44	48	91.66
Column T*	83	94	114	98	76	102	567	
PA ** (%)	87.95	88.29	73.68	86.73	68.42	43.13		
Overall A (%): 74.25 Kappa: 0.69								

(a)

Classes	Corn	Grass Land	Rice	Sugar beet	Tomato	Wheat	Row T*	UA*** (%)
Corn	83	1	10	1	29	9	133	62.40
Grass Land	0	92	3	1	0	50	146	63.01
Rice	0	0	88	0	0	0	88	100
Sugar beet	0	0	4	80	0	0	84	95.23
Tomato	0	1	9	16	47	0	73	64.38
Wheat	0	0	0	0	0	43	43	100
Column T*	83	94	114	98	76	102	567	
PA ** (%)	100	97.87	77.19	81.63	61.84	42.15		
Overall A (%): 76.36 Kappa: 0.71								

(b)

Table I.3 Confusion matrix of the (a) pixel-based and (b) segment-based MLC, respectively, for the map of August classified with Kompsat-2 data.

Classes	Corn	Grass Land	Rice	Sugar beet	Tomato	Wheat	Row T*	UA*** (%)
Corn	71	0	20	0	3	0	94	75.53
Grass Land	0	72	0	0	24	7	103	69.90
Rice	0	0	63	5	3	0	71	88.73
Sugar beet	1	0	10	65	21	0	97	67.01
Tomato	3	15	5	13	35	4	75	46.66
Wheat	0	25	0	0	0	102	127	80.31
Column T*	75	112	98	83	86	113	567	
PA ** (%)	94.66	64.28	64.28	78.31	40.69	90.26		
Overall A (%): 71.95 Kappa: 0.66								

(a)

Table I.3 (Cont'd)

Classes	Corn	Grass Land	Rice	Sugar beet	Tomato	Wheat	Row T*	UA*** (%)
Corn	70	0	19	1	6	0	96	72.91
Grass Land	0	87	1	0	23	3	114	76.31
Rice	0	0	71	0	0	0	71	100
Sugar beet	0	0	2	77	21	0	100	77
Tomato	5	13	5	5	36	6	70	51.42
Wheat	0	12	0	0	0	102	114	89.47
Column T*	75	112	98	83	86	113	567	
PA ** (%)	93.33	77.67	72.44	92.77	41.86	90.26		
Overall A (%): 78.13 Kappa: 0.73								

(b)

Table I.4 Confusion matrix of the (a) pixel-based and (b) segment-based MLC, respectively, for the map of June-July classified with Kompsat-2 data.

Classes	Corn	Grass Land	Rice	Sugar beet	Tomato	Wheat	Row T*	UA*** (%)
Corn	57	7	3	1	30	6	104	54.80
Grass Land	1	85	1	3	5	34	129	65.89
Rice	0	0	90	1	1	0	92	97.82
Sugar beet	2	1	0	67	1	0	71	94.36
Tomato	10	2	1	11	53	1	78	67.94
Wheat	2	14	0	0	0	77	93	82.79
Column T*	72	109	95	83	90	118	567	
PA ** (%)	79.16	77.98	94.73	80.72	58.88	65.25		
Overall A (%): 75.66 Kappa: 0.70								

(a)

Classes	Corn	Grass Land	Rice	Sugar beet	Tomato	Wheat	Row T*	UA*** (%)
Corn	68	0	2	1	35	5	111	61.26
Grass Land	0	98	0	0	0	20	118	83.05
Rice	0	0	89	0	0	0	89	100
Sugar beet	2	0	0	77	0	0	79	97.46
Tomato	2	0	4	5	55	2	68	80.88
Wheat	0	11	0	0	0	91	102	89.21
Column T*	72	109	95	83	90	118	567	
PA ** (%)	94.44	89.90	93.68	92.77	61.11	77.11		
Overall A (%): 84.30 Kappa: 0.81								

(b)

Table I.5 Confusion matrix of the (a) pixel-based and (b) segment-based MLC, respectively, for the map of June-August classified with Kompsat-2 data.

Classes	Corn	Grass Land	Rice	Sugar beet	Tomato	Wheat	Row T*	UA*** (%)
Corn	60	3	12	1	6	3	85	70.58
Grass Land	3	75	0	1	22	19	120	62.50
Rice	0	0	75	4	1	0	80	93.75
Sugar beet	1	1	4	64	18	0	88	72.72
Tomato	7	5	2	12	43	1	70	61.42
Wheat	0	25	2	1	0	95	124	76.61
Column T*	72	109	95	83	90	118	567	
PA ** (%)	83.33	68.80	78.94	77.10	47.77	80.50		
Overall A (%): 72.66 Kappa: 0.67								

(a)

Classes	Corn	Grass Land	Rice	Sugar beet	Tomato	Wheat	Row T*	UA*** (%)
Corn	66	0	5	0	13	3	87	75.86
Grass Land	0	93	0	1	30	6	130	71.53
Rice	0	0	90	0	0	0	90	100
Sugar beet	1	0	0	75	16	0	92	81.52
Tomato	5	0	0	7	31	0	43	72.09
Wheat	0	16	0	0	0	109	125	87.20
Column T*	72	109	95	83	90	118	567	
PA ** (%)	91.66	85.32	94.73	90.36	34.44	92.37		
Overall A (%): 81.83 Kappa: 0.78								

(b)

Table I.6 Confusion matrices of the (a) pixel-based and (b) segment-based MLC, respectively, for the map of July-August classified with Kompsat-2 data.

Classes	Corn	Grass Land	Rice	Sugar beet	Tomato	Wheat	Row T*	UA*** (%)
Corn	66	3	17	1	25	3	115	57.39
Grass Land	0	78	0	0	7	13	98	79.59
Rice	0	0	70	2	0	0	72	97.22
Sugar beet	0	0	8	63	3	0	74	85.13
Tomato	6	3	0	17	55	3	84	65.47
Wheat	0	25	0	0	0	99	124	79.83
Column T*	72	109	95	83	90	118	567	
PA ** (%)	91.66	71.56	73.68	75.90	61.11	83.89		
Overall A (%): 76.01 Kappa: 0.71								

(a)

Table I.6 (Cont'd)

Classes	Corn	Grass Land	Rice	Sugar beet	Tomato	Wheat	Row T*	UA*** (%)
Corn	92	1	14	1	29	6	143	64.33
Grass Land	0	91	0	1	0	5	97	93.81
Rice	0	0	80	0	0	0	80	100
Sugar beet	1	0	1	53	1	0	56	94.64
Tomato	3	3	1	19	53	1	80	66.25
Wheat	0	11	0	0	0	100	111	90.09
Column T*	72	109	95	83	90	118	567	
PA ** (%)	95.83	85.84	83.33	71.62	63.85	89.28		
		Overall A (%): 82.71		Kappa: 0.79				

(b)

Table I.7 Confusion matrices of the (a) pixel-based and (b) segment-based MLC, respectively, for the combined map (June-July-August) classified with Kompsat-2 data.

Classes	Corn	Grass Land	Rice	Sugar beet	Tomato	Wheat	Row T*	UA*** (%)
Corn	63	6	11	1	25	4	110	57.27
Grass Land	1	75	0	1	8	18	103	72.81
Rice	0	0	80	3	0	0	83	96.38
Sugar beet	1	1	4	63	3	0	72	87.50
Tomato	6	2	0	15	54	2	79	68.35
Wheat	1	25	0	0	0	94	120	78.33
Column T*	72	109	95	83	90	118	567	
PA ** (%)	87.50	68.80	84.21	75.90	60	79.66		
		Overall A (%): 75.66		Kappa: 0.70				

(a)

Classes	Corn	Grass Land	Rice	Sugar beet	Tomato	Wheat	Row T*	UA*** (%)
Corn	68	0	2	1	35	7	113	60.17
Grass Land	0	93	0	0	0	2	95	97.89
Rice	0	0	89	0	0	0	89	100
Sugar beet	2	0	1	71	0	0	74	95.94
Tomato	2	0	3	11	55	2	73	75.34
Wheat	0	16	0	0	0	107	123	86.99
Column T*	72	109	95	83	90	118	567	
PA ** (%)	94.44	85.32	93.68	85.54	61.11	90.67		
		Overall A (%): 85.18		Kappa: 0.82				

(b)

Table I.8 Confusion matrix of the (a) pixel-based and (b) segment-based MLC, respectively, for the map of June classified with Kompsat-2 data and Envisat ASAR data.

Classes	Corn	Grass Land	Rice	Sugar beet	Tomato	Wheat	Row T*	UA*** (%)
Corn	12	5	0	0	7	6	30	40
Grass Land	33	61	0	21	14	45	174	35.05
Rice	3	2	91	0	3	0	99	91.91
Sugar beet	21	4	1	60	19	1	106	56.60
Tomato	3	6	3	6	32	0	50	64
Wheat	7	19	6	6	18	52	108	48.14
Column T*	79	104	101	93	93	104	567	
PA ** (%)	15.19	62.88	90.09	64.51	34.40	50		
Overall A (%): 54.32 Kappa: 0.44								

(a)

Classes	Corn	Grass Land	Rice	Sugar beet	Tomato	Wheat	Row T*	UA*** (%)
Corn	12	0	0	0	3	0	15	80
Grass Land	32	80	0	13	13	45	183	43.71
Rice	3	0	98	0	0	2	103	95.14
Sugar beet	22	0	1	70	13	1	107	65.42
Tomato	1	0	0	2	46	1	50	92
Wheat	9	17	2	8	18	55	109	50.45
Column T*	79	97	101	93	93	104	567	
PA ** (%)	15.19	82.47	97.03	75.26	49.46	52.88		
Overall A (%): 63.66 Kappa: 0.56								

(b)

Table I.9 Confusion matrix of the (a) pixel-based and (b) segment-based MLC, respectively, for the map of July classified with Kompsat-2 data and Envisat ASAR data.

Classes	Corn	Grass Land	Rice	Sugar beet	Tomato	Wheat	Row T*	UA*** (%)
Corn	75	9	16	0	18	6	124	60.48
Grass Land	3	82	0	1	3	47	136	60.29
Rice	0	0	83	0	0	0	83	100
Sugar beet	0	0	8	85	2	0	95	89.47
Tomato	5	0	6	12	53	1	77	68.83
Wheat	0	3	1	0	0	48	52	92.30
Column T*	83	94	114	98	76	102	567	
PA ** (%)	90.36	87.23	72.80	86.73	69.73	47.05		
Overall A (%): 75.13 Kappa: 0.70								

(a)

Table I.9 (Cont'd)

Classes	Corn	Grass Land	Rice	Sugar beet	Tomato	Wheat	Row T*	UA*** (%)
Corn	83	1	11	2	10	9	116	71.55
Grass Land	0	93	2	0	0	47	142	65.49
Rice	0	0	88	0	0	0	88	100
Sugar beet	0	0	4	80	0	0	84	95.23
Tomato	0	0	9	16	66	0	91	72.52
Wheat	0	0	0	0	0	46	46	100
Column T*	83	94	114	98	76	102	567	
PA ** (%)	100	98.93	77.19	81.63	86.84	45.09		
Overall A (%): 80.42 Kappa: 0.76								

(b)

Table I.10 Confusion matrix of the (a) pixel-based and (b) segment-based MLC, respectively, for the map of August classified with Kompsat-2 data and Envisat ASAR data.

Classes	Corn	Grass Land	Rice	Sugar beet	Tomato	Wheat	Row T*	UA*** (%)
Corn	72	0	15	0	2	0	89	80.89
Grass Land	0	81	0	0	2	4	87	93.10
Rice	0	0	71	5	3	0	79	89.87
Sugar beet	1	1	7	66	18	0	93	70.96
Tomato	2	12	5	12	56	6	93	60.21
Wheat	0	18	0	0	5	103	126	81.74
Column T*	75	112	98	83	86	112	567	
PA ** (%)	96	72.32	72.44	79.51	65.11	91.15		
Overall A (%): 79.18 Kappa: 0.75								

(a)

Classes	Corn	Grass Land	Rice	Sugar beet	Tomato	Wheat	Row T*	UA*** (%)
Corn	69	0	14	1	6	0	90	76.66
Grass Land	0	89	0	0	4	4	97	91.75
Rice	0	0	77	0	0	0	77	100
Sugar beet	0	0	1	75	21	0	97	77.32
Tomato	6	11	6	7	55	5	90	61.11
Wheat	0	12	0	0	0	104	116	89.65
Column T*	75	112	98	83	86	113	567	
PA ** (%)	92	79.46	78.57	90.36	63.95	92.03		
Overall A (%): 82.71 Kappa: 0.79								

(b)

Table I.11 Confusion matrices of the (a) pixel-based and (b) segment-based MLC, respectively, for the map of June-July classified with the MS Kompsat-2 and Envisat ASAR data

Classes	Corn	Grass Land	Rice	Sugar beet	Tomato	Wheat	Row T*	UA*** (%)
Corn	74	8	4	1	23	4	114	64.91
Grass Land	2	62	1	3	0	38	106	58.49
Rice	0	0	106	0	0	0	106	100
Sugar beet	0	3	0	72	2	0	77	93.50
Tomato	5	2	4	15	45	0	71	63.38
Wheat	1	10	1	3	0	78	93	83.87
Column T*	82	85	116	94	70	120	567	
PA ** (%)	90.24	72.94	91.37	76.59	64.28	65		
Overall A (%): 77.07		Kappa: 0.72						

(a)

Classes	Corn	Grass Land	Rice	Sugar beet	Tomato	Wheat	Row T*	UA*** (%)
Corn	80	1	1	1	17	9	109	73.39
Grass Land	0	76	1	1	0	19	97	78.35
Rice	0	0	112	0	0	0	112	100
Sugar beet	0	0	0	83	0	0	83	100
Tomato	2	1	2	7	53	0	65	81.53
Wheat	0	7	0	2	0	92	101	91.08
Column T*	82	85	116	94	70	120	567	
PA ** (%)	97.56	89.41	96.55	88.29	75.71	76.66		
Overall A (%): 87.48		Kappa: 0.84						

(b)

Table I.12 Confusion matrices of the (a) pixel-based and (b) segment-based MLC, respectively, for the map of June-August classified with the MS Kompsat-2 and Envisat ASAR data

Classes	Corn	Grass Land	Rice	Sugar beet	Tomato	Wheat	Row T*	UA*** (%)
Corn	75	4	13	0	2	0	94	79.78
Grass Land	4	69	0	0	8	14	95	72.63
Rice	5	0	78	3	0	0	86	90.69
Sugar beet	1	0	2	81	12	0	96	84.37
Tomato	1	4	0	18	47	1	71	66.19
Wheat	2	22	0	0	4	97	125	77.60
Column T*	82	99	93	102	73	112	567	
PA ** (%)	85.22	69.69	83.87	79.41	64.38	86.60		
Overall A (%): 78.83		Kappa: 0.74						

(a)

Table I.12 (Cont'd)

Classes	Corn	Grass Land	Rice	Sugar beet	Tomato	Wheat	Row T*	UA*** (%)
Corn	63	0	0	1	9	2	75	84
Grass Land	0	93	0	0	6	2	101	92.07
Rice	0	0	92	0	0	0	92	100
Sugar beet	3	0	2	71	3	0	79	89.87
Tomato	6	0	1	11	72	2	92	78.26
Wheat	0	16	0	0	0	112	128	87.50
Column T*	72	109	95	83	90	118	567	
PA ** (%)	87.50	85.32	96.84	85.54	80	94.91		
Overall A (%): 88.71 Kappa: 0.86								

(b)

Table I.13 Confusion matrices of the (a) pixel-based and (b) segment-based MLC, respectively, for the map of July-August classified with the MS Kompasat-2 and Envisat ASAR data

Classes	Corn	Grass Land	Rice	Sugar beet	Tomato	Wheat	Row T*	UA*** (%)
Corn	84	5	10	0	12	2	113	74.33
Grass Land	0	82	0	0	1	13	96	85.41
Rice	0	0	78	3	1	0	82	95.12
Sugar beet	0	0	5	46	7	0	58	79.31
Tomato	11	4	3	25	60	1	104	57.69
Wheat	1	15	0	0	2	96	114	84.21
Column T*	96	106	96	74	83	112	567	
PA ** (%)	87.50	77.35	81.25	62.16	72.28	85.71		
Overall A (%): 78.66 Kappa: 0.74								

(a)

Classes	Corn	Grass Land	Rice	Sugar beet	Tomato	Wheat	Row T*	UA*** (%)
Corn	83	1	11	1	10	6	112	74.10
Grass Land	0	92	0	1	0	2	95	96.84
Rice	0	1	84	0	0	0	85	98.82
Sugar beet	1	0	0	53	4	0	58	91.37
Tomato	12	2	1	19	69	1	104	66.34
Wheat	0	10	0	0	0	103	113	91.15
Column T*	96	106	96	74	83	112	567	
PA ** (%)	86.45	86.79	87.50	71.62	83.13	91.96		
Overall A (%):85.36 Kappa: 0.82								

(b)

Table I.14 Confusion matrices of the (a) pixel-based and (b) segment-based MLC, respectively, for the combined map (June-July-August) classified with the MS Kompsat-2 and Envisat ASAR data

Classes	Corn	Grass Land	Rice	Sugar beet	Tomato	Wheat	Row T*	UA*** (%)
Corn	67	6	6	1	19	4	103	65.04
Grass Land	1	77	0	0	1	19	98	78.57
Rice	0	0	84	2	0	0	86	97.67
Sugar beet	1	0	3	63	6	0	73	86.30
Tomato	2	3	2	17	64	1	89	71.91
Wheat	1	23	0	0	0	94	118	79.66
Column T*	72	109	95	83	90	118	567	
PA ** (%)	93.05	70.64	88.42	75.90	71.11	79.66		
Overall A (%): 79.18 Kappa: 0.75								

(a)

Classes	Corn	Grass Land	Rice	Sugar beet	Tomato	Wheat	Row T*	UA*** (%)
Corn	63	0	2	1	9	6	81	77.77
Grass Land	0	93	0	0	0	2	95	97.89
Rice	0	0	90	0	0	0	90	100
Sugar beet	2	0	0	71	3	0	76	93.42
Tomato	7	0	3	11	78	2	101	77.22
Wheat	0	16	0	0	0	108	124	87.09
Column T*	72	109	95	83	90	118	567	
PA ** (%)	87.50	85.32	94.73	85.54	86.66	91.52		
Overall A (%): 88.71 Kappa: 0.86								

(b)

Table I.15 Confusion matrix of the (a) pixel-based and (b) segment-based SVM, respectively, for the map of June classified with Kompsat-2 data.

Classes	Corn	Grass Land	Rice	Sugar beet	Tomato	Wheat	Row T*	UA*** (%)
Corn	16	10	0	1	6	6	39	41.02
Grass Land	24	39	0	14	24	47	148	26.35
Rice	7	9	94	0	11	1	122	77.04
Sugar beet	18	9	0	68	18	0	113	60.17
Tomato	1	4	2	3	26	0	36	72.22
Wheat	13	26	5	7	8	50	109	45.87
Column T*	79	97	101	93	93	104	567	
PA ** (%)	20.25	40.20	93.06	73.11	27.95	48.07		
Overall A (%): 51.67 Kappa: 0.41								

(a)

Table I.15 (Cont'd)

Classes	Corn	Grass Land	Rice	Sugar beet	Tomato	Wheat	Row T*	UA*** (%)
Corn	16	3	0	0	3	0	22	72.72
Grass Land	27	60	0	3	26	48	164	36.58
Rice	6	0	98	1	9	5	119	82.35
Sugar beet	24	4	0	80	13	0	121	66.11
Tomato	0	0	0	2	33	0	35	94.28
Wheat	6	30	3	7	9	51	106	48.11
Column T*	79	97	101	93	93	104	567	
PA ** (%)	20.25	61.85	97.03	86.02	35.48	49.03		
		Overall A (%): 59.61		Kappa: 0.51				

(b)

Table I.16 Confusion matrix of the (a) pixel-based and (b) segment-based SVM, respectively, for the map of July classified with Kompsat-2 data.

Classes	Corn	Grass Land	Rice	Sugar beet	Tomato	Wheat	Row T*	UA*** (%)
Corn	71	12	12	0	6	7	108	65.74
Grass Land	2	63	0	0	0	15	80	78.75
Rice	0	0	72	0	0	0	72	100
Sugar beet	0	0	0	78	1	0	86	90.69
Tomato	10	14	22	20	69	2	137	50.36
Wheat	0	5	1	0	0	78	84	92.85
Column T*	83	94	114	98	76	102	567	
PA ** (%)	85.54	67.02	63.15	79.59	90.78	76.47		
		Overall A (%): 76.01		Kappa: 0.71				

(a)

Classes	Corn	Grass Land	Rice	Sugar beet	Tomato	Wheat	Row T*	UA*** (%)
Corn	83	5	8	1	7	7	111	74.77
Grass Land	0	84	2	0	0	11	97	86.59
Rice	0	0	83	0	0	0	83	100
Sugar beet	0	0	4	76	0	0	80	95
Tomato	0	5	17	21	69	2	114	60.52
Wheat	0	0	0	0	0	82	82	100
Column T*	83	94	114	98	76	102	567	
PA ** (%)	100	89.36	72.80	77.55	90.78	80.39		
		Overall A (%): 84.12		Kappa: 0.81				

(b)

Table I.17 Confusion matrix of the (a) pixel-based and (b) segment-based SVM, respectively, for the map of August classified with Kompsat-2 data.

Classes	Corn	Grass Land	Rice	Sugar beet	Tomato	Wheat	Row T*	UA*** (%)
Corn	74	0	33	0	1	0	108	68.51
Grass Land	0	55	2	0	17	8	82	67.07
Rice	0	1	62	14	1	0	78	79.48
Sugar beet	0	0	8	39	5	0	52	75
Tomato	9	16	8	44	51	4	132	38.63
Wheat	0	22	1	1	1	90	115	78.26
Column T*	83	94	114	98	76	102	567	
PA ** (%)	89.15	58.51	54.38	39.76	67.10	88.23		
Overall A (%): 65.43 Kappa: 0.58								

(a)

Classes	Corn	Grass Land	Rice	Sugar beet	Tomato	Wheat	Row T*	UA*** (%)
Corn	70	0	31	1	1	0	103	67.96
Grass Land	0	59	1	0	13	6	79	74.68
Rice	0	0	59	0	0	0	59	100
Sugar beet	0	0	2	40	5	0	47	85.10
Tomato	5	10	5	42	67	2	131	51.14
Wheat	0	43	0	0	0	105	148	70.94
Column T*	75	112	98	83	86	113	567	
PA ** (%)	93.33	52.67	60.20	48.19	77.90	92.92		
Overall A (%): 70.54 Kappa: 0.64								

(b)

Table I.18 Confusion matrix of the (a) pixel-based and (b) segment-based SVM, respectively, for the map of June-July classified with Kompsat-2 data.

Classes	Corn	Grass Land	Rice	Sugar beet	Tomato	Wheat	Row T*	UA*** (%)
Corn	64	12	3	0	4	7	90	71.11
Grass Land	7	65	1	0	3	15	91	71.42
Rice	4	1	102	0	1	0	108	94.44
Sugar beet	2	2	2	82	5	0	93	88.17
Tomato	6	6	5	16	63	1	97	64.94
Wheat	0	8	1	0	0	79	88	89.77
Column T*	83	94	114	98	76	102	567	
PA ** (%)	77.10	69.14	89.47	83.67	82.89	77.45		
Overall A (%): 80.24 Kappa: 0.76								

(a)

Table I.18 (Cont'd)

Classes	Corn	Grass Land	Rice	Sugar beet	Tomato	Wheat	Row T*	UA*** (%)
Corn	79	0	0	0	6	7	92	85.87
Grass Land	0	92	0	0	0	9	101	91.08
Rice	4	0	111	1	1	0	117	94.87
Sugar beet	0	0	0	85	0	0	85	100
Tomato	0	2	1	12	69	2	86	80.23
Wheat	0	0	2	0	0	84	86	97.67
Column T*	83	94	114	98	76	102	567	
PA ** (%)	95.18	97.87	97.36	86.73	90.78	82.35		
Overall A (%): 91.71 Kappa: 0.90								

(b)

Table I.19 Confusion matrix of the (a) pixel-based and (b) segment-based SVM, respectively, for the map of June-August classified with Kompsat-2 data.

Classes	Corn	Grass Land	Rice	Sugar beet	Tomato	Wheat	Row T*	UA*** (%)
Corn	57	6	3	0	2	2	70	81.42
Grass Land	12	57	0	0	19	10	98	58.16
Rice	4	1	106	10	7	0	128	82.81
Sugar beet	5	3	1	55	6	0	70	78.57
Tomato	4	7	3	32	37	2	85	43.52
Wheat	1	20	1	1	5	88	116	75.86
Column T*	83	94	114	98	76	102	567	
PA ** (%)	68.67	60.63	92.98	56.12	48.68	86.27		
Overall A (%): 70.54 Kappa: 0.64								

(a)

Classes	Corn	Grass Land	Rice	Sugar beet	Tomato	Wheat	Row T*	UA*** (%)
Corn	79	1	0	0	6	0	86	91.86
Grass Land	0	73	0	0	21	1	95	76.84
Rice	4	0	112	1	10	3	130	86.15
Sugar beet	0	1	0	69	0	0	70	98.57
Tomato	0	2	0	28	39	2	71	54.93
Wheat	0	17	2	0	0	96	115	83.47
Column T*	83	94	114	98	76	102	567	
PA ** (%)	95.18	77.66	98.24	70.40	51.31	94.11		
Overall A (%): 82.54 Kappa: 0.78								

(b)

Table I.20 Confusion matrix of the (a) pixel-based and (b) segment-based SVM, respectively, for the map of July-August classified with Kompsat-2 data.

Classes	Corn	Grass Land	Rice	Sugar beet	Tomato	Wheat	Row T*	UA*** (%)
Corn	73	7	19	0	3	4	106	68.86
Grass Land	0	70	0	0	0	6	76	92.10
Rice	0	1	78	3	1	0	83	93.97
Sugar beet	0	0	3	69	1	0	73	94.52
Tomato	10	10	13	25	71	3	132	53.78
Wheat	0	6	1	1	0	89	97	91.75
Column T*	83	94	114	98	76	102	567	
PA ** (%)	87.95	74.46	68.42	70.40	93.42	87.25		
Overall A (%): 79.36 Kappa: 0.75								

(a)

Classes	Corn	Grass Land	Rice	Sugar beet	Tomato	Wheat	Row T*	UA*** (%)
Corn	79	1	10	1	7	7	105	75.23
Grass Land	0	89	2	0	0	8	99	89.89
Rice	0	0	97	0	0	0	97	100
Sugar beet	0	0	2	72	0	0	74	97.29
Tomato	4	4	3	25	69	2	107	64.48
Wheat	0	0	0	0	0	85	85	100
Column T*	83	94	114	98	76	102	567	
PA ** (%)	95.18	94.68	85.08	73.46	90.78	83.33		
Overall A (%): 86.59 Kappa: 0.83								

(b)

Table I.21 Confusion matrix of the (a) pixel-based and (b) segment-based SVM, respectively, for the map of the combined map (June-July-August) classified with Kompsat-2 data.

Classes	Corn	Grass Land	Rice	Sugar beet	Tomato	Wheat	Row T*	UA*** (%)
Corn	66	9	4	0	3	3	85	77.64
Grass Land	5	68	0	0	3	5	81	83.95
Rice	4	0	103	3	2	0	112	91.96
Sugar beet	2	2	1	73	4	0	82	89.02
Tomato	6	6	5	21	64	3	105	60.95
Wheat	0	9	1	1	0	91	102	89.21
Column T*	83	94	114	98	76	102	567	
PA ** (%)	79.51	72.34	90.35	74.49	84.21	89.21		
Overall A (%): 82.01 Kappa: 0.78								

(a)

Table I.21 (Cont'd)

Classes	Corn	Grass Land	Rice	Sugar beet	Tomato	Wheat	Row T*	UA*** (%)
Corn	79	1	0	0	6	7	93	84.94
Grass Land	0	87	0	0	0	1	88	98.86
Rice	4	0	111	1	1	0	117	94.87
Sugar beet	0	0	0	80	0	0	80	100
Tomato	0	3	1	17	69	2	92	75
Wheat	0	3	2	0	0	92	97	94.84
Column T*	83	94	114	98	76	102	567	
PA ** (%)	95.18	92.55	97.36	81.63	90.78	90.19		
Overall A (%): 91.85 Kappa: 0.89								

(b)

Table I.22 Confusion matrix of the (a) pixel-based and (b) segment-based SVM, respectively, for the map of June classified with Kompsat-2 data and Envisat ASAR data.

Classes	Corn	Grass Land	Rice	Sugar beet	Tomato	Wheat	Row T*	UA*** (%)
Corn	19	12	0	2	8	5		41.30
Grass Land	21	46	0	2	14	46		35.65
Rice	5	7	95	0	9	0		81.89
Sugar beet	20	5	0	77	20	2		62.09
Tomato	1	4	1	4	35	0		77.77
Wheat	13	23	5	8	7	51		47.66
Column T*	79	97	101	93	93	104	567	
PA ** (%)	24.05	47.42	94.05	82.79	37.63	49.03		
Overall A (%): 56.96 Kappa: 0.48								

(a)

Classes	Corn	Grass Land	Rice	Sugar beet	Tomato	Wheat	Row T*	UA*** (%)
Corn	17	4	0	0	4	1	26	65.38
Grass Land	19	71	0	3	14	42	149	47.65
Rice	3	0	97	0	9	3	112	86.60
Sugar beet	31	1	0	79	13	3	127	62.20
Tomato	0	0	0	4	44	1	49	89.79
Wheat	9	21	4	7	9	54	104	51.92
Column T*	79	97	101	93	93	104	567	
PA ** (%)	21.51	73.19	96.04	84.94	47.31	51.92		
Overall A (%): 63.84 Kappa: 0.56								

(b)

Table I.23 Confusion matrix of the (a) pixel-based and (b) segment-based SVM, respectively, for the map of July classified with Kompsat-2 data and Envisat ASAR data.

Classes	Corn	Grass Land	Rice	Sugar beet	Tomato	Wheat	Row T*	UA*** (%)
Corn	74	9	10	0	8	7	108	68.51
Grass Land	2	78	1	0	1	11	93	83.87
Rice	0	0	73	0	0	0	73	100
Sugar beet	0	0	8	77	1	0	86	89.53
Tomato	7	4	21	21	66	3	122	54.09
Wheat	0	3	1	0	0	81	85	95.29
Column T*	83	94	114	98	76	102	567	
PA ** (%)	89.15	82.97	64.03	78.57	86.84	79.41		
Overall A (%): 79.18 Kappa: 0.75								

(a)

Classes	Corn	Grass Land	Rice	Sugar beet	Tomato	Wheat	Row T*	UA*** (%)
Corn	83	0	9	1	6	7	106	78.30
Grass Land	0	92	2	0	0	11	105	87.61
Rice	0	0	81	0	0	0	81	100
Sugar beet	0	0	2	76	0	0	78	97.43
Tomato	0	2	20	21	70	2	115	60.87
Wheat	0	0	0	0	0	82	82	100
Column T*	83	94	114	98	76	102	567	
PA ** (%)	100	97.87	71.05	77.55	92.10	80.39		
Overall A (%): 85.36 Kappa: 0.82								

(b)

Table I.24 Confusion matrix of the (a) pixel-based and (b) segment-based SVM, respectively, for the map of August classified with Kompsat-2 data and Envisat ASAR data.

Classes	Corn	Grass Land	Rice	Sugar beet	Tomato	Wheat	Row T*	UA*** (%)
Corn	71	0	23	0	5	0	99	71.71
Grass Land	0	67	0	0	0	4	71	94.36
Rice	0	0	63	3	1	0	67	94.03
Sugar beet	1	0	9	50	3	0	63	79.36
Tomato	3	13	3	30	76	5	130	58.46
Wheat	0	32	0	0	1	104	137	75.91
Column T*	75	112	98	83	86	113	567	
PA ** (%)	94.66	59.82	64.28	60.24	88.37	92.03		
Overall A (%): 76.01 Kappa: 0.71								

(a)

Table I.24 (Cont'd)

Classes	Corn	Grass Land	Rice	Sugar beet	Tomato	Wheat	Row T*	UA*** (%)
Corn	69	0	26	1	1	0	97	71.13
Grass Land	0	92	1	0	0	7	100	92
Rice	0	0	62	0	0	0	62	100
Sugar beet	0	0	3	40	8	0	51	78.43
Tomato	6	1	6	42	77	2	134	57.46
Wheat	0	19	0	0	0	104	123	84.55
Column T*	75	112	98	83	86	113	567	
PA ** (%)	92	82.14	63.26	48.19	89.53	92.03		
Overall A (%): 78.30				Kappa: 0.73				

(b)

Table I.25 Confusion matrix of the (a) pixel-based and (b) segment-based SVM, respectively, for the map of June-July classified with Kompsat-2 data and Envisat ASAR data.

Classes	Corn	Grass Land	Rice	Sugar beet	Tomato	Wheat	Row T*	UA*** (%)
Corn	61	10	3	0	3	7	84	72.61
Grass Land	4	73	0	0	2	13	92	79.34
Rice	4	0	104	0	1	0	109	95.41
Sugar beet	9	3	0	84	13	1	110	76.36
Tomato	3	3	5	14	56	1	82	68.29
Wheat	2	5	2	0	1	80	90	88.88
Column T*	83	94	114	98	76	102	567	
PA ** (%)	73.49	77.66	91.22	85.71	73.68	78.43		
Overall A (%): 80.77				Kappa: 0.76				

(a)

Classes	Corn	Grass Land	Rice	Sugar beet	Tomato	Wheat	Row T*	UA*** (%)
Corn	75	0	0	1	6	7	89	84.27
Grass Land	0	93	1	0	0	1	95	97.89
Rice	4	0	111	1	1	0	117	94.87
Sugar beet	4	0	0	85	0	1	90	94.44
Tomato	0	1	1	11	69	1	83	83.13
Wheat	0	0	1	0	0	92	93	98.92
Column T*	83	94	114	98	76	102	567	
PA ** (%)	90.36	98.93	97.36	86.73	90.78	90.19		
Overall A (%): 92.59				Kappa: 0.91				

(b)

Table I.26 Confusion matrix of the (a) pixel-based and (b) segment-based SVM, respectively, for the map of June-August classified with Kompsat-2 data and Envisat ASAR data.

Classes	Corn	Grass Land	Rice	Sugar beet	Tomato	Wheat	Row T*	UA*** (%)
Corn	56	2	2	0	0	3	63	88.88
Grass Land	5	70	0	1	2	7	85	82.35
Rice	4	0	108	1	5	0	118	91.52
Sugar beet	14	2	0	81	11	1	109	74.31
Tomato	2	2	3	14	56	0	77	72.72
Wheat	2	18	1	1	2	91	115	79.13
Column T*	83	94	114	98	76	102	567	
PA ** (%)	67.47	74.46	94.73	82.65	73.68	89.21		
Overall A (%): 81.48 Kappa: 0.77								

(a)

Classes	Corn	Grass Land	Rice	Sugar beet	Tomato	Wheat	Row T*	UA*** (%)
Corn	75	1	0	0	6	1	83	90.36
Grass Land	0	80	0	0	0	0	80	100
Rice	4	0	112	1	10	3	130	86.15
Sugar beet	4	0	0	86	0	1	96	89.58
Tomato	0	2	0	11	55	1	69	79.71
Wheat	0	11	2	0	0	96	109	88.07
Column T*	83	94	114	98	76	102	567	
PA ** (%)	90.36	85.10	98.24	87.75	72.36	94.11		
Overall A (%): 88.88 Kappa: 0.86								

(b)

Table I.27 Confusion matrix of the (a) pixel-based and (b) segment-based SVM, respectively, for the map of July-August classified with Kompsat-2 data and Envisat ASAR data.

Classes	Corn	Grass Land	Rice	Sugar beet	Tomato	Wheat	Row T*	UA*** (%)
Corn	72	2	12	0	3	5	94	76.59
Grass Land	1	82	1	0	0	6	90	91.11
Rice	0	0	89	4	1	0	94	94.68
Sugar beet	0	0	2	64	2	0	68	94.11
Tomato	10	3	9	29	70	1	122	57.37
Wheat	0	7	1	1	0	90	99	90.90
Column T*	83	94	114	98	76	102	567	
PA ** (%)	86.74	87.23	78.07	65.30	92.10	88.23		
Overall A (%): 82.36 Kappa: 0.78								

(a)

Table I.27 (Cont'd)

Classes	Corn	Grass Land	Rice	Sugar beet	Tomato	Wheat	Row T*	UA*** (%)
Corn	79	1	9	2	7	7	105	75.23
Grass Land	0	89	2	0	0	8	99	89.89
Rice	0	0	99	0	0	0	99	100
Sugar beet	0	0	2	69	0	0	71	97.18
Tomato	4	3	2	27	69	1	106	65.09
Wheat	0	1	0	0	0	86	87	98.85
Column T*	83	89	114	98	76	102	567	
PA ** (%)	95.18	94.68	86.84	70.40	90.78	84.31		
Overall A (%): 86.59				Kappa: 0.83				

(b)

Table I.28 Confusion matrix of the (a) pixel-based and (b) segment-based SVM, respectively, for the combined map (June-July-August) classified with Kompsat-2 data and Envisat ASAR data.

Classes	Corn	Grass Land	Rice	Sugar beet	Tomato	Wheat	Row T*	UA*** (%)
Corn	59	3	4	0	0	3	69	85.50
Grass Land	4	78	0	0	1	6	89	87.64
Rice	4	0	106	1	1	0	112	94.64
Sugar beet	11	2	0	81	10	1	105	77.14
Tomato	3	2	3	15	64	1	88	72.72
Wheat	2	9	1	1	0	91	104	87.50
Column T*	83	94	114	98	76	102	567	
PA ** (%)	71.08	82.97	92.98	82.65	84.21	89.21		
Overall A (%): 84.48				Kappa: 0.81				

(a)

Classes	Corn	Grass Land	Rice	Sugar beet	Tomato	Wheat	Row T*	UA*** (%)
Corn	75	1	1	1	6	4	88	85.22
Grass Land	0	89	0	0	0	1	90	98.88
Rice	4	0	111	1	1	0	117	94.87
Sugar beet	4	0	0	83	0	1	88	94.31
Tomato	0	0	0	13	69	1	83	83.13
Wheat	0	4	2	0	0	95	101	94.05
Column T*	90.36	94.68	97.36	84.69	90.78	93.13	567	
PA ** (%)								
Overall A (%): 92.06				Kappa: 0.90				

(b)

Table I.29 Segment-based results of the MLC method of the (a) class pea and (b) late corn computed for the Kompsat-2 and Envisat ASAR data.

Classes	Corn	Grass Land	Rice	Sugar beet	Tomato	Wheat	Pea	Row T*	UA*** (%)
Corn	9	3	0	1	1	8	1	23	39.13
Grass Land	29	51	1	2	17	28	6	134	38.06
Rice	1	0	88	2	2	1	10	104	84.61
Sugar beet	3	2	2	63	7	3	2	82	76.82
Tomato	3	5	0	3	17	1	5	34	50
Wheat	5	18	4	2	6	76	25	136	55.88
Pea	6	2	1	0	4	6	35	54	64.81
Column T*	56	81	96	73	54	123	84	567	
PA ** (%)	16.07	62.96	91.66	86.30	31.48	61.78	41.66		
		Overall A (%): 59.78		Kappa: 0.52					

(a)

Classes	Corn	Grass Land	Rice	Sugar beet	Tomato	Wheat	Late Corn	Row T*	UA*** (%)
Corn	64	1	0	0	13	0	31	111	57.65
Grass Land	0	54	0	0	0	31	4	89	60.67
Rice	0	0	83	1	4	1	0	89	93.25
Sugar beet	0	0	4	71	1	0	0	76	93.42
Tomato	3	0	1	9	51	0	1	65	78.46
Wheat	0	14	2	0	0	63	9	88	71.59
Late Corn	1	9	0	0	6	3	30	49	61.22
Column T*	68	78	90	81	75	98	77	567	
PA ** (%)	94.11	69.23	92.22	87.65	68	64.28	38.96		
		Overall A (%): 73.36		Kappa: 0.68					

(b)

Table I.30 Confusion matrix of the MLC field-based results for all the reference fields computed for the Kompsat-2 and Envisat ASAR data

	Corn	Grass Land	Rice	Sugar beet	Tomato	Wheat	Row T	UA	
Corn	26	0	1	0	1	6	34	76.47	
Grass Land	0	25	0	0	0	2	27	92.59	
Rice	0	0	48	0	0	1	49	97.95	
Sugar beet	0	0	0	54	0	0	54	100	
Tomato	1	0	0	5	8	0	14	57.14	
Wheat	0	3	0	0	0	84	87	96.55	
Column T	27	28	49	59	9	93	265		
PA	96.29	89.28	97.95	91.52	88.88	90.32			
		Overall A (%): 92.45		Kappa: 0.90					

Table I.31 Confusion matrix of the field-based results for the MLC method computed for small fields (0.1-4.9 ha) with the Kompsat-2 and Envisat ASAR data.

	Corn	Grass Land	Rice	Sugar beet	Tomato	Wheat	Row T	UA
Corn	25	0	0	0	1	5	31	80.64
Grass Land	0	7	0	0	0	2	9	77.77
Rice	0	0	34	0	0	1	35	97.14
Sugar beet	0	0	0	48	0	0	48	100
Tomato	1	0	0	5	8	0	14	57.14
Wheat	0	3	0	0	0	55	58	94.82
Column T	26	10	34	53	9	63	195	
PA	96.15	70	100	90.56	88.88	87.30		
Overall A (%): 90.76 Kappa: 0.81								

Table I.32 Confusion matrix of the field-based results for the MLC method computed for medium fields (5 - 9.9 ha) with the Kompsat-2 and Envisat ASAR data.

	Grass Land	Rice	Sugar beet	Wheat	Row T	UA
Grass Land	6	0	0	0	6	100
Rice	0	12	0	0	12	100
Sugar beet	0	1	1	0	2	50
Wheat	0	0	0	12	12	100
Column T	6	13	0	0	32	
PA	100	92.30	100	100		
Overall A (%): 96.87 Kappa: 0.95						

Table I.33 Confusion matrix of the field-based results for the MLC method computed for large fields (10 - 38 ha) with the Kompsat-2 and Envisat ASAR data.

	Grass Land	Rice	Wheat	Row T	UA
Grass Land	9	0	0	9	100
Rice	0	1	0	1	100
Wheat	0	0	12	12	100
Column T	9	1	12	22	
PA	100	100	100	100	
Overall A (%): 100 Kappa: 100					

Table I.34 Confusion matrix of the field-based results for the SVMs method computed for all the fields with the Kompsat-2 and Envisat ASAR data.

	Corn	Grass Land	Rice	Sugar beet	Tomato	Wheat	Row T	UA
Corn	24	0	0	0	0	3	27	88.88
Grass Land	0	24	0	0	0	4	28	85.71
Rice	1	0	49	0	0	1	51	96.07
Sugar beet	2	0	0	53	0	2	57	92.98
Tomato	0	2	0	6	9	0	17	52.94
Wheat	0	2	0	0	0	83	85	97.64
Column T	27	28	49	59	9	93	265	
PA	88.88	85.71	100	89.83	100	89.24		
Overall A (%): 91.31 Kappa: 0.88								

CURRICULUM VITAE

PERSONAL INFORMATION

Surname, Name: Özdarıcı Ok, Asli
Nationality: Turkish (T.C.)
Date and Place of Birth: 01 January 1981, Kırsehir
Marital Status: Married
Phone: +90 533 813 2194
e-mail: aozdarici@gmail.com

EDUCATION

Degree	Institution	Graduation Year
M.Sci.	Geodetic and Geographic Information Technologies Dept., Ankara	2005
B.Sci.	Zonguldak Karaelmas Univ., Dept. of Landscape Architecture, Zonguldak	2002
High School	Kızılırmak High School, Kirsehir	1998

WORK EXPERIENCE

Year	Place	Enrollment
2002 – Present	METU, Geodetic and Geographic Information Technologies Dept.	Research Assistant

PUBLICATIONS

Thesis Submitted

Ozdarici, A., 2005, Comparison of Different Spatial Resolution Images for Polygon-Based Crop Mapping. Thesis in Geodetic and Geographic Information Technologies, Middle East Technical University, Ankara, Turkey.

Peer-Reviewed Journal Papers

Turker M. and **Ozdarici A.**, 2011, Field-based crop classification using SPOT4, SPOT5, IKONOS, and QuickBird imagery for agricultural areas: A comparison study, *International Journal of Remote Sensing*, vol.32, pp. 9735-9768.

Ozdarici Ok A. and Akyurek Z., 2011, Evaluation of image fusion methods on agricultural lands, *Journal of Earth Science and Engineering* vol.1, pp.107-113.

International Conference Papers

Ozdarici Ok, A. and Akyurek, Z., 2011. Automatic training site selection for agricultural crop classification: A case study on Karacabey Plain, Turkey. In: *ISPRS Hannover Workshop, High Resolution Earth Imaging for Geospatial Information*, 14-17 June, Hannover, Germany.

Ozdarici, A. and Akyurek, Z., 2010, A comparison of SAR filtering techniques on agricultural area identification. In: *ASPRS Annual Conference*, San Diego, California.

Ozdarici, A. and M. Turker, 2007. Field-based classification of different resolution images and the filtering effects on the accuracies. In: *3rd International Conference on Recent Advances in Space Technologies*, Istanbul, Turkey, 14-16 June 2007.

Ozdarici, A. and M. Turker, 2006. Field-based classification of agricultural crops using multi-scale images. In: *First International Conference on Object-based Image Analysis (OBIA 2006)*, 4-5 July, Salzburg, Avusturya.

Ozdarici, A. and Turker, M., 2006. Comparison of multiscale images of an agricultural land using polygon-based classification techniques. In: *ISPRS Mid-Term Symposium 'From Pixels to Processes'*, 6-11 May, Enschede, The Netherland, CD.

Ozdarici, A. and Turker, M., 2005. Comparison of different spatial resolution images for polygon-based crop mapping. In: *ISPRS Conference of Spatio-Temporal data Mining*, Ankara, Turkey, CD.

National Conference Papers

Ozdarici A., Akar O. ve Gungor U., 2011. Rastgele Orman Sınıflandırma Yöntemi Yardımıyla Tarım Alanlarındaki Ürün Çeşitliliğinin Sınıflandırılması (*Classification of Crops in Agricultural Lands Using Random Forest Classification Method*), In: *Türkiye Ulusal Fotogrammetri ve Uzaktan Algılama Birliği (TUFUAB) VI. Teknik Sempozyumu*, 23-26 February, Antalya, Turkey.

Ozdarici A., Clinton N. ve Akyurek Z., 2010, “Ortalama Kaydırma ve Berkeley Görüntü Bölütleme (BIS) Yönteminin Çok Zamanlı Kompsat-2 Görüntüleri kullanılarak Değerlendirilmesi (*Evaluation of Mean-shift and Berkeley Image Segmentation (BIS) Results on Multitemporal Kompsat-2 Images*)”, In: *III. Uzaktan Algılama ve Coğrafi Bilgi Sistemleri Sempozyumu (UZAL CBS)*, 11-13 October, Kocaeli, Turkey.

Ozdarici, A. and Akyurek Z., 2009. Görüntü keskinleştirme yöntemlerinin tarımsal ürün sınıflandırması üzerindeki etkilerinin incelenmesi (*Evaluating the contribution of image fusion methods into the classification accuracies of agricultural lands*), In: *Türkiye Ulusal Fotogrametri ve Uzaktan Algılama Birliği v. Teknik Sempozyumu (TUFUAB)*, 4-6 February, Ankara, Turkey.

Ozdarici, A. ve Akyurek Z., 2008. Tarım alanlarının uydu görüntülerinden görsel belirlenmesinde görüntü zenginleştirme yöntemlerinin etkileri (*Influence of image fusion methods for visualization purposes on agricultural lands*). In: *Uzaktan Algılama ve Coğrafi Bilgi Sistemleri (UZAL CBS) Sempozyumu*, 13-15 October, Kayseri, Turkey.

Ozdarici, A. ve Ok, A. O., 2007. Mean-Shift segmentasyon algoritması destekli ‘En Büyük Olasılık’ sınıflandırma yöntemi kullanılarak tarım alanlarının sınıflandırılması (*Maximum Likelihood Classification Method supported with “Mean-Shift” segmentation algorithm to classify agricultural lands*). In: *Coğrafi Bilgi Sistemleri Kongresi*, 30 October -2 November, Trabzon, Turkey.